Waveform Synthesis for Active Sensing with Emerging Applications

BY

ARINDAM BOSE
B.Tech., West Bengal University of Technology, 2012
M.S., University of Illinois at Chicago, 2020

THESIS

Submitted as partial fulfillment of the requirements
for the degree of Doctor of Philosophy in Electrical and Computer Engineering
in the Graduate College of the
University of Illinois at Chicago, 2021

Chicago, Illinois

Defense Committee:

Mojtaba Soltanalian, Chair and Advisor
Dan Schonfeld
Daniela Tuninetti
Rashid Ansari
Perry Wang, Mitsubishi Electric Research Laboratories

To

Maa and Baba

ACKNOWLEDGMENTS

First and foremost, I would like to express my deepest gratitude to the entire universe for leading me toward this moment. This Ph.D. journey had been a truly enlightening experience for me. It was not an easy walk, nevertheless, it would not have been possible without the significant role everyone played in my life before and during this time.

I extend sincere gratitude to my advisor, Dr. Mojtaba Soltanalian, who has affectionately guided me throughout the entire Ph.D. journey with his extensive knowledge and unmatched patience. I will always remember the time when I first joined the WaveOpt lab. It was the summer of 2016 and I was merely an amateur Ph.D. student without a proper direction. It was he who accepted me despite having little research experience in the field and I can not thank him enough for providing me with the wonderful learning opportunity. It has been an exceptionally enriching experience to work with Dr. Soltanalian in these past years. He has always inspired me through his extraordinary mentorship and dedication to research. This dissertation would not exist without his vision, and his unwavering research as well as financial support.

I acknowledge my committee members: Dr. Dan Schonfeld, Dr. Daniela Tuninetti, and Dr. Rashid Ansari of the University of Illinois at Chicago (UIC); and Dr. Perry Wang of Mitsubishi Electric Research Laboratories (MERL) for agreeing to be a part of my Ph.D. dissertation committee. I am indeed grateful for the time and efforts they put in reviewing and evaluating this thesis and my research prospect in general.

ACKNOWLEDGMENTS (Continued)

Furthermore, I am grateful for the excellent collaborations with Dr. Jian Li of University of Florida, Florida; Dr. Bo Tang of University of Science and Technology of China, Hefei; Dr. Petre Stoica of Uppsala University, Sweden; Dr. Israel A. Arriaga-Trejo of CONACYT - the Autonomous University of Zacatecas, Mexico City, Mexico; and Dr. Aldo G. Orozco-Lugo of Center for Research and Advanced Studies, Mexico City, Mexico. I heartily appreciate their contributions of ideas that motivated my research and made this journey productive. I am also grateful for all the co-authors who have helped me by contributing their valuable inputs to the published and submitted journal and conference articles.

I am also fortuitous to work with an enthusiastic group of fellow students and members at the WaveOPT lab, UIC. I treasure all the selfless aid and heartily encouragements that I received from Shahin Khobahi, Naveed Naimipour, Aria Ameri, and everyone else during professional as well as personal time. My research life would not be such colorful without all the witty remarks made by these folks in the lab.

I am also grateful for all the roommates I have had and the friends I made since the time I came to the United States to pursue higher education. Especially I am thankful to have Chirag Agarwal as a friend who made this journey more interesting in every possible way. It had been more than a decade since I know him and he has always been a trusted and valuable friend to me. Not to mention, he has been a wonderful source of inspiration and I am glad that I started this Ph.D. journey with him.

During the course of my Ph.D., I have been fortunate to intern with research laboratories and companies. I am thankful to Dr. Perry Wang from MERL once again and Bryan Cattle

from KMB Telematics for giving me the wonderful opportunities to work on real-world problems and for teaching me valuable work and life lessons. The experiences I have gained through these internships have shown me how our research impacts the lives of millions of people around the world and has given me a different perspective toward research problems.

I would also like to thank the electrical and computer engineering department of UIC for all the times they have helped me in every step of the way toward the completion of this degree.

Moreover, I extend my gratitude toward the United States of America for giving me this excellent opportunity to grow into my best self. Not only it had remained as a patron for my higher educational endeavor, but also I have had the privilege of meeting the brightest minds and making friendships with wonderful welcoming people in this country. America has set me forward to a course I didn't even know was possible and helped me find myself a little bit more.

Finally, but not least, I am truly and deeply indebted to my parents Tapash Kumar Bose and Santi Bose, and my sister Kaberi Bose for their unconditional support. Apart from all the sacrifices they made, they also have provided me with immense understanding and moral support all these years. This dissertation is dedicated to them.

AB

PREFACE

This dissertation is an original intellectual product of the author, A. Bose. All of the work presented here has been conducted in the WaveOPT Lab at the University of Illinois at Chicago. The research effort has been partially supported by the National Science Foundation (NSF) under grants CCF-1704401, ECCS-1809225, and ECCS-1708509. Parts of the thesis are also partially supported by the Illinois Discovery Partners Institute (DPI) Seed Award and Cátedras Conacyt Project 3066. The results of these works have previously appeared (or are appearing) as journal articles and conference presentations. The copyright permissions for reusing the published materials have been presented in Appendix D.

Arindam Bose
March 19, 2021

CONTRIBUTION OF AUTHORS

In the works *Constructing binary sequences with good correlation properties: An efficient analytical-computational interplay*, and *Efficient construction of polyphase sequences with optimal peak sidelobe level growth*, Mojtaba Soltanalian was the lead investigator. Arindam Bose and Mojtaba Soltanalian carried out the derivation and experiment. Arindam Bose wrote the manuscripts with support from Mojtaba Soltanalian.

In the work *Designing signals with good correlation and distribution properties*, Arindam Bose and Neshat Mohammadi worked on the technical details and wrote the paper with the help from Mojtaba Soltanalian.

In the works *Design of unimodular sequence sets with good correlation and complementary correlation properties*, and *Generalized cyclic algorithms for designing unimodular sequence sets with good (complementary) correlation properties*, Arindam Bose and Israel A. Arriaga-Trejo formulated the problems and carried out experiments. The manuscripts were written with the inputs from Mojtaba Soltanalian and Aldo G. Orozco-Lugo.

In the works *Efficient waveform covariance matrix design and antenna selection for MIMO radar*, and *Joint optimization of waveform covariance matrix and antenna selection for MIMO radar*, both Arindam Bose and Shahin Khobahi contributed equally. They devised and designed the conceptual idea, performed the numerical experiments, and wrote the manuscripts with support from Mojtaba Soltanalian.

CONTRIBUTION OF AUTHORS (Continued)

The main idea of the works *Waveform design for mutual interference mitigation in automotive radar*, and *Mutual interference mitigation for multiple connected automotive radar systems* was originated in an earlier published work by Bo Tang, Wenjie Huang, and Jian Li. Later it was extended in the aforementioned works by Arindam Bose and Mojtaba Soltanalian. Arindam Bose wrote the final manuscripts with the help of Mojtaba Soltanalian, Bo Tang, and Jian Li.

In the work *Waveform design for one-bit radar systems under uncertain interference statistics*, Aria Ameri and Arindam Bose derived the problem formulation with the help from Mojtaba Soltanalian. The paper was written with inputs from all authors.

In the work *Deep Radar Waveform Design for Efficient Automotive Radar Sensing*, Shahin Khobahi coined the conceptual idea and Arindam Bose performed the numerical experiments. Both Shahin Khobahi and Arindam Bose contributed to the writing of the final version of the manuscript with inputs from Mojtaba Soltanalian.

AB

TABLE OF CONTENTS

TABLE OF CONTENTS (Continued)

CHAPTER **PAGE**

TABLE OF CONTENTS (Continued)

TABLE OF CONTENTS (Continued)

CHAPTER **PAGE**

LIST OF TABLES

LIST OF FIGURES

LIST OF FIGURES (Continued)

FIGURE **PAGE**

LIST OF FIGURES (Continued)

LIST OF FIGURES (Continued)

FIGURE **PAGE**

LIST OF ALGORITHMS

LIST OF ABBREVIATIONS

ACC	Adaptive Cruise Control
ADAS	advanced driver-assistance systems
ADC	Analog-to-Digital Converters
ADMM	Alternating Direction Method of Multipliers
AF	Ambiguity Function
AWGN	Additive White Gaussian Noise
CAF	Cross Ambiguity Function
CDMA	Code Division Multiple Access
CPI	Coherent Processing Interval
DFT	Discrete Fourier Transformation
DNN	Deep Neural Network
DoA	Direction of Arrival
DSP	Digital Signal Processor
DUN	Deep Unfolded Network
EM	Electro-Magnetic
EVD	Eigen Value Decomposition
FFT	Fast Fourier Transform

LIST OF ABBREVIATIONS (Continued)

FIR	Finite Impulse Response
FMCW	Frequency-modulated continuous-wave radar
GLRT	Generalized Likelihood Ratio Test
GPS	Global Positioning System
GPU	Graphics Processing Unit
IEEE	Institute of Electrical and Electronics Engineers
IFFT	Inverse Fast Fourier Transform
IoT	Internet of Things
ISL	Integrated Sidelobe Level
LIDAR	Light Detection and Ranging
LS	Least Squares
MF	Matched Filter
MIMO	Multiple Input Multiple Output
MMF	Mismatched Filter
MSE	Mean Squared Error
NAPC	Normalized Aperiodic Auto-correlation
NC	Normalized Cross-correlation
OFDM	Orthogonal Frequency Division Modulation

LIST OF ABBREVIATIONS (Continued)

PC	Personal Computer
PCAF	Periodic Cross Ambiguity Function
PD	Parkinson's Disease
PMLI	Power-Method-Like Iterations
PN	Pseudo Noise
PRF	Pulse Repetition Frequency
PSD	Positive Semi-Definite
PSL	Peak Sidelobe Level
PSNR	Peak Signal-to-Noise Ratio
RADAR	RAdio Detecting And Ranging
RF	Radio Frequency
RTML	Real Time Machine Learning
SCIR	Signal-to-Clutter-plus-Interference Ratio
SDP	Semi-Definite Programming
SDR	Semi-Definite Relaxation
SI	System Identification
SINR	Signal-to-Interference-plus-Noise Ratio
SISO	Single Input Single Output

LIST OF ABBREVIATIONS (Continued)

SL	Strictly Linear
SNR	Signal-to-Noise Ratio
SPS	Smooth Pursuit System
SQP	Semidefinite Quadratic Programming
SVD	Singular Value Decomposition
TPU	Tensor Processing Unit
ULA	Uniform Linear Array
UPDRS	Unified Parkinson's Disease Rating Scale
UQP	Unimodular Quadratic Program
WISL	Weighted Integrated Sidelobe Level
WL	Widely Linear
w.r.t.	with respect to
ZCZ	Zero Correlation Zone

NOTATIONS

Bold lowercase letters are used to denote the vectors while bold uppercase letters are for matrices.

The following mathematical notations are used throughout this thesis:

$\lvert x \rvert$	the absolute value of a scalar x
$[x]$	the integral part of a real scalar x, *i.e.*, the greatest integer $\leq x$
$\{x\}$	the fractional part of a real scalar x, *i.e.*, $\{x\} = x - [x]$
$\boldsymbol{x}_m(k)$	the k^{th} element of vector $\boldsymbol{x}_m$
$[\boldsymbol{X}]_{i,j}$	the $(i,j)^{\text{th}}$ element of matrix $\boldsymbol{X}$
$\lVert \boldsymbol{x} \rVert_p$	the l_p-norm of $\boldsymbol{x}$, defined as $(\sum_k \lvert \boldsymbol{x}(k) \rvert^p)^{\frac{1}{p}}$
$\lVert \boldsymbol{x} \rVert$	the l_2-norm of $\boldsymbol{x}$
$\boldsymbol{x} \circledast \boldsymbol{y}$	denotes convolution of $\boldsymbol{x}$ and $\boldsymbol{y}$
$\lVert \boldsymbol{X} \rVert_F$	the Frobenius norm of matrix $\boldsymbol{X}$ defined as $\sqrt{\sum_{i=1}^{m} \sum_{j=1}^{n} \lvert [\boldsymbol{X}]_{i,j} \rvert^2}$
$\boldsymbol{X}^*$	the complex conjugate of the matrix $\boldsymbol{X}$
$\boldsymbol{X}^T$	the transpose of the matrix $\boldsymbol{X}$
$\boldsymbol{X}^H$	the complex conjugate transpose of the matrix $\boldsymbol{X}$
$\boldsymbol{X}^\dagger$	the Moore-Penrose pseudoinverse of the matrix $\boldsymbol{X}$
$\text{Tr}\,(\boldsymbol{X})$	the trace of matrix $\boldsymbol{X}$
$\text{vec}\,(\boldsymbol{X})$	the vector obtained by column-wise stacking of matrix $\boldsymbol{X}$

NOTATIONS (Continued)

$\mathrm{diag}\,(\boldsymbol{X})$	denotes a vector formed by diagonal entries of the matrix $\boldsymbol{X}$
$\mathrm{Diag}\,(\boldsymbol{x})$	denotes a diagonal matrix formed by the entries of the vector $\boldsymbol{x}$
$\arg(\boldsymbol{X})$	the phase angle (in radians) of $\boldsymbol{X}$
$\mathrm{cov}\,(\boldsymbol{X})$	the covariance matrix of $\boldsymbol{X}$
$\Re(\boldsymbol{X})$	the real part of $\boldsymbol{X}$
$\Im(\boldsymbol{X})$	the imaginary part of $\boldsymbol{X}$
$\sigma_n(\boldsymbol{X})$	the n^{th} maximal eigenvalue of $\boldsymbol{X}$
$\lambda_n(\boldsymbol{X})$	the n^{th} maximal singular value of $\boldsymbol{X}$
$\boldsymbol{X} \otimes \boldsymbol{Y}$	the Kronecker product of two matrices $\boldsymbol{X}$ and $\boldsymbol{Y}$
$\boldsymbol{X} \odot \boldsymbol{Y}$	the Hadamard product of two matrices $\boldsymbol{X}$ and $\boldsymbol{Y}$
$\boldsymbol{X} \succ \boldsymbol{Y}$	$\boldsymbol{X} - \boldsymbol{Y}$ is positive definite
$\boldsymbol{X} \succeq \boldsymbol{Y}$	$\boldsymbol{X} - \boldsymbol{Y}$ is positive semidefinite
$\boldsymbol{I}_n$	the identity matrix of dimension n
$\mathbf{1}_n$	the all-one vector of size $n \times 1$
$\mathbf{0}_n$	the all-zero vector of size $n \times 1$
$\mathbf{0}$	the matrix with all elements as zero
$\boldsymbol{e}_n$	the n^{th} standard basis of $\mathbb{C}^n$ or n^{th} column of an identity matrix
$\mathbb{R}$	the set of real numbers

NOTATIONS (Continued)

$\mathbb{R}_+$	the sets of real non-negative numbers
$\mathbb{C}$	the set of complex numbers
$\mathbb{N}$	the set of natural numbers
$\mathbb{Z}$	the set of integers
$\mathbb{B}_N^M$	the set of binary vectors with size M and N non-zero elements, $N \leq M$
$\mathcal{S}^M$	the set of all real symmetric matrices of size $M \times M$
$\mathbf{F}_n$	the n dimensional discrete Fourier transform matrix
$\mathbb{E}\{\cdot\}$	the mathematical expectation of a random variable
$\mathbb{P}\mathrm{r}\{\cdot\}$	denotes the probability of a random event
$\mathrm{sign}(\cdot)$	the element-wise signum operator
$\mathrm{csign}(\cdot)$	the element-wise complex signum operator as $\mathrm{sign}(\Re\{\cdot\}) + j\mathrm{sign}(\Im\{\cdot\})$
$\mathcal{N}(\cdot,\cdot)$	the normal distribution with mean, and covariance as first and second arguments, respectively
j	the imaginary unit *i.e.*, $j = \sqrt{-1}$
$f(n) = \mathcal{O}(g(n))$	$f(n) < cg(n)$ for at least one $0 < c < \infty$
$f(n) = o(g(n))$	$f(n) < cg(n)$ for all $0 < c < \infty$
$f(n) = \Omega(g(n))$	$g(n) < cf(n)$ for some $0 < c < \infty$
$f(n) = \Theta(g(n))$	$f(n) = \mathcal{O}(g(n))$ and $f(n) = \Omega(g(n))$

SUMMARY

Throughout the history of mankind, we have sought ways and means to extend the boundaries of our sensory system with the help of science and technology. Active sensing systems have played a vital role in the advancement of human civilization— in navigation, communication, system identification, defense, energy cultivation, meteorology, space exploration, *etc.* It is well known that a judicious design of the transmit signals improves the performance of an active sensing system by enhancing the target detection and estimation capability by manyfold. This thesis is concerned with synthesizing waveforms for smart active sensing systems of forthcoming decades, *viz.*, (i) improved system identification and (ii) advanced radar systems. Several problems of signal optimization in the context of practical scenarios have been considered. The associated problems are studied and several novel algorithms are proposed and supported by several numerical examples.

CHAPTER 1

INTRODUCTION

Throughout history, humans have always sought to find ways to comprehend themselves and the world around them. The ability to acquire information is the key to understand the universe and by asking the *right* questions one may be able to understand it properly. *Signal Processing* is one branch of science that seeks to answer these questions. Consequently, collecting information, or in other words, *sensing* has always been an important part of our lives. Humans can perceive the physical reality using observations made by mostly five basic sensory systems: sight (visual sense), hearing (auditory sense), smell (olfactory sense), taste (gustatory sense), and touch (somatosensory sense). Ever since the beginning of humanity, we have tried to extend the boundaries of our sensory ability by building intelligent instruments through contemporary science and technology, and often we succeeded. For instance, now we know that there lies a whole electromagnetic spectrum beyond our observable range and the visible light is in fact merely a thin slice of the entire spectrum. Thus building better sensors have always been a particularly challenging, nevertheless highly sought-after objective among scientists.

Modern remote sensing instruments are primarily of two types [1]—

Passive sensors are able to detect and measure natural energy (or radiation) that is emitted or reflected by the subject or scene being observed. They mostly operate in the visible, microwave, infrared, and thermal infrared portions of the electromagnetic spectrum. Cameras are arguably the most popular and widely available passive sensors known to mankind. Advanced passive

sensors include Accelerometer, Radiometer, Spectrometer, *etc.* A benefit of using passive sensors is that they do not require any transmission power source to operate.

Active sensors, on the other hand, are able to provide their own source of power to illuminate the subject or scene that is under observation. Such sensors first emit suitable radiation in the direction of the target object to be investigated. They then detect and measure the radiated energy that is reflected or backscattered from the target object. One may find perfect examples of active sensing in the natural world, for instance, bats and dolphins use acoustic signals to communicate and to map their surroundings. Active sensing has played a vital role in the advancement of human civilization: navigation, communication, system identification, defense, energy cultivation, meteorology, space exploration, to name a few [2]. Most man-made remote sensors are active *e.g.*, Radar, Sonar, LIDAR, Laser altimeter, X-ray, GPS, Scatterometer, *etc.*

It is of paramount importance that the active sensing system must know the emitted waveforms completely in order to extract the most information about the target from the received waveforms. The judicious design of the transmit waveforms thus improves the performance of such systems by performing the act of *asking the right questions*. In the past decades, researchers have invested a tremendous amount of effort and resources into the design of efficient waveforms for smart active systems. This thesis aims to improve the state-of-the-art technologies for the synthesis of such smart waveforms for various active sensing systems that have tremendous potential in emerging applications for the coming decades *viz.*,

- Improved system identification, and
- Radar systems with advanced objectives.

1.1 Organization of the Thesis

This thesis is organized into two parts, each of which is devoted to one of the above applications. Part I describes waveform synthesis for the purpose of system identification. Part II is focused on signal design for the context of emerging applications in radar systems with advanced objectives. In the subsequent, we provide a detailed background and the relevant context for each of the advanced radar systems considered here and point out the contributions of this thesis.

1.1.1 Part I: Waveform Synthesis for Improved System Identification

System identification (SI) is the field of study where modeling of dynamic systems is done using experimental data [3, 4]. Mean square estimation (MSE) is one of the most fundamental and widely used tools for SI in statistical signal processing, assuming the underlying system regression is linear. The result of MSE is usually given when the input and output of the system are real-valued. However, the analysis remains valid when these quantities are complex-valued. Interestingly, when the input and the output are real and jointly normally distributed with zero-mean value, the regression simply stands as linear. Unfortunately, for the normal complex data it is no longer valid, and hence handling such scenario demands special consideration [5]. Based on the type of the systems being considered, they can be categorized into two classes: (a) *strictly linear* systems for real data (SL), and (b) *widely linear* (WL) systems for complex data. In the following, we unwrap these two classes in a detailed manner.

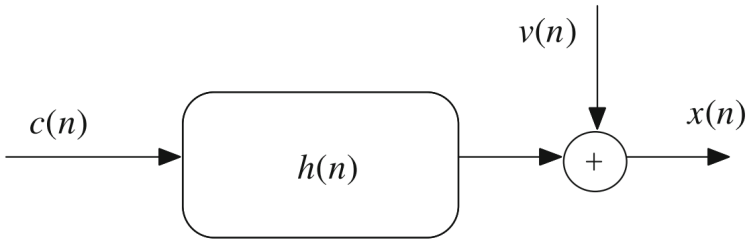

Figure 1. An illustration of SL system $h(n)$ with input $c(n)$, output $x(n)$ and disturbance $v(n)$ (Source: [4]).

1.1.1.1 Part I-A: Strictly Linear Systems

In SL processing, a discrete dynamic system can be characterized by a finite impulse response (FIR) $\{h(n)\}_{n=0}^{M-1}$, as depicted in Figure 1. Here n denotes the discrete-time and M is the length of the filter. The objective is to identify the M coefficients of the filter by probing the system using a training sequence $c(n)$ while observing the response $x(n)$ that is perturbed by additive white Gaussian noise (AWGN) $v(n)$ whose first and second-order statistics are known *a priori*. The observation $x(n)$ is then simply given as,

$$x(n) = (h \circledast c)(n) + v(n). \tag{1.1}$$

The configuration depicted in Figure 1 and Equation 1.1 is rather common in modeling the *channel estimation* problem in a wireless communication system. In a communication system, Figure 1 represents a baseband model where $\{h(n)\}_{n=0}^{M-1}$ is a filter with M coefficients that captures the effects of the channel and embeds them into the transmitted symbols. Owing to

the unique spectral characteristics of sequences with *good*[1] auto-correlation and cross-correlation properties, they are the keys to efficiently identify an SL system [6–8]. Several metrics have been proposed in the literature to measure the goodness of such sequences, for example, *peak sidelobe level* (PSL), *integrated sidelobe level* (ISL), *merit factor* (MF), *etc.*

Due to the simplicity in terms of hardware design, binary sequences with good correlation properties are excellent choices not only for system identification applications but also they play an important role in many active sensing and communication systems, ranging from modulation techniques to data encryption [9] *etc.* Moreover, the analytical construction of binary sequences requires only a little computational cost. Especially, the use of binary sequences or sequence sets with low aperiodic auto-correlation and small cross-correlation sidelobes in radar and sonar pulse compression systems is well regarded as they provide an efficient method of synchronization for modern active sensing and digital communication systems [10]. However, the optimization problems arising from designing such sequences are computationally expensive and NP-hard in general [11], especially for long binary sequences. Nevertheless, several numerical approaches have been suggested in the literature to construct binary sequences and many of its variance, including the skew-symmetric binary sequences [12], Rudin-Shapiro sequences [13], offset Legendre sequences [14], among others [11,15,16]. However, these methods seek to construct binary sequences whose *asymptotical* behavior of PSL growth is optimal. Hence the challenge remains open, baffling researchers for decades.

---

[1]In the literature, *good correlation properties* of a sequence means the out-of-phase correlation coefficients have significantly low magnitude, ideally zero.

It is interesting to note that sequence sets with asymptotically optimal auto/cross-correlation PSL growth have been known in the literature for a long time, and their construction has been studied both analytically and numerically. However, it has been a long-standing problem whether we can construct a family of binary sequences whose auto-correlation PSL grows in an optimal manner. In **Chapter 2**, we bridge the gap between analytical construction and computational search. Here we introduce a construction approach for binary sequences with *asymptotically* optimal PSL growth from the sequence sets with good correlation properties. A key component of the design follows from the observation that if the PSL of the sequence set grows *optimally* or *nearly optimally*, then the PSL of the constructed binary sequence will experience similar growth as a consequence. The proposed construction is simple-to-implement and is shown to be accomplished in polynomial-time.

This chapter is based on the following published articles[1]:

[J1] Bose, A. and Soltanalian, M.: Constructing binary sequences with good correlation properties: An efficient analytical-computational interplay. IEEE Transactions on Signal Processing, 66(11):2998–3007, June 2018.

[C1] Bose, A. and Soltanalian, M.: Efficient construction of polyphase sequences with optimal peak sidelobe level growth. In 2017 IEEE Global Conference on Signal and Information Processing (GlobalSIP), pages 81–85, Montreal, Canada, November 2017.

---

[1][J]: Journal papers, [C]: Peer-reviewed conference papers.

Chapter 3, on the other hand, addresses the problem of designing sequences with not only good correlation but also good distribution properties. Sequences with specific distribution properties play an important role in biomedical system identification. In this chapter, we propose an efficient computational framework for designing sequences with two key properties: (i) an impulse-like auto-correlation, and (ii) a probability distribution of sequence entries which is uniform in nature; although the results can be easily extended to an arbitrary distribution. The proposed method is based on utilizing the Fast Fourier Transform (FFT) operations and thus can generate very long sequences in small time frames.

The material for this chapter is based on the following article:

[C2] Bose, A., Mohammadi, N., and Soltanalian, M.: Designing signals with good correlation and distribution properties. In 2018 IEEE International Conference on Acoustics, Speech and Signal Processing (ICASSP), pages 4349–4353, Calgary, Alberta, Canada, April 2018.

1.1.1.2 Part I-B: Widely Linear Systems

WL systems, unlike SL systems, exploit the complex conjugate of the input signal as an additional degree of freedom for linear processing. Using the complete second-order characterization (*i.e.*, the complementary correlation properties), the performance of the sensing and identification systems can be enhanced by performing WL signal processing, as shown in [5, 17].

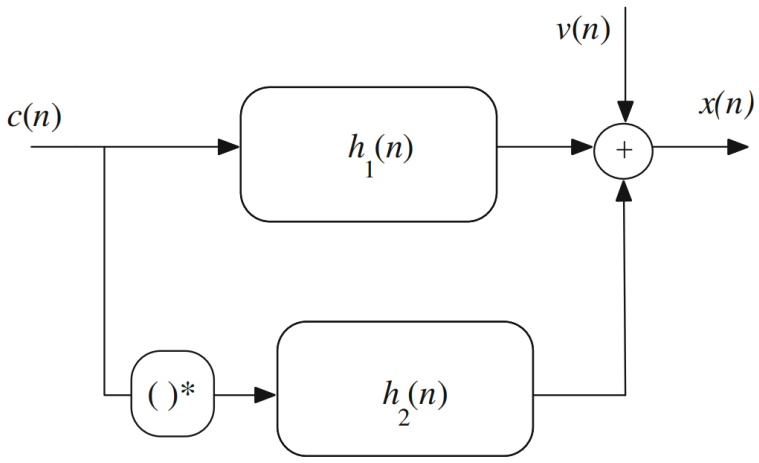

Figure 2. An illustration of WL system with input $c(n)$ probed into $h_1(n)$ and $c^*(n)$ probed into $h_2(n)$, output $x(n)$ and disturbance $v(n)$ (Source: [4]).

A WL system can be characterized by two impulse responses $\{h_1(n)\}_{n=0}^{M-1}$ and $\{h_2(n)\}_{n=0}^{M-1}$ as depicted in Figure 2. The observation $x(n)$ is modeled as,

$$x(n) = (h_1 \circledast c)(n) + (h_2 \circledast c^*)(n) + v(n). \tag{1.2}$$

Modeling of systems using WL structures often arises especially in wireless communication systems since in such systems non-linear radio frequency (RF) impairments are considered in the analysis of signal modeling [4, 18, 19]. Such impairments include in-phase and quadrature-phase (I/Q) imbalances that introduce interference in direct conversion transceivers employing multi-carrier techniques such as Orthogonal Division Frequency Modulation (OFDM). In order to alleviate such interference, one is required to synthesize sequences that are especially adequate to

handle WL systems. **Chapter 4** presents the problem of designing sets of unimodular sequences with good cross-correlation as well as complementary cross-correlation properties over a zero-correlation-zone (ZCZ) for the systems that especially employ WL signal processing. We provide a gradient-based optimization approach to minimize a weighted ISL (WISL) criterion.

This chapter is based on the following published article:

[C3] Arriaga-Trejo, I. A., Bose, A., Orozco-Lugo, A. G., and Soltanalian, M.: Design of unimodular sequence sets with good correlation and complementary correlation properties. In 2018 IEEE Global Conference on Signal and Information Processing (GlobalSIP), pages 121–125, Anaheim, California, USA, November 2018.

Furthermore, **Chapter 5** introduces another novel generalized cyclic algorithm for the aforementioned problem that seeks to minimize the same WISL criteria for the processing of WL systems. The proposed algorithm is based on a well-known cyclic algorithm named WeCAN, which was first proposed in [20].

The material for this chapter comes from the following publication:

[C4] Bose, A., Arriaga-Trejo, I. A., Orozco-Lugo, A. G., and Soltanalian, M.: Generalized cyclic algorithms for designing unimodular sequence sets with good (complementary) correlation properties. In 2018 IEEE 10th Sensor Array and Multichannel Signal Processing Workshop (SAM), pages 287–291, Sheffield, UK, July 2018.

1.1.2 Part II: Waveform Synthesis for Advanced Radar Systems

In real-life applications, the problem of waveform synthesis is often paired with a secondary objective. Engineers often aim to generate smart waveforms that focus on specific objectives serving specific applications. Furthermore, in order to receive the full benefit of the realized waveform, one may as well need to consider designing a secondary aspect of the said application. In this part of the thesis, we consider several of such design objectives along with waveform synthesis for the context of radar (RAdio Detecting And Ranging) technology.

Similar to the problem of system identification, a radar system uses electromagnetic energy pulses to acquire information about its surroundings. Here the idea of identification of a system is more abstract. As shown in Figure 3, the RF energy is transmitted to and reflected from the target object. Depending on many factors such as antenna gains, transmit power, the distance of the target from the transmitter-receiver, radar cross-section (RCS) of the target, *etc.* , a portion of the reflected energy (also known as *echo*) returns back to the radar receiver. The radar system then uses the echoed signal to determine the direction, distance, and other dynamical information of the target. For instance, a land-based surveillance radar system transmits electromagnetic (EM) waves toward the sky in order to find passing targets such as airplanes, birds, drones *etc.* Once the targets interact with the inbound EM field, a small portion of the transmitted signal returns back to the radar receiver with a unique signature imprinted by the targets' dynamical as well as material properties. For example, by simply measuring the round-trip time delay of the returned signal, the distance (a.k.a. range) between the radar system and

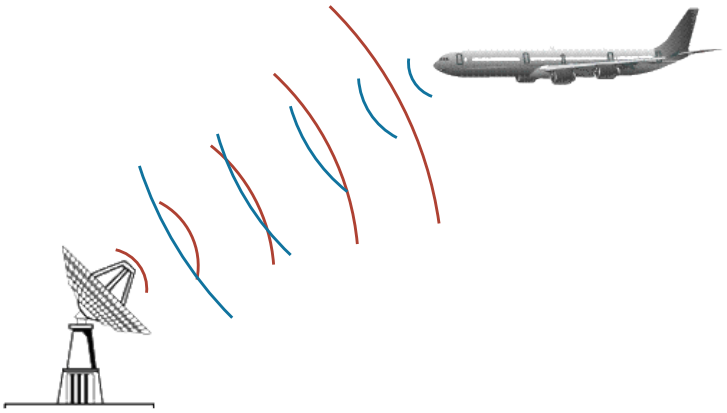

Figure 3. An illustration of basic wave propagation in a radar system.

the target object can be estimated since the speed of propagation for radio waves is known[1]. Moreover, by carefully processing the received signal, additional target properties can also be attained, as we shall see later in this chapter. For instance, any Doppler shift in the received signal indicates the dynamical information of the target [21].

Since the publication of "Theory of the Electromagnetic Field" by Scottish physicist James Clerk Maxwell in 1865, physicists have known that electric and magnetic waves travel through space at a constant speed. However, using EM waves as active sensing agents due to such properties did not get popularized until the late nineteenth and early twentieth century. In 1904, Christian Hülsmeyer, a German physicist and engineer conducted the first set of radar experiments using his invention named "telemobiloscope" to identify ships in the presence of dense fog using EM waves [22]. A decade later in 1914, a Canadian-American engineer named

---

[1]The *round-trip* speed of EM wave in vacuum is 299792458 m/s.

Reginald A. Fessenden, demonstrated the same wave functionality using an acoustic echo device termed as Fessenden oscillator, in order to detect icebergs off the east coast of Canada after the tragic 1912 *Titanic* disaster [21]. Mostly impelled by scientific innovations for general war events, radar technology underwent a strong advancement boost especially in the course of the two world wars, and since then it has become an integral part of our civilization. Later on, this technology had spread into diverse fields including weather monitoring, flight control, and underwater and underground sensing.

A fundamental objective of radar engineers is to design waveforms (also known as *waveform diversity*) that constructively make use of radar resources *i.e.*, transmitters and receivers that are possibly distributed in the time, frequency, and polarization domains [23]. According to IEEE Radar Standard P686/D2 (January 2008), the definition of waveform diversity is the "Adaptivity of the radar waveform to dynamically optimize the radar performance for the particular scenario and tasks. May also exploit adaptivity in other domains, including the antenna radiation pattern (both on transmit and receive), time domain, frequency domain, coding domain, and polarization domain." The insatiable demand for extreme remote sensing capabilities in military applications has always fueled the research of a new paradigm of waveform diversity whose potential has led to many more interesting and promising remote sensing ideas even in civil applications [24] such as in automotive radars [25, 26], Google's hand gesture recognition radars [27], and many more. Often waveform synthesis for these applications demands low SWaP-C (size, weight, power, and cost) radar devices. For these reasons, as we have discussed earlier, one needs to address additional requirements and explore secondary degrees of freedom

in conjunction with waveform design. Part II of the thesis aims to explore various ideas to optimize for such secondary degrees of freedom while designing waveforms that focus on particular applications. Especially, we investigate the following ideas while synthesizing signals:

(a) Designing the positions of radar antenna elements for multiple-input-multiple-output (MIMO) radars,

(b) Mitigating mutual interference between multiple radar systems mounted on automotive radars,

(c) Designing receive filter for one-bit cognitive radars, and

(d) Radars systems that use deep neural networks (*deep radars*).

In the following, we discuss the design context of each of the advanced applications in a detailed manner.

1.1.2.1 Part II-A: Antenna Array Design for MIMO Radar

In this part, we devise a joint design scheme of antenna array positions along with waveform synthesis for MIMO radars with non-uniform linear arrays. MIMO radar refers to a unique radar architecture that employs multiple spatially distributed transmitters and receivers— an emerging technology in the last two decades, attracting a great deal of interest from researchers in the radar signal processing community as well as the industry [28–34]. The presence of multiple transmitters and receivers inherently enables waveform diversity that not only improves parameter identifiability significantly but also introduces enhanced flexibility for transmitting beam-pattern and waveform design for more precise target parameter estimation and imaging

[24, 31, 32]. It is well known that the accuracy of target detection and parameter estimation revamps with the number of available independent channels of an adaptive MIMO array.

Unlike a conventional phased array radar, a MIMO transmitter can transmit a set of arbitrary waveforms in order to increase the spatial diversity [31, 35]. One way to exploit such diversity in MIMO systems is by transmitting orthogonal waveforms, and the echo signals can then be re-assigned to the single transmitter. Figure 4(a) shows an example of a MIMO array system with M transmitter and N receiver antennas [36]. Note that from such an antenna array system, a MIMO architecture results in a virtual array of $M \times N$ independent elements by using only $M \cdot N$ physical elements, as depicted in Figure 4(b). For instance, let us assume that a target is located at $\boldsymbol{u}$, the m^{th} transmit antenna and n^{th} receive antenna are located at $r_{T,m}$ and $r_{R,n}$ positions, respectively, and furthermore, $\{x_m(t)\}_{m=1}^{M}$ is the signal being transmitted at time t. The received signal $y_n(t)$ at n^{th} receive antenna can be expressed as [36]:

$$y_n(t) = \sum_{m=1}^{M} x_m(t) \exp\left(j\frac{2\pi}{\lambda}\boldsymbol{u}^T(r_{T,m} + r_{R,n})\right) \tag{1.3}$$

where λ is the wavelength of the transmitted electromagnetic wave and $j^2 = -1$. Note that term $(r_{T,m} + r_{R,n})$ in Equation 1.3 contains the information of individual propagation path that is crucial to extract M signals from n^{th} receive antenna, *iff* one uses $\{x_m(t)\}_{m=1}^{M}$ as an orthogonal set [37]. Many methods are widely available to achieve orthogonality of the transmitted waveforms, such as time-division multiplexing (TDM), frequency-division multiplexing (FDM), and spatial coding [38].

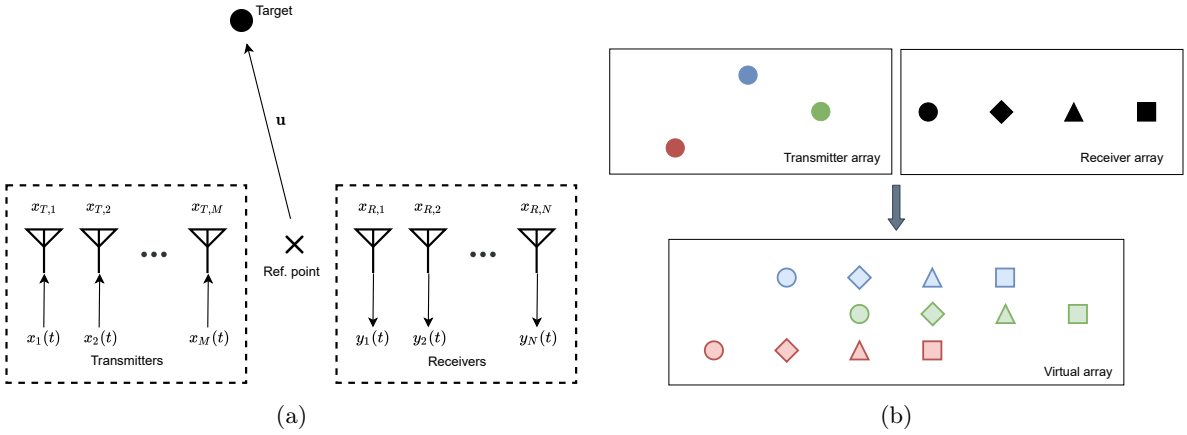

Figure 4. A MIMO radar system: (a) Diagram of a MIMO array system with M transmit and N receive antennas (Source: [36]), (b) Illustration of an example of 12 virtual arrays created by 3 transmit and 4 receive antennas.

Virtual array thus provides additional degrees of freedom to improve the spatial resolution [39, 40], immunity to interference [41], and an improved target localization capability [42–44] in a radar system. The advantages of MIMO radar over traditional phased array radar have inspired researchers to address various associated waveform design problems. Among them, one important problem is to design the probing waveforms to approximate a desired transmit beam-pattern under practical constraints *e.g.*, maximum transmit power, maximum mainlobe width or sidelobe height, *etc.* [45–48]. The main focus of this design problem is to control the spatial distribution of the transmit power. One may impose additional constraints on the class of transmit waveform (*e.g.*, unimodular sequences) based on the intended applications. Alternatively, one can consider the design of the probing signal *covariance matrix* in lieu of the

probing signal itself. The covariance matrix acts as an oracle for the waveform design problem and provides more degrees of freedom compared to designing the waveforms directly [49–55].

Moreover, interestingly, it has been pointed out in the literature [54,56,57] that the selection of the array position can introduce additional degrees of freedom and enhance target detection capability of the radar. Especially, by carefully choosing the position of the transmit and/or receive antennas, one will be able to design a desired beam-pattern using a fewer number of antennas. In other words, one can achieve the desired beam-pattern by carefully redistributing the available antennas in a wider transmit/receive field which amounts to increased virtual aperture. As a consequence, a joint design of the covariance matrix and the antenna selection vector can procure superior performance compared with current state-of-the-art methods using uniform linear arrays (ULA) with the same number of antennas.

Chapter 6 investigates the problem of designing the waveform covariance matrix while approximating the desired beam-pattern for the case of a distributed MIMO radar system where antenna positions are not fixed. We jointly design the antenna position vector and the transmit covariance matrix, as well as minimize the cross-correlation sidelobe of the received waveforms reflected back from the targets. We formulate this design task as a non-convex optimization problem and then propose a cyclic optimization approach to approximate its solution. We further propose a local binary search algorithm in order to efficiently design the corresponding antenna positions. We show that the proposed method can be extended to the more general case of approximating the given beam-pattern using a minimal number of antennas while optimizing their positions.

This chapter is based on the following published articles:

[J2] Bose, A., Khobahi, S., and Soltanalian, M.: Efficient waveform covariance matrix design and antenna selection for MIMO radar. Signal Processing, 183:107985, 2021.

[C5] Bose, A., Khobahi, S., and Soltanalian, M.: Joint optimization of waveform covariance matrix and antenna selection for MIMO radar. In 2019 53rd Asilomar Conference on Signals, Systems, and Computers, Pacific Grove, CA, USA, November 2019.

1.1.2.2 Part II-B: Mutual Interference Mitigation for Automotive Radar

Automotive radars have become more relevant in the last decade or so, especially as the means to safely drive in consumer motor vehicles as a part of their advanced driver-assistance systems (ADAS). It is reported that every year about 1.35 million[1] people die from road accidents, with thousands more being injured. Automotive radar systems not only play a key role in improving car safety measures but also meet key criteria such as low size and cost. Because of high market demand, various automotive radar systems are now widely used in consumer vehicles that enjoy cutting edge ADAS such as adaptive cruise control (ACC), stop-and-go, blind spot detection (BSD), autonomous emergency brake (AEB), rear crash warning (RCW), lane change assistance (LCA), front/rear cross-traffic-functions (FCTA/RCTA), lane change assistance (LCA), parking assistance (PA), reverse-autonomous emergency braking (R-AEB), *etc.* to name a few [58].

---

[1]World Health Organization – Global status report on road safety 2018.

Automotive radar sensors can be categorized into two classes: short-range radars (SRR) are used to detect targets within 30 m, and long-range radars (LRR) are used for targets that are at 200 m and beyond. According to FCC guidelines, 24-26 GHz (K band) frequency is used in SRRs and are mostly used for short-range applications *e.g.*, BSD, PA, obstacle detection and collision avoidance *etc.* On the other hand, LRRs use 77-81 GHz (W band) that provides better resolution and accuracy in a smaller size. These radars are primarily used for measuring the range and velocity of target vehicles and sensing objects within a wider field of view *e.g.*, for traffic alert systems in cross-sections. Such long-range applications require higher resolution within a more limited scanning range [59]. These long-range automotive radars are mostly powered by frequency modulated continuous waveform (FMCW) technology. Unlike the traditional pulsed radars, FMCW radars use continuous wave modulation for transmission that does not have a high peak-to-average power ratio (PAPR), making the hardware design flexible and simplified for antennas and other RF components like mixers and power amplifiers.

FMCW radar sensors can continuously transmit signals like a simple continuous-wave (CW) radar. However, unlike CW radar, the operating frequency of FMCW can be regulated during the sensing process, therefore making transmitted signal frequency modulated. The main advantages of using FMCW radar are following [59–61]:

- Potential narrow resolution allows measurement of very small ranges. The minimal measurable range is comparable to the transmitted wavelength.
- Very high accuracy of range measurements.

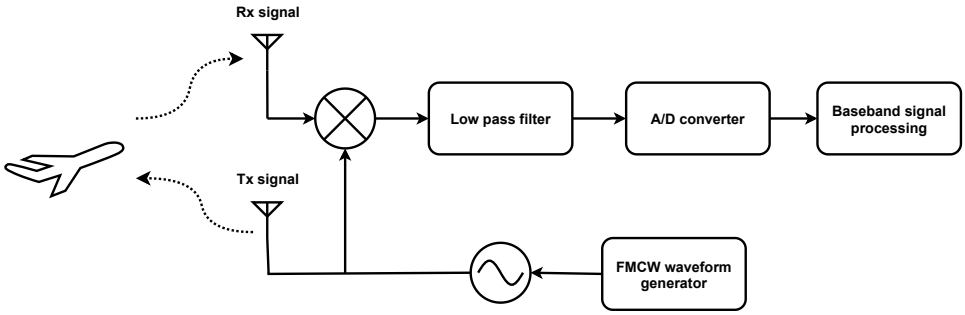

Figure 5. Block diagram of an FMCW radar system.

- Unlike pulsed radar, with FMCW, one can simultaneously transmit and measure the received signal.
- Because the transmit and receive signals are "always-on", there is zero blind range. This means that there is no "blind spot" in between transmit and receive, where something could be missed.
- Pulsed radar systems have high levels of peak power; this is not the case for FMCW.
- The received signal is mixed down to lower frequencies, so the processing circuitry and algorithms need not be so complicated and expensive.
- Because of the simpler circuit design, and the capabilities of modern digital signal processors (DSPs), overall cost and the size and weight of FMCW radar modules are lower than other radar standards.

An FMCW radar system consists of a transmitter, a receiver, a mixer to produce a signal with an intermediate frequency, and finally, an analog-to-digital converter (ADC) to sample and

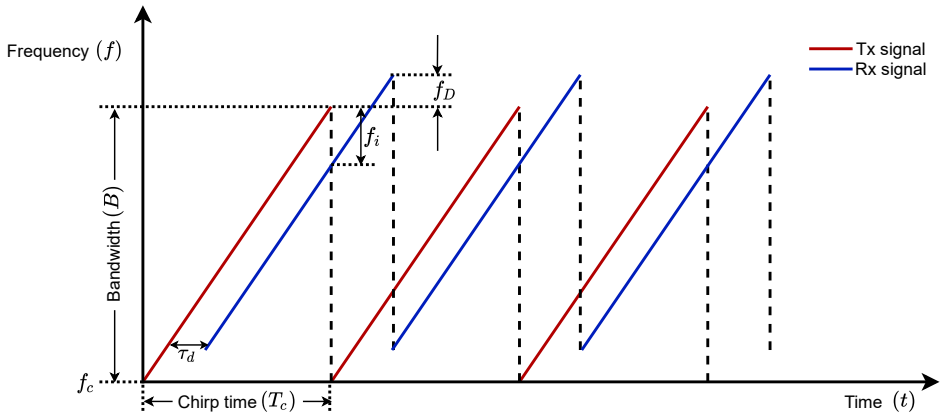

Figure 6. FMCW sawtooth signal model.

quantize the received signal as shown in Figure 5. The transmitter broadcasts a frequency modulated signal called a "chirp" toward the field of interest. A chirp is nothing but a sinusoid whose frequency increases linearly for a certain amount of time which is termed as "chirp duration" (T_c). Several modulations techniques are used for FMCW transmit signals such as sawtooth, triangle, square-wave (simple frequency-shift keying, FSK), stepped modulation (staircase voltage) and sinusoidal [38]. Figure 6 shows an example of a simple sawtooth FMCW signal where f_c is the starting frequency and B is the bandwidth of FMCW transmission. The horizontal axis represents the time (t) in a coherent processing interval (CPI) with 3 chirps and the vertical axis represents the instantaneous frequency (f).

The transmitted FMCW waveform can be expressed as [62]

$$s_T(t) = A_T \cos\left(2\pi f_c t + 2\pi \int_0^t f_T(\tau) d\tau\right) \tag{1.4}$$

where $\frac{B}{T_c}$ is the slope of the frequency increment, $f_T(t) = \frac{B}{T_c}t$ denotes the instantaneous transmit frequency expressed as a linear function of time, and A_T represents the transmitted signal amplitude. Assume a target at a distance R_0 from the radar, is moving away at a radial velocity of v m/s. The receiver will then collect the reflected signal that resembles the transmitted signal, that has a temporal shift $\tau_d = 2\frac{R_0+vt}{c}$, and a Doppler shift $f_D = -2\frac{f_c v}{c}$, where c is the speed of EM wave in free space. Thus the receive frequency is denoted as $f_R(t) = \frac{B}{T_c}(t - \tau_d) + f_D$. Finally, the received signal can be expressed as

$$\begin{aligned} s_R(t) &= A_R \cos\left(2\pi f_c(t-\tau_d) + 2\pi \int_0^t f_R(\tau)d\tau\right) \\ &= A_R \cos\left(2\pi\left(f_c(t-\tau_d) + \frac{B}{T_c}\left(\frac{t^2}{2} - \tau_d \cdot t\right) + f_D t\right)\right) \end{aligned} \tag{1.5}$$

where A_R is the amplitude of the received signal that depends on multiple factors such as transmitted power, antenna gains, the target's distance from the radar sensors, and RCS of the target. Generally, the value of A_R is significantly small *w.r.t.* that of A_T. Once, the reflected signal is captured, $s_R(t)$ is then mixed with $s_T(t)$ by multiplication in the time domain, and passed through a low-pass filter (LPF). This process allows to bring the operating frequency down to a lower level, making the design process less complicated. The intermediate frequency (IF) signal $S_i(t)$ of the LPF output is then obtained as

$$s_i(t) = \frac{1}{2}\cos\left(2\pi f_c \frac{2R_0}{c} + 4\pi\left(\frac{R_0}{c}\frac{B}{T_c} + \frac{f_c v}{c}\right)t\right). \tag{1.6}$$

In the above expression, some terms that are not time-dependent (phase terms) contain the range information, and terms that are proportional to t are seen in the spectrum of the signal. In a reasonably high SNR scenario, the frequency peak then can be observed at

$$f_p = \frac{R_0}{c}\frac{B}{T_c} + \frac{f_c v}{c} \tag{1.7}$$

so that there is one peak containing both the Doppler and range information and from which it is not very difficult to extract velocity information of the target once the range is resolved [63, 64].

FMCW has gained considerable popularity in the automotive industry due to its simplicity in signal processing. Given the tendency to mass-produce radars in civilian applications, such systems, however, tend to be quite similar, or even almost identical. The increasing number of similar or identical radar systems increases the probability of mutual interference, which may result in severely reduced radar sensitivity, poor performance quality, and increased false alarm rates [65, 66]. In **Chapter 7**, we address the problem of interference mitigation in similar radar systems. To this end, we begin by proposing two algorithms for designing slow-time codes to modulate the chirps for a simple SISO scenario. Specifically, the first coding scheme relies on Doppler shifting and the second one is devised based on an optimization approach. The difficulty and complexity of the problem of mutual interference increases when the vehicles are equipped with MIMO radar systems. We thus extend our discussion to the more general case of MIMO radars and propose an efficient algorithm to design waveforms to mitigate mutual interference in such systems. We propose an efficient waveform design algorithm that seeks to

minimize a collective cross-ambiguity function. Our quest does not stop here as the interference intensifies even further with a growing number of vehicles present on the scene. We hence provide a generalized formulation of the problem for multiple-MIMO cases. The proposed coding schemes are computationally efficient in practice and the incorporation of such schemes requires only a slight modification of the existing systems. Although for the multiple-MIMO case, the computational complexity becomes cumbersome as the number of MIMO radars grows, the design can be performed online in a collaborative manner, or offline, in which case the radar codes can be designed and stored in a codebook for future use.

This chapter is based on the following submitted articles:

[J3] Bose, A., Tang, B., Huang, W., Soltanalian, M., and Li, J.: Waveform design for mutual interference mitigation in automotive radar. 2021.

[J4] Bose, A., Tang, B., Soltanalian, M., and Li, J.: Mutual interference mitigation for multiple connected automotive radar systems. 2021.

1.1.2.3 Part II-C: Receive Filter Design for One-Bit Cognitive Radar

It is important to note that some of the most power-consuming modules in a radar system are the digital sampling devices and the ADCs. As we have discussed in the previous sections (*cf.* Section 1.1.2.2), recently, in many civilian applications, the demand for low SWaP-C radar systems has increased significantly [25–27, 67]. High precision RF sampling in digital radar is a barrier to meet such demands as in most sophisticated radar techniques, the receiver is assumed to have high precision ADC that are bulky and consume the most power. On the other hand,

using a lower precision ADC in a sensing system puts more burden on post-processing techniques. In classical signal processing, the quantization noise is usually modeled under the assumption of additive noise that minimally affects the accuracy of algorithms that consider the infinite or very high precision case, especially when the sampling interval is low [68]. The assumption of high-precision data is, however, inappropriate when the measurements are extremely quantized to very low bit-rates. In the most extreme case, the sampling process is done by utilizing a simple sign comparator and the received signal is represented using only one bit per sample [67, 69]. The one-bit RF sampling strategy used in digital radar is a promising approach to meet these demands in practical low resource scenarios [67].

One-bit quantizers, on one hand, are not only low SWaP-C devices but also much faster and simpler than the traditional digital quantizers, thus significantly reducing the complexity of hardware implementation. On the other hand, it is now well known that signals can be recovered with high accuracy from one-bit measurements, thanks to recent advancement in sensing theory, however at a slightly increased computational cost [70–73]. In an *one-bit radar* system, the conventional radar measurement scheme simply is replaced by the direct one-bit RF sampling as shown in Figure 7. The aforementioned increased cost incurs from the fact that by using a one-bit receiver, the knowledge of statistics of the surroundings is available only in a normalized sense and such uncertainties prohibit one from using traditional algorithms.

In cognitive active sensing applications, one of the objectives is to jointly optimize the transmit sequence, as well as the receive filter as a smart listener using *a priori* knowledge of *interference* and *clutter* in order to increase the estimation accuracy of the target parameters

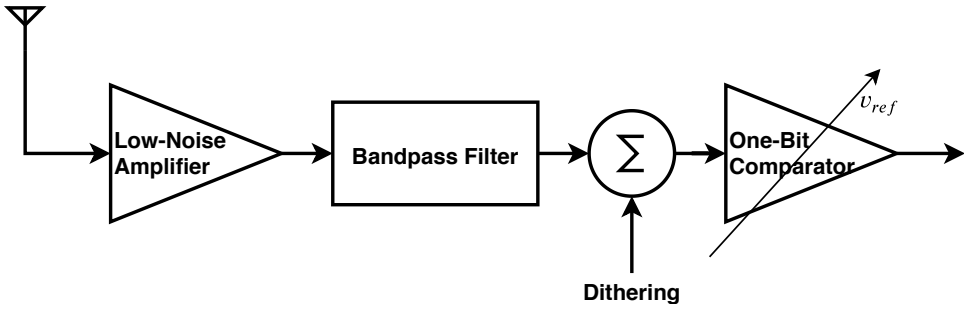

Figure 7. RF sampling front end of one-bit radar with unknown dithering.

[74–76]. In radar literature, clutter refers to the unwanted echoes that are usually correlated with the transmitted waveform, while the signal independent noise as well as (adverse) jamming signals are termed as interference [75]. A natural way to minimize the effects of clutter and interference is to aim for maximization of the signal-to-clutter-plus-interference ratio (SCIR) of the received energy. In such cases, the knowledge of interference statistics (particularly the covariance) plays a vital role in the effective design of the radar waveforms. In a one-bit radar, however, the received signal and interference statistics are available subject to some uncertainties, as the interference covariance matrix can be obtained merely in a normalized form. **Chapter 8** formulates such a waveform optimization problem and devises an algorithm to design the transmit waveform and the receive filter of one-bit radars given uncertainties in acquired interference statistics.

This chapter is based on the following article:

[C6] Bose, A., Ameri, A., and Soltanalian, M.: Waveform design for one-bit radar systems under uncertain interference statistics. In 2019 53rd Asilomar Conference on Signals, Systems, and Computers, Pacific Grove, CA, USA, November 2019.

1.1.2.4 Part II-D: Deep Radar

Bear in mind that all the aforementioned techniques rely on different physics-based parametric mathematical models that are central to the understanding and design of complex active sensing systems. These models, however, usually do not consider the sophisticated interactions intrinsic to the system and thus fail to fully elaborate a complex system. Purely data-driven or learning-based models, on the other, hand shed light on these blind spots. Such approaches do not rely on explicit mathematical models for data interpretation and thus have broader applicability, although at the cost of lower interpretability. On one hand in modern times, the continually exploding amount of information produced by humans and machines has created a unique opportunity for learning from the data itself. On the other hand, the advent of low-cost and powerful computing resources (*e.g.*, Graphical processing units (GPUs), and more recently Tensor processing units (TPUs)) have made it possible to realize highly complex computations within fractions of seconds. These two crucial factors together have paved the way for *deep neural networks* (DNNs) and machine learning-based models to showcase their effectiveness in modern socio-economic and engineering applications. Interestingly, such deep learning-based methods employ non-linear transformations of a generic linear structure to obtain an abstract representation of the underlying data. In contrast, they do lack interpretability and thus relia-

bility by being often ignorant of the underlying mathematical intricacies which are implicit in model-based signal processing.

In the scientific community, hence, there has been a demand to develop hybrid frameworks that enjoy the fruits of both model-based and data-driven approaches to enhance the accuracy, computational complexity, and efficiency of the data acquisition model in complex, large-scale scenarios. Recent advancement in the *deep unfolding networks* (DUNs) has paved the way to combine well-established signal processing approaches with data-driven architectures [77–81]. Deep unfolding architectures rely on the already established optimization or inference frameworks that are iterative in nature. The iterations of such algorithms are then *unfolded* onto the layers of a deep network, where each layer closely resembles one iteration of the underlying algorithm. This way such hybrid methods benefit not only from the low computational complexity of deep architectures but also from the flexibility and reliability of model-based methods.

Figure 8 depicts the stark comparison between DNNs and DUNs with respect to their general architectures. Deterministic DNNs are constructed in a fashion that inference is straightforward where the output of the network is obtained via consecutive matrix multiplications resulting in a fixed computational complexity inference model. However, they are neither necessarily faithful nor aware of the underlying mathematical model. Furthermore, massive networks often are difficult to handle, making them impractical for real-time machine learning (RTML) applications. On the contrary, DUNs incorporate sparser networks responsive to RTML by employing problem-level reasoning in the deep architecture. The success of DUNs in classical signal process-

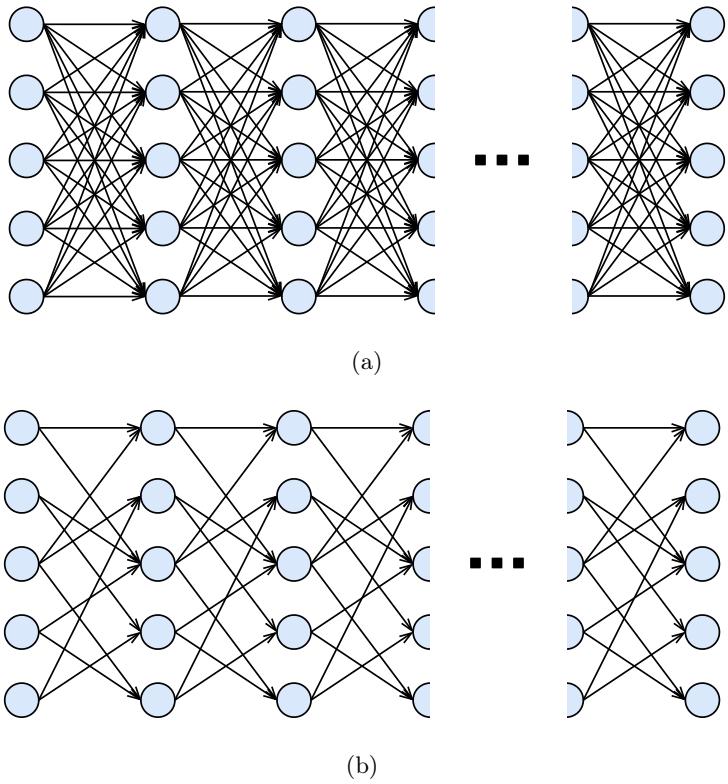

Figure 8. The comparison of general architectures between (a) generic DNNs and (b) DUNs.

ing has called for a new research paradigm in the radar community to investigate the usability of deep networks in radar systems or in other words *deep radars*.

In **Chapter 9**, we propose a novel technique to synthesis waveform for radar systems using such a deep unfolded network. Note that the goal of smart waveform design for radar systems is to acquire the maximum amount of information from the desirable sources in the environment, where in fact, *the transmit signal can be viewed as a medium that collects information*. In light of this, we employ the deep unfolding framework that aims to take the well-established iterative

approaches, and design a deep architecture for waveform design in radar systems under unimodular signal constraint, and boost the performance of the underlying inference optimization algorithm in terms of speed of convergence and effectiveness.

This chapter is based on following published article:

[C7] Khobahi, S., Bose, A., and Soltanalian, M.: Deep Radar Waveform Design for Efficient Automotive Radar Sensing. In 2020 IEEE 11th Sensor Array and Multichannel Signal Processing Workshop (SAM), Hangzhou, China, June 2020.

In each chapter, several numerical examples are provided to evaluate the performance of each of the proposed methods. When applicable, the results are further compared with the state-of-the-art methods. Finally, **Chapter 10** summarizes the contributions and concludes the thesis.

1.2 Other Contributions by Author

In addition to the articles listed above, the author has had the following publications during his Ph.D. studies:

[J5] Ameri, A., Bose, A., Li, J., and Soltanalian, M.: One-bit radar processing with time-varying sampling thresholds. IEEE Transactions on Signal Processing, 67(20):5297–5308, October 2019.

[C8] Bose, A. and Soltanalian, M.: Non-convex shredded signal reconstruction via sparsity enhancement. In 2017 IEEE International Conference on Acoustics, Speech and Signal Processing (ICASSP), pages 4691–4695, New Orleans, LA, March 2017.

[C9] Bose, A., Ameri, A., Klug, M., and Soltanalian, M.: Low-rank matrix recovery from one-bit comparison information. In 2018 IEEE International Conference on Acoustics, Speech and Signal Processing (ICASSP), pages 4734–4738. IEEE, Calgary, Alberta, Canada, April 2018.

[C10] Ameri, A., Bose, A., and Soltanalian, M.: Comprehensive personalized ranking using one-bit comparison data. In 2019 IEEE Data Science Workshop (DSW), pages 338–342, Minneapolis, Minnesota, USA, June 2019.

[C11] Bose, A., *et al.*: THz multi-layer imaging via nonlinear inverse scattering. In 2019 44th International Conference on Infrared, Millimeter, and Terahertz Waves (IRMMW-THz), pages 1–2, Paris, France, September 2019.

[C12] Wang, P., *et al.*: Learning-based shadow mitigation for Terahertz multi-layer imaging. In 2019 44th International Conference on Infrared, Millimeter, and Terahertz Waves (IRMMW-THz), pages 1–2, Paris, France, September 2019.

[C13] Khobahi, S., Bose, A., and Soltanalian, M.: Deep one-bit compressive autoencoder. In 2020 IEEE International Conference on Acoustics, Speech and Signal Processing (ICASSP), Barcelona, Spain, May 2020.

Part I

Waveform Synthesis for Improved System Identification

I-A

Strictly Linear Systems

CHAPTER 2

CONSTRUCTING BINARY SEQUENCES WITH GOOD CORRELATION PROPERTIES: AN EFFICIENT ANALYTICAL-COMPUTATIONAL INTERPLAY

Overview: Binary sequence sets with asymptotically optimal auto/cross-correlation peak sidelobe level (PSL) growth have been known in the literature for a long time, and their construction has been studied both analytically and numerically. In contrast, it has been a long-standing problem whether we can construct a family of binary sequences whose auto-correlation PSL grows in an optimal manner. In this chapter, we devise a construction methodology for binary sequences with asymptotically optimal PSL growth using sequence sets with good correlation properties. A key component of the design follows from the observation that if the PSL of the sequence set grows *optimally* or *nearly optimally*, then the PSL of the constructed binary sequence will experience similar growth as a consequence. The proposed construction is simple-to-implement and is shown to be accomplished in polynomial-time. With such a construction, we not only bridge the gap between analytical construction and computational search but also pave the way to settle the long-standing design problem of binary sequences with optimal growth of the auto-correlation PSL.

2.1 Introduction

Binary sequences with small auto/cross-correlation also referred to as good correlation properties form an essential component of a large set of information processing systems, ranging from information collection in active sensing to information embedding and transmission in communication systems. For instance, they are widely used in Code Division Multiple Access (CDMA) schemes to distinguish between different users while at the same time enabling the system to synchronize [84], whereas in active sensing applications, usage of such sequences for pulse modulation paves the way to conveniently retrieve the received signal from the range bin of interest by employing a matched filter, and thus suppress inputs from other range bins [85].

Although several families of *sequence sets* with small auto/cross-correlation have been proposed in the past decades, sequences with low auto-correlation have seen little progress in the analytical arena (see Section 2.2 for details). In fact, the task of finding sequences with low auto-correlation is infamously known as a difficult computational problem. The complexity of the optimization problems associated with low auto-correlation binary sequences is discussed in [86–88]. On the other hand, the rapid increase in computational resources has motivated the researchers to perform an exhaustive search of such sequences with larger lengths compared with what could have been considered before. The literature on this topic is quite extensive (*e.g.*, see [15, 20, 85, 86, 89–113]). Nonetheless, we note that an exhaustive search over a set of binary sequences with a cardinality larger than 10^{20} (*i.e.*, approximate sequence lengths of $N \sim 100$ or larger) is still deemed to be impractical[1] using the current standard computational

tools. On the contrary, to analytically construct such binary sequences, requires only a little computational cost. In this chapter, we bridge the gap between *exhaustive search*, also referred to as *computational design*, and *analytical constructions* of binary sequences by resorting to a polynomial-time approach that exploits the strengths of both worlds. The proposed method constructs the binary sequences from sequence sets with good correlation properties through a non-convex quadratic program that can be handled in polynomial-time. In particular, we show that if the PSL of the sequence sets grows optimally in the periodic case and nearly optimally in the aperiodic case, the PSL of the constructed binary sequences also grows in a similar manner.

As a cornerstone of our performance analysis, we present several examples of binary sequence design and the obtained PSL values. Besides the usual design examples, we also present some interesting results on the application of the constructed sequences in information embedding applications, where a high degree of both imperceptibility and robustness must be guaranteed (see *e.g.*, [114–118], and the references therein). We will use the optimally constructed binary sequences in lieu of sequence families commonly used in practice such as m-sequences, Gold, or Kasami sequences in the pre-existing watermarking frameworks to ensure robustness and imperceptibility of the authorized watermark information and enhance the efficiency of the information embedding algorithm. While being one of many, the presented example hints at the significant potential of our approach in practical applications.

---

[1]Assuming that a standard PC can handle 5×10^9 simple math operations per second, an exhaustive search over a space of 10^{20} sequences is *guaranteed to take more than 634 years*.

The rest of this chapter is organized as follows. The formulation as well as a useful background review of the problem is provided in Section 2.2. Our design approach is presented in Section 2.3. Section 2.4 is dedicated to the numerical results, including discussions on the information embedding application. Finally, Section 2.5 concludes the chapter.

2.2 Preliminaries

2.2.1 *Goodness* of a Sequence

We start by developing the underlying concepts that define what constitutes the *goodness* of a sequence. Let $\boldsymbol{x} = [x(1)\ x(2)\ \cdots\ x(N)]$ be a complex sequence of length N where $x(n) \in \Omega$. Here Ω is the set of alphabets that are chosen appropriately to fit the application. The aperiodic $(r(k))$ and periodic auto-correlations $(c(k))$ of the sequence $\boldsymbol{x}$ are given, respectively as [2],

$$r(k) = \sum_{n=1}^{N-k} x(n)x^*(n+k) = r^*(-k), \qquad 0 \leq |k| \leq N-1 \tag{2.1a}$$

$$c(k) = \sum_{n=1}^{N} x(n)x^*(n+k)_{\text{mod } N}, \qquad 0 \leq |k| \leq N-1 \tag{2.1b}$$

It is interesting to note that both auto-correlations are symmetric with respect to the in-phase lag (*i.e.*, $k = 0$) a.k.a mainlobe. Furthermore, this in-phase component in both auto-correlations represents the energy, $E = \sum_{n=1}^{N} |x(n)|^2$ of the sequence. The problem of designing sequences for good correlation properties usually seek to minimize the effect of out-of-phase (*i.e.*, $k \neq 0$) components a.k.a the sidelobes. Several metrics have been formulated in the literature to

quantify the quality of a sequence based on its auto-correlation properties. For instance, the *peak sidelobe level* (PSL) is defined as,

$$\text{PSL} \triangleq \max\{|r(k)|\}_{k=1}^{N-1}. \tag{2.2}$$

Another metric is *integrated sidelobe level* (ISL) that can be given as,

$$\text{ISL} \triangleq \sum_{k=1}^{N-1} |r(k)|^2. \tag{2.3}$$

Sequences with low PSL and ISL are usually considered to have good correlation properties. Moreover, *Merit factor* (MF) is another important metric that can often be found in the literature and defined as,

$$\text{MF} \triangleq \frac{|r(0)|^2}{2\sum_{k=1}^{N-1} |r(k)|^2} = \frac{E^2}{2\text{ISL}}. \tag{2.4}$$

It is clear that MF is inversely proportional to ISL, and thus designing sequences with good correlation properties constitutes to maximize the MF. Note that although for the sake of brevity, we only express these metrics in terms of aperiodic auto-correlation, they can, however be defined for both periodic and aperiodic cases. For the case of sequence sets, such metrics can be extended in a similar manner. In the next section, we define these metrics for a sequence set and formulate the problem.

2.2.2 Problem Formulation for Sequence Sets

Let X be a set of M sequences of length N denoted as $\{\boldsymbol{x}_m\}_{m=1}^{M}$, each having identical energy of $\|\boldsymbol{x}_m\|_2^2 = N$. Let $\boldsymbol{x}_{m_1}$ and $\boldsymbol{x}_{m_2}$ be two generic sequences from the set X. In a similar manner, the aperiodic $\{r_{m_1,m_2}(k)\}$ and periodic $\{c_{m_1,m_2}(k)\}$ cross-correlations of the sequences $\boldsymbol{x}_{m_1}$ and $\boldsymbol{x}_{m_2}$ at shift k are given as,

$$r_{m_1,m_2}(k) \triangleq \sum_{n=1}^{N-k} \boldsymbol{x}_{m_1}(n)\boldsymbol{x}_{m_2}^*(n+k) = r_{m_1,m_2}^*(-k), \tag{2.5a}$$

$$c_{m_1,m_2}(k) \triangleq \sum_{n=1}^{N} \boldsymbol{x}_{m_1}(n)\boldsymbol{x}_{m_2}^*(n+k)_{(\text{mod } N)}, \tag{2.5b}$$

for $0 \leq k \leq (N-1)$. The aperiodic and periodic auto-correlation of any $\boldsymbol{x}_m \in X$ can be obtained from Equation 2.5b and Equation 2.5a by using $\boldsymbol{x}_{m_1} = \boldsymbol{x}_{m_2}$. Furthermore, the inner product of $\boldsymbol{x}_{m_1}$ and $\boldsymbol{x}_{m_2}$ is given as $\boldsymbol{x}_{m_1}^H \boldsymbol{x}_{m_2} = c_{m_1,m_2}(0) = r_{m_1,m_2}(0)$.

In the sequel, we focus on the aperiodic case as well as the periodic case. The periodic correlations are generally considered to be easier to study than their aperiodic counterparts. Often the study of sequences with good aperiodic correlations concerns obtaining sequences with good periodic correlation properties and then examine their aperiodic correlations. There has been a long-standing interest in the study of design methods capable of finding binary sequence sets whose periodic and aperiodic correlations are, in some measurable sense, collectively small. To formalize this outcome, several measures of "smallness" have been typically employed, including

the PSL, defined for the aperiodic ($\mathrm{PSL}^{\mathcal{AP}}(X)$) and periodic ($\mathrm{PSL}^{\mathcal{P}}(X)$) cases, respectively, as [119]

$$\mathrm{PSL}^{\mathcal{AP}}(X) \triangleq \max(\{|r_{m_1,m_2}(k)|\}_{m_1\neq m_2;k} \cup \{|r_{m,m}(k)|\}_{m;k\neq 0}), \tag{2.6a}$$

$$\mathrm{PSL}^{\mathcal{P}}(X) \triangleq \max(\{|c_{m_1,m_2}(k)|\}_{m_1\neq m_2;k} \cup \{|c_{m,m}(k)|\}_{m;k\neq 0}),, \tag{2.6b}$$

which are the most relevant to our analysis. Consequently, the aperiodic and periodic PSL of a sequence $\boldsymbol{x}$ can be derived from its auto-correlations as follows,

$$\mathrm{PSL}^{\mathcal{AP}}(\boldsymbol{x}) \triangleq \max(|r_{m,m}(k)|_{m;k\neq 0}), \tag{2.7a}$$

$$\mathrm{PSL}^{\mathcal{P}}(\boldsymbol{x}) \triangleq \max(|c_{m,m}(k)|_{m;k\neq 0}). \tag{2.7b}$$

Likewise, the ISL can also be defined in terms of aperiodic and periodic cross-correlations as,

$$\mathrm{ISL}^{\mathcal{AP}}(X) \triangleq \sum_{m_1\neq m_2;k} |r_{m_1,m_2}(k)|^2 + \sum_{m;k\neq 0} |r_{m,m}(k)|^2, \tag{2.8a}$$

$$\mathrm{ISL}^{\mathcal{P}}(X) \triangleq \sum_{m_1\neq m_2;k} |c_{m_1,m_2}(k)|^2 + \sum_{m;k\neq 0} |c_{m,m}(k)|^2. \tag{2.8b}$$

In the subsequent, we restrict our discussion only to PSL.

2.2.3 Earlier Results

2.2.3.1 Periodic Auto-correlations of Binary Sequences

In an ideal setup, a binary sequence with all its out-of-phase periodic auto-correlations equal to zero, is called a *perfect* sequence [120]. A necessary condition required for a perfect sequence to exist is given in the following lemma.

Lemma 1. *([120]) All periodic auto-correlations of a binary sequence $\boldsymbol{x}$ of length N are compatible with N mod 4.*

$$PSL^{\mathcal{P}}(\boldsymbol{x}) \geq \begin{cases} 0 & \text{for } N \equiv 0 \text{ mod } 4 \\ 1 & \text{for } N \equiv 1 \text{ or } 3 \text{ mod } 4 \\ 2 & \text{for } N \equiv 2 \text{ mod } 4 \end{cases} \tag{2.9}$$

It can be concluded from Lemma 1 that the perfect binary sequence can only exist when the length N is divisible by 4. However, the corollary given in [121] states that *there exist no perfect binary sequence of length N for $4 < N < 548964900$*. A detailed analysis of the existence of perfect binary sequences can be found in [120]. Moreover, a binary sequence is called *optimal* in the sense that the equality holds in Equation 2.9. Sequence families such as Legendre, Sidelnikov, and Galois sequences are good examples of optimal sequences with respect to their periodic auto-correlations [120].

Furthermore, considering sequence sets instead of a single sequence, it is indeed possible to generate binary sequence sets with periodic PSL asymptotically bounded as $\mathcal{O}\left(\sqrt{N}\right)$. For ex-

TABLE I

KNOWN BARKER SEQUENCES

Length	Codes
2	+ −
	+ +
3	+ + −
4	+ + − +
	+ + + −
5	+ + + − +
7	+ + + − − + −
11	+ + + − − − + − − + −
13	+ + + + + − − + + − + − +

ample, [119] states that the well-known Gold family contains sets of binary sequences of length $N = 2^K - 1$ and with cardinality $M = 2^K + 1$ where K is odd. The periodic PSL growth of a Gold sequence set is determined as $1 + \sqrt{2^{K+1} - 2}$. Additionally, for even length K, the Kasami sequence sets can be generated for $(N, M) = (2^K - 1, 2^{K/2})$ whose periodic PSL grows as $1 + 2^{K/2}$. Another example is the Weil family, that can be constructed for $(N, M) = (K, \frac{K-1}{2})$, where K is prime, and shows a periodic PSL growth rate of $5 + 2\sqrt{K}$.

2.2.3.2 Aperiodic Auto-correlations of Binary Sequences

On a related note, the *Barker sequences* have the ideal property of all out-of-phase aperiodic auto-correlations are either 0 or 1 in magnitude. According to [120], there is no known Barker sequence of odd length greater than 13. Table I represents the only known Barker sequences from

lengths 2 to 13 [122]. In order to the address the presumed absence of long Barker sequences, researchers have shown interests rather into the study of the *asymptotic* behavior of the aperiodic auto-correlations of the sequences. Let $\mathcal{X}_N$ denote the set of all binary sequences of length N. The ultimate goal is to optimally compute and understand the asymptotic behavior, *i.e.*, as $N \to \infty$, of

$$\mathcal{P}_{min} \triangleq \min_{\boldsymbol{x} \in \mathcal{X}_N} \mathrm{PSL}^{\mathcal{AP}}(\boldsymbol{x}). \tag{2.10}$$

Note that to calculate $\mathcal{P}_{min}$ numerically for a given sequence length N, even in the most ingenious way, requires testing an exponential number of combinations. The exponential term of the complexity can be reduced from $\mathcal{O}\left(2^N\right)$ to roughly $\mathcal{O}\left(1.4^N\right)$ by using more sophisticated and efficient algorithms [123–125]. The value of $\mathcal{P}_{min}$ has been computed up to $N = 105$ in the literature [125–127] using exhaustive search.

1. $\mathcal{P}_{min} \leq 1$ for $N \leq 5$ [120];
2. $\mathcal{P}_{min} \leq 2$ for $N \leq 21$ [126], (Note that $\mathcal{P}_{min} = 1$ has been essentially obtained for $N = 2, 3, 4, 5, 7, 11, 13$ through *Barker sequences* [122]);
3. $\mathcal{P}_{min} \leq 3$ for $N \leq 48$ (see [127] for $N \leq 40$, and [123] for $N \leq 48$);
4. $\mathcal{P}_{min} \leq 4$ for $N \leq 82$ (see [128] for $49 \leq N \leq 61$, and [124, 125] for $61 \leq N \leq 70$);
5. $\mathcal{P}_{min} \leq 5$ for $N \leq 105$ [120].

In [129], Ein-Dor *et al.* provided an "educated guess" about the growth of $\mathcal{P}_{min}$ using a heuristic argument and conjectured that, as $N \to \infty$, we have $\dfrac{\mathcal{P}_{min}}{\sqrt{N}} \to d$, where $d = 0.435...$ Historically, Moon and Moser [108] first studied the asymptotic behavior, as $N \to \infty$, of $\mathcal{P}_{min}$ for the binary sequences as early as 1968.

Theorem 1. *([108]) let $\mathcal{G}(N)$ be a function of N such that $\mathcal{G}(N) = o\left(\sqrt{N}\right)$, then the sequences $\boldsymbol{x} \in \mathcal{X}_N$ which have $PSL^{\mathcal{AP}}(\boldsymbol{x}) > \mathcal{G}(N)$ approaches 1, as N approaches ∞.*

Theorem 2. *([108]) For any fixed $\epsilon > 0$, the sequences $\boldsymbol{x} \in \mathcal{X}_N$ which have $PSL^{\mathcal{AP}}(\boldsymbol{x}) \leq (2+\epsilon)\sqrt{N \log_e N}$ approaches 1, as N approaches ∞.*

According to Theorem 1 and 2, as $N \to \infty$, for almost all sequences satisfy the condition $\mathcal{G}(N) < \mathrm{PSL}^{\mathcal{AP}}(\boldsymbol{x}) \leq (2+\epsilon)\sqrt{N \log_e N}$ for any $\epsilon > 0$. Mercer [130] further improved the upper bound by showing that for any fixed $\epsilon > 0$, $\mathcal{P}_{min} \leq (\sqrt{2}+\epsilon)\sqrt{N \log_e N}$ when N is sufficiently large. Dmitriev and Jedwab [131] postulated that the typical PSL growth behaves as $\Theta(\sqrt{N \log_e N})$ and provided experimental evidence for the same.

We note that there are sequence families (*i.e.*, families of *single* sequences) for which the aperiodic PSL grows faster than $\Theta(\sqrt{N \log_e N})$. One such example is the sequence family $\mathcal{F} = \{\boldsymbol{\psi}_N = 1 : N \in \mathbb{N}\}$. Nonetheless, the literature does not currently conclude regarding the existence of any sequence family whose asymptotic aperiodic PSL grows like the lower bound $o\left(\sqrt{N}\right)$, nor even like $\Theta(\sqrt{N})$. Furthermore, it has been shown in [91] that the *average* value of the PSL of m-sequences of length $N = 2^m - 1$ exhibits a growth rate of $\Omega(\sqrt{N})$ and $\mathcal{O}\left(\sqrt{N \log_e N}\right)$. However, the assertion that the asymptotic PSL of such sequences has a

growth rate of $\mathcal{O}\left(\sqrt{N}\right)$, which appears frequently in the radar literature, "*is concluded to be unproven and not currently supported by data*" [91]. However, aperiodic correlations of families of unimodular sequences, namely Frank and Chu sequences show optimal nature in an asymptotic sense. In particular, [120] suggests that there exists an infinite number of unimodular sequences of length N that have the aperiodic PSL growth proportional to $\sqrt{N}$.

Sequence sets with aperiodic PSL values behaving like $\mathcal{O}\left(\sqrt{N}\right)$ as $N \to \infty$ are usually referred to as *asymptotically optimal* owing to the fact that their aperiodic PSL growth has similar behavior to that of the well-known Welch PSL bound [132]. We refer the interested reader to [91] for further details on this aspect. Note that finding sequence sets with such behavior is an achievable goal [84, 119] at least computationally. In particular, such sequence can be conveniently designed via numerical tools such as fast Cyclic Algorithm-New (CAN) algorithms (see, *e.g.*, [20, 85, 133]), MISL algorithm [110], ADMM approach [134], ISL-NEW algorithm [135] among others.

By tapping into the potential of sequence sets in achieving an asymptotically optimal aperiodic PSL growth, in the following, we propose a construction algorithm of binary sequences whose aperiodic PSL grows like $\mathcal{O}\left(\sqrt{N}\right)$.

2.3 The Proposed Construction

In this section, we show that sets of sequences with good correlation properties can be used as bases for designing binary sequences with good auto-correlation. Observe that, for any subset of the sequence sets the PSL growth optimality result holds, as considering a subset only can

decrease the PSL. Let $X = \{\boldsymbol{x}_1, \boldsymbol{x}_2, \cdots, \boldsymbol{x}_M\}$ be such a subset of sequences of length N with $\|\boldsymbol{x}_m\|_2^2 = N,\ \forall\ m$, having good correlation properties; namely, X is constructed to achieve

$$\mathrm{ISL}^{\mathcal{AP}}(X) \triangleq \sum_{m=1}^{M} \sum_{0<|k|<(N-1)} |r_{m,m}(k)|^2 + \sum_{m_1=1}^{M} \sum_{m_2 \neq m_1} \sum_{k=-(N-1)}^{N-1} |r_{m_1,m_2}(k)|^2 \tag{2.11}$$

that is as small as possible. We assume that $2 \leq M \ll N$, and particularly that M behaves as $\mathcal{O}(1)$ with respect to sequence length N. The lower bound of the aperiodic ISL metric in Equation 2.11 is given by [133]

$$B_{\mathrm{ISL}^{\mathcal{AP}}}(X) \triangleq N^2 M(M-1). \tag{2.12}$$

Also note that, using the above lower bound one can achieve the well-known Welch lower bound on $\mathrm{PSL}^{\mathcal{AP}}(X)$:

$$B_{\mathrm{PSL}^{\mathcal{AP}}}(X) \triangleq N\sqrt{\frac{M-1}{2NM-M-1}}. \tag{2.13}$$

Interestingly, it was shown in [133] that the above lower bounds for the aperiodic ISL and PSL metrics can be approached conveniently via computational design algorithms such as the fast CAN algorithm in [85]. With this in mind, we further observe that

$$\mathrm{PSL}^{\mathcal{AP}}(X) \sim \sqrt{\frac{M-1}{2M}}\ \sqrt{N} \tag{2.14}$$

as $N \to \infty$, which implies

$$\mathrm{PSL}^{\mathcal{AP}}(X) \lesssim \frac{1}{\sqrt{2}}\,\sqrt{N}. \tag{2.15}$$

2.3.1 Approaching the Optimal PSL Growth

Let $\boldsymbol{b}$ be a binary sequence (with ± 1 entries) obtained by a linear combination of the sequences $\{\boldsymbol{x}_m\}$, *viz.*,

$$\boldsymbol{b} = w_1\boldsymbol{x}_1 + w_2\boldsymbol{x}_2 + \cdots + w_M\boldsymbol{x}_M = \boldsymbol{X}\boldsymbol{w} \tag{2.16}$$

where

$$\boldsymbol{X} = \begin{bmatrix} \boldsymbol{x}_1 & \boldsymbol{x}_2 & \cdots & \boldsymbol{x}_M \end{bmatrix}, \text{ and}$$
$$\boldsymbol{w} = \begin{bmatrix} w_1 & w_2 & \cdots & w_M \end{bmatrix}^T \in \mathbb{C}^M.$$

Note that although $\boldsymbol{X}$ and $\boldsymbol{w}$ can be complex vectors, their product $\boldsymbol{X}\boldsymbol{w}$ is not necessarily complex-valued.

Theorem 3. *Let $\boldsymbol{X}$ be a set of M sequences each of length N, whose aperiodic PSL is asymptotically upper bounded as in Equation 2.15. In such a case, the aperiodic PSL of the binary sequence $\boldsymbol{b} = \boldsymbol{X}\boldsymbol{w}$ of Equation 2.16 will be asymptotically upper bounded by $\frac{\mu^2}{\sqrt{2}}\sqrt{N}$ where $\mu = \|\boldsymbol{w}\|_1 = \sum_{m=1}^{M} |w_m|$.*

The significance of Theorem 3 stems from the fact that the asymptotic growth of the aperiodic PSL of the generated binary sequence behaves similarly as that of the original sequence set. The proof of the Theorem 3 goes as follows. The aperiodic auto-correlation lags of $\boldsymbol{b}$ are given by

$$\begin{aligned} r_{\boldsymbol{b}}(k) &= \sum_{l=1}^{N-k} \boldsymbol{b}(l)\boldsymbol{b}^*(l+k) \\ &= \sum_{l=1}^{N-k} \left(\sum_{m_1=1}^{M} w_{m_1} \boldsymbol{x}_{m_1}(l) \right) \left(\sum_{m_2=1}^{M} w^*_{m_2} \boldsymbol{x}^*_{m_2}(l+k) \right) \\ &= \sum_{m_1=1}^{M} \sum_{m_2=1}^{M} \left(w_{m_1} w^*_{m_2} \sum_{l=1}^{N-k} \boldsymbol{x}_{m_1}(l) \boldsymbol{x}^*_{m_2}(l+k) \right) \\ &= \boldsymbol{w}^H \boldsymbol{R}_k \boldsymbol{w} \end{aligned} \tag{2.17}$$

where $[\boldsymbol{R}_k]_{m_1,m_2} = r_{m_1,m_2}(k)$. It follows from Equation 2.17 that

$$\begin{aligned} |r_{\boldsymbol{b}}(k)| &\leq \sum_{m_1=1}^{M} \sum_{m_2=1}^{M} |w_{m_1}||w_{m_2}||r_{m_1,m_2}(k)| \\ &\leq \max_{m_1,m_2} \{|r_{m_1,m_2}(k)|\} \left(\sum_{m_1=1}^{M} \sum_{m_2=1}^{M} |w_{m_1}||w_{m_2}| \right) \\ &\leq \mathrm{PSL}^{\mathcal{AP}}(X) \, \|\boldsymbol{w}\|_1^2. \end{aligned} \tag{2.18}$$

As a result, using Equation 2.15 we have that

$$\mathrm{PSL}^{\mathcal{AP}}(\boldsymbol{b}) \lesssim \frac{\mu^2}{\sqrt{2}} \sqrt{N}. \tag{2.19}$$

In order to determine the growth rate of μ, observe that

$$\left[\boldsymbol{X}^H\boldsymbol{X}\right]_{m,n} = \begin{cases} N & m = n, \\ \alpha_{m,n} & m \neq n, \end{cases} \qquad m,n \in \{1,2,\cdots,M\}, \tag{2.20}$$

where according to Equation 2.13,

$$|\alpha_{m,n}| \leq N\sqrt{\frac{M-1}{2NM-M-1}}.$$

Let $\boldsymbol{X} = \boldsymbol{U}\boldsymbol{\Sigma}\boldsymbol{V}^H$ represent the Singular Value Decomposition (SVD) of $\boldsymbol{X}$, where $\boldsymbol{V}$ and $\boldsymbol{U}$ are complex unitary matrices of size $M \times M$ and $N \times N$, respectively, and $\boldsymbol{\Sigma}$ is an $N \times M$ diagonal matrix. Note that $\boldsymbol{X}^H\boldsymbol{X} = \boldsymbol{V}\boldsymbol{\Sigma}^2\boldsymbol{V}^H$, where

$$\boldsymbol{\Sigma}^2 = \begin{bmatrix} |\sigma_1|^2 & & \mathbf{0} \\ & \ddots & \\ \mathbf{0} & & |\sigma_M|^2 \end{bmatrix} \tag{2.21}$$

with $\{\sigma_m\}_{m=1}^M$ being the singular values of $\boldsymbol{X}$.

Now observe that,

$$\boldsymbol{V}\boldsymbol{\Sigma}^2\boldsymbol{V}^H = \boldsymbol{X}^H\boldsymbol{X} \triangleq N\boldsymbol{I}_M + \boldsymbol{Q}, \tag{2.22}$$

where,

$$\|\boldsymbol{Q}\|_F \leq N\sqrt{(M^2-M)\left(\frac{M-1}{2NM-M-1}\right)}. \tag{2.23}$$

As a result,

$$|\sigma_m|^2 = \boldsymbol{e}_m^T\boldsymbol{\Sigma}^2\boldsymbol{e}_m = N + \boldsymbol{e}_m^T\boldsymbol{V}^H\boldsymbol{Q}\boldsymbol{V}\boldsymbol{e}_m. \tag{2.24}$$

The bound in Equation 2.23 implies that

$$|\boldsymbol{e}_m^T\boldsymbol{V}^H\boldsymbol{Q}\boldsymbol{V}\boldsymbol{e}_m| \leq N\sqrt{(M^2-M)\left(\frac{M-1}{2NM-M-1}\right)}. \tag{2.25}$$

Consequently, one can easily verify the following:

$$|\sigma_m|^2 \geq N - N\sqrt{(M^2-M)\left(\frac{M-1}{2NM-M-1}\right)}. \tag{2.26}$$

Further note that,

$$\begin{aligned} \|\boldsymbol{X}^\dagger\|_F^2 &= \sum_{m=1}^{M}\frac{1}{|\sigma_m|^2} \\ &\leq \frac{M}{N - N\sqrt{(M^2-M)\left(\frac{M-1}{2NM-M-1}\right)}}. \end{aligned} \tag{2.27}$$

Moreover as $\boldsymbol{X}^{\dagger}\boldsymbol{X} = \boldsymbol{I}_M$, we conclude that $\boldsymbol{w} = \boldsymbol{X}^{\dagger}\boldsymbol{b}$, and therefore,

$$\begin{aligned} \|\boldsymbol{w}\|_2^2 &\leq \|\boldsymbol{X}^{\dagger}\|_F^2 \|\boldsymbol{b}\|_2^2 \\ &\leq \frac{M}{1 - \sqrt{(M^2 - M)\left(\frac{M-1}{2NM - M - 1}\right)}}. \end{aligned} \tag{2.28}$$

Note that, due to the Cauchy-Schwarz inequality,

$$\left(\sum_{m=1}^{M} |w_m|\right)^2 \leq \left(\sum_{m=1}^{M} |w_m|^2\right)\left(\sum_{m=1}^{M} 1\right). \tag{2.29}$$

It follows from the above that

$$\begin{aligned} \mu &= \|\boldsymbol{w}\|_1 \\ &\leq M \sqrt{\frac{1}{1 - \sqrt{\frac{M(M-1)^2}{2NM - M - 1}}}} \\ &\triangleq f(M, N), \end{aligned} \tag{2.30}$$

where

$$\lim_{N \to \infty} f(M, N) = M, \tag{2.31}$$

showing that μ behaves as $\mathcal{O}(1)$ with respect to the sequence length N, as N grows large. Finally, from Equation 2.19 and Equation 2.31 one can observe that $\mathrm{PSL}^{\mathcal{AP}}(\boldsymbol{b})$ behaves like $\mathcal{O}\left(\sqrt{N}\right)$.

This conclusion is summarized in Theorem 4. Note that, a similar asymptotic behavior of the periodic PSL of a binary sequence can also be drawn from the above formulations, with minor modifications. A detailed discussion on this observation, however, is omitted here in for the sake of brevity.

Theorem 4. *Let $\boldsymbol{X}$ be a matrix comprised of M sequences each of length N, whose aperiodic PSL grows like $\mathcal{O}\left(\sqrt{N}\right)$. A binary sequence created as $\boldsymbol{b} = \boldsymbol{X}\boldsymbol{w}$ with $\boldsymbol{w} \in \mathbb{C}^M$ will similarly have an asymptotic aperiodic PSL growth bounded as $\mathcal{O}\left(\sqrt{N}\right)$.*

Remark 1. It is interesting to observe that $|\sigma_m|^2 = N$ occurs *iff* all the sequences included in $\boldsymbol{X}$ are *orthogonal*, which will follow in a zero cross-correlation case. However, in a usual case where the sequences only have a *low* cross-correlation, the orthogonality condition is nearly met, which would lead to a μ that is upper bounded at a value larger than M. ■

2.3.2 The Optimal Construction

In the sequel, we investigate an optimal approach to constructing $\boldsymbol{b}$ through considering $\boldsymbol{X}$ as a *basis*—namely, we can construct the binary vectors $\boldsymbol{b}$ using the optimization problem

$$\min_{\boldsymbol{w},\boldsymbol{b}} \ \|\boldsymbol{X}\boldsymbol{w} - \boldsymbol{b}\|_2^2 \tag{2.32}$$

A possible approach to deal with constructing such binary sequences is to apply a cyclic minimization of Equation 2.32; namely, for fixed $\boldsymbol{b}$ the minimizer $\boldsymbol{w}$ of Equation 2.32 is given by

$$\boldsymbol{w} = \boldsymbol{X}^{\dagger}\boldsymbol{b}. \tag{2.33}$$

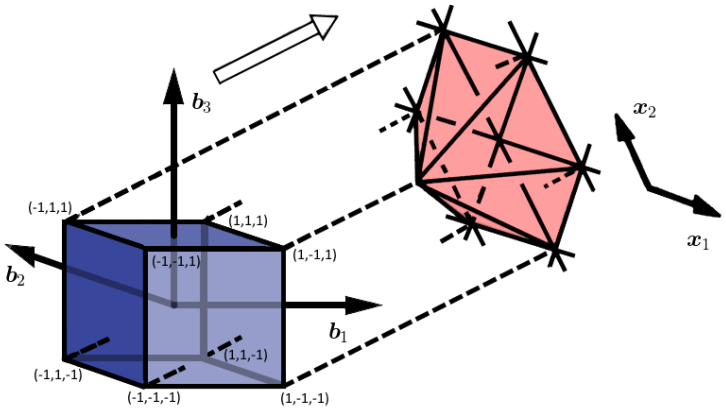

Figure 9. An illustration of the simplified geometry of construction from the linear combination of sequence sets, and the binary sequence with good correlation in three-dimensional case.

Moreover, for fixed $\boldsymbol{w}$ the minimizer $\boldsymbol{b}$ of Equation 2.32 can be obtained as

$$\boldsymbol{b} = \operatorname{sign}\left(\Re(\boldsymbol{X}\boldsymbol{w})\right). \tag{2.34}$$

Figure 9 illustrates the simplified geometry of such a construction from a linear combination of sequences, and the binary sequences in their *neighborhood* for the three-dimensional case.

Remark 2. The careful reader may argue that the above approach, while optimal, does not guarantee finding a binary vector in the subspace spanned by the sequence sets—particularly as $M \ll N$. This is a valid observation, and pertains to situations where $\left\|\tilde{\boldsymbol{b}} - \boldsymbol{X}\boldsymbol{w}\right\|_2$ is non-zero at the optimum $\tilde{\boldsymbol{b}}$. Hence, we will have a non-zero fitting error vector $\boldsymbol{\epsilon} \triangleq \tilde{\boldsymbol{b}} - \boldsymbol{X}\boldsymbol{w}$, whose

ℓ_2-norm is being minimized in our construction. Consequently, the auto-correlation sequence in this case can be rewritten as

$$
\begin{aligned}
r_{\tilde{\boldsymbol{b}}}(k) &= \sum_{l=1}^{N-k} \tilde{\boldsymbol{b}}(l)\tilde{\boldsymbol{b}}^*(l+k) \qquad (2.35)\\
&= \sum_{l=1}^{N-k} \left(\sum_{m_1=1}^{M} w_{m_1}\boldsymbol{x}_{m_1}(l) + \boldsymbol{\epsilon}(l) \right) \left(\sum_{m_2=1}^{M} w^*_{m_2}\boldsymbol{x}^*_{m_2}(l+k) + \boldsymbol{\epsilon}^*(l+k) \right)\\
&= \sum_{m_1=1}^{M}\sum_{m_2=1}^{M} \left(w_{m_1}w^*_{m_2} \sum_{l=1}^{N-k} \boldsymbol{x}_{m_1}(l)\boldsymbol{x}^*_{m_2}(l+k) \right) + \sum_{l=1}^{N-k} \epsilon(l)\epsilon^*(l+k)\\
&\qquad + \left[\sum_{m_1=1}^{M} \left(w_{m_1} \sum_{l=1}^{N-k} \boldsymbol{x}_{m_1}(l)\epsilon^*(l+k) \right) + \sum_{m_2=1}^{M} \left(w^*_{m_2} \sum_{l=1}^{N-k} \boldsymbol{x}^*_{m_2}(l+k)\epsilon(l) \right) \right]\\
&= r_{\boldsymbol{b}}(k) + r_{\boldsymbol{\epsilon}}(k) + 2\Re r_{\boldsymbol{b}\boldsymbol{\epsilon}}(k),
\end{aligned}
$$

where $\{r_{\boldsymbol{b}}(k)\}$ is the *desired* auto-correlation of the binary sequence, and the extra terms $\{r_{\boldsymbol{\epsilon}}(k)\}$ and $\{r_{\boldsymbol{b}\boldsymbol{\epsilon}}(k)\}$ represent the auto-correlation lags of $\boldsymbol{\epsilon}$ and the cross-correlation lags between the *desired* binary sequence $\boldsymbol{b}$ and $\boldsymbol{\epsilon}$, respectively. Interestingly, one can expect that both extra terms $\{r_{\boldsymbol{\epsilon}}(k)\}$ and $\{r_{\boldsymbol{b}\boldsymbol{\epsilon}}(k)\}$ to be small, even if $\boldsymbol{\epsilon}$ is non-zero. This is due to the fact that the optimality of $\tilde{\boldsymbol{b}}$ leads to an $\boldsymbol{\epsilon}$ that has noise-like properties, including a low auto-correlation, as well a low cross-correlation with the binary vector of interest [136]. Therefore, the proposed algorithm performs well even if $\|\boldsymbol{b} - \boldsymbol{X}\boldsymbol{w}\| \neq 0$, as is also evident by the numerical results presented in section 2.4. ■

Interestingly, the global optimization of Equation 2.32 for finding the *optimal* binary sequences with good auto-correlation can be accomplished in polynomial-time. To see how this

goal can be achieved in practice, note that by substituting the minimizer $\boldsymbol{w}$ in Equation 2.32, the design problem boils down to the following minimization problem:

$$\min_{\boldsymbol{b}} \ \left\| \boldsymbol{X}\boldsymbol{X}^{\dagger}\boldsymbol{b} - \boldsymbol{b} \right\|_2^2 \tag{2.36}$$

Now considering that $\boldsymbol{X}\boldsymbol{X}^{\dagger}$ is Hermitian, the objective function of the above minimization problem can be rewritten as

$$\begin{aligned} \left\| \boldsymbol{X}\boldsymbol{X}^{\dagger}\boldsymbol{b} - \boldsymbol{b} \right\|_2^2 = & \ \left(\boldsymbol{X}\boldsymbol{X}^{\dagger}\boldsymbol{b} - \boldsymbol{b} \right)^H \left(\boldsymbol{X}\boldsymbol{X}^{\dagger}\boldsymbol{b} - \boldsymbol{b} \right) \\ = & \ \boldsymbol{b}^H \boldsymbol{X}\boldsymbol{X}^{\dagger}\boldsymbol{X}\boldsymbol{X}^{\dagger}\boldsymbol{b} - 2\boldsymbol{b}^H \boldsymbol{X}\boldsymbol{X}^{\dagger}\boldsymbol{b} + \boldsymbol{b}^H\boldsymbol{b} \\ = & \ -\boldsymbol{b}^H \boldsymbol{X}\boldsymbol{X}^{\dagger}\boldsymbol{b} + N. \end{aligned} \tag{2.37}$$

Therefore, Equation 2.36 is equivalent to the computation of the binary vector that maximizes the quadratic form $\boldsymbol{b}^H \boldsymbol{X}\boldsymbol{X}^{\dagger}\boldsymbol{b}$; more precisely,

$$\boldsymbol{b}_{opt} \triangleq \arg\max_{\boldsymbol{b}} \ \boldsymbol{b}^H \boldsymbol{X}\boldsymbol{X}^{\dagger}\boldsymbol{b} \tag{2.38}$$

in which $\mathrm{rank}(\boldsymbol{X}\boldsymbol{X}^{\dagger}) = M$, that specifically behaves as $\mathcal{O}(1)$ with respect to the problem dimension N. The maximization of a positive (semi-)definite complex quadratic form over a binary vector set is an NP-hard problem in general and can be tackled by exhaustive search when the quadratic form is full-rank. However, as the quadratic form in the above is rank-deficient, the optimum can be found with polynomial complexity in the sequence length N [137, 138]. In

particular, [137] proposes an $\mathcal{O}\left(N^{2M}\right)$ cost algorithm that constructs a set of candidates with cardinality $\mathcal{O}\left(N^{2M-1}\right)$ including the global optimum of Equation 2.38 and reduces the size of the feasible set from exponential to polynomial. This is due to the fact that the number of local optima for rank-deficient quadratic forms such as Equation 2.38 enjoys a polynomial growth, whereas that of a full-rank quadratic form grows exponentially with the sequence length N. Note that the approach presented above can easily be extended to the design of Q-phase (also known as Q-ary) sequences. To this end, one only needs to perform the maximization of the quadratic form in Equation 2.38 over the set of Q-phase vectors in lieu of binary vectors; which can be completed with polynomial complexity similar to the binary case (see [138] for details).

Finally, the algorithm for the construction of the desired binary sequences from the sequence sets with good correlation is summarized in Algorithm 1.

Remark 3. We note that norms other than ℓ_2 can also be easily used if one resorts to a cyclic/local optimization of the non-convex problem in Equation 2.32. But the above discussion reaffirms the key motivation behind using the ℓ_2-norm for our optimization approach: by using ℓ_2-norm, one can formulate the original design problem as a *rank-deficient* quadratic optimization problem. This particular formulation, used along with the computational approach of [137], guarantees not only to (i) find the global optimum sequence of Equation 2.32, but also to (ii) achieve this goal with a polynomial-time computation cost. These guarantees are central to the promise of the chapter, namely finding binary sequences with desirable correlation properties in polynomial-time. Such critical guarantees are not available when using other metrics such as ℓ_1 or ℓ_∞ norms. ■

Algorithm 1 For construction of binary sequence families with optimal PSL growth

Input: Set N to the lowest feasible sequence length.

1: Form $\boldsymbol{X}$ from a well-known family of sequence sets with good correlation properties such as Gold, Kasami, Legendre, Weil families or sequence sets generated by a numerical approach such as the CAN algorithm [85].
2: Find $\boldsymbol{w}$ using Equation 2.33.
3: Find $\boldsymbol{b}$ using Equation 2.34.
4: Find $\boldsymbol{b}_{opt}$ using Equation 2.38 following the efficient approach proposed in [138].
5: Increase N to the next available value for which the sequence sets can be generated.
6: Repeat steps 1–4.

2.4 Numerical Simulations

In this section, several numerical examples will be presented to examine the performance of our construction in approaching an optimal growth of the PSL metrics. We also show that our optimally constructed sequences are effective in information embedding applications in the sense that they outperform the traditionally employed sequences.

2.4.1 Construction of the Sequences

We construct new families of binary sequences by leveraging sequences drawn from well-known sequence sets including Gold [139], Kasami [140], Weil [141] and Legendre sets [142, 143]. We compare the growth of the obtained periodic PSL values (denoted by $\mathcal{P}_{opt}$) of the optimally constructed sequences $\boldsymbol{b}_{opt}$ with the function $\sqrt{N}$, where N denotes the sequence length. Our main interest is to test (through numerical investigations) our claim that the PSL of constructed sequences grows like $\mathcal{O}\left(\sqrt{N}\right)$. Moreover, we show that although CAN algorithms are not very effective in finding binary sequences with low PSL, they can be effectively used to lower the PSL

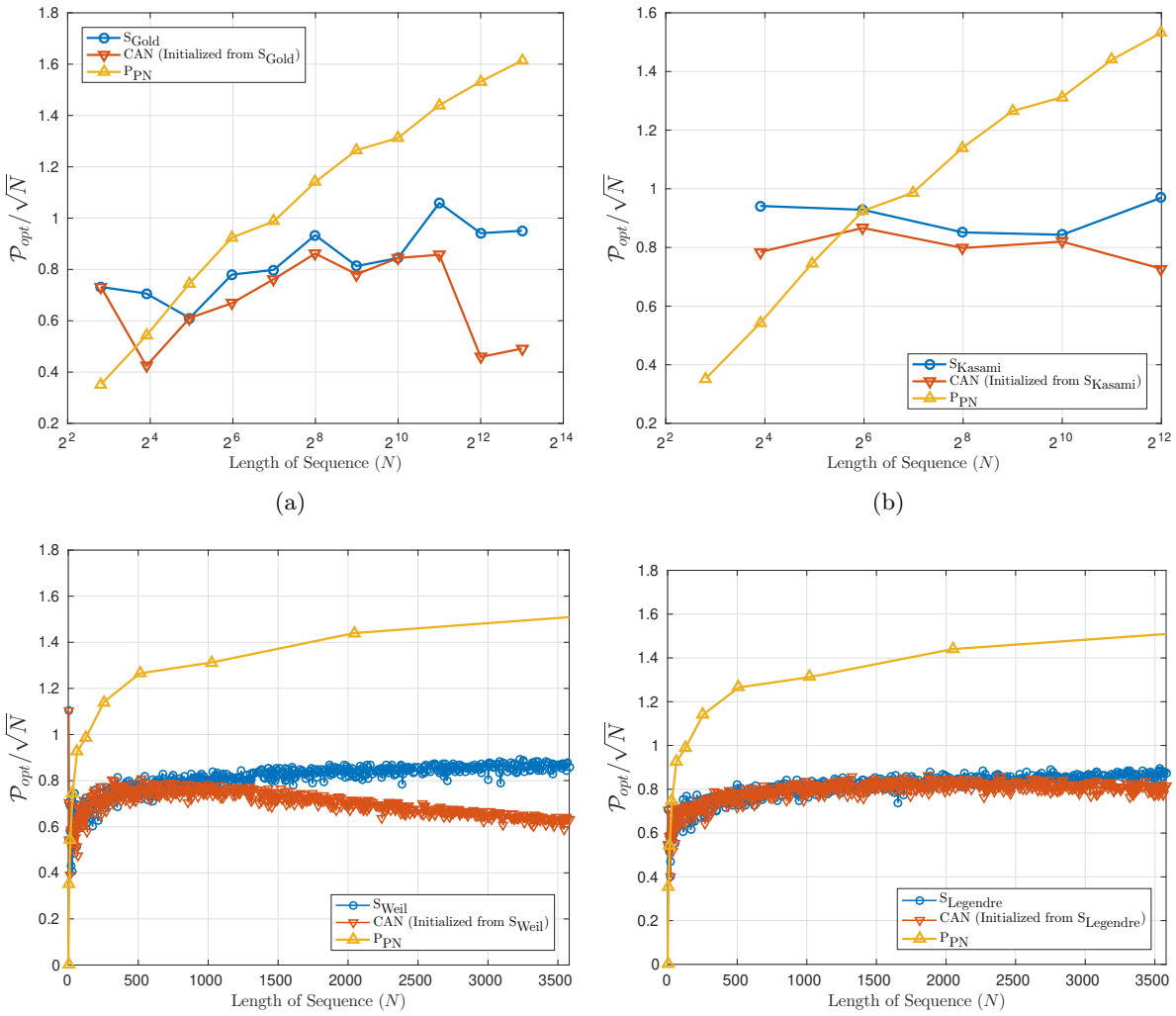

Figure 10. The PSL growth of constructed binary sequences vs. length N obtained from different sequence families: (a) Gold sequence, (b) Kasami sequence, (c) Weil sequence and (d) Legendre sequence.

of the obtained sequences. This is achieved by using the obtained sequences as initialization for the CAN algorithms. The notations used for the sequence families in the forthcoming discussions and the length of sequences that are used are given in Table II.

For comparisons, we make use of the PN sequence as it is very easy to generate for virtually any length of power 2 and is frequently used in literature. We calculate the variations of $\mathcal{P}_{opt}$ with the sequence length N and compare the outcome with $\sqrt{N}$ for the constructed sequences from different sequence sets. Figure 10 provides evidence of an *almost constant* nature of $\mathcal{P}_{opt}/\sqrt{N}$ as N grows large (from which we conclude that the original function must grow as $\mathcal{O}\left(\sqrt{N}\right)$). Figure 10 also compares the value $\mathcal{P}_{opt}/\sqrt{N}$ of obtained sequences with that of the sequences from the CAN algorithm (CAN-aided) by using the obtained sequence as initialization, and also with that of PN sequences. It can be observed that the CAN algorithm can effectively reduce the PSL of the obtained sequences from our construction. As a result, by our analysis, the *CAN-aided* sequences should also have an optimal PSL growth. The plots also appear to support the claim that the PSL of PN sequences grows as $\mathcal{O}\left(\sqrt{N\log_e N}\right)$.

2.4.2 Information Embedding Application

Finally, it is of interest to see the performance of our construction in a practical example. We use our constructed sequences as *orthogonal feeding sequence* in a certain digital watermarking algorithm to examine its effectiveness towards imperceptibility and robustness of the watermarked information. The scheme followed in this chapter invisibly embeds a binary watermark image into a gray-scale cover image which makes the information about the authentication more secure. The watermarking technique described in [114, 115] employs a Pseudo Noise (PN)

TABLE II

NOTATION AND NUMBER OF SEQUENCES

Notation	Sequence name	Maximum length of sequences (N)
P_{PN}	PN sequence	$2^{13} - 1 = 8191$
S_{Gold}	Binary sequence constructed from Gold sequence	$2^{13} - 1 = 8191$
S_{Kasami}	Binary sequence constructed from Kasami sequence	$2^{12} - 1 = 4095$
S_{Weil}	Binary sequence constructed from Weil sequence	3581 (first 500 odd prime numbers)
$S_{Legendre}$	Binary sequence constructed from Legendre sequence	3581 (first 500 odd prime numbers)

sequence as its primary feeding sequence. In this chapter, instead of using PN sequences we use our constructed binary sequences for the embedding purpose. The rest of the algorithm closely follows the technique described in [114]. The detailed block diagram of the algorithm is described in Figure 11.

In order to examine the effectiveness of the aforementioned watermarking technique using the binary sequences generated by the proposed algorithm, multiple experiments are conducted on several random test images. We use a set of gray cover images of standard size for this purpose. For each test image, a qualitative analysis has been drawn by measuring the Peak Signal to Noise Ratio (PSNR) between the original cover image and the watermarked image, and further compared with the widely used PN sequences. At the receiver, the watermark is extracted from the watermarked image by using the orthogonal codes, and evaluation of extracted watermark

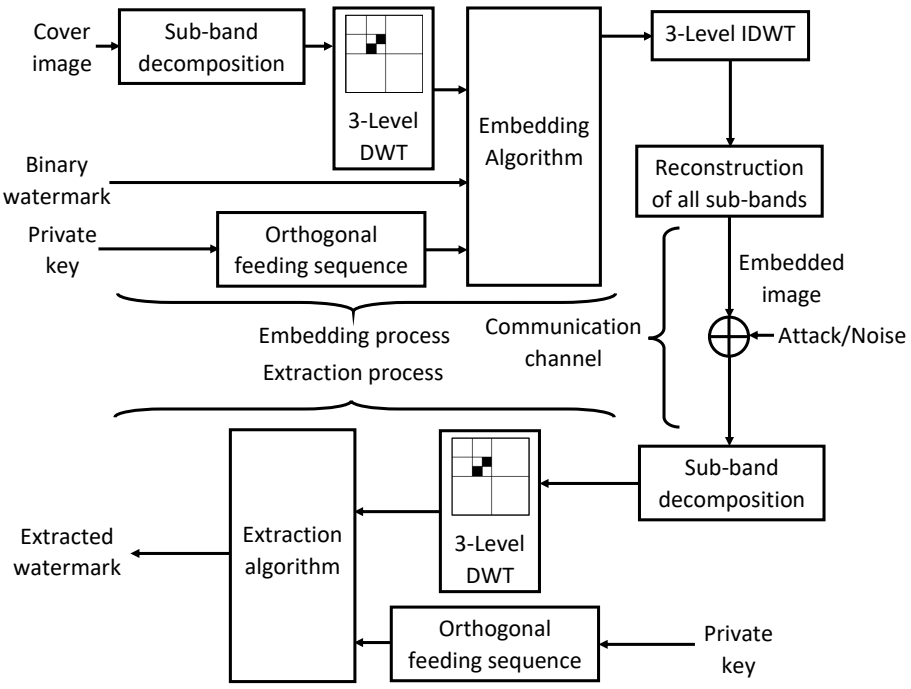

Figure 11. Block diagram of watermark embedding and extraction algorithm using generated binary sequence.

is done by measuring Normalized Cross-correlation (NC) with the original watermark—see [114] for details.

Figure 12 compares the variation of PSNR (dB) in the watermarked image and NC of original and extracted watermarks with varying *watermarking strength* or *gain factor* (k) for the binary sequences constructed from Gold, Kasami and, Legendre sequence families with that of PN sequences. The overall PSNR decreases and the NC increase with increasing k. However, in all cases, our constructed sequences outperform the PN sequence. It can also be observed

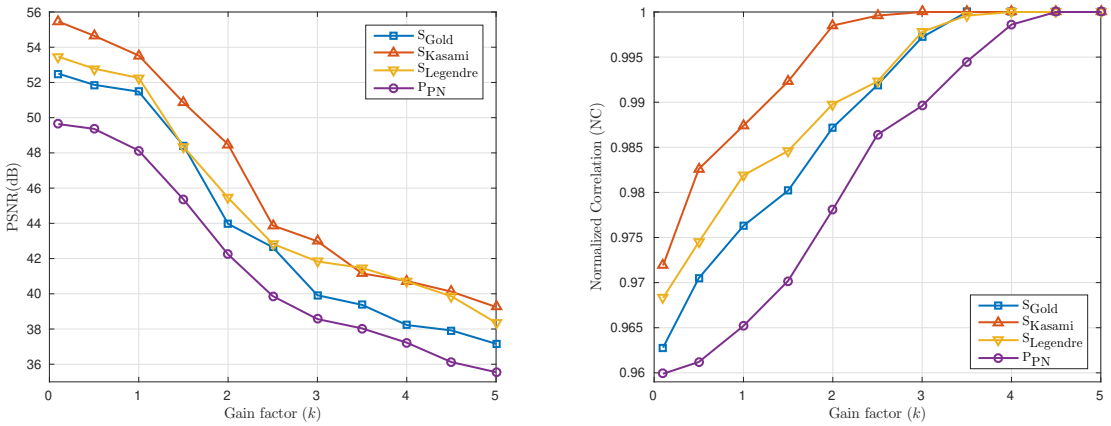

(a) (b)

Figure 12. The variation of (a) PSNR (dB) and (b) NC with Gain factor (k) for different sequence sets: PN sequence (P_{PN}) and binary sequence constructed from Gold sequence (S_{Gold}), Kasami sequence (S_{Kasami}) and Legendre sequence ($S_{Legendre}$).

from Figure 12 that the binary sequence obtained from the Kasami sequence set performs best in both cases. Also to comment on the robustness of the embedding scheme, several spatial and geometrical attacks are applied to the watermarked image. The quality of the watermark extracted from the attacked image is qualitatively analyzed using NC between the original and extracted watermark. Table III summarizes the results from various attacks for binary sequences constructed as described before in comparison with the PN sequence. Similar to the previous case, the constructed binary sequences appear to outperform the PN sequence, with S_{Kasami} producing the best result.

TABLE III

COMPARISON OF RESULTS FROM VARIOUS ATTACKED WATERMARKED IMAGE AT GAIN FACTOR $K = 2$

Name of the Attack	NC for Sequences			
	P_{PN}	S_{Gold}	$S_{Legendre}$	S_{Kasami}
Lowpass filter	0.9362	0.9563	0.9725	0.9854
Wiener filter	0.9073	0.9234	0.9541	0.9635
Laplacian high pass filter	0.9463	0.9547	0.9623	0.9841
Edge sharpening	0.9236	0.9339	0.99521	0.9751
JPEG compression	0.9523	0.9712	0.9795	0.9911
Histogram equalization	0.9562	0.9743	0.9829	0.9863
Gaussian noise	0.9672	0.9645	0.9861	0.9910
Speckle noise	0.9629	0.9719	0.9851	0.9884
Salt and Pepper noise	0.9503	0.9739	0.9791	0.9938

2.5 Concluding Remarks

In this chapter, a polynomial-time construction approach for designing binary sequences with optimal PSL growth was proposed. The suggested approach taps into the potential of sequence sets in achieving an asymptotically optimal PSL growth both in a periodic and aperiodic sense, and makes effective use of efficient algorithms available for (a specific subset of) non-convex quadratic optimization problems. Several numerical examples have been presented to investigate the PSL growth of the constructed sequences, particularly for rather long sequences (with length $N \sim 2^{12}$). Moreover, it was shown that the constructed sequences can outperform the widely used PN sequence in information embedding applications.

CHAPTER 3

DESIGNING SIGNALS WITH GOOD CORRELATION AND DISTRIBUTION PROPERTIES

Overview: Sequences with good correlation and distribution properties play a central role in various areas of signal processing. In this chapter, we propose an efficient computational framework for designing sequences with two key properties: (i) an impulse-like auto-correlation, and (ii) a probability distribution of sequence entries which is uniform in nature; although the results can be easily extended to an arbitrary distribution. The proposed method is based on utilizing the Fast Fourier Transform (FFT) operations and thus can generate very long sequences in small time frames.

3.1 Introduction

As discussed in previous chapters, sequences with good correlation properties are necessary components in a wide range of signal and information processing applications including active sensing, spread spectrum communication systems, radar sensing, signal synchronization, and cryptography [3, 24, 85, 93, 122, 144, 145]. Although, one can find a rich literature on the design of signals with small auto-correlation sidelobe [7, 20, 85, 90, 91, 93, 95], there has been very little effort on designing sequences possessing good correlation and good distribution properties which has crucial potential applications in biomedical system identification [146]. In this chapter, we focus on this critical aspect missing from the recent signal design approaches developed in the

---

literature— *i.e.*, the distribution properties of the signal itself. Some important applications such as biomedical signal processing often require sequences with good correlation properties as well as a user-defined distribution property for the purpose of system identification. Such an application in the context of Parkinson's Disease (PD) diagnosis and treatment, has been discussed in Section 3.1.1.

In our approach, we will use the *Cyclic Algorithm-New* (CAN), a computational framework introduced in [20], in order to achieve low out-of-phase auto-correlation, and at the same time, achieve the desired distribution by incorporating a sort-based algorithm to form partitions for various distribution bins. Note that the CAN framework uses FFT operations as its core computation and thus, can be effectively used to design longer sequences (up to $N \sim 10^6$ or even more).

The remainder of the chapter is organized as follows. The application of signals with good correlation and good distribution properties in PD diagnosis and treatment has been put forward in Section 3.1.1. Section 3.2 talks about the necessary background required for the proposed algorithm which is discussed in Section 3.3. Numerical simulation results are given in Section 3.4. Section 3.5 then summarizes the chapter with a brief discussion about aspects of future work.

3.1.1 An Application to Biomedical System Identification

According to the current practice, a Unified Parkinson's Disease Rating Scale (UPDRS) is used to evaluate and diagnose the status of PD in a patient [146]. Such an approach, however, is very time-consuming and prone to human error. Hence, it is of great interest to search for tools

that facilitate a quick and objective quantification of the PD status. The new framework of eye-tracking for quantifying (or *system identification* [3] of) the human smooth pursuit system (SPS) promises a solution to such difficulties with a revolutionary potential [147]. It has been concluded in the literature that not only the human SPS is meaningfully affected by the PD, but also the seriousness of such affliction is correlated to the status of the disease [148–150]. Nonetheless, among the several methods for SPS quantification, eye-tracking is the only non-invasive method suggested by the literature.

In an eye-tracking system, the visual stimulus consists of a moving circle whose trajectory is the signal to be designed, and the eye's gaze direction is the output. One approach for the SPS analysis is the system theory approach where the SPS is mathematically modeled as a parameterized dynamical system correlating gaze direction to a visual stimulus using the behavior of the SPS by imposing general restrictions on the model variables. In such a scenario, sequences with not only good correlation properties but also a well-defined distribution are required in order to identify the system with a high degree of accuracy [146].

It is widely known that a judicious design of the probing signals has a significant impact on the performance of identification. In particular, it was shown that signals with good correlation properties (*i.e.*, with low out-of-phase auto-correlation lags) are influential for high-performance SPS quantification, owing to their unique spectral properties [6]. The goal of this chapter is thus not only to design and study signals possessing good correlation properties but also signals that follow a given distribution; preferably a uniform distribution, however can be converted to any other distributions.

3.2 Problem Formulation

The main objective of this chapter is not only on the minimizing the ISL or ISL-related metrics over a set of sequences, but also the elements of generated sequences should be sampled from a uniform distribution. For the definition of ISL and other metrics, please refer to Section 2.2.1. The significantly large application area of sequences with good correlation (in particular, with small ISL) has produced an active area of research in sequence design, and as a result, there is a rich (yet growing) literature on this topic.

On the other hand, a generic definition of (sequence $\boldsymbol{x}$ with) uniform distribution can be given as follows [151, 152]: The sequence $\boldsymbol{x} = \{x_n\}_{n=1}^{N}$ of real numbers can be considered to be uniformly distributed if for every pair a, $b \in \mathbb{R}$ with $0 \leq a < b \leq 1$, the following is satisfied:

$$\lim_{N\to\infty} \frac{\mathcal{C}([a,b);\boldsymbol{x})}{N} = b - a \tag{3.1}$$

where, $\mathcal{C}(E;\boldsymbol{x})$ is the counting function defined as the number of values x_n $(1 \leq n \leq N)$ for which $\{x_n\} \in E$.

In our proposed method, we achieve sequences with uniform distribution by partitioning the sequence entries into a number of bins and populating each bin with (almost) the same number of elements building a uniform histogram). In a discrete sense, for the sake of simplicity, we rewrite the definition of uniform distribution as follows:

Theorem 5. *A sequence* $\boldsymbol{x} = \{x_n\}_{n=1}^{N}$ *of real numbers partitioned into* P *equi-spaced bins denoted as* $\{p_i\}_{i=1}^{P}$*, can be called uniformly distributed if the number of elements in each bin, denoted as* $\mathcal{C}(p_i; \boldsymbol{x})$ *follows:*

$$\left| \mathcal{C}(p_i; \boldsymbol{x}) - \frac{N}{P} \right| \simeq 0, \qquad i \in \{1, 2, \cdots, P\}, \tag{3.2}$$

where the above expression is as small as possible, pertinent to cases where N *is not perfectly divisible by* P*.*

Surprisingly, defining a sequence based on its elements' membership to the bins will also provide an extra degree of control to modify the distribution of the sequence itself at a later point.

3.3 The Proposed Method

In the following, we describe in detail our proposed design approach for generating highly uncorrelated sequences with a uniform distribution.

3.3.1 Construction with Low Correlation

The CAN algorithm in [20] provides an efficient mathematical formalism confirming our intuitive observation that a sequence with small out-of-phase periodic correlation has an almost uniform frequency spectrum. Following such observation, the periodic out-of-phase correlations of a sequence $\boldsymbol{x}$ of length N can be optimized conveniently by following minimization problem:

$$\min_{\boldsymbol{x}, \boldsymbol{v}} \quad \|\boldsymbol{A}^H \boldsymbol{x} - \boldsymbol{v}\|_2^2 \tag{3.3}$$

Algorithm 2 Optimal modification of $\boldsymbol{h}$ according to the edge values, and their corresponding bins.

Ensure: $\boldsymbol{h}, N, P$

$\hat{\boldsymbol{h}} \triangleq \{\hat{h}_n\}_{n=1}^{N}$ initialize $n = 1$ maxnum $\leftarrow$ floor(N/P)
while $n \leq N$ **do** bin_index $\leftarrow$ ceil$(n/$maxnum$)$
    if $h_n <$ lower_edge(bin_index) **then** $\hat{h}_n \leftarrow$ lower_edge(bin_index)
    else if $h_n >$ upper_edge(bin_index) **then** $\hat{h}_n \leftarrow$ upper_edge(bin_index)
    else$\hat{h}_n \leftarrow h_n$
    end if$n \leftarrow n + 1$
end while

where $\boldsymbol{A}$ denotes the $N \times N$ (inverse) discrete Fourier transformation (DFT) matrix, whose elements can be given as,

$$[A]_{k,l} = \frac{1}{\sqrt{N}} \exp\{j2\pi kl/N\}, \qquad k, l = 1, \cdots, N \tag{3.4}$$

where $j^2 = -1$ and $\boldsymbol{v}$ is the representation of $\boldsymbol{x}$ in Fourier domain. Here, $\boldsymbol{x}$ is constrained to have given distribution, as in Equation 3.2. Observe that, the aperiodic correlations of $\boldsymbol{x}$ can be given in terms of periodic correlations of the sequence $\tilde{\boldsymbol{x}} = [\boldsymbol{x}\ \boldsymbol{0}_N]^T$.

Hence, in the aperiodic case, one can consider the following design problem in frequency-domain aiming for minimization of the out-of-phase correlations of $\boldsymbol{x}$:

$$\min_{\tilde{\boldsymbol{x}}, \tilde{\boldsymbol{v}}} \quad \|\tilde{\boldsymbol{A}}^H \tilde{\boldsymbol{x}} - \tilde{\boldsymbol{v}}\|_2^2 \tag{3.5}$$

in which $\tilde{\boldsymbol{A}}$ denotes the $2N \times 2N$ (inverse) DFT matrix, and also $\boldsymbol{x}$ is constrained to have uniform distribution as previously described.

Algorithm 3 Algorithm for construction of uniformly distributed sequences with low auto-correlation

Require: sequence length N, number of bins P.
Ensure: $\boldsymbol{x}$ using a randomly generated sequence

1: **repeat**
2: Compute $\hat{\boldsymbol{v}}$ using Equation 3.7
3: Compute $\hat{\boldsymbol{x}}$ using Equation 3.9
4: Compute $\boldsymbol{h}$ using Equation 3.10 and preserve the index of each elements of original sequence $\hat{\boldsymbol{x}}$ in $\mathcal{I}_a(\hat{\boldsymbol{x}})$
5: Partition $\boldsymbol{h}$ into P bins of equal length and compute the edges of each bin
6: Modify the elements of $\boldsymbol{h}$ using Algorithm 2
7: Compute $\bar{\boldsymbol{x}}$ by restoring the index order previously stored in step 3
8: **until** $|d^{(s)} - d^{(s-1)}| \leq 10^{-6}$ where $d = \|\tilde{\boldsymbol{A}}^H \tilde{\boldsymbol{x}} - \tilde{\boldsymbol{v}}\|_2$, and s denotes the iteration number

Note that for a given $\tilde{\boldsymbol{x}}$, the minimization of Equation 3.5 *w.r.t.* $\tilde{\boldsymbol{v}}$ is straightforward. Let

$$\boldsymbol{f} \triangleq \{f_n\}_{n=1}^{2N} = \tilde{\boldsymbol{A}}^H \tilde{\boldsymbol{x}} \tag{3.6}$$

denote the FFT of $\tilde{\boldsymbol{x}}$. The optimum $\tilde{\boldsymbol{v}}$, denoted as $\hat{\boldsymbol{v}}$ can be obtained as

$$\hat{\boldsymbol{v}} = \frac{1}{\sqrt{2}} [e^{j\psi_1} \ \cdots \ e^{j\psi_{2N}}]^T \tag{3.7}$$

where $\psi_n = \arg\{f_n\}$, for $n = 1, \cdots, 2N$. Similarly, for fixed $\tilde{\boldsymbol{v}}$, we denote inverse FFT (IFFT) of $\tilde{\boldsymbol{v}}$ as, $\boldsymbol{g} \triangleq \{g_n\}_{n=1}^{2N} = \tilde{\boldsymbol{A}}\tilde{\boldsymbol{v}}$.

Observe that,

$$\|\tilde{\boldsymbol{A}}^H \tilde{\boldsymbol{x}} - \tilde{\boldsymbol{v}}\|_2^2 = \|\tilde{\boldsymbol{x}} - \tilde{\boldsymbol{A}}\tilde{\boldsymbol{v}}\|_2^2. \tag{3.8}$$

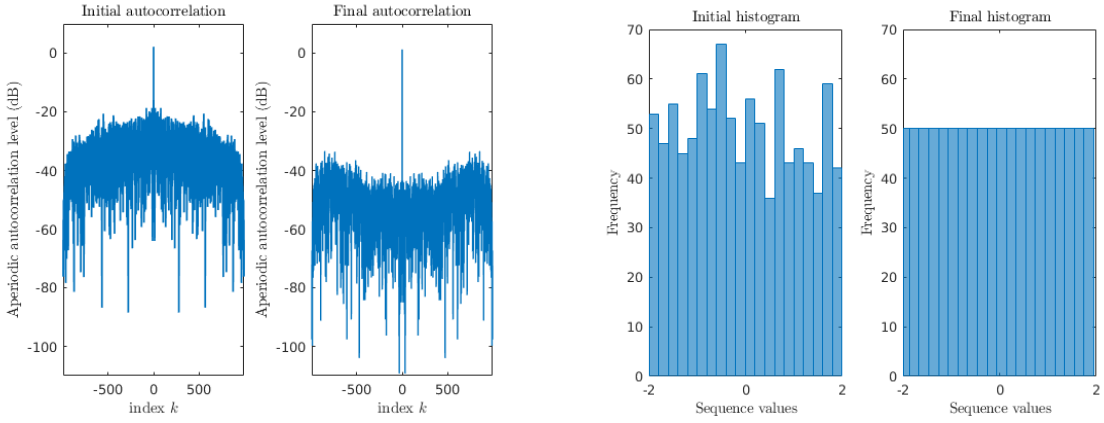

Figure 13. The initial and final (a) normalized aperiodic auto-correlation, and (b) histogram of constructed sequence of length $N = 10^3$ and $P = 20$ using the proposed algorithm.

It follows from the above that the minimizer $\boldsymbol{x}$ of Equation 3.5, denoted as $\hat{\boldsymbol{x}} \triangleq \{\widehat{x}_n\}_{n=1}^{N}$ is simply given by

$$\widehat{x}_n = g_n, \qquad n = 1, \cdots, N. \tag{3.9}$$

3.3.2 Construction with Uniform Distribution

In this section, we extend our previous formulations to enforce a uniform distribution for the sequences obtained from the above framework, and particularly Equation 3.8. This goal will be accomplished by finding the minimizer $\boldsymbol{x}$ of Equation 3.5 that has a uniform distribution. In other words, the *nearest-vector* problem in Equation 3.8 is to be solved by a projection on the

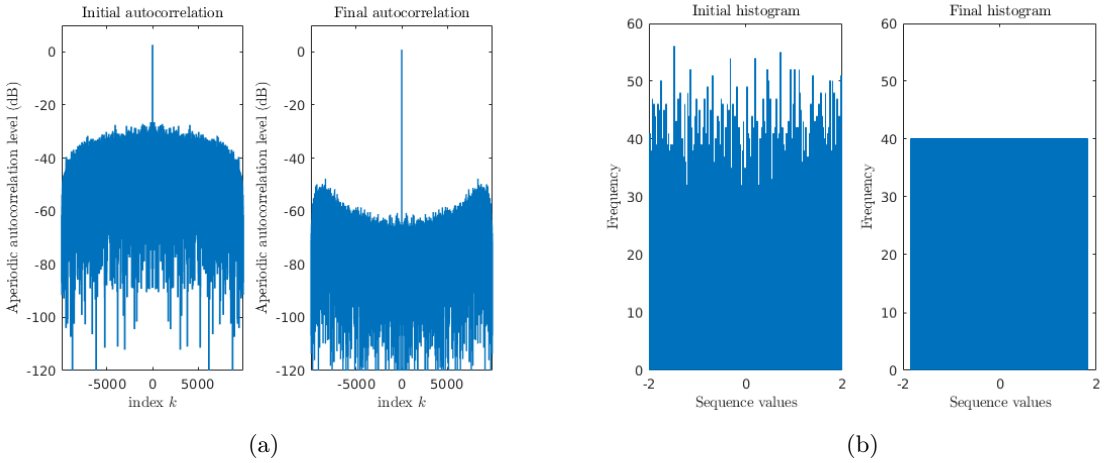

Figure 14. The initial and final (a) normalized aperiodic auto-correlation, and (b) histogram of constructed sequence of length $N = 10^4$ and $P = 250$ using the proposed algorithm.

set of sequences with a uniform distribution. Therefore, we will revisit the concept of histogram equalization.

It is not difficult to verify that the aforementioned projection can be computed by segmenting the sequence entries into smaller bins, and aiming to achieve a uniform distribution inside these smaller bins so that by controlling the smaller bins, a sequence with a given distribution can be generated. The algorithm is as follows: we first sort the sequence entries in an ascending order to form

$$\boldsymbol{h} = \mathcal{S}_a(\hat{\boldsymbol{x}}) \tag{3.10}$$

where $\mathcal{S}_a(\cdot)$ denotes a sorting operation (in ascending order) on the vector argument. Along with sorting, we also preserve the index of each element in the original sequence $\hat{\boldsymbol{x}}$ in an index array $\mathcal{I}_a(\hat{\boldsymbol{x}})$.

Next, we partition $\boldsymbol{h}$ into P equi-sized bins, where $1 \leq P \leq N$. Note that, $P = 1$ resembles the whole sequence in one single bin, whereas $P = N$ suggests each bin p_i contains only one element $\widehat{x_i}$. Naturally, both situations are not desirable for optimum distribution induction. Therefore, we choose P such that the sequence length N is divisible (or closely divisible, if N is prime) by P and also large enough to achieve a smooth transition between two consecutive bins. Finally, we compare the values of each element with the corresponding bin's edge values and modify those elements according to Algorithm 2. Once we have modified $\hat{\boldsymbol{h}}$, we are easily back to our optimal sequence $\bar{\boldsymbol{x}}$ by employing the index array of $\mathcal{I}_a(\hat{\boldsymbol{x}})$. Note that the optimality of projection can be shown easily but is omitted herein for the sake of brevity.

The iterative algorithm for the construction of the desired sequences with good correlation and good distribution properties is summarized in Algorithm 3.

3.4 Numerical Simulations

We provide several numerical examples to investigate the performance of the proposed method. We use the proposed approach to design uniformly distributed sequences of length (i) $N = 10^3$ with number of partitions $P = 20$, and (ii) $N = 10^4$ with partition $P = 250$ using `rand` function in Matlab. Although `rand` provides fairly uniformly distributed random sequences but is not at all uniform inside a bin. For both cases the initial and final normalized aperiodic auto-correlation level (NAPC) $= 20 \log_{10} |r_k/r_0|$ in dB.

The initial and final normalized aperiodic auto-correlations are presented in Figure 13(a) and 14(a). We also present the initial and final histogram of the both sequences in Figure 13(b) and 14(b). A significant improvement in terms of both auto-correlation and distribution can be observed in both cases. It should also be noted that the generation of sequences using the proposed method was relatively fast in terms of computational time. Particularly, it took 1.56 secs and 57.39 secs on a standard PC to accomplish the sequence design for the first and second cases described above, respectively.

3.5 Concluding Remarks

Signals with both good auto-correlation and good distribution properties are required in eye-tracking for Parkinson's Disease diagnosis and treatment. We have presented a new framework to design such signals based on the CAN computational framework. The proposed method is computationally efficient and can design very long sequences (of lengths up to $N \sim 10^6$ and even more) in relatively short time frames. The designed sequences using the proposed algorithm show significant enhancement in terms of out-of-phase auto-correlation as well as distribution properties. While the numerical examples showed promising results, as a future research direction, it would be of great interest to study the behavior of ISL or other correlation-related metrics and particularly their relationship with given marginal distributions.

I-B

Widely Linear Systems

CHAPTER 4

DESIGN OF UNIMODULAR SEQUENCE SETS WITH GOOD CORRELATION AND COMPLEMENTARY CORRELATION PROPERTIES

Overview: In this chapter, we address the problem of identification and sensing systems that especially employ widely linear (WL) signal processing by designing sets of unimodular sequences with good cross-correlation and complementary cross-correlation properties over a zero-correlation-zone, which has been proven to be beneficial for such systems. The sequence sets are designed by exploiting a complete second-order characterization, which depicts a WL system more powerfully.

4.1 Introduction

In Part I-A of this thesis, we have discussed designing sequences with low auto-correlation sidelobe levels that are well suited for strictly linear (SL) systems. This chapter shifts our attention to widely linear (WL) systems where it is extremely beneficial to take the complete second-order characterization of the signals and system into consideration [154]. Such characterization includes the correlation and complementary correlation functions (or relation functions [18, 155]). For a set of sequences $\{x_m(n)\}_{n=0}^{N-1}$ for $m = 1, 2, \ldots, M$, the definitions of auto-

---

and cross-correlations have been established in Section 2.2.1. A pair of sequences $x_m(n)$ and $x_{m'}(n)$ from this set, have aperiodic cross-correlation coefficients given as,

$$r_{m,m'}(l) = \sum_{n=l}^{N-1} x_m^*(n) x_{m'}(n-l), \qquad -(N-1) \leq l \leq (N-1). \tag{4.1}$$

On the other hand, the aperiodic complementary correlation coefficients are defined as

$$\gamma_{m,m'}(l) = \sum_{n=l}^{N-1} x_m(n) x_{m'}(n-l), \qquad -(N-1) \leq l \leq (N-1). \tag{4.2}$$

As has been documented, the correlation and the complementary correlation functions can be used to completely characterize the second-order statistics of complex signals. In wireless communications, WL systems are used to analyze baseband models that consider radio frequency impairments such as in-phase and quadrature-phase (I/Q) imbalances [18].

Designing unimodular sequences with good correlation properties for an SL system is a long-standing problem and the literature on this topic is quite extensive (*e.g.*, see [20, 85, 90]). Consider an SL (*e.g.*, a radar or a communication) system that takes M and mutually orthogonal unimodular sequences as input. Let the code length of each waveform be N. Then the full waveform matrix can be written in a matrix form as $\boldsymbol{X} \triangleq [\boldsymbol{x}_1, \cdots, \boldsymbol{x}_M]$ of size $N \times M$. Here the mth column $\boldsymbol{x}_m$ corresponds to the mth orthogonal waveform. In case of an unimodular waveform, the nth element of $\boldsymbol{x}_m$ is expressed as $x_m(n) = e^{j\phi_n^{(m)}}$ where $\phi_n^{(m)} \in [-\pi, \pi]$ is an arbitrary phase value. The use of unimodular sequences is quite common in many active sensing and communication systems due to their unique equi-energy and modulation properties.

Although, there are many numerical techniques and computational frameworks available in the literature (see *e.g.*, [20] and the references within), it can be noted that designing such sequences with lengths $N \sim 10^4$ or larger is still deemed to be impractical using the current standard computational tools. Recently, the use of numerical techniques to generate sequences with good cross-correlation properties has gained increased attention ([20, 82, 85, 90, 110, 135, 156, 157]). These methods seek to minimize a function that incorporates a weighted sum of the energy in the sidelobe levels of the sequences, referred to as the weighted integrated sidelobe level (WISL). For the case of an SL system, the definition of WISL for the waveforms $\{x_m(n)\}_{m=1,n=0}^{M,N-1}$ can be expressed as [20],

$$\mathcal{C}_{SL} = \sum_{m=1}^{M} \sum_{\substack{l=-(N-1),\\ l\neq 0}}^{N-1} \left(\alpha_{m,m}^{(l)}\right)^2 |r_{m,m}(l)|^2 + \sum_{m=1}^{M} \sum_{\substack{m'=1,\\ m'\neq m}}^{M} \sum_{l=-(N-1)}^{N-1} \left(\alpha_{m,m'}^{(l)}\right)^2 \left|r_{m,m'}(l)\right|^2 \tag{4.3}$$

where $\{\alpha_{m,m'}^{(l)}\}_{l=-N+1}^{N-1}$ are real-valued symmetric weights used for manipulation of the sidelobe levels corresponding to different lags. Note that $\alpha_{m,m'}^{(l)} = 0$ implies the sidelobe level associated with the corresponding lth lag is not being considered. On the other hand, $\{\alpha_{m,m'}^{(l)}\} = 1$ means $\mathcal{C}_{SL}$ in Equation 4.3 coincides with the ISL defined in Equation 2.8a. With that in mind, using Equation 4.3, the unimodular signal design problem by WISL minimization can be formally introduced as,

$$\begin{aligned} \min_{\boldsymbol{X}} \quad & \mathcal{C}_{SL} \\ \text{s.t.} \quad & |x_m(n)| = 1, \ \forall\ m, n. \end{aligned} \tag{4.4}$$

where the constraints ensure the unimodularity of the waveforms, while the orthogonality between waveforms is guaranteed by the objective. The optimization in Equation 4.4 often imposes a non-convex problem particularly due to the unimodularity constraint. However, by judicious mathematical manipulation, the solution can be achieved by using alternating projections via the Fast Fourier Transform [20], quasi-Newton methods [156], [158], [159] and the majorization-minimization method [110, 135, 157] among others [90].

Nonetheless, there has been very little attention to generating unimodular sequences that take a complete second-order description ([4, 154, 160, 161]) into account in order to consider especially WL systems [5], which is, essentially incorporating the complementary correlation in the design procedure. In this chapter, we address the design of sequence sets with good correlation and complementary correlation properties. They are constructed by optimizing a cost function that minimizes the second-order descriptors of the sequences over a subset of lags. A gradient-based approach is considered to perform the optimization since this family of methods has proven to be successful in the design of unimodular sequences [156, 158, 159]. It is shown via numerical examples, that the statistical properties of the designed sequences can be fully exploited to identify both SL and WL systems.

The rest of this chapter is organized as follows. A brief but useful description of the problem formulation is provided in Section 4.2. For more information on this please refer to [4, 154]. The numerical design approach and the corresponding optimization method are described in Section 4.3. Section 4.4 is dedicated to the numerical results that show the difference in the performance

of the optimized sequence between MIMO-SL and MIMO-WL scenarios. Finally, Section 4.5 concludes the chapter.

Notation. For a function of n variables, collected in the vector $\mathbf{\Phi} = [\phi_0, \phi_1, \ldots, \phi_n]^T$, its partial derivatives *w.r.t.* $\phi_0, \phi_1, \ldots, \phi_n$ are represented in a compact form by $\dfrac{\partial f(\mathbf{\Phi})}{\partial \mathbf{\Phi}} = \left[\dfrac{\partial f}{\partial \phi_0}, \ldots, \dfrac{\partial f}{\partial \phi_n}\right]^T$.

4.2 Problem Formulation

The problem addressed herein is the design of unimodular sequences that possess good correlation and good complementary correlation properties for given lags. Let $\{x_m(n)\}_{n=0,m=1}^{N-1,M}$ denote a set of M sequences with length N. We are interested in determining the sequences that minimize the following criterion [4, 154],

$$\mathcal{C}_{WL} = \mathcal{C}_1 + \mathcal{C}_2 + \mathcal{C}_3 + \mathcal{C}_4 \tag{4.5}$$

where

$$\mathcal{C}_1 = \sum_{m=1}^{M} \sum_{\substack{l=-(N-1),\\ l\neq 0}}^{N-1} \left(\alpha_{m,m}^{(l)}\right)^2 \left|r_{m,m}(l)\right|^2, \tag{4.6a}$$

$$\mathcal{C}_2 = \sum_{m=1}^{M} \sum_{l=-(N-1)}^{N-1} \left(\beta_{m,m}^{(l)}\right)^2 \left|\gamma_{m,m}(l)\right|^2, \tag{4.6b}$$

$$\mathcal{C}_3 = \sum_{m=1}^{M} \sum_{\substack{m'=1,\\ m'\neq m}}^{M} \sum_{l=-(N-1)}^{N-1} \left(\alpha_{m,m'}^{(l)}\right)^2 \left|r_{m,m'}(l)\right|^2, \tag{4.6c}$$

$$\mathcal{C}_4 = \sum_{m=1}^{M} \sum_{\substack{m'=1,\\ m'\neq m}}^{M} \sum_{l=-(N-1)}^{N-1} \left(\beta_{m,m'}^{(l)}\right)^2 \left|\gamma_{m,m'}(l)\right|^2, \tag{4.6d}$$

subject to the restrictions $|x_m(n)|^2 = 1$ for $n = 0, 1, \ldots, N-1$ and $m = 1, 2, \ldots, M$. The scalars $\{\alpha^{(l)}_{m,m}\}$ and $\{\beta^{(l)}_{m,m'}\}$ are positive symmetric real numbers used for the purpose of weighing the correlation and complementary correlation functions of the sequences in the set to be designed.

Remark 4. Note that, the expressions given by Equation 4.6a - Equation 4.6d have straightforward interpretations. $\mathcal{C}_1$ and $\mathcal{C}_3$ are responsible for the auto-correlation and the cross-correlation functions of the sequences in the set and the weights $\{\alpha^{(l)}_{m,m'}\}$, define the desired zero-correlation-zone (ZCZ) region. Similarly, $\mathcal{C}_2$ and $\mathcal{C}_4$ impose complementary correlation values according to the weights $\{\beta^{(l)}_{m,m'}\}$. Moreover, Equation 4.5 can be considered to define a Generalized Weighted Integrated Sidelobe Level (GWISL) [154, 161], where a complete second order characterization (that encompasses the correlation and the relation functions) is considered to construct the set of interest. In fact, if we set all $\{\beta^{(l)}_{m,m'}\}$ to 0, then Equation 4.5 reduces to a WISL criterion as reported in Equation 4.3. ■

4.3 Numerical Design Approach

In this section, we take advantage of the inherent symmetries in each of the functions given by Equation 4.6a - Equation 4.6d, to write Equation 4.5 in vector notation. This is done with the objective of deriving a closed form expression for the gradient that enables us to use a quasi-Newton based method to solve the stated optimization problem. Due to the constant magnitude restriction, it is possible to consider the parameterization $x_m(n) = e^{j\phi^{(m)}_n}$ for $n = 0, 1, \ldots, N-1$ and $m = 1, 2, \ldots, M$. Hence, the problem reduces to find the values of $M \times N$ phases that minimize Equation 4.5.

4.3.1 Correlation and Complementary Correlation of Extended Sequences

In order to simplify Equation 4.5, the following vectors are considered $\boldsymbol{\Phi}_m = [\phi_0^{(m)}, \phi_1^{(m)}, \ldots, \phi_{N-1}^{(m)}]^T$, for $m = 1, 2, \ldots, M$ and $\boldsymbol{\Phi} = [\boldsymbol{\Phi}_1^T \ \boldsymbol{\Phi}_2^T \cdots \ \boldsymbol{\Phi}_N^T]^T$ with $\dim(\boldsymbol{\Phi}) = MN \times 1$. Additionally, we define $\bar{\boldsymbol{x}}_m = \left[e^{i\phi_0^{(m)}}, e^{i\phi_1^{(m)}}, \ldots, e^{i\phi_{N-1}^{(m)}}, 0, 0, \ldots, 0\right]^T$, with $\dim(\bar{\boldsymbol{x}}_m) = 2N \times 1$ for $m = 1, 2, \ldots, M$. The vectors $\bar{\boldsymbol{x}}_m$ contain the elements of the extended sequences $\{\bar{x}_m(n)\}_{n=0}^{N-1}$ which result from appending N zeros to $x_m(n)$. The extended sequences are used to compute the correlation and complementary correlation between $x_m(n)$ and $x_{m'}(n)$, for the lags $l = 0, 1, \ldots, N-1$, via a DFT by,

$$\bar{\boldsymbol{r}}_{m,m'} = \frac{1}{2N}\boldsymbol{F}_{2N}\left((\boldsymbol{F}_{2N}\bar{\boldsymbol{x}}_m)^* \circ (\boldsymbol{F}_{2N}\bar{\boldsymbol{x}}_{m'})\right) \tag{4.7}$$

and

$$\bar{\boldsymbol{\gamma}}_{m,m'} = \frac{1}{2N}\boldsymbol{F}_{2N}\left((\boldsymbol{R}_{2N}\boldsymbol{F}_{2N}\bar{\boldsymbol{x}}_m) \circ (\boldsymbol{F}_{2N}\bar{\boldsymbol{x}}_{m'})\right), \tag{4.8}$$

respectively. The matrix $\boldsymbol{R}_{2N}$ in Equation 4.8 satisfies $\boldsymbol{R}_{2N} = 2N \times 2N$, and it is given by $\boldsymbol{R}_{2N} = [\boldsymbol{e}_0, \boldsymbol{e}_{2N-1}, \ldots, \boldsymbol{e}_1]$ where $\{\boldsymbol{e}_0, \boldsymbol{e}_1, \ldots, \boldsymbol{e}_{2N-1}\}$ denotes the standard basis for $\mathbb{C}^{2N\times 1}$.

4.3.2 On the Optimization *w.r.t.* $\mathcal{C}_1$

The function $\mathcal{C}_1$ can be simplified, if we impose the restrictions $\alpha_{m,m}^{(-l)} = \alpha_{m,m}^{(l)}$ for $l = 1, 2, \ldots, N-1$ (symmetric weights for positive and negative correlation lags). Furthermore, by

making use of the Hermitian symmetry of the auto-correlation function, $r_{m,m}(-l) = r^*_{m,m}(l)$, we can write $\mathcal{C}_1$ as,

$$\mathcal{C}_1(\boldsymbol{\Phi}) = \sum_{m=1}^{M} \bar{\boldsymbol{r}}^H_{m,m} \boldsymbol{U}_{m,m} \bar{\boldsymbol{r}}_{m,m} \tag{4.9}$$

where $\boldsymbol{U}_{m,m} = \text{Diag}\left([0, \alpha^{(1)}_{m,m}, \alpha^{(2)}_{m,m}, \ldots, \alpha^{(N-1)}_{m,m}, 0, 0, \ldots, 0]\right)$. From Equation 4.9 it is possible to compute the partial derivatives of $\mathcal{C}_1$ *w.r.t.* $\phi^{(m)}_0, \ldots, \phi^{(m)}_{N-1}$, by

$$\frac{\partial \mathcal{C}_1(\boldsymbol{\Phi})}{\partial \boldsymbol{\Phi}_m} = 2\Re\left\{ \left(\frac{\partial \bar{\boldsymbol{r}}_{m,m}(\boldsymbol{\Phi}_m)}{\partial \boldsymbol{\Phi}_m} \right)^T \boldsymbol{U}^T_{m,m} \bar{\boldsymbol{r}}^*_{m,m} \right\} \tag{4.10}$$

for $m = 1, 2, \ldots, M$, where $\dfrac{\partial \bar{\boldsymbol{r}}_{m,m}}{\partial \boldsymbol{\Phi}_m}$ denotes the Jacobian of $\bar{\boldsymbol{r}}_{m,m}$ which satisfies $\dim \dfrac{\partial \bar{\boldsymbol{r}}_{m,m}}{\partial \boldsymbol{\Phi}_m} = 2N \times N$. Furthermore, the columns of $\dfrac{\partial \bar{\boldsymbol{r}}_{m,m}}{\partial \boldsymbol{\Phi}_m}$ are computed from,

$$\frac{\partial \bar{\boldsymbol{r}}_{m,m}}{\partial \phi^{(m)}_n} = \frac{\boldsymbol{F}_{2N}}{N} \Re\left\{ (\boldsymbol{F}_{2N} \bar{\boldsymbol{x}}_m)^* \circ \left(\boldsymbol{F}_{2N} \frac{\partial \bar{\boldsymbol{x}}_m}{\partial \phi^{(m)}_n} \right) \right\} \tag{4.11}$$

for $n = 0, 1, \ldots, N-1$. Now, from the structure of each of the vectors containing the elements of the extended sequences, we have that $\dfrac{\partial \bar{\boldsymbol{x}}_m}{\partial \phi^{(m)}_n} = i e^{i\phi^{(m)}_n} \boldsymbol{e}_n$. Hence, the gradient of $\mathcal{C}_1$ can be computed from Equation 4.10 as,

$$\frac{\partial \mathcal{C}_1(\boldsymbol{\Phi})}{\partial \boldsymbol{\Phi}} = \left[\left(\frac{\partial \mathcal{C}_1}{\partial \boldsymbol{\Phi}_1} \right)^T, \ldots, \left(\frac{\partial \mathcal{C}_1}{\partial \boldsymbol{\Phi}_M} \right)^T \right]^T. \tag{4.12}$$

4.3.3 On the Optimization *w.r.t.* $\mathcal{C}_2$

If symmetric weights are used for positive and negative lags, and the even symmetry of the complementary correlation function is taken into account, this is $\gamma_{m,m}(-l) = \gamma_{m,m}(l)$, then Equation 4.6b can be cast in vector notation as,

$$\mathcal{C}_2(\boldsymbol{\Phi}) = \sum_{m=1}^{M} \bar{\boldsymbol{\gamma}}_{m,m}^{H} \boldsymbol{V}_{m,m} \bar{\boldsymbol{\gamma}}_{m,m}. \tag{4.13}$$

The matrix $\boldsymbol{V}_{m,m}$ satisfies $\dim \boldsymbol{V}_{m,m} = 2N \times 2N$ and it is computed from

$$\boldsymbol{V}_{m,m} = \text{Diag}\left(\left[\beta_{m,m}^{(0)}, \beta_{m,m}^{(1)}, \ldots, \beta_{m,m}^{(N-1)}, 0, 0, \ldots, 0\right]\right) \tag{4.14}$$

for $m = 1, 2, \ldots, M$. Furthermore, $\dfrac{\partial \mathcal{C}_2}{\partial \boldsymbol{\Phi}_m}$, is evaluated through the expression,

$$\frac{\partial \mathcal{C}_2(\boldsymbol{\Phi})}{\partial \boldsymbol{\Phi}_m} = 2\Re\left\{\left(\frac{\partial \bar{\boldsymbol{\gamma}}_{m,m}}{\partial \boldsymbol{\Phi}_m}\right)^{T} \boldsymbol{V}_{m,m} \bar{\boldsymbol{\gamma}}_{m,m}^{*}\right\}. \tag{4.15}$$

The columns of the Jacobian matrix $\dfrac{\partial \bar{\boldsymbol{\gamma}}_{m,m}}{\partial \boldsymbol{\Phi}_m}$, which satisfies $\dim \dfrac{\partial \bar{\boldsymbol{\gamma}}_{m,m}}{\partial \boldsymbol{\Phi}_m} = 2N \times N$, are computed in turn by,

$$\frac{\partial \bar{\boldsymbol{\gamma}}_{m,m}}{\partial \phi_n^{(m)}} = \frac{\boldsymbol{F}_{2N}}{2N}\left((\boldsymbol{R}_{2N}\boldsymbol{F}_{2N}\bar{\boldsymbol{x}}_m) \circ \left(\boldsymbol{F}_{2N}\frac{\partial \bar{\boldsymbol{x}}_m}{\partial \phi_n^{(m)}}\right) + \left(\boldsymbol{R}_{2N}\boldsymbol{F}_{2N}\frac{\partial \bar{\boldsymbol{x}}_m}{\partial \phi_n^{(m)}}\right) \circ (\boldsymbol{F}_{2N}\bar{\boldsymbol{x}}_m)\right). \tag{4.16}$$

Similarly, the gradient of $\mathcal{C}_2$ is obtained from the M vectors $\dfrac{\partial \mathcal{C}_2}{\partial \boldsymbol{\Phi}_m}$, arranged as

$$\frac{\partial \mathcal{C}_2}{\partial \boldsymbol{\Phi}} = \left[\left(\frac{\partial \mathcal{C}_2}{\partial \boldsymbol{\Phi}_1} \right)^T, \ldots, \left(\frac{\partial \mathcal{C}_2}{\partial \boldsymbol{\Phi}_M} \right)^T \right]^T. \tag{4.17}$$

4.3.4 On the Optimization *w.r.t.* $\mathcal{C}_3$

The function $\mathcal{C}_3$ can be expressed as,

$$\mathcal{C}_3(\boldsymbol{\Phi}) = \sum_{m=1}^{M-1} \sum_{m'=m+1}^{M} \bar{\boldsymbol{r}}_{m,m'}^H \boldsymbol{U}_{m,m'} \bar{\boldsymbol{r}}_{m,m'} + \sum_{m=1}^{M-1} \sum_{m'=m+1}^{M} \bar{\boldsymbol{r}}_{m',m}^H \boldsymbol{U}_{m',m} \bar{\boldsymbol{r}}_{m',m} \tag{4.18}$$

if the restrictions $\alpha_{m,m'}^{(-l)} = \alpha_{m',m}^{(l)}$ are imposed. Their matrices $\boldsymbol{U}_{m,m'}$ and $\boldsymbol{U}_{m',m}$ contain the weights $\alpha_{m,m'}^{(l)}$ and $\alpha_{m',m}^{(l)}$, respectively in their diagonals. Furthermore, $\dfrac{\partial \mathcal{C}_3}{\partial \boldsymbol{\Phi}_m}$ is computed from,

$$\begin{aligned} \frac{\partial \mathcal{C}_3(\boldsymbol{\Phi})}{\partial \boldsymbol{\Phi}_m} &= 2 \sum_{l=1}^{m-1} \Re \left\{ \left(\frac{\partial \bar{\boldsymbol{r}}_{l,m}}{\partial \boldsymbol{\Phi}_m} \right) \boldsymbol{U}_{l,m}^T \bar{\boldsymbol{r}}_{l,m}^* \right\} + 2 \sum_{l=1}^{m-1} \Re \left\{ \left(\frac{\partial \bar{\boldsymbol{r}}_{m,l}}{\partial \boldsymbol{\Phi}_m} \right) \boldsymbol{U}_{m,l}^T \bar{\boldsymbol{r}}_{m,l}^* \right\} \\ &+ 2 \sum_{l=m+1}^{M} \Re \left\{ \left(\frac{\bar{\boldsymbol{r}}_{l,m}}{\partial \boldsymbol{\Phi}_m} \right)^T \boldsymbol{U}_{l,m}^T \bar{\boldsymbol{r}}_{l,m}^* \right\} + 2 \sum_{l=m+1}^{M} \Re \left\{ \left(\frac{\partial \bar{\boldsymbol{r}}_{m,l}}{\partial \boldsymbol{\Phi}_m} \right)^T \boldsymbol{U}_{m,l}^T \bar{\boldsymbol{r}}_{m,l}^* \right\}. \end{aligned} \tag{4.19}$$

The columns of the matrices $\dfrac{\bar{\boldsymbol{r}}_{m',m}}{\partial \boldsymbol{\Phi}_m}$ and $\dfrac{\bar{\boldsymbol{r}}_{m,m'}}{\partial \boldsymbol{\Phi}_m}$, which satisfy $\dim \dfrac{\bar{\boldsymbol{r}}_{m',m}}{\partial \boldsymbol{\Phi}_m} = \dim \dfrac{\bar{\boldsymbol{r}}_{m,m'}}{\partial \boldsymbol{\Phi}_m} = 2N \times N$, are obtained in a similar way by evaluating $\dfrac{\bar{\boldsymbol{r}}_{m,m'}}{\partial \phi_n^{(m)}}$ and $\dfrac{\bar{\boldsymbol{r}}_{m',m}}{\partial \phi_n^{(m)}}$ respectively for $n = 0, 1, \ldots, N-1$. The gradient of $\mathcal{C}_3$ is obtained from its M sub-blocks given by Equation 4.19.

4.3.5 On the Optimization *w.r.t.* $\mathcal{C}_4$

The function $\mathcal{C}_4$ is obtained from Equation 4.6c by replacing $\boldsymbol{r}_{m,m'}$ with $\boldsymbol{\gamma}_{m,m'}$. Similarly, the matrices $\boldsymbol{U}_{m,m'}$ and $\boldsymbol{U}_{m',m}$ are substituted with $\boldsymbol{V}_{m,m'}$ and $\boldsymbol{V}_{m',m}$, which are constructed

by considering the weights $\beta_{m,m'}^{(l)}$ for $l = 0, 1, \ldots, N-1$. The vector $\dfrac{\partial \mathcal{C}_4}{\partial \mathbf{\Phi}_m}$ is obtained from Equation 4.19 as well by replacing $\bar{\boldsymbol{r}}_{m,m'}$ and $\bar{\boldsymbol{r}}_{m',m}$ with $\bar{\boldsymbol{\gamma}}_{m,m'}$ and $\bar{\boldsymbol{\gamma}}_{m',m}$ respectively.

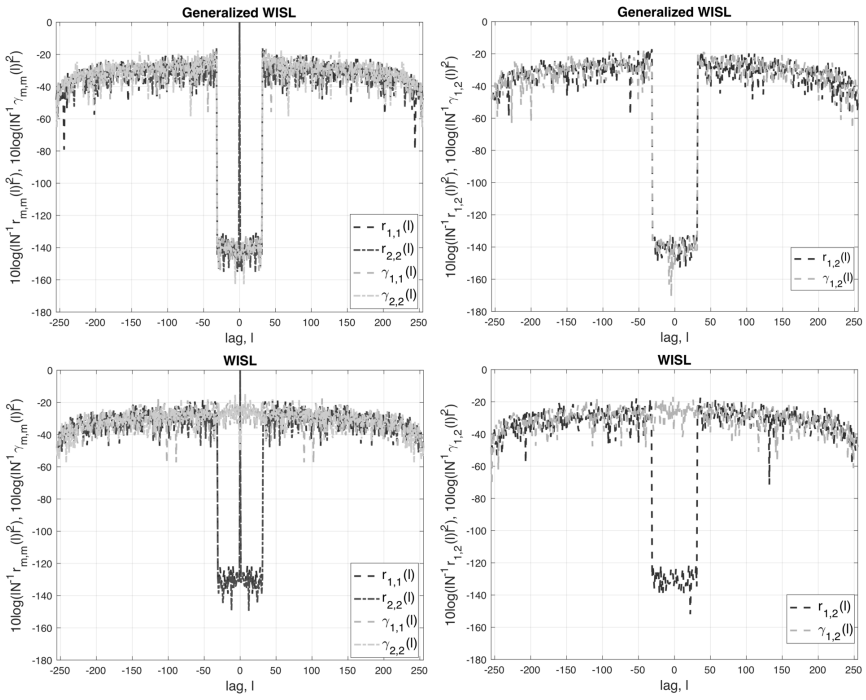

Figure 15. Correlation and complementary correlation of the designed set for $N = 256$ and $M = 2$.

4.3.6 Optimization Method

A gradient-based approach, the L-BFGS method as implemented in the SciPy toolbox [162], is hereby used to solve the optimization problem given by Equation 4.5. This technique has been considered in the design of a set of sequences with good correlation [156] and good comple-

mentary correlation properties [154,160]. The algorithm requires as inputs the cost function, its gradient, and a suitable starting point to initialize the optimization algorithm which has been detailed in the following section.

4.4 Numerical Simulations

4.4.1 Design of a Set of Sequences with N = 256, M = 2

We consider the design of a set of $M = 2$ sequences with length $N = 256$. The weights that define the auto- and complementary auto-correlation windows were selected as $\alpha_{m,m}^{(l)} = 1$ if $l \in [-31,-1] \cup [1,31]$ and $\beta_{m,m}^{(l)} = 1$ if $l = [-31,31]$ for $m = 1,2$, zero otherwise. Concerning the cross- and complementary cross-correlation weights, $\alpha_{m,m'}^{(l)} = \beta_{m,m'}^{(l)} = 1$ for $l \in [-31,31]$ and $\alpha_{m,m}^{(l)} = \beta_{m,m}^{(l)} = 0$ were used for $m, m' = 1,2$. The normalized correlation and complementary cross-correlation of the resultant set are depicted in Figure 15 and are labeled as Generalized WISL. For comparison, a set of sequences with good correlation properties for $l \in [-31,31]$ is also considered. The set was generated with the algorithm in [157] and the results obtained are labeled as WISL. For both cases, a common initialization point is used to start the algorithms, halting the iterations once $\dfrac{f^{(n-1)} - f^{(n)}}{\max\{f^{(n-1)}, f^{(n)}, 1\}} < 2.22 \times 10^{-9}$ was reached.

4.4.2 Application to MIMO System Identification

As the second numerical example, we exhibit an identification of (Multiple-Input-Multiple-Output) MIMO systems with $P = 2$ inputs and $Q = 2$ outputs for strictly linear (SL) and widely linear (WL) systems.

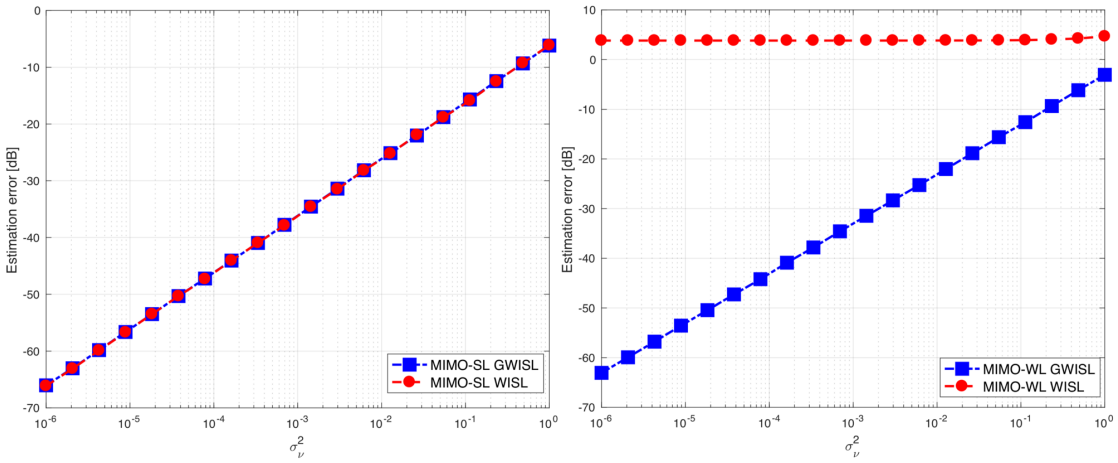

Figure 16. Estimation error of a 2×2 MIMO system.

4.4.2.1 MIMO-SL System

We consider that the output of the systems is given by $y_q(n) = \sum_{p=0}^{1}(h_{p,q} \star x_p)(n) + \nu(n)$ for $q = 1, 2$, where $\{h_{p,q}(n)\}_{n=0}^{3}$ is the response of the filter that relates the pth input ($p = 1, 2$) with $y_q(n)$. The taps of the filters are complex numbers with their real and imaginary part drawn from a standard normal distribution. Each of the output branches is affected with additive white Gaussian noise, with $E\{|\nu(n)|^2\} = \sigma_\nu^2$. The MIMO-SL system is sounded with two sequences $x_p(n)$ of length $N = 64$, that posses good correlation and complementary correlation in a window of length 16. The identification is done with a matched filter at each output, $\hat{h}_{p,q}(l) = N^{-1}(\boldsymbol{x}_p^{(l)})^H \boldsymbol{y}_q$, $\boldsymbol{y}_q = [y_q(0), y_q(1), \ldots, y_q(N+L-2)]^T$ and $\boldsymbol{x}_p^{(l)} = [\mathbf{0}_{l\times 1}^T \ \boldsymbol{x}_p^T \ \mathbf{0}_{L-l-1\times 1}^T]^T$ with $\boldsymbol{x}_p = [x_p(0), x_p(1), \ldots, x_p(N-1)]^T$. The results of the estimation process are depicted in Figure 16, where the estimation error is plotted as a function of the average power of the noise

σ_ν^2 (trace labeled as MIMO-SL GWISL). For comparison, the estimation process was done also with a set of sequences of length $N = 64$ and good correlation properties in a window of length 16, generated with the algorithm in [157] (trace labeled as MIMO-SL WISL).

4.4.2.2 MIMO-WL System

In the WL case, the output of the system is given by $y_q(n) = \sum_{p=0}^{1}(h_{p,q}^{(1)} \star x_p)(n) + \sum_{p=0}^{1}(h_{p,q}^{(2)} \star x_p^*)(n) + \nu(n)$, where $\{h_{p,q}^{(1)}(l)\}_{l=0}^{3}$ and $\{h_{p,q}^{(2)}(l)\}_{l=0}^{3}$ are the filter responses that relate the pth input with $y_q(n)$. The filter coefficients were generated similarly, and estimated with $\hat{h}_{p,q}^{(1)} = N^{-1}(\boldsymbol{x}_p^{(l)})^H \boldsymbol{y}_q$ and $\hat{h}_{p,q}^{(2)} = N^{-1}(\boldsymbol{x}_p^{(l)})^T \boldsymbol{y}_q$. The estimation error, using the previous set of sequences, is depicted in Figure 16. It can be verified that sequences which minimize the GWISL criterion, are able to identify MIMO-SL and MIMO-WL systems, by making use of the second-order statistics of the output signals. However, for sequences that minimize only the WISL, there is interference that degrades the estimates for the WL scenario.

4.5 Concluding Remarks

We have proposed the design of unimodular sequences by considering a complete second-order characterization that encompasses its correlation and complementary correlation functions. It is shown via numerical examples, that due to the properties of the proposed sequences, they are well suited to estimate SL and WL systems.

CHAPTER 5

GENERALIZED CYCLIC ALGORITHMS FOR DESIGNING UNIMODULAR SEQUENCE SETS WITH GOOD (COMPLEMENTARY) CORRELATION PROPERTIES

Overview: In this chapter, we reconsider the problem of designing unimodular sequence sets with good correlation and complementary correlation properties for widely linear (WL) systems using generalized cyclic algorithms for the minimization of weighted integrated sidelobe level (WISL) based metrics. The algorithm proposed here is based on a well-known framework called WeCAN that is used for designing unimodular sequences for strictly linear systems.

5.1 Introduction

Previously, in Chapter 4, we have undertaken the problem of designing unimodular sequence sets with good correlation and complementary correlation properties for WL systems. The proposed approach especially seeks to minimize the weighted ISL (WISL) criteria using a gradient-based approach. However, the aforementioned approach is computationally expensive. In this chapter, we reformulate the WISL criterion in Equation 4.5, and solve the corresponding optimization problem for a unimodular constraint using a fast cyclic algorithm. For the sake

---

of readers' convenience, in the following we reintroduce the said WISL criterion that is to be minimized,

$$\mathcal{E} \triangleq \sum_{m=1}^{M} \sum_{\substack{n=-N+1 \\ n\neq 0}}^{N-1} \alpha_n^2 |r_{mm}(n)|^2 + \sum_{m=1}^{M} \sum_{n=-N+1}^{N-1} \beta_n^2 |\gamma_{mm}(n)|^2 \tag{5.1}$$
$$+ \sum_{m_1=1}^{M} \sum_{\substack{m_2=1 \\ m_2\neq m_1}}^{M} \sum_{n=-(N-1)}^{N-1} \alpha_n^2 |r_{m_1m_2}(n)|^2 + \sum_{m_1=1}^{M} \sum_{\substack{m_2=1 \\ m_2\neq m_1}}^{M} \sum_{n=-(N-1)}^{N-1} \beta_n^2 |\gamma_{m_1m_2}(n)|^2$$

where $\{\alpha_n\}_{n=0}^{N-1}$ and $\{\beta_n\}_{n=0}^{N-1}$ are real-valued weights with $\alpha_n = \alpha_{-n}$ and $\beta_n = \beta_{-n}$. The detailed derivation of Equation 5.1 can be found in Section 4.1. In particular, we introduce a generalized approach to minimize the criterion in Equation 5.1 by using the minimization techniques for ISL-related metrics such as CAN and WeCAN, introduced in [20, 85].

The rest of the chapter is organized as follows. Section 5.2 discusses a generalized local minimization algorithm for WISL based on cyclic optimization. We provide a specialization of the aforementioned algorithm in Section 5.3 when all weights are one. Numerical results are presented in Section 5.4 and finally, Section 5.5 summarizes the paper.

5.2 Generalized WeCAN

In this section, we formulate a generalized cyclic algorithm: Generalized Weighted CAN (G-WeCAN) which is based on the WeCAN framework devised in [85]. To facilitate the discussion in the following, we denote the unimodular sequence set in its matrix form, *i.e.*, $\boldsymbol{X} = [\boldsymbol{x}_1\ \boldsymbol{x}_2\ \cdots\ \boldsymbol{x}_m\ \cdots\ \boldsymbol{x}_M]_{N\times M}$ where $\boldsymbol{x}_m = [x_m(0)\ x_m(1)\ \cdots\ x_m(N-1)]^T$. Moreover, the

covariance and complementary covariance matrices of the sequences are given for different lags as

$$\boldsymbol{R}_n = \begin{bmatrix} r_{11}(n) & r_{12}(n) & \cdots & r_{1M}(n) \\ r_{21}(n) & r_{22}(n) & \cdots & r_{2M}(n) \\ \vdots & \vdots & \ddots & \vdots \\ r_{M1}(n) & r_{M2}(n) & \cdots & r_{MM}(n) \end{bmatrix}_{M\times M}, \quad \boldsymbol{\Gamma}_n = \begin{bmatrix} \gamma_{11}(n) & \gamma_{12}(n) & \cdots & \gamma_{1M}(n) \\ \gamma_{21}(n) & \gamma_{22}(n) & \cdots & \gamma_{2M}(n) \\ \vdots & \vdots & \ddots & \vdots \\ \gamma_{M1}(n) & \gamma_{M2}(n) & \cdots & \gamma_{MM}(n) \end{bmatrix}_{M\times M}, \tag{5.2}$$

where $n = -(N-1), \cdots, 0, \cdots, N-1$. The G-WeCAN algorithm is associated with the criterion $\mathcal{E}$ in (Equation 5.1), which can be written in matrix form as,

$$\begin{aligned} \mathcal{E} = & \ \alpha_0^2 \|\boldsymbol{R}_0 - N\boldsymbol{I}_M\|_F^2 + \beta_0^2\|\boldsymbol{\Gamma}_0\|_F^2 + 2\sum_{n=1}^{N-1} \alpha_n^2\|\boldsymbol{R}_n\|_F^2 + \beta_n^2\|\boldsymbol{\Gamma}_n\|_F^2 \\ = & \sum_{n=-(N-1)}^{N-1} \alpha_n^2\|\boldsymbol{R}_n - N\boldsymbol{I}_M\delta_n\|_F^2 + \sum_{n=-(N-1)}^{N-1} \beta_n^2\|\boldsymbol{\Gamma}_n\|_F^2 \end{aligned} \tag{5.3}$$

where δ_n denotes the Kronecker delta. Furthermore, following the proof in [20] for the case of $M = 1$, it can be shown that the criterion in Equation 5.3 can be equivalently written as a Parseval-type equality:

$$\mathcal{E} = \frac{1}{2N}\sum_{p=1}^{2N} \|\boldsymbol{\Phi}_r(\omega_p) - \alpha_0 N\boldsymbol{I}_M\|_F^2 + \|\boldsymbol{\Phi}_\gamma(\omega_p)\|_F^2 \tag{5.4}$$

in which,

$$\boldsymbol{\Phi}_r(\omega) = \sum_{n=-(N-1)}^{N-1} \alpha_n \boldsymbol{R}_n e^{-jn\omega}, \tag{5.5a}$$

$$\boldsymbol{\Phi}_\gamma(\omega) = \sum_{n=-(N-1)}^{N-1} \beta_n \boldsymbol{\Gamma}_n e^{-jn\omega}, \tag{5.5b}$$

and $\{\omega_p\}$ are the Fourier frequencies given as, $\omega_p = \frac{2\pi}{2N}p$ for $p = 1, \cdots, 2N$.

Note that, by choosing α_n and β_n appropriately, we can help shape the correlation lags in the desired form. Particularly for convenience, we choose α_0 and β_0 large enough to ensure that the matrices

$$\boldsymbol{A} = \begin{bmatrix} \alpha_0 & \cdots & \alpha_{N-1} \\ \alpha_1 & \cdots & \alpha_{N-2} \\ \vdots & \ddots & \vdots \\ \alpha_{N-1} & \cdots & \alpha_0 \end{bmatrix}, \quad \boldsymbol{B} = \begin{bmatrix} \beta_0 & \cdots & \beta_{N-1} \\ \beta_1 & \cdots & \beta_{N-2} \\ \vdots & \ddots & \vdots \\ \beta_{N-1} & \cdots & \beta_0 \end{bmatrix} \tag{5.6}$$

become positive semidefinite (*i.e.*, $\boldsymbol{A} \succeq 0$ and $\boldsymbol{B} \succeq 0$).

Now, note that the following discrete (inverse) Fourier transform relations hold:

$$\{\alpha_n \boldsymbol{R}_n\} \xleftrightarrow{\text{(I)DFT}} \boldsymbol{\Phi}_r(\omega) = A(\omega) * (\boldsymbol{\chi}(\omega)\boldsymbol{\chi}^H(\omega)) \tag{5.7a}$$

$$\{\beta_n \boldsymbol{\Gamma}_n\} \xleftrightarrow{\text{(I)DFT}} \boldsymbol{\Phi}_\gamma(\omega) = B(\omega) * (\boldsymbol{\chi}(\omega)\boldsymbol{\chi}^T(\omega)) \tag{5.7b}$$

where,

$$\boldsymbol{\chi}(\omega) = \sum_{n=0}^{N-1} \tilde{\boldsymbol{x}}(n) e^{-jn\omega}, \tag{5.8a}$$

$$A(\omega) = \sum_{k=-(N-1)}^{N-1} \alpha_k e^{-jk\omega}, \tag{5.8b}$$

$$B(\omega) = \sum_{k=-(N-1)}^{N-1} \beta_k e^{-jk\omega}, \tag{5.8c}$$

and $\tilde{\boldsymbol{x}}(n) = [x_1(n)\ x_2(n)\ \cdots\ x_M(n)]^T$. Consequently, one can verify that,

$$\begin{aligned}
\boldsymbol{\Phi}_r(\omega_p) &= \frac{1}{2\pi} \int_{-\pi}^{\pi} A(\omega_p - \psi)\ \boldsymbol{\chi}(\psi) \boldsymbol{\chi}^H(\omega)\ d\psi \\
&= \frac{1}{2\pi} \int_{-\pi}^{\pi} \sum_{k=-(N-1)}^{N-1} \alpha_k e^{-jk(\omega_p - \psi)} \boldsymbol{\chi}(\psi) \boldsymbol{\chi}^H(\psi)\ d\psi \\
&= \sum_{k=-(N-1)}^{N-1} \sum_{n=0}^{N-1} \sum_{\tilde{n}=0}^{N-1} \alpha_k \tilde{\boldsymbol{x}}(n) \tilde{\boldsymbol{x}}^*(\tilde{n})\ e^{-jk\omega_p} \times\ \frac{1}{2\pi} \int_{-\pi}^{\pi} e^{j(k-n+\tilde{n})\psi}\ d\psi \\
&= \sum_{n=0}^{N-1} \sum_{\tilde{n}=0}^{N-1} \alpha_{n-\tilde{n}} \tilde{\boldsymbol{x}}(n) \tilde{\boldsymbol{x}}^*(\tilde{n}) e^{-j(n-\tilde{n})\omega_p} \\
&= \tilde{\boldsymbol{\chi}}^T(\omega_p) \boldsymbol{A} \tilde{\boldsymbol{\chi}}^*(\omega_p) \\
&= (\tilde{\boldsymbol{\chi}}^H(\omega_p) \boldsymbol{A} \tilde{\boldsymbol{\chi}}(\omega_p))^T,
\end{aligned} \tag{5.9}$$

where $\tilde{\boldsymbol{\chi}}(\omega_p) = [\tilde{\boldsymbol{x}}(0) e^{-j0\omega_p}\ \cdots\ \tilde{\boldsymbol{x}}(N-1) e^{-j(N-1)\omega_p}]^T$. Similarly for $\boldsymbol{\Phi}_\gamma(\omega_p)$, it can be given as

$$\boldsymbol{\Phi}_\gamma(\omega_p) = \tilde{\boldsymbol{\chi}}^T(\omega_p) \boldsymbol{B} \tilde{\boldsymbol{\chi}}(\omega_p). \tag{5.10}$$

Therefore, by denoting $\tilde{\boldsymbol{\chi}}(\omega_p)$ simply as $\tilde{\boldsymbol{\chi}_p}$, the criterion in Equation 5.4 can be rewritten as

$$\mathcal{E} = \frac{1}{2N}\sum_{p=1}^{2N} \|\tilde{\boldsymbol{\chi}_p}^H \boldsymbol{A}\tilde{\boldsymbol{\chi}_p} - \alpha_0 N \boldsymbol{I}_M\|_F^2 + \|\tilde{\boldsymbol{\chi}_p}^T \boldsymbol{B}\tilde{\boldsymbol{\chi}_p}\|_F^2. \tag{5.11}$$

Note that the above function is quartic in $\{x_m(n)\}_{n=0,m=1}^{N-1,M}$, which makes the optimization difficult. To facilitate a transformation to a quadratic objective, we simplify Equation 5.11 as

$$\begin{aligned}
\mathcal{E} \;&=\; \frac{1}{2N}\sum_{p=1}^{2N} \mathrm{Tr}\left(\left(\tilde{\boldsymbol{\chi}_p}^H \boldsymbol{A}\tilde{\boldsymbol{\chi}_p} - \alpha_0 N \boldsymbol{I}_M\right)^H \times \left(\tilde{\boldsymbol{\chi}_p}^H \boldsymbol{A}\tilde{\boldsymbol{\chi}_p} - \alpha_0 N \boldsymbol{I}_M\right)\right) \\
&\qquad +\; \mathrm{Tr}\left((\tilde{\boldsymbol{\chi}_p}^T \boldsymbol{B}\tilde{\boldsymbol{\chi}_p})^H (\tilde{\boldsymbol{\chi}_p}^T \boldsymbol{B}\tilde{\boldsymbol{\chi}_p})\right) \\
&\leq\; \frac{1}{2N}\sum_{p=1}^{2N} \|\boldsymbol{A}\|_F^2 \|\tilde{\boldsymbol{\chi}_p}\|_F^4 - 2\alpha_0 N \|\boldsymbol{A}\|_F \|\tilde{\boldsymbol{\chi}_p}\|_F^2 + \alpha_0^2 N^2 M + \|\boldsymbol{B}\|_F^2 \|\tilde{\boldsymbol{\chi}_p}\|_F^4 \\
&= \frac{\|\boldsymbol{A}\|_F^2 + \|\boldsymbol{B}\|_F^2}{2N} \times \sum_{p=1}^{2N} \left(\|\tilde{\boldsymbol{\chi}_p}\|_F^2 - \frac{\alpha_0 N \|\boldsymbol{A}\|_F}{\|\boldsymbol{A}\|_F^2 + \|\boldsymbol{B}\|_F^2}\right)^2 + \text{const.}
\end{aligned} \tag{5.12}$$

Next, instead of minimizing Equation 5.12 *w.r.t.* $\{x_m(n)\}_{n=0,m=1}^{N-1,M}$, we resort to the following minimization problem:

$$\begin{aligned}
\min_{\tilde{\boldsymbol{\chi}_p}, \boldsymbol{v}_p} \quad & \sum_{p=1}^{2N} \|\tilde{\boldsymbol{\chi}_p} - \boldsymbol{v}_p\|_F^2 \\
\text{s.t.} \quad & |x_m(n)| = 1,\ \|\boldsymbol{v}_p\|_F^2 = \kappa
\end{aligned} \tag{5.13}$$

where $\kappa = \dfrac{\alpha_0 N \|\boldsymbol{A}\|_F}{\|\boldsymbol{A}\|_F^2 + \|\boldsymbol{B}\|_F^2}$. Without loss of generality, one can see that the criterion in Equation 5.12 and Equation 5.13 are "almost equivalent" to each other in the sense that if one takes

on a small value, so does the other; particularly, the quadratic terms in Equation 5.12 become zero if Equation 5.13 is zero, and vice versa.

To address the minimization problem in Equation 5.13, we define:

$$\boldsymbol{f}_p = [e^{-j\omega_p} \ \cdots \ e^{-j2N\omega_p}]^T, \tag{5.14a}$$

$$\boldsymbol{F} = [\boldsymbol{f}_1 \ \cdots \ \boldsymbol{f}_{2N}], \tag{5.14b}$$

$$\bar{\boldsymbol{X}} = [\boldsymbol{X} \ \boldsymbol{0}]^T_{M\times 2N}, \tag{5.14c}$$

$$\boldsymbol{V} = [\boldsymbol{v}_1 \ \cdots \ \boldsymbol{v}_{2N}]^T. \tag{5.14d}$$

Consequently, one can readily rewrite the minimization problem in Equation 5.13 as

$$\begin{aligned} \min_{\substack{\{x_m(n)\}_{n=0,m=1}^{N-1,M},\\ \{\boldsymbol{v}_p\}_{p=1}^{2N}}} \quad & \left\|\boldsymbol{F}^H\bar{\boldsymbol{X}} - \boldsymbol{V}\right\|_F^2 \\ \text{s.t.} \quad & |x_m(n)| = 1, \ \|\boldsymbol{v}_p\|_F^2 = \kappa. \end{aligned} \tag{5.15}$$

The criterion in Equation 5.15 can be efficiently handled via a cyclic minimization approach. For a given $\{x_m(n)\}_{n=0,m=1}^{N-1,M}$, the solution $\{\boldsymbol{v}_p\}_{p=1}^{2N}$ can be given as

$$\boldsymbol{v}_p = \sqrt{\kappa}\frac{\boldsymbol{d}_p}{\|\boldsymbol{d}_p\|_2} \tag{5.16}$$

where $\boldsymbol{d}_p^T$ = the p^{th} row of $(\boldsymbol{F}^H\bar{\boldsymbol{X}})$. Furthermore, note that $\left\|\boldsymbol{F}^H\bar{\boldsymbol{X}}-\boldsymbol{V}\right\|_F^2 = \left\|\bar{\boldsymbol{X}}-\boldsymbol{F}\boldsymbol{V}\right\|_F^2$ as $\boldsymbol{F}$ is unitary. Hence, for a given $\{\boldsymbol{v}_p\}_{p=1}^{2N}$, the solution $\{x_m(n)\}_{n=0,m=1}^{N-1,M}$ to Equation 5.13 can be found as

$$x_m(n) = \exp(j\arg([\boldsymbol{F}\boldsymbol{V}]_{m,n})). \tag{5.17}$$

It must be noted that the terms $\boldsymbol{F}^H\bar{\boldsymbol{X}}$ in Equation 5.16 and $\boldsymbol{F}\boldsymbol{V}$ in Equation 5.17 are nothing but the FFT of columns of $\bar{\boldsymbol{X}}$ and the IFFT of columns of $\boldsymbol{V}$, respectively. Owing to the nature of these solutions, G-WeCAN is very fast and can essentially be used for generating sequence sets with $N \sim 10^5$ and $M \sim 10^2$.

5.3 Generalized CAN from G-WeCAN

Based on the above formulations we further introduce a generalized version of the CAN algorithm [85], referred to as (G-CAN). G-CAN is even more computationally efficient than G-WeCAN when lowering all the out-of-phase correlation and complementary correlation lags have the same importance. Assuming $\{\alpha_n\}_{n=0}^{N-1} = \{\beta_n\}_{n=0}^{N-1} = 1$, the criterion in Equation 5.1 can be simplified as

$$\begin{aligned}\tilde{\mathcal{E}} &= \sum_{n=-(N-1)}^{N-1} \|\boldsymbol{R}_n - N\boldsymbol{I}_M\delta_n\|_F^2 + \sum_{n=-(N-1)}^{N-1} \|\boldsymbol{\Gamma}_n\|_F^2 \\ &= \frac{1}{2N}\sum_{p=1}^{2N} \|\tilde{\boldsymbol{\Phi}}_r(\omega_p) - N\boldsymbol{I}_M\|_F^2 + \|\tilde{\boldsymbol{\Phi}}_\gamma(\omega_p)\|_F^2\end{aligned} \tag{5.18}$$

where $\tilde{\boldsymbol{\Phi}}_r(\omega_p) = \sum_n \boldsymbol{R}_n e^{-jn\omega_p}$; $\tilde{\boldsymbol{\Phi}}_\gamma(\omega_p) = \sum_n \boldsymbol{\Gamma}_n e^{-jn\omega_p}$. Furthermore, following the simplification in Equation 5.9, one can write $\tilde{\boldsymbol{\Phi}}_r(\omega) = \boldsymbol{\chi}(\omega)\boldsymbol{\chi}^H(\omega)$ and $\tilde{\boldsymbol{\Phi}}_\gamma(\omega) = \boldsymbol{\chi}(\omega)\boldsymbol{\chi}^T(\omega)$. Consequently, Equation 5.18 can be given as

$$\tilde{\mathcal{E}} = \frac{1}{2N}\sum_{p=1}^{2N} \|\boldsymbol{\chi}_p\boldsymbol{\chi}_p^H - N\boldsymbol{I}_M\|_F^2 + \|\boldsymbol{\chi}_p\boldsymbol{\chi}_p^T\|_F^2 \tag{5.19}$$

which can be further simplified as

$$\begin{aligned}\tilde{\mathcal{E}} &= \frac{1}{2N}\sum_{p=1}^{2N} (2\|\boldsymbol{\chi}_p\|_2^4 - 2N\|\boldsymbol{\chi}_p\|_2^2 + N^2M) \\ &= N\sum_{p=1}^{2N}\left(\left\|\frac{\boldsymbol{\chi}_p}{\sqrt{N}}\right\|_2^2 - \frac{1}{2}\right)^2 + N^2\left(M - \frac{1}{4}\right).\end{aligned} \tag{5.20}$$

Finally, using the same argument following Equation 5.13, the minimization problem can be defined as

$$\begin{aligned}\min_{\boldsymbol{\chi}_p, \tilde{\boldsymbol{v}}_p} \quad & \sum_{p=1}^{2N}\left\|\frac{\boldsymbol{\chi}_p}{\sqrt{N}} - \tilde{\boldsymbol{v}}_p\right\|_2^2 \\ \text{s.t.} \quad & |x_m(n)| = 1,\ \|\tilde{\boldsymbol{v}}_p\|_2^2 = \frac{1}{2}.\end{aligned} \tag{5.21}$$

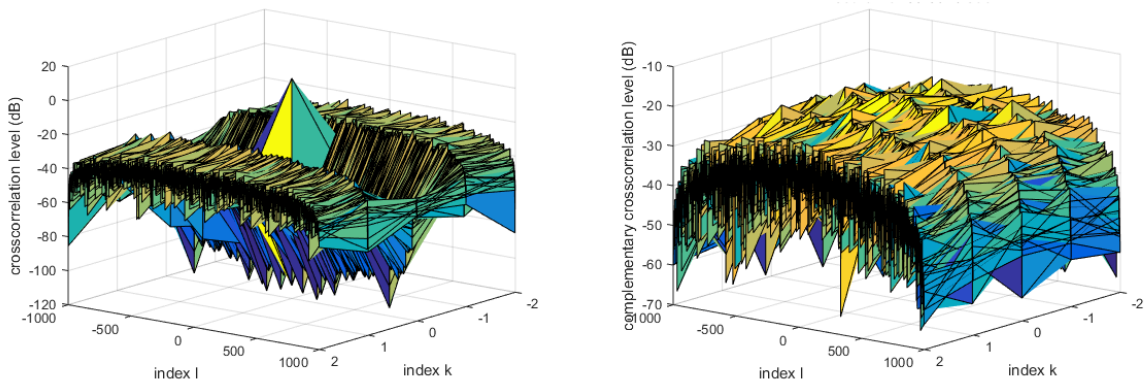

(a) (b)

Figure 17. (a) Cross-correlation and (b) complementary cross-correlation levels of the G-WeCAN sequences for $N = 1000, M = 3$.

To solve the minimization criterion in Equation 5.21, we define $\tilde{\boldsymbol{F}} = \frac{1}{\sqrt{N}}[\boldsymbol{f}_1 \ \cdots \ \boldsymbol{f}_{2N}]$. Hence, the minimization problem for G-CAN can simply be given in a matrix form as

$$\begin{aligned} \min_{\bar{\boldsymbol{X}}, \tilde{\boldsymbol{V}}} \quad & \left\| \tilde{\boldsymbol{F}}^H \bar{\boldsymbol{X}} - \tilde{\boldsymbol{V}} \right\|_F^2 \\ \text{s.t.} \quad & |x_m(n)| = 1, \ \|\tilde{\boldsymbol{v}}_p\|_2^2 = \frac{1}{2}. \end{aligned} \tag{5.22}$$

To find the solutions to Equation 5.22, one can resort to similar cyclic minimization techniques as detailed in Section 5.2.

5.4 Numerical Simulations

In this section we consider minimizing the criterion in Equation 5.15 for $N = 1000$ and $M = 3$. We initialize the algorithm with a randomly generated set of sequences with the said

length. However, other sequence families with known good correlation properties such as Golay sequences can also be used for initialization. To construct the matrices $\boldsymbol{A}$ and $\boldsymbol{B}$ in Equation 5.6 that are needed in G-WeCAN, we choose $\alpha_n^2 = \beta_n^2 = 1$ for $n \in [1, 250]$ and zero otherwise. α_0 and β_0 are chosen to make sure that $\boldsymbol{A} \succeq 0$ and $\boldsymbol{B} \succeq 0$. For G-CAN we choose $\alpha_n^2 = \beta_n^2 = 1$ for all n. 17(a) shows the cross-correlation levels of the constructed G-WeCAN set of sequences for different lags.

We also compare the generalized algorithm with previously suggested CAN and WeCAN algorithms in terms of overall ISL metrics for different sequence lengths. We generate sets of sequences with sequence length $N = \{10, 30, 100, 300, 1000\}$ and $M = 3$ for CAN, WeCAN and G-WeCAN. 18(a) depicts that G-WeCAN shows better performance than its CAN and WeCAN counterparts. It can be noted that, whereas WeCAN requires $2N$ computations of SVD of an $N \times M$ matrix, G-WeCAN relies on computations of FFT coefficients. Due to this fact, G-WeCAN is much faster than WeCAN and can be essentially used for generating sequences with length in the order of 10^5. 18(b) shows the comparison of required computation times for CAN, WeCAN and G-WeCAN sequences with $N = \{10, 30, 100, 300, 1000\}$ and $M = 3$ on a standard PC.

5.5 Concluding Remarks

We presented two cyclic algorithms, referred to as G-WeCAN and G-CAN, to minimize a generalized WISL criterion to design sets of unimodular sequences that have good correlation and complementary correlation properties. A number of numerical examples were provided

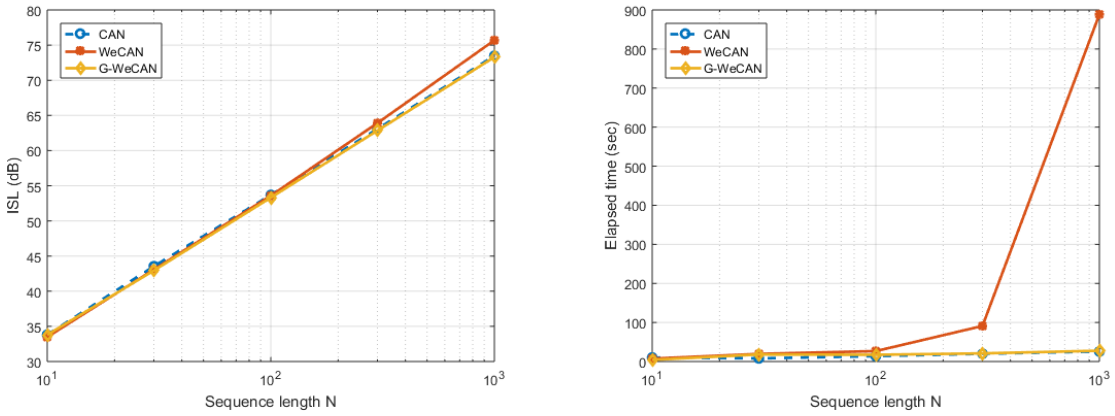

Figure 18. Comparison of (a) the WISL metrics and (b) computation times for CAN, WeCAN and G-WeCAN sequences with $N = \{10, 30, 100, 300, 1000\}$ and $M = 3$.

to demonstrate the good correlation and complementary correlation properties of the sets of unimodular sequences obtained by the proposed algorithms.

Part II

Waveform Synthesis for Advanced Radar Systems

II-A

Antenna Array Design for MIMO Radar

CHAPTER 6

EFFICIENT WAVEFORM COVARIANCE MATRIX DESIGN AND ANTENNA SELECTION FOR MIMO RADAR

Overview: Controlling the radar beam-pattern by optimizing the transmit covariance matrix is a well-established approach for performance enhancement in multiple-input-multiple-output (MIMO) radars. In this chapter, we investigate the joint optimization of the transmit waveform covariance matrix and the antenna position vector for a MIMO radar system to approximate a given transmit beam-pattern. The sequences are further designed to minimize the cross-correlation sidelobes at a number of predetermined target locations. We formulate this design task as a non-convex optimization problem and then propose a cyclic optimization approach to efficiently approximate its solution. We further propose a local binary search algorithm in order to efficiently design the corresponding antenna positions. We show that the proposed method can be extended to the more general case of approximating the given beam-pattern using a minimal number of antennas as well as optimizing their positions.

6.1 Introduction and Prior Works

MIMO radar refers to a unique radar architecture that employs multiple spatially distributed transmitters and receivers— an emerging technology in the last two decades, attracting a great

---

deal of interest from researchers in the radar signal processing community as well as industry [29–34, 41, 165]. Unlike a conventional phased array radar, a MIMO transmitter can transmit a set of arbitrary waveforms orthogonal to each other in order to increase the spatial diversity [31,35]. As previously discussed in Section 1.1.2.1, one way to exploit such diversity in MIMO systems is by transmitting orthogonal waveforms, and the echo signals can then be re-assigned to the single transmitter. Thus, from an antenna array of M_T transmitters and M_R receivers, a MIMO architecture results in a virtual array of $M_T M_R$ elements with enlarged size of virtual aperture which provides additional degrees of freedom to improve the spatial resolution [39,40], immunity to interference [41], and an improved target localization capability [42–44]. The advantages of MIMO radar over traditional phased array radar have inspired researchers to address various associated waveform design problems. Among them, is the problem of maximization of the output signal-to-interference-plus-noise ratio (SINR) by jointly designing the probing signals for transmitters and the filter coefficients for receivers [76, 166, 167]. The designed signals can be utilized not only to shape a desired beam-pattern, but also to minimize the effects of cross-correlation sidelobes between the transmitted waveforms at certain given target locations of interest [45–48]. Here, not only the main focus of this design problem is to control the spatial distribution of the transmit power, but also to improve the statistical performance of the radar system. It is known that the said performance of MIMO radar depends heavily on the cross-correlation beam-pattern which is completely missing in the phased-array case [37].

An extensive body of work already exists on designing the covariance matrix of radar transmit waveforms in lieu of designing the waveforms directly; which leads to extra degrees of

freedom in the design stage. For example, in [37], the authors describe a method to optimize the waveform covariance matrix to approximate the desired beam-pattern and minimize the correlation sidelobes using semidefinite quadratic programming (SQP), while in [45] an alternating minimization algorithm is proposed to synthesize unimodular waveform matrix to approximate the desired covariance matrix. Furthermore, in [168], a closed-form solution is suggested to design the covariance matrix to achieve the desired beam-pattern based on discrete Fourier transform (DFT) coefficients and Toeplitz matrices. An extension of the DFT-based methods to a planar-antenna-array for constant-modulus waveforms design can be found in [169] and [170]. Although the DFT-based techniques for matching the transmit beam-pattern benefit from a lower computational complexity, the performance is not satisfactory for a small number of antennas. Ahmed *et al.*, proposes two algorithms in [171] to configure a covariance matrix for a given beam-pattern. In the first algorithm, the objective is to design the square-root of the covariance matrix that is parameterized using the coordinates of a hypersphere that allows to implicitly design the square matrix as a positive semidefinite matrix in an iterative manner. The second algorithm, on the other hand, proposes a closed-form solution that exploits the design constraints and redundant information in the covariance matrix. The proposed technique although may yield a 'pseudo'-covariance matrix, the outcome is not guaranteed to be positive semidefinite. For a further study on transmit beam-pattern synthesis approaches, we refer the interested readers to consult [49–54], and the references therein.

Note that in order to match the desired transmit beam-pattern while designing the covariance matrix of the transmit signals, all the aforementioned algorithms consider a uniform linear

array (ULA) with $\lambda/2$ inter-element spacing where λ is the wavelength of the transmit signal. However, it was shown in Cheng et al. [54] that the selection of the array position can introduce additional degrees of freedom for designing transmit beam-pattern. Namely, by carefully choosing the position of antennas, one can design the desired beam-pattern using a fewer number of antennas. In other words, one can achieve a similar beam-pattern by carefully redistributing the available antennas in a wider transmit field which amounts to increased virtual aperture. As a consequence, a joint design of the covariance matrix and the antenna selection vector can procure superior performance compared with current state-of-the-art methods using the ULA with the same number of antennas. In [54], authors describe a method based on the Alternating Direction Method of Multipliers (ADMM) [172] to design the antenna selection vector. However, a convex relaxation is used to approximate the solution which is not guaranteed to produce an optimal outcome to the non-convex problem (that is NP-hard in general).

In this chapter, we tackle the aforementioned problems using an iterative greedy local search approach inspired by dynamic programming and evolutionary algorithms. In each iteration, a set of optimization parameter vectors is chosen to be perturbed and the corresponding objective values are calculated. The best parameters are then selected to form the population for the next generation, and then the entire procedure is repeated until a stopping criterion based on the original objective function is met. The main contributions in this chapter can be described as follows:

- A novel cyclic algorithm is proposed in order to jointly design the covariance matrix of the transmit waveforms and antenna selection vector. The proposed method further allows for

minimizing the cross-correlation among the transmit signals at a number of predetermined target locations.

- We design the antenna selection vector using a novel greedy search framework for binary variables. We show that by using the all-one vector as initialization, the proposed algorithm can provide a good approximate solution in a specific number of iterations. Our new framework may be of interest on its own as a general non-convex solver for waveform design in MIMO radar systems with practical constraints.
- We further provide an extension to the general antenna selection scenario where the algorithm selects the minimum number of antennas.

To promote reproducible research, the codes for generating the results presented are made publicly available [1]. The remainder of the chapter is presented as follows. Sections 6.2 and 6.3 describe the considered general signal model and the problem formulation for jointly designing the covariance matrix of the probing signals and the antenna position vector. In Section 6.3.1, we propose a novel cyclic optimization approach to tackle the aforementioned problem, while in Section 6.4, we discuss the antenna selection strategy using an iterative greedy search algorithm in detail. We extend the antenna selection problem to a more general case in Section 6.5 using a minimal number of antennas. Section 6.6 lays out several numerical examples for the proposed framework. Finally, Section 6.7 concludes the chapter.

---

[1]The codes are available on GitHub and through the link:
`https://github.com/arindam-bose/evolutionary-antenna-design-in-mimo`

6.2 Signal Model

We consider the problem of selecting N transmit antennas placed on a linear array positions with $M(\geq N)$ grid points with equal grid spacing d, in order to achieve a desired beam-pattern as depicted in Figure 19. A generalized version of the problem requires choosing the minimum number of antenna positions out of M grid points for the similar purpose. In the subsequent sections we consider both scenarios in a detailed manner. Let us consider a binary antenna position vector to represent the antenna configuration, viz.

$$\boldsymbol{p} = [p_1, p_2, \cdots, p_M]^T, \qquad p_m \in \{0, 1\},\ m \in \{1, \cdots, M\}, \tag{6.1}$$

where $p_m = 1$ indicates that the m-th grid point is chosen for antenna placement; otherwise, we have $p_m = 0$.

We consider a MIMO radar system transmitting distinct waveforms from each transmission antenna to achieve a desirable beam-pattern. Let $s_m(l)$, with $m \in \{1, \cdots, M\}$ and $l \in \{1, \cdots, L\}$, denote the transmit signal from m-th antenna, where L is the signal length in discrete-time. Assuming that the signal propagation follows a non-dispersive model and that the transmit waveforms are narrow-band, the baseband waveform at the desired target location θ can be expressed as [31]

$$\sum_{m=1}^{M} e^{-j\frac{2\pi}{\lambda} md\sin(\theta)} s_m(l) \triangleq \boldsymbol{a}^H(\theta)\boldsymbol{s}(l), \quad l \in \{1, \ldots, L\}, \tag{6.2}$$

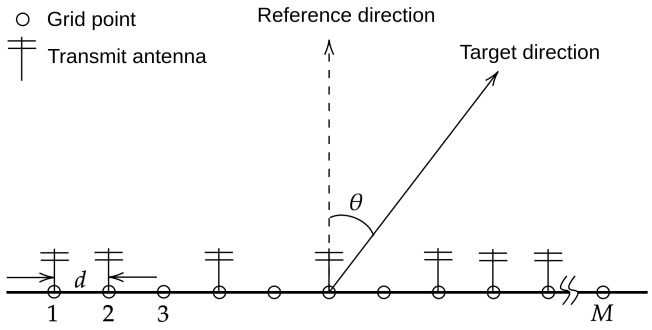

Figure 19. Geometry of a colocated MIMO radar with M grid points with inter-spacing d. Only N grid points can be used for antenna placement.

where λ is the wavelength of the transmitted signal, and $\boldsymbol{s}(l) = [s_1(l), s_2(l), \cdots, s_M(l)]^T$ is the space-time transmit waveform with length M, and $\boldsymbol{a}(\theta)$ is the *steering vector* of the ULA at the direction θ, defined as

$$\boldsymbol{a}(\theta) = [1, e^{j\frac{2\pi}{\lambda}d\sin(\theta)}, \cdots, e^{j\frac{2\pi}{\lambda}(M-1)d\sin(\theta)}]^T. \tag{6.3}$$

We seek to select N antennas out of M grid point to design the desired beam-pattern. Let $\boldsymbol{p} \in \mathbb{B}_N^M$ denote the antenna selection vector. The corresponding waveform at the target location at the generic angle θ *w.r.t.* the ULA is then given by,

$$x(l) = (\boldsymbol{p} \odot \boldsymbol{a}(\theta))^H \boldsymbol{s}(l), \qquad l \in \{1, \cdots, L\}. \tag{6.4}$$

Consequently, the power produced by the waveforms at angle θ can be expressed as

$$\begin{aligned} P(\theta) &= \mathbb{E}\left\{|x(l)|^2\right\} \\ &= (\boldsymbol{p} \odot \boldsymbol{a}(\theta))^H \mathbb{E}\left\{\boldsymbol{s}(l)\boldsymbol{s}^H(l)\right\}(\boldsymbol{p} \odot \boldsymbol{a}(\theta)) \\ &= \boldsymbol{p}^T \boldsymbol{R} \odot \left(\boldsymbol{a}(\theta)\boldsymbol{a}^H(\theta)\right)^* \boldsymbol{p}, \end{aligned} \tag{6.5}$$

where

$$\boldsymbol{R} = \mathbb{E}\left\{\boldsymbol{s}(l)\boldsymbol{s}^H(l)\right\} \tag{6.6}$$

is the time-averaged covariance matrix of the transmit waveforms $\{\boldsymbol{s}(l)\}$. As usual in the literature, we refer to the spatial power spectrum defined in Equation 6.5, as the *transmit beam-pattern*. Note that, in a similar manner, one can define the cross-correlation terms between the probing signals at locations θ and $\bar{\theta}$ as

$$\bar{P}(\theta, \bar{\theta}) \triangleq \boldsymbol{p}^T \Re\left\{\boldsymbol{R} \odot \left(\boldsymbol{a}(\theta)\boldsymbol{a}^H(\bar{\theta})\right)^*\right\} \boldsymbol{p}. \tag{6.7}$$

Our goal is to jointly design the antenna selection vector $\boldsymbol{p}$ and the covariance matrix $\boldsymbol{R}$ of the transmitted waveforms in order to generate the desired beam-pattern while reducing the cross-correlation terms. Once $\boldsymbol{R}$ has been determined, a signal sequence $\boldsymbol{s}(l)$ can be designed that has $\boldsymbol{R}$ as its covariance matrix [30, 37].

6.3 Problem Formulation

Let $\phi(\theta)$ denote the desired transmit beam-pattern, and $\{\theta_k\}_{k=1}^{K}$ be the grid of points that covers the field of view in azimuth. We presume that the aforementioned grid comprises points that are good estimates of the locations of $\tilde{K}$ targets of interest that we wish to probe at locations $\{\theta_k\}_{k=1}^{\tilde{K}}$. In addition, we assume that some partial information regarding the target positions are available at hand, *i.e.*, we possess some initial estimates $\{\tilde{\theta}_k\}_{k=1}^{\tilde{K}}$ of $\{\theta_k\}_{k=1}^{\tilde{K}}$. In practice, one can obtain $\{\tilde{\theta}_k\}_{k=1}^{\tilde{K}}$ using the Capon spatial spectrum or the generalized likelihood ratio test (GLRT) function for target localization. In this chapter, we express the desired beam-pattern as,

$$\phi(\theta) = \begin{cases} 1, & \theta \in [\tilde{\theta}_k - \frac{\triangle}{2}, \tilde{\theta}_k + \frac{\triangle}{2}], \text{ for } k \in \{1, \cdots, \hat{K}\}, \\ 0, & \text{elsewhere}, \end{cases} \tag{6.8}$$

where $\{\tilde{\theta}_k\}_{k=1}^{\hat{K}}$ are the dominant peak locations of the GLRT pseudo-spectrum, with $\hat{K}$ being the resulting estimate of $\tilde{K}$, and $\triangle$ denotes the given beam-width for each estimated target. Note that the value of $\triangle$ should be more than the expected error in $\{\tilde{\theta}_k\}$; see [31].

Our goal is to design $\boldsymbol{R}$ such that the transmit beam-pattern $P(\theta)$, approximates the desired beam-pattern $\phi(\theta)$ over the radial sectors of interest in a least squares (LS) sense, and moreover, such that the contribution from all cross-correlation terms $\bar{P}(\theta, \bar{\theta})$ (for $\theta \neq \bar{\theta}$), are minimized

(again, in an LS sense) over the set of possible target locations $\{\tilde{\theta}_k\}_{k=1}^{\tilde{K}}$. Formally, we make use of the following cost function that incorporates the aforementioned criteria as follows [31]:

$$\begin{aligned} J(\boldsymbol{p}, \boldsymbol{R}, \alpha) &= \frac{1}{K}\sum_{k=1}^{K} w_k \left|P(\theta_k) - \alpha\phi(\theta_k)\right|^2 + \frac{2\omega_c}{\tilde{K}(\tilde{K}-1)}\sum_{p=1}^{\tilde{K}-1}\sum_{q=k+1}^{\tilde{K}}\left|\bar{P}(\hat{\theta}_p, \hat{\theta}_q)\right|^2 \\ &= \frac{1}{K}\sum_{k=1}^{K} w_k \left|\boldsymbol{p}^T\boldsymbol{R}\odot\left(\boldsymbol{a}(\theta_k)\boldsymbol{a}^H(\theta_k)\right)^*\boldsymbol{p} - \alpha\phi(\theta_k)\right|^2 \\ &\quad + \frac{2\omega_c}{\tilde{K}(\tilde{K}-1)}\sum_{p=1}^{\tilde{K}-1}\sum_{q=p+1}^{\tilde{K}}\left|\boldsymbol{p}^T\Re\left\{\boldsymbol{R}\odot\left(\boldsymbol{a}(\tilde{\theta}_p)\boldsymbol{a}^H(\tilde{\theta}_q)\right)^*\right\}\boldsymbol{p}\right|^2 \end{aligned} \tag{6.9}$$

where $\alpha > 0$ is a scaling factor to be designed. Furthermore, $\omega_k \geq 0$ is considered as the weight factor at the k-th grid point (for $k = 1, \cdots, K$), and $\omega_c \geq 0$ is the weight factor for the cross-correlation terms. Note that we introduce α as a design parameter in order to achieve the desired transmit beam-pattern that approximates an appropriately scaled version of $\phi(\theta)$ to take into account different transmit energy allocations.

In the sequel, we formulate the problem of designing beam-pattern with low cross-correlation for a MIMO radar system as a constrained optimization problem and further impose proper constraints for designing $\boldsymbol{R}$ and $\boldsymbol{p}$. First, one should impose the constraint that the designed matrix $\boldsymbol{R}$ must be positive semi-definite since it is a covariance matrix. Next, under a uniform elemental power constraint, all the diagonal elements of $\boldsymbol{R}$ must attain the same value as all

antennas are required to transmit uniform power. Hence, the feasible region for the desired transmit covariance matrix can be compactly expressed as,

$$\boldsymbol{R} \succeq \mathbf{0}, \tag{6.10a}$$

$$R_{mm} = \frac{c}{M}, \quad \text{for } m = 1, \cdots, M, \tag{6.10b}$$

with given $c > 0$, and R_{mm} denoting the m-th diagonal element of $\boldsymbol{R}$. In the case of designing unimodular sequences, one can simply set $c = 1$.

Secondly, since we are placing only N antennas in $M(\geq N)$ grid points to achieve the desired beam-pattern, we further impose the constraint that the binary antenna selecting vector $\boldsymbol{p}$ should contain N non-zero elements. More precisely, we aim to design $\boldsymbol{p}$ according to the following constraints,

$$\|\boldsymbol{p}\|_1 = N, \tag{6.11a}$$

$$p_m = \{0, 1\}, \text{ for } m = 1, \cdots, M, \tag{6.11b}$$

or, equivalently $\boldsymbol{p} \in \mathbb{B}_N^M$. Therefore, the overall transmit covariance optimization problem can be formulated as

$$\min_{\boldsymbol{p},\boldsymbol{R},\alpha} \quad J(\boldsymbol{p}, \boldsymbol{R}, \alpha) \tag{6.12a}$$

$$\text{s.t.} \quad \boldsymbol{R} \succeq \boldsymbol{0}, \tag{6.12b}$$

$$R_{mm} = \frac{c}{M}, \quad \text{for } m = 1, \cdots, M, \tag{6.12c}$$

$$\|\boldsymbol{p}\|_1 = N, \tag{6.12d}$$

$$p_m = \{0, 1\}, \quad \text{for } m = 1, \cdots, M, \tag{6.12e}$$

$$\alpha > 0. \tag{6.12f}$$

It is easy to verify that the optimization problem in Equation 6.12 can be categorized as a mixed Boolean-nonconvex problem, especially due to the constraints imposed on $\boldsymbol{p}$, the likes of which is very difficult and computationally expensive to solve. In the next subsection, we propose an efficient and novel *cyclic* optimization approach based on semi-definite programming and a greedy search algorithm to tackle the non-convexity of the said problem in Equation 6.12.

6.3.1 Cyclic Optimization Algorithm

Hereafter, we address the problem of designing the desired covariance matrix $\boldsymbol{R}$, the scaling factor α, and the corresponding antenna selection vector $\boldsymbol{p}$ according to the objective function J and by proposing an alternating optimization approach to tackle the problem of Equation 6.12. Specifically, the minimization of $J(\boldsymbol{p}, \boldsymbol{R}, \alpha)$ in Equation 6.12 can be tackled via employing a *cyclic optimization* approach *w.r.t.* the design variables $(\boldsymbol{R}, \alpha)$ and $\boldsymbol{p}$.

6.3.1.1 Optimization *w.r.t.* $\boldsymbol{R}$ and α:

For a fixed $\boldsymbol{p}$, the minimization problem in Equation 6.12 *w.r.t.* $(\boldsymbol{R}, \alpha)$ can be recast as

$$\min_{\boldsymbol{R},\alpha} \quad J(\boldsymbol{p}, \boldsymbol{R}, \alpha) \tag{6.13a}$$

$$\text{s.t.} \quad \boldsymbol{R} \succeq \boldsymbol{0}, \tag{6.13b}$$

$$R_{mm} = \frac{c}{M}, \quad \text{for } m = 1, \cdots, M, \tag{6.13c}$$

$$\alpha > 0. \tag{6.13d}$$

Interestingly, it was shown in [37] that the above minimization problem *w.r.t.* design variables $(\boldsymbol{R}, \alpha)$ is convex and can be reformulated as a semi-definite program (SDP), which can then be efficiently solved using numerical methods (*e.g.*, interior point method [173]).

6.3.1.2 Optimization *w.r.t.* $\boldsymbol{p}$:

On the other hand, for fixed $(\boldsymbol{R}, \alpha)$ the optimization problem of Equation 6.12 with respect to the antenna selection vector $\boldsymbol{p}$ can be expressed as

$$\min_{\boldsymbol{p}} \quad J(\boldsymbol{p}, \boldsymbol{R}, \alpha) \tag{6.14a}$$

$$\text{s.t.} \quad \boldsymbol{p} \in \mathbb{B}_N^M, \tag{6.14b}$$

where M and N denote the total number of grid points and the total number of antennas we are restricted to choose, in order to form the desired beam-pattern, respectively. Note that the constraint set $\mathbb{B}_N^M$ is not convex due to the (discrete) Boolean constraint of $\boldsymbol{p} \in \{0, 1\}$ imposed

on the antenna selection vector. Put differently, we are interested in minimizing the objective function J over a subset of vertices of a hypercube of dimension M, which is represented by $\mathbb{B}_N^M$. We tackle this problem using a greedy search algorithm which is discussed in Section 6.4 in a detailed manner.

Finally, as mentioned earlier, the cyclic optimization method alternates between the following optimization problems at each cycle:

$$\begin{aligned} \left(\boldsymbol{R}^{(t)}, \alpha^{(t)}\right) = \arg\min_{\boldsymbol{R},\alpha} \quad & J(\boldsymbol{p}^{(t-1)}, \boldsymbol{R}, \alpha) \\ \text{s.t.} \quad & \boldsymbol{R} \succeq \mathbf{0}, \\ & R_{mm} = \frac{c}{M}, \\ & \qquad \text{for } m = 1, \cdots, M, \\ & \alpha > 0, \end{aligned} \tag{6.15}$$

and

$$\begin{aligned} \boldsymbol{p}^{(t+1)} = \arg\min_{\boldsymbol{p}} \quad & J(\boldsymbol{p}, \boldsymbol{R}^{(t)}, \alpha^{(t)}) \\ \text{s.t.} \quad & \boldsymbol{p} \in \mathbb{B}_N^M, \end{aligned} \tag{6.16}$$

where t denotes the iteration index of the cyclic optimization method.

6.4 The Proposed Antenna Position Design Technique

In this section, we develop a heuristic optimization approach inspired by the dynamic programming and genetic algorithms (a special case of evolutionary optimization technique [174]) equipped with a simple local search to tackle the non-convexity of Equation 6.14. Note that the objective function $J(\boldsymbol{p}, \boldsymbol{R}, \alpha)$ is *quartic w.r.t.* the vector $\boldsymbol{p}$, and thus, it is deemed extremely difficult to solve. Cheng et al. [54] propose one approach Equation 6.14 based on a relaxation of the Boolean constraint (*e.g.*, via the linear relaxation of $\mathbf{0} \leq \boldsymbol{p} \leq \mathbf{1}$), which yields a suboptimal solution at the expense of heavy computation. In this chapter, we resort to a greedy search algorithm that can solve the exact problem in Equation 6.14 in an efficient manner.

Especially we mimic the process of natural selection for solving an optimization process by iteratively improving the generated set of feasible solutions. The fitness of each feasible solution is usually governed by an objective function. Then, according to a predefined criterion, the algorithm maintains the best subset of feasible solutions at each iteration to generate a better solution *individuals* accordingly. Here in each generation, we produce the set of feasible solutions and select the best individual according to a greedy policy, however by design, the particular choice of policy allows for shrinking the cardinality of feasible set in each generation. In the following, we go through the main ingredients of the proposed method in order to design the antenna position vector $\boldsymbol{p}$.

6.4.1 Generation of Feasible Solutions Set

As mentioned earlier that our search space for a solution is a subset of vertices of an M-dimensional hypercube represented by $\mathbb{B}_N^M$. Hence we undertake a deterministic strategy for

the generation of feasible solutions set. Note that the binary vector $\boldsymbol{p}$ of length M represents a hypercube with 2^M vertices. Given the most fitted solution (parent solution) at iteration k, *e.g.*, $\boldsymbol{p}^{(k)}$, we generate a new set of feasible (candidate) solutions (*i.e.*, offspring of the parent solution) $\boldsymbol{p}_{\text{CS}}^{(k+1)}$ as follows:

$$\boldsymbol{p}_{\text{CS}}^{(k+1)} = \left\{ \boldsymbol{p} \;\middle|\; H\left(\boldsymbol{p}, \boldsymbol{p}^{(k)}\right) = 1,\ \|\boldsymbol{p}\|_1 < \|\boldsymbol{p}^{(k)}\|_1 \right\}, \tag{6.17}$$

where $H(\boldsymbol{x}, \boldsymbol{y})$ denotes the Hamming distance between the two vectors, and is defined to be the number of positions i such that $x_i \neq y_i$, where the subscript i denotes the i-th element of the corresponding vector. In other words, given a parent solution $\boldsymbol{p}^{(k)}$, the new set of candidate solutions (CS) is generated as the set of vectors which only differs from $\boldsymbol{p}^{(k)}$ in one bit (with one less non-zero element only). Then each candidate solution is mutated using a predefined probability (`prob_mut`), meaning one randomly selected bit (using uniform sampling) is toggled with the said probability. It is well known that mutation introduces diversity into the candidate solution set. Particularly, mutation operators prevent the active codes of candidates (*i.e.*, chromosomes) from becoming too similar to each other, thus avoiding local minima and broadening the exploration area in the solution space [174]. Hence, at each iteration the cardinality of the new candidate solution is upper bounded by $\left|\boldsymbol{p}_{\text{CS}}^{(k+1)}\right| \leq \|\boldsymbol{p}^{(k)}\|_1$. This procedure is summarized in Algorithm 4.

Algorithm 4 For generating children set of $\boldsymbol{p}$ which are not in `seen_children` using mutation

```
1: procedure GenerateChildren(p, seen_children, prob_mut)
2:     children.push(p)
3:     for i = 1, 2, ··· , len(p) do
4:         if p_i = 1 then
5:             child ← Toggle i-th bit of p
6:             if rand(1) ≤ prob_mute then
7:                 child ← Toggle uniformly selected one bit of child with probability
   prob_mut
8:             end if
9:             if child is not in children and seen_children then
10:                children.push(child)
11:            end if
12:        end if
13:    end for
14:    return children
15: end procedure
```

6.4.2 Selection of the Fittest Solution

The goal of the selection procedure is to propagate the fittest candidate solution, *i.e.*, the one with the highest fitness value, or in other words lowest objective value, to have a higher probability of generating new offspring or CS for the next iteration (generation) of the algorithm. There exist several stochastic and deterministic methods in the literature for the selection procedure, and in this chapter, we consider a deterministic approach. For fixed $(\boldsymbol{R}, \alpha)$, let us denote the objective function Equation 6.9 as $J(\boldsymbol{p})$. Having the current CS $\boldsymbol{p}_{\text{CS}}^{(k)}$ at hand, we

Algorithm 5 For choosing the best child of $\boldsymbol{p}$

1: **procedure** BESTCHILD(`children`)
2: Calculate the functional values of $J(\texttt{child}, \boldsymbol{R}, \alpha)$ in Equation 6.9 for each `child` in `children`
3: **return** the `child` for which the functional value is minimum
4: **end procedure**

select the fittest solution $\boldsymbol{p}^{(k)}$ to be considered for generating new candidate solutions at the next stage as follows:

$$\boldsymbol{p}^{(k)} = \arg \min_{\boldsymbol{p} \in \boldsymbol{p}_{\mathrm{CS}}^{(k)}} J(\boldsymbol{p}). \tag{6.18}$$

Next, $\boldsymbol{p}^{(k)}$ is used as the seed for generating new CS in the crossover procedure for the next stage of the algorithm. This procedure is summarized in Algorithm 5.

6.4.3 Stopping Criteria

Once the selection procedure selects a vector $\boldsymbol{p}^{(k)}$ as its output such that $\boldsymbol{p}^{(k)} \in \mathbb{B}_N^M$ or equivalently $\|\boldsymbol{p}^{(k)}\|_1 = N$, then one can easily argue that a suboptimal solution is obtained. Note that $\boldsymbol{p}^{(k)} \in \mathbb{B}_N^M$ implies $\boldsymbol{p}^{(k-1)} \in \mathbb{B}_{N+1}^M$. Hence, one can conclude that if $\boldsymbol{p}^{(k)} \in \mathbb{B}_N^M$, then $\boldsymbol{p}^{(k)}$ is a local optimal point in a 1-Hamming distance neighborhood of $\boldsymbol{p}^{(k+1)}$ such that $\|\boldsymbol{p}^{(k)}\|_1 < \|\boldsymbol{p}^{(k-1)}\|_1$, and that $\boldsymbol{p}^{(k-1)} \in \mathbb{B}_{N+1}^M$. Moreover, the cardinality of the search space in the 1-Hamming distance local search in Equation 6.18 is at most $\|\boldsymbol{p}^{(k-1)}\|_1$ and as a result the search space is reduced in each generation. The corresponding search process is summarized in Algorithm 7.

Algorithm 6 For updating `seen_children`

```
1: procedure UpdateSeenChildren(seen_children, children)
2:     for each child in children do
3:         if child is not in seen_children then
4:             seen_children.push(child)
5:         end if
6:     end for
7:     return seen_children
8: end procedure
```

Algorithm 7 For choosing the best $\boldsymbol{p}$ using greedy search algorithm (The procedure UpdateSeenChildren is described in Algorithm 6)

Require: $\boldsymbol{R}, \alpha$, total number of antennas N, total number of grid points M, `prob_mut`
Ensure: $\boldsymbol{p} \leftarrow \mathbf{1}_M$, `seen_children` $\leftarrow \emptyset$, `flag` $\leftarrow 1$

```
1: while flag do
2:     children ← GenerateChildren(p, seen_children, prob_mut)
3:     p ← BestChild (children)
4:     seen_children ← UpdateSeenChildren (seen_children, children)
5:     if ‖p‖_1 = N then
6:         flag ← 0
7:     end if
8: end while
9: return p
```

The above greedy search approach can be best manifested via considering a toy example. Assume $M = 3$, $N = 1$, and the initial antenna position vector $\boldsymbol{p}^{(0)} = \mathbf{1}_M$. Figure 20 illustrates the iterations of the proposed greedy search algorithm, where the red vertices denote the parent solution (output of the selection procedure), yellow vertices correspond to the candidate solutions $\boldsymbol{p}_{\text{CS}}$, and the blue vertices are the selected solution for the next iteration. At the first iteration,

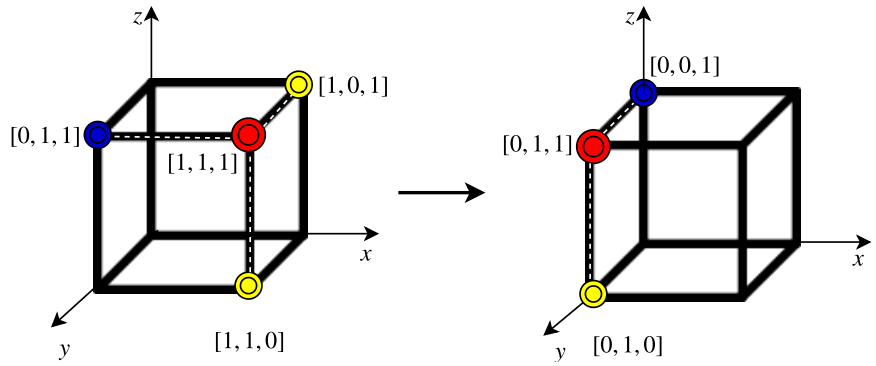

Figure 20. Illustration of the iterations of the proposed greedy search algorithm, where the red vertices denote the parent solution (output of the selection procedure), yellow vertices correspond to the candidate solutions $\boldsymbol{p}_{\text{CS}}$, and the blue vertices denote the selected solution for the next iteration.

the candidate solutions $\boldsymbol{p}_{\text{CS}}^{(1)} = \{[0,1,1],[1,0,1],[1,1,0]\} \subseteq \mathbb{B}_2^3$, and each member of $\boldsymbol{p}_{\text{CS}}^{(1)}$ is also in a 1-Hamming distance of $\boldsymbol{p}^{(0)}$. Next, we introduce mutation to each of the candidate solutions according to a predefined mutation probability. Generally, such probability is kept low (< 0.5) to introduce a controlled diversity so that only a small number of candidates are mutated but not all. Let us assume, during the mutation process, only one candidate: $[1,0,1]$ is mutated to $[1,0,0]$, and thus the new candidate set becomes: $\hat{\boldsymbol{p}}_{\text{CS}}^{(1)} = \{[0,1,1],[1,0,0],[1,1,0]\}$ Next, during the selection procedure, let us assume that the vertex $[0,1,1]$ is chosen as the fittest solution and then used to generate offspring (candidate solutions), *e.g.*$\boldsymbol{p}^{(1)} = [0,1,1]$. The new CS generated from $\boldsymbol{p}^{(1)}$ is the set $\boldsymbol{p}_{\text{CS}}^{(2)} = \{[0,0,1],[0,1,0]\} \subseteq \mathbb{B}_1^3$. Once again, we apply mutation to all the candidates, however, assume that due to the smallness of the predefined mutation probability, none of the candidates are mutated in this iteration. The fittest solution is then $\boldsymbol{p}^{(2)} = [0,0,1]$

and since it is a member of the desired set $\mathbb{B}_1^3$, the algorithm stops. Next, the antenna position vector $\boldsymbol{p}^{(2)}$ is used to design the covariance matrix $\boldsymbol{R}$.

As it was discussed earlier, we consider the alternating (cyclic) optimization approach to solve the joint optimization of the covariance matrix and the antenna position vector. Namely, after performing the above greedy search technique for obtaining the solution to Equation 6.14 at the t-th iteration, *i.e.*obtaining the antenna selection vector $\boldsymbol{p}^{(t)}$, we fix $\boldsymbol{p} = \boldsymbol{p}^{(t)}$ and optimize the objective function *w.r.t.* the design variables $(\boldsymbol{R}, \alpha)$ according to the method described in Section 6.3.1.1. Finally, the proposed cyclic optimization approach is summarized in Table IV.

6.5 Extension to General Antenna Selection Scenario

So far, we have discussed the joint optimization of the transmitted signal covariance matrix and the antenna position while restricted to placing N antennas into M grid points in an optimal manner. However, the same proposed greedy search algorithm can be extended to a more general scenario in which we aim to choose the minimum number of antennas $N_{\min}$ for placing in M grid points. Namely, in the general antenna selection scenario, we consider the optimization of the signal covariance matrix to form the desired beam-pattern, by letting the algorithm choose

the best placement positions while using the *minimum* number of antennas. For this general scenario, we consider the following relaxed optimization problem,

$$\begin{aligned} \min_{\boldsymbol{p},\boldsymbol{R},\alpha} \quad & J(\boldsymbol{p},\boldsymbol{R},\alpha) + \rho\left(|\|\boldsymbol{p}\|_1 - N|\right) \\ \text{s.t.} \quad & \boldsymbol{R} \succeq \mathbf{0}, \\ & R_{mm} = \frac{c}{M}, \quad \text{for } m = 1, \cdots, M, \\ & p_m = \{0, 1\}, \quad \text{for } m = 1, \cdots, M, \\ & \alpha > 0, \end{aligned} \tag{6.19}$$

where $\rho > 0$ denotes the penalty parameter. Note that a lower value of ρ relaxes the solution $\boldsymbol{p}$ to have less (than N) number of active antennas by encouraging the total number of non-zero elements $\|\boldsymbol{p}\|_1$ of the solution to go far from N. Conversely, a larger value of ρ keeps the total number of non-zero elements of the solution near N. Hence, depending on the application, one can choose a lower weight for the total number of active antennas via varying the penalty factor ρ. Also, N in Equation 6.19 can be interpreted and chosen accordingly as an approximation of the number of antennas one can afford to use.

Let $J_2(\boldsymbol{p},\boldsymbol{R},\alpha) \triangleq J(\boldsymbol{p},\boldsymbol{R},\alpha) + \rho\left(|\|\boldsymbol{p}\|_1 - N|\right)$ denote the augmented objective function in Equation 6.19. Then, with a slight modification, the same cyclic optimization approach described in Section 6.3.1 can be employed to solve it. Note that the extra term in $J_2(\boldsymbol{p},\boldsymbol{R},\alpha)$ only depends on $\boldsymbol{p}$, and hence the optimization of J_2 *w.r.t.* the variables $(\boldsymbol{R},\alpha)$ remains unchanged and is the same as the procedure described in Section 6.3.1.1. In the previous scenario,

we were restricted to a solution $\boldsymbol{p}$ such that it satisfies $\boldsymbol{p} \in \mathbb{B}_N^M$. However, we have no such restriction in the generalized scenario but only to have $\boldsymbol{p} \in \{0,1\}^M$ and instead, we are interested in choosing the minimum number of antennas while optimizing their positions.

In order to optimize the new augmented objective function J_2 *w.r.t.* the vector $\boldsymbol{p}$, we only need to change the stopping criteria and the fitness function. In this general case, the fitness function is considered to be $J_2(\boldsymbol{p}, \boldsymbol{R}, \alpha)$ and the corresponding stopping criteria for the greedy search approach can be described as follows. As it was discussed earlier in Section 6.4, starting with the initialization $\boldsymbol{p}^{(0)} = \mathbf{1}_M$, at each iteration of the proposed search algorithm, the parent node $\boldsymbol{p}^{(k)} \in \mathbb{B}_{N-k}^M$ is a local optimal point in a 1-Hamming distance neighborhood of $\boldsymbol{p}^{(k-1)}$. Hence, a heuristic proper stopping criteria can be assumed when the following condition is satisfied at the k-th inner iteration of the search process:

$$H\left(\boldsymbol{p}^{(k)}, \boldsymbol{p}^{(k-1)}\right) = 0. \tag{6.20}$$

In other words, the above criteria implies that the solution $\boldsymbol{p}^{(k)}$ is a 1-Hamming distance optimal point for its parent $\boldsymbol{p}^{(k-1)}$ as well as the newly generated candidate solutions $\boldsymbol{p}_{\mathrm{CS}}^{(k+1)}$.

6.6 Numerical Simulations

In this section, we present several scenarios through numerical simulations in order to assess the performance of our proposed algorithm. In the following experiments we assume a colocated narrow-band MIMO radar with a linear array with $M = 15$ grid points and half-wavelength inter-grid interval *i.e.*$d = \lambda/2$. The range of angle is $(-90^\circ, 90^\circ)$ with 1° resolution. We set the weights

TABLE IV

THE PROPOSED JOINT OPTIMIZATION METHOD

Step 0: Initialize the antenna position vector $\boldsymbol{p}^{(0)} = \mathbf{1}_M$, the complex covariance matrix $\boldsymbol{R}^{(0)} \in \mathbb{C}N \times N$, and the scaling factor $\alpha^{(0)} \in \mathbb{R}_+$, and the outer loop index $t = 1$.
Step 1: Solve the convex program of Equation 6.15 using the procedure described in Section 6.3.1.1 and obtain $\left(\boldsymbol{R}^{(t)}, \alpha^{(t)}\right)$.
Step 2: Employ the proposed greedy search approach described in Section 6.4 and solve the antenna position design program of Equation 6.16 to obtain the vector $\boldsymbol{p}^{(t+1)}$.
Step 3: Repeat steps 1 and 2 until a predetermined stopping criteria is satisfied.

for the k-th angular direction as $w_k = 1$, for $k = 1, \cdots, K$. Note that the optimization problem *w.r.t.* the variables $(\boldsymbol{R}, \alpha)$ is carried out using the convex optimization toolbox CVX [175]. Furthermore, we consider the mutation probability as 0.1.

In Figure 21, we consider a design scenario where initial direction of arrival (DoA) information about $\tilde{K} = 3$ targets with unit complex amplitudes, and approximately located at angles $\{-50^\circ, 0^\circ, 50^\circ\}$ is available through the Capon or GLRT method. Hence, we desire to design a symmetric beam-pattern with three directions of interest: $\tilde{\theta}_1 = -50^\circ$, $\tilde{\theta}_2 = 0^\circ$, and $\tilde{\theta}_3 = 50^\circ$, respectively and the beam-pattern of width $\triangle = 20^\circ$ and thus the given transmit pattern is

$$\phi(\theta) = \begin{cases} 1, & \theta \in [\tilde{\theta}_k - \frac{\triangle}{2}, \tilde{\theta}_k + \frac{\triangle}{2}], \quad k = 1, 2, 3, \\ 0, & \text{otherwise.} \end{cases}$$

Herein, we compare the resulting beam-pattern with the desired one for the two cases of $\omega_c = 1$ (with cross-correlation) and $\omega_c = 0$ (without cross-correlation). It is interesting to note

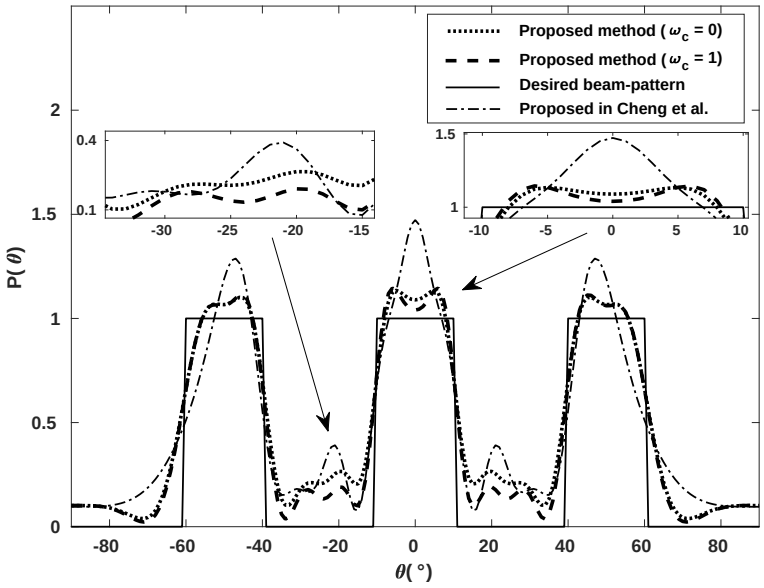

Figure 21. The transmit beam-pattern design for $M = 15, N = 10$ with and without the cross-correlation suppression with three mainlobes at $\tilde{\theta} = \{-50^\circ, 0^\circ, 50^\circ\}$ with a beam-width $\triangle = 20^\circ$. It is noticeable that our algorithm outperforms the method described in [54].

.

that the designed beam-patterns obtained with and without considering the cross-correlation terms are able to match the desired beam-pattern in a similar manner. However, the probing signals corresponding to $\omega_c = 1$, are almost uncorrelated with each other resulting in much better cross-correlation behavior than its other counterpart. This can be verified from Figure 22, where we provided the comparison of the normalized magnitudes of the cross-correlation coefficients (as formulated in the second term of the right hand side of Equation 6.9) for the same three targets of interest at directions $\tilde{\theta} = \{-50^\circ, 0^\circ, 50^\circ\}$, as functions of ω_c. It is evident from Figure 22 that when ω_c is very small (close to zero), the first and third reflected signals are highly correlated.

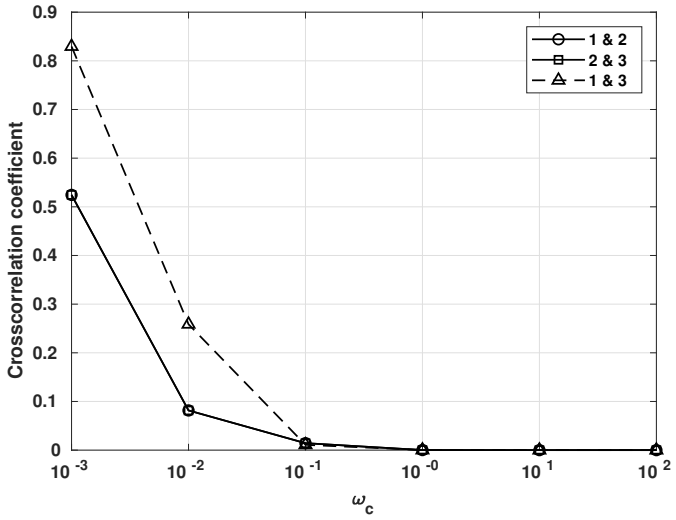

Figure 22. The comparison of the normalized magnitudes of the cross-correlation coefficients for three targets of interest at directions $\{-50^\circ, 0^\circ, 50^\circ\}$ as functions of ω_c.

On the other hand, for $\omega_c > 0.1$ all cross-correlation coefficients are approximately zero. The proposed algorithm outperforms the method described in [54] in terms of accuracy (measured in MSE), and additionally, is capable of designing waveform covariance matrices with low cross-correlation.

In Figure 23, we further consider the design scenario of approximating the beam-patterns with one mainlobe at $\tilde{\theta} = 0^\circ$, with a width of 60°, with and without cross-correlation suppression. Note that in both cases of $\omega_c = 0$ and $\omega_c = 1$, our proposed method can accurately approximate the desired beam-pattern and provide a better beam-pattern than that of [54].

Figure 24 shows the beam-pattern with five mainlobes at $\tilde{\theta} = \{-60^\circ, -30^\circ, 0^\circ, 30^\circ, 60^\circ\}$ with a shorter beam-width of 10° for $M = 20$ and $N = 15$. We compare the beam-pattern

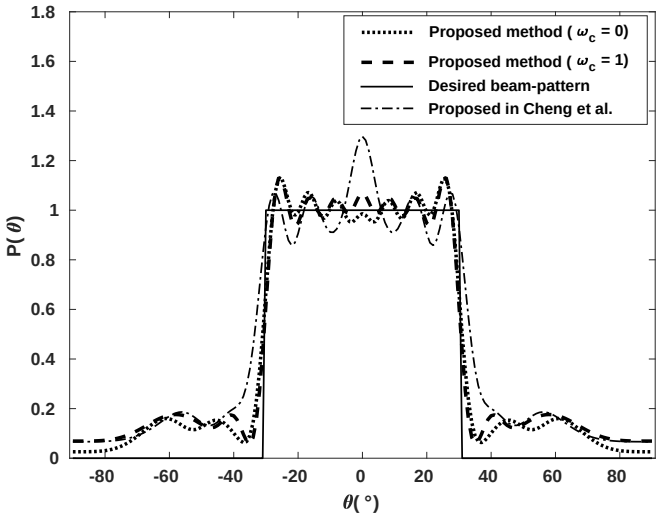

Figure 23. The transmit beam-pattern design for $M = 15, N = 10$ with and without the cross-correlation suppression with one mainlobe at $\tilde{\theta} = 0^{\circ}$ with a beam-width of $\triangle = 60^{\circ}$.

approximated by our framework (*i.e.*, with the configuration of 15 antennas placed in an array of 20 grid points) with that generated by a full linear array *i.e.*15 antenna elements tightly placed in all 15 grid points. It can be clearly seen from the Figure 24 that the proposed method approximates the beam-pattern better than that of the full array. One can further notice that the transmitted power values are almost the same in all mainlobe despite being farther away from the central mainlobe, as compared to the full array.

In Figure 25, we demonstrate the final antenna position vectors suggested by the proposed algorithm for the scenario considered in Figure 24 for the two cases of $\omega_c = 0$ and $\omega_c = 1$. It is interesting to note that the effective antenna aperture of the array is $M = 15$, which can

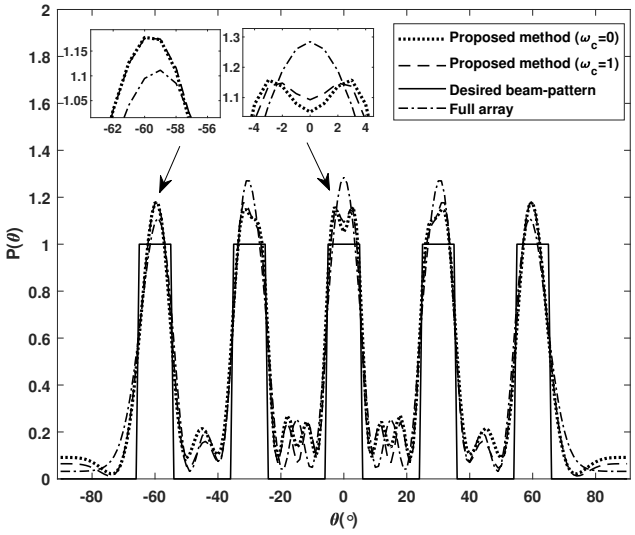

Figure 24. The transmit beam-pattern design for $M = 20, N = 15$ with and without the cross-correlation suppression with five mainlobes at $\tilde{\theta} = \{-60°, -30°, 0°, 30°, 60°\}$ with a beam-width of $\triangle = 10°$. Full array represents the 15 antenna elements tightly placed in all 15 grid points.

be safely reached by selecting only $N = 10$ antennas. The corresponding beam-patterns are depicted in Figure 21.

In addition, Figure 26 shows the final $M \times M$ covariance matrix of the transmit signals, which can be used to design the transmitted sequence following specific requirements. It can be readily shown that the generated matrix is symmetric and its eigenvalues are all non-negative (*i.e.*, $\boldsymbol{R}$ is a positive semidefinite matrix). It is interesting to note that the structure of the final covariance matrix is in agreement with the final antenna position vector, as reflected in the corresponding rows and columns of the rejected grid points, which are all zeros.

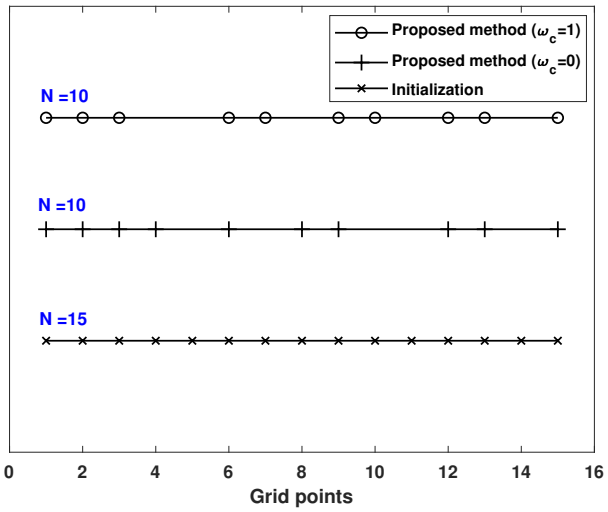

Figure 25. The antenna positions for $M = 15, N = 10$ with and without the correlation suppression.

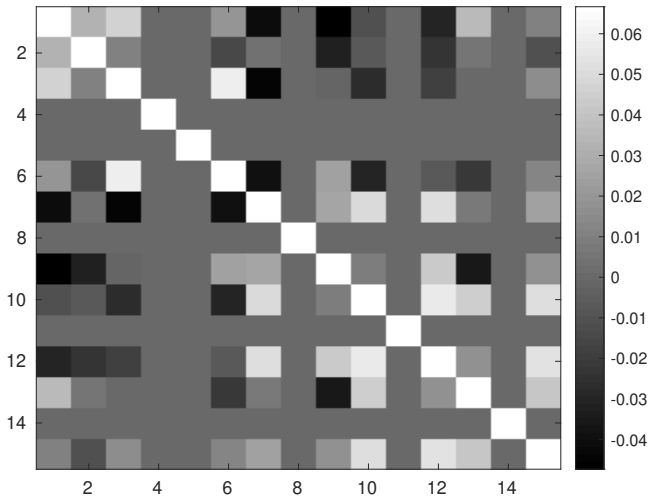

Figure 26. The generated $M \times M$ covariance matrix for $M = 15, N = 10$ with cross-correlation suppression.

In Figure 27, the comparison of the computational cost of the proposed algorithm and that of the method in [54] for the different number of grid points and antennas are shown. For this experiment, we consider $M = 4$ and $N = 3$ as initialization, and then linearly scale M and N by the factor of $\beta \in \{1, 2, 3, 4\}$. The proposed algorithm significantly reduces the computational cost of the ADMM-based method in [54] by *a factor of more than* 200. To give it a perspective, [54] takes ~ 4500 seconds to design the beam-pattern for $M = 15$ and $N = 10$, in around 20 outer iterations (on average) in a standard PC with 8-core processor and 16 GB memory. Whereas, our proposed method finishes the same task in just 17 seconds using 3 outer iterations in the same standard PC, making the proposed framework particularly suitable for real-time applications.

Furthermore, Figure 28 illustrates the beam-pattern design for the generalized case described in Section 6.5. In the generalized case, we relax the constraints of Equation 6.12d (*i.e.*, $\|\boldsymbol{p}\|_1 = N$), and allow the total number of active antennas to deviate from N (which can be chosen depending on the applications) via changing the penalty variable ρ. For this simulation, we set $M = 20$ and $N = 15$ and provide the obtained beam-patterns and the final arrangement and total number of antennas suggested by the proposed algorithm, in Figure 28-(a) and Figure 28-(b), respectively for different values of ρ. It is interesting to note that for $\rho = 0.1$, the proposed algorithm successfully returns an arrangement with 15 antennas as requested in the design parameter. However, for $\rho = 0.01$, the algorithm suggests an arrangement with 10 antennas, which remains unchanged for $\rho < 0.01$, suggesting $N = 10$ is the minimum number of antenna

that can be utilized. Further note that the resulting beam-patterns for the two cases are similar in the mainlobes, although having a different number of antennas.

In the next experiment, we further examine the convergence performance of the proposed algorithm. Especially, we perform a Monte-Carlo simulation ($n = 1000$) with fixed parameters used in the experiment shown in Figure 21. In each run, we initialize the waveform covariance matrix $\boldsymbol{R}$ with a randomly generated positive semidefinite (PSD) matrix while keeping all the other parameters unchanged. It is interesting to observe that, in each experiment, the designed beam pattern converges to the one shown in Figure 29 for all $n = 1000$. Furthermore, in each case, the optimized antenna positions are also the same as shown in Figure 29 which implies that the proposed algorithm has satisfactory convergence performance.

6.7 Concluding Remarks

In this chapter, the problem of jointly designing the probing signal covariance matrix as well as the antenna positions to approximate a given beam-pattern was studied. In order to tackle the problem, a novel cyclic (alternating) optimization method based on the non-convex formulation of the problem, was proposed. In addition, we used a greedy local search algorithm to tackle the non-convex problem of designing antenna positions. Several numerical examples were provided which demonstrates the superiority of the proposed method over the existing methods in terms of accuracy and computational efficiency.

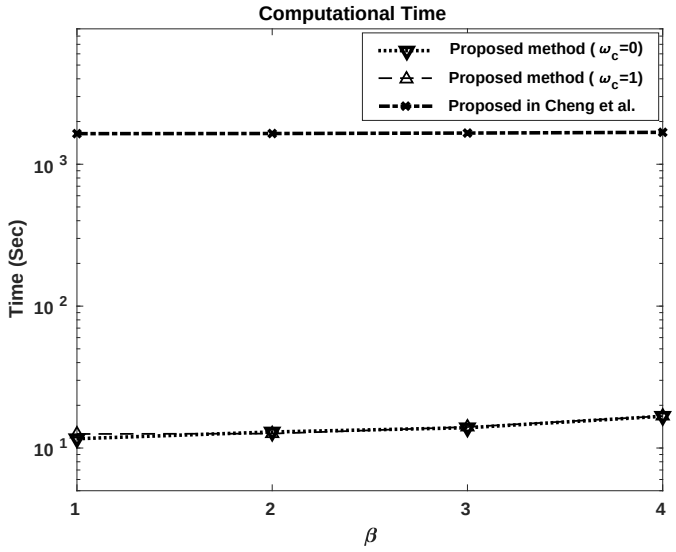

Figure 27. Comparison of the computational cost of our proposed algorithm and that of proposed by Cheng et al. for different number of grid points and that of antennas. We consider $M = 4$ and $N = 3$ as initialization, and then linearly scale M and N by the factor of $\beta = \{1, 2, 3, 4\}$.

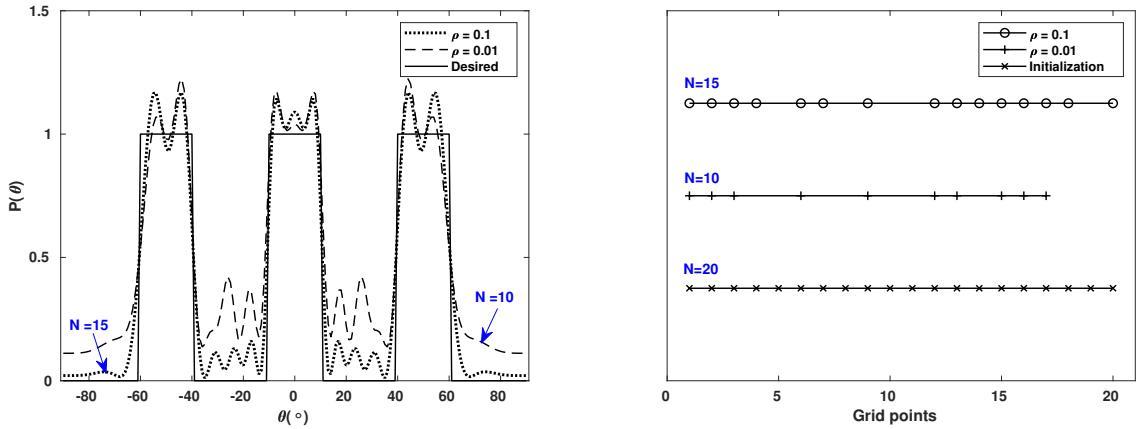

(a) (b)

Figure 28. The (a) beam-pattern and, (b) final arrangements and total number of selected antennas for $M = 20$ grid points and penalty parameter $\rho = \{0.1, 0.01\}$.

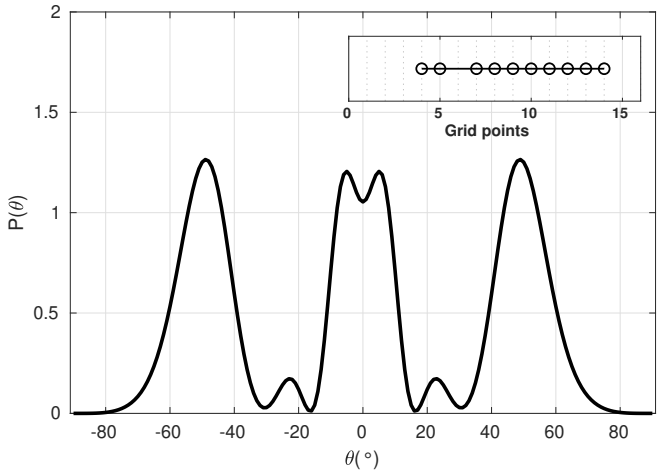

Figure 29. Convergence of the proposed algorithm: the approximated transmit beam-pattern and the optimized antenna positions (inset) for $n = 1000$ experiments.

II-B

Mutual Interference Mitigation for Automotive Radar

CHAPTER 7

WAVEFORM DESIGN FOR MUTUAL INTERFERENCE MITIGATION IN AUTOMOTIVE RADAR

Overview: Automotive radars are an integral part of modern vehicles with assistive driving technology. With more vehicles on the road, comes the prospect of significant mutual interference among the waveforms transmitted by similar radar systems mounted on the connected vehicles, which results in a significant reduction in radar sensitivity and increases false alarm rates. In this chapter, we address the problem of interference mitigation in similar radar systems. To this end, two algorithms are proposed to design slow-time codes for a simple SISO scenario. The difficulty and complexity of the problem of mutual interference increases when the vehicles are equipped with MIMO radar systems and even further with a growing number of vehicles present on the scene. We thus further extend our discussion onto a more general case of MIMO radars and propose an efficient algorithm to design waveforms to mitigate mutual interference in such systems. The proposed technique seeks to minimize a collective cross-ambiguity function. Our quest does not stop here. We then provide a generalized formulation of the problem for a multiple-MIMO case. The proposed coding schemes are computationally efficient in practice and the incorporation of the coding schemes requires only a slight modification of the existing

---

Parts of this chapter is taken from submitted journal article [176], submitted correspondence article [177] and a published conference article [60].

systems. Although for the multiple-MIMO case, the computational complexity becomes cumbersome as the number of MIMO radars grows, the design can be performed online in a collaborative manner, or offline, in which case the radar codes can be designed and stored in a codebook for future use.

7.1 Introduction

The radar technology exhibits an unmatched performance in a variety of vehicular applications, owing to excellent resolving capabilities and immunity to bad weather conditions in comparison with visible and infrared imaging techniques [24, 178–181]. Due to their high accuracy, smaller size, and simplified sensing technology, the millimeter wave (mmWave) radars especially in W-band (75-110 GHz), have gained significant popularity not only in automotive radar systems but also in drone radar applications and the internet of things (IoT) [182–186]. Given the tendency to mass-produce radars in civilian applications, such systems, however, tend to be quite similar, or even almost identical. The increasing number of similar or identical radar systems increases the probability of mutual interference, which may result in severely reduced radar sensitivity and poor performance quality [65, 66, 165]. Thus it is vitally important to enhance radar signal processing performance in severe mutual interference scenarios [187–190].

In the literature, the effects of mutual interference due to identical radar parameters and their corresponding methods of mitigation have been discussed widely, *e.g.*, see [7, 61, 191–194] and the references within. A judicious signal separation method for synchronous and asynchronous interference mitigation is proposed in [191]. In [192], the authors analyzed the mutual interference between frequency-modulated continuous-wave (FMCW) radar systems and proposed several techniques to mitigate the interference problem, including pre-possessing and

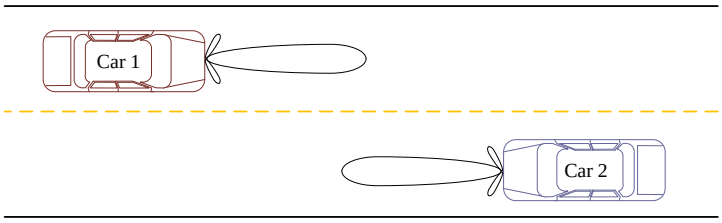

Figure 30. Mutual interference between automotive radars: potential source of mutual interference.

FIR filtering. Contrary to addressing the mutual interference in the receiver side, the authors in [195–197] investigated the problems between automotive radar systems with different types of transmissions. In this chapter, we address the mutual interference mitigation problem in similar or identical radar systems using smart transmit waveforms. To this end, we first formulate the problem for a simple SISO case as shown in Figure 30. Particularly, we propose two slow-time coding schemes to reduce the interference power level.

The interference multiplies many-fold when several cars with similar or almost identical MIMO radar systems are in close proximity. In the not-so-far future, it is reasonable to expect that connected vehicles will go beyond academic pursuit and will be introduced to real-world smart-road networks. Many existing studies show the effectiveness of connected vehicles, and that transportation systems can be enhanced with more connected vehicles on the road [198]. In the later part of this chapter, we further consider the general scenario in which multiple cars, that are able to communicate and agree on the optimal radar waveforms to be used among them, come into contact in traffic (as depicted in Figure 31). We thus extend the formulation to

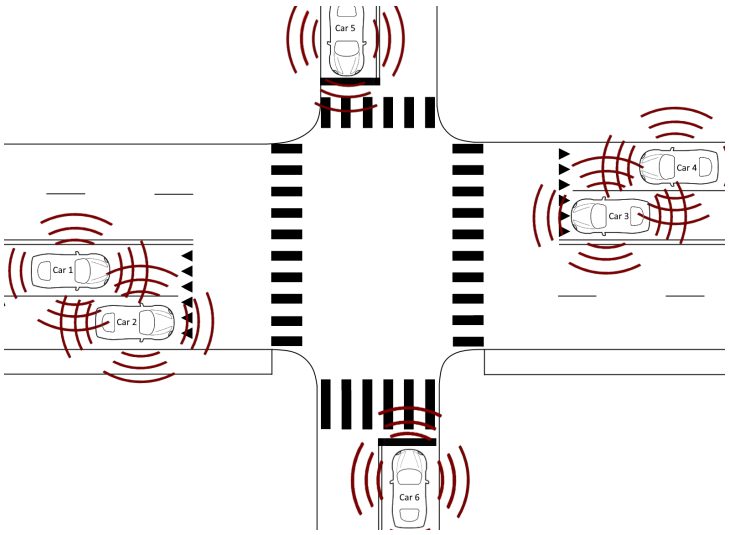

Figure 31. Mutual interference among multiple automotive radar systems.

design such waveforms to suppress mutual interference in the case of similar or identical MIMO radar systems for multiple connected vehicles. Note that the design can be done online in a collaborative manner, or offline; meaning that such radar codes can be designed and stored in a radar codebook for future use. The main contributions of this chapter are listed as follows:

- We begin our study of mutual interference with the SISO case and propose two coding schemes to reduce the interference power level. The first coding scheme aims to shift the Doppler frequency of the interference and separate it from the target in the Doppler region. The second coding scheme aims to minimize the discrete periodic cross-ambiguity function (CAF) in the desired area.

- We further formulate the problem of minimizing the discrete periodic CAF for a general MIMO scenario and propose an efficient cyclic algorithm to design the transmit waveforms.
- The problem formulation is then extended to the case when multiple MIMO antennas with varying numbers of antennas are present in the scene.

The rest of this chapter is organized as follows. In Section 7.2, we discuss the mutual interference for two identical FMCW radar systems. We propose two coding schemes for the SISO scenario in Section 7.3. Section 7.4 is devoted to waveform design for a MIMO scenario. Numerical simulation results are presented in Section 7.6. Finally, Section 7.7 concludes this chapter.

7.2 Preliminaries

In this section, we start by formulating the problem for a SISO scenario. Consider two identical FMCW radar systems shown in Figure 30, that are operating within the same frequency band and same B/T_c ratio where B and T_c are the FMCW signal bandwidth and chirp time, respectively, as shown in Figure 32. A brief description of FMCW radar technology and workflow can be found in Section 1.1.2.2. In this section, we are interested in synthesizing waveforms for such radars. The transmitted waveform, in particular, can be expressed as a train of pulses given as

$$s(t) = \sum_{n=-\infty}^{\infty} u(t - nT_c) \tag{7.1}$$

where $u(t) = \exp(j(2\pi f_c t + \pi K t^2))$, f_c is the carrier frequency and $K = B/T_c$.

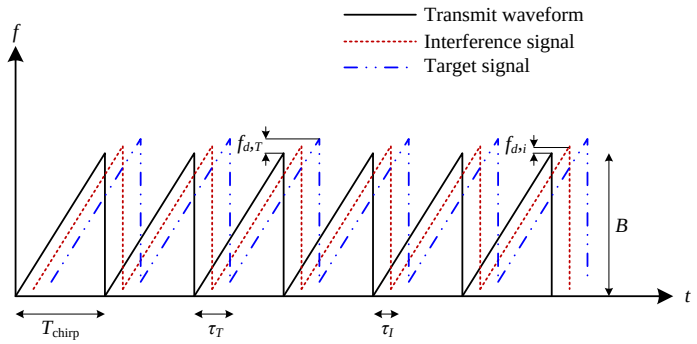

Figure 32. Time-frequency illustration of the transmit waveform, the target signal, and the interference.

When the two radar systems are operating simultaneously, the received signal by one radar includes not only the target reflections but also the interference signal due to the transmission from the other radar system. As a result, we can express the received signal by one radar (*e.g.*, the radar mounted on Car 1 in Figure 30) as,

$$r(t) = y_T(t) + y_I(t) + w(t) \tag{7.2}$$

where $y_T(t) = \alpha_T s(t-\tau_T)\exp(j\pi f_{d,T}t)$ is the target return, and $y_I(t) = \alpha_I s(t-\tau_I)\exp(j\pi f_{d,I}t)$ is the interference signal with α_T, α_I being the corresponding amplitudes, τ_T is the two-way target propagation delay, τ_I is the one-way delay associated with the interference, $f_{d,T}, f_{d,I}$ are the corresponding Doppler frequencies, and $w(t)$ is the internal disturbance, including, *e.g.*, the receiver noise.

Typically, FMCW radar systems collect the received signal from N consecutive pulses within a CPI for target detection and parameter estimation. The received signal is then conjugately mixed with the transmitted signal to produce a low-frequency intermediate (de-chirped) signal. As a result, the de-chirped version of $r(t)$ for the n^{th} (slow-time) pulse is given by

$$r_{dc}^{n}(t) = \alpha_T \exp(j2\pi(f_{B,T}t + nf_{d,T}T_c)) + \alpha_I \exp(j2\pi(f_{B,I}t + nf_{d,I}T_c)) + w^n(t) \tag{7.3}$$

where $f_{B,T} = K\tau_T + f_{d,T}$, $f_{B,I} = K\tau_I + f_{d,I}$ are the beat frequencies corresponding to the target and the interference signal, respectively, and to lighten the notations, we absorb the constant phase terms into α_T and α_I, and use $w^n(t)$ to denote the de-chirped noise.

The de-chirped signal is then passed through a series of ADCs and the m^{th} (fast-time) digital sample can be expressed as,

$$r(m,n) = \alpha_T \exp(j2\pi(\hat{f}_{B,T}m + \hat{f}_{d,T}n)) + \alpha_I \exp(j2\pi(\hat{f}_{B,I}m + \hat{f}_{d,I}n)) + w(m,n) \tag{7.4}$$

where $\hat{f}_{B,T} = f_{B,T}T_s,\ \hat{f}_{B,I} = f_{B,I}T_s$ are the corresponding normalized beat frequencies, $\hat{f}_{d,T} = f_{d,T}T_c,\ \hat{f}_{d,I} = f_{d,I}T_c$ are the corresponding normalized Doppler frequencies, and $T_s = 1/f_s$, with f_s being the sampling frequency.

Applying 2-D FFT to Equation 7.4 for $m = 1, \cdots, M$ and $n = 1, \cdots, N$, we can obtain the range-Doppler image as,

$$\begin{aligned} \mathrm{RD}(k,p) = \alpha_T D_M(\hat{f}_{B,T} - k/M) D_N(\hat{f}_{d,T} - p/N) \\ + \alpha_I D_M(\hat{f}_{B,I} - k/M) D_N(\hat{f}_{d,I} - p/N) + W(k,p) \end{aligned} \tag{7.5}$$

where $D_n(x) = \sin(n\pi x)/\sin(\pi x)$ is the Dirichlet function and $W(k,p)$ represents the 2-D FFT of noise.

One can observe from Equation 7.5 that the interference signal will form a sharp peak in the range-Doppler image. In particular, it is worth noting that, although the interference might be attributable to the transmission from the antenna sidelobe of one radar and received by the antenna sidelobe of the other, the potential interference level can be significantly higher than the target reflections due to the non-ideal antenna sidelobe characteristic. This is attributable to the one-way propagation characteristic of the interference signal and the direct (without reflection) blast from one's transmission to the other's reception [60]. Specifically, according to the radar range-equation, the power of the target returns (*i.e.*, $|\alpha_T|^2$) can be determined by

$$P_{T,r} = \frac{P_t G_T^2 \lambda^2 \sigma_t L_t}{(4\pi)^3 R_T^4}, \tag{7.6}$$

where P_t is the system transmit power, G_T is the antenna gain in the target direction, $\lambda = c/f_c$ is the wavelength, c is the light speed, σ_t is the radar cross section (RCS) of the target, L_t is

the propagation loss, and R_T denotes the target range. The power of interference (*i.e.*, $|\alpha_I|^2$) is given by

$$P_{I,r} = \frac{P_t G_{t,I} G_{r,I} \lambda^2 L_I}{(4\pi)^2 R_I^2}, \tag{7.7}$$

where we have assumed the two automotive radar systems have the same transmit power, $G_{t,I}$ and $G_{r,I}$ denote the transmit and receive antenna gains associated with the interference, respectively, L_I denotes the propagation loss, and R_I is the range between the two radar systems. Thus, considering a target with RCS of 1m^2 and ignoring the propagation loss, we have the power ratio at the receiver input as,

$$\frac{P_{I,r}}{P_{T,r}} = \frac{4\pi R_T^4 G_{t,I} G_{r,I}}{G_T^2 R_I^2}. \tag{7.8}$$

Therefore, the non-negligible interference power will result in serious interference for both automotive radar systems. In the following, we formulate the problem of mutual interference mitigation for a simple SISO scenario and then extend it to the MIMO case.

7.3 SISO Coding Scheme

Consider two systems that use N periodic consecutive pulses: $\mathbf{x} = [x_1, x_2. \cdots, x_N]^T$and $\mathbf{y} = [y_1, y_2. \cdots, y_N]^T$, respectively, as depicted in Figure 33. That is to say, in the n^{th} pulse of a CPI, the first radar system transmits $x_n u(t)$ and the second radar system transmits $y_n u(t)$. Moreover, to keep constant transmit power over the N pulses, we constrain the code sequences

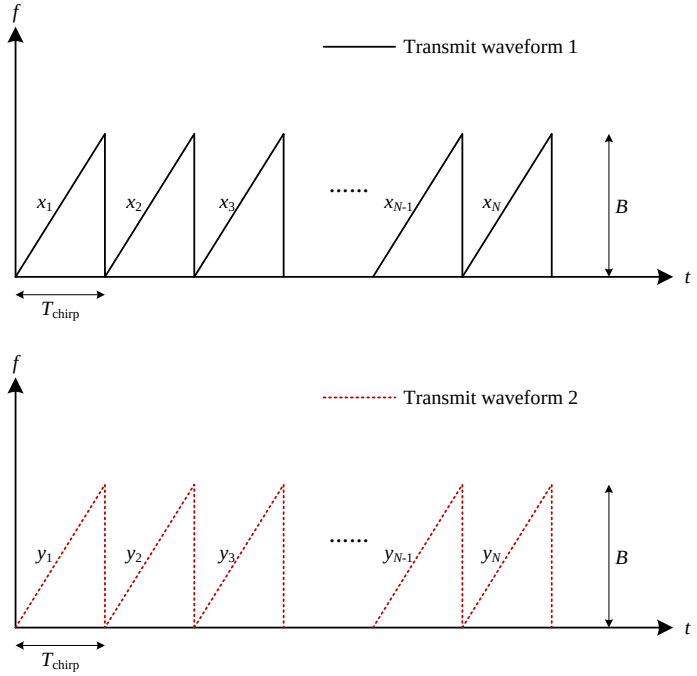

Figure 33. An illustration of the SISO coding scheme for two radar systems operating under same FMCW parameters.

to be unimodular, *i.e.*, $|x_n| = |y_n| = 1, n = 1, 2, \cdots, N$. With this coding scheme, the m^{th} (fast-time) sample of the n^{th} de-chirped signal is denoted by,

$$r^c(m,n) = \alpha_T \exp(j2\pi(\hat{f}_{B,T}m + \hat{f}_{d,T}n)) + \alpha_I x_n^* y_{(n+l) \bmod N} \exp(j2\pi(\hat{f}_{B,I}m + \hat{f}_{d,I}n)) + w(m,n) \quad (7.9)$$

for correlation lags $l \in \{-N+1, \cdots, N-1\}$. The corresponding range-Doppler image, is thus given by

$$\begin{aligned} \mathrm{RD}^c(k,p) &= \alpha_T D_M(\hat{f}_{B,T} - k/M) D_N(\hat{f}_{d,T} - p/N) \\ &\quad + \alpha_I D_M(\hat{f}_{B,I} - k/M) r_{xy}^l(\hat{f}_{d,I} - p/N) + W(k,p) \end{aligned} \tag{7.10}$$

where

$$r_{xy}^l(f) = \sum_{n=1}^{N} x_n^* y_{(n+l) \bmod N} \exp(j2\pi n f) \tag{7.11}$$

is the periodic CAF of $\mathbf{x}$ and $\mathbf{y}$, and is to be minimized [199–201].

To suppress the interference power in the range-Doppler image, we aim at designing $\mathbf{x}$ and $\mathbf{y}$ to minimize $r_{xy}^l(f)$ within a range of interest for f. To this end, we propose two methods to design $\mathbf{x}$ and $\mathbf{y}$ in the following subsections.

7.3.1 The Doppler-Shifting Scheme

First, we propose a simple heuristic coding scheme to mitigate the interference. For simplicity and without loss of generality, we assume that the Doppler frequency of the interference signal satisfies $f_{D,I} \in [-f_{d,\max}, f_{d,\max}]$, where $f_{d,\max}$ denotes the maximum possible Doppler frequency (for both the target reflections and the interference signal). Note that for an automotive radar system with sweep time T_c, the unambiguous Doppler frequency that the system can identify is determined by

$$\frac{-f_r}{2} \leq f_d \leq \frac{f_r}{2}, \tag{7.12}$$

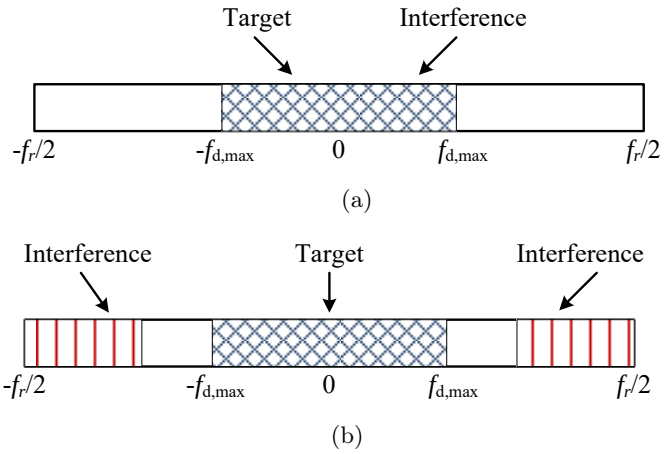

Figure 34. The Doppler spectra of target and interference (a) without coding and (b) with Doppler-shifting coding.

with $f_r = 1/T_c$ (we can treat f_r as the pulse repetition frequency (PRF)). Assuming that $f_{d,\max} \leq f_r/2$, the possibly occupied Doppler frequencies of the interference signal can be illustrated in Figure 34(a). We can observe that, without slow-time coding, the Doppler frequency of target reflections and interference signal might occupy the same area and it results in mutual interference.

In order to mitigate the interference in the Doppler region, we introduce a coding scheme to shift the Doppler spectrum of the interference signal into the high frequency area ($> f_{d,\max}$ or $< -f_{d,\max}$). We call the resulting code the *Doppler-shifting code*. With such a coding scheme, it is possible to separate the target reflections and interference signal in the Doppler domain. As a result, we can apply low-pass filtering in the Doppler domain to mitigate the interference. To

this end, we propose using the following codes to shift the Doppler spectrum of the interference signal:

$$\mathbf{x} = [1, 1, \cdots, 1]^T, \tag{7.13a}$$

$$\mathbf{y} = \begin{cases} [1, -1, \cdots, -1, 1]^T, \text{if } N \text{ is odd}, \\ [1, -1, \cdots, 1, -1]^T, \text{if } N \text{ is even}. \end{cases} \tag{7.13b}$$

Note that, the two sequences are orthogonal for even N and quasi-orthogonal for odd N. It is easy to verify that,

$$\begin{aligned} |r_{xy}^l| &= \left| \sum_{n=1}^{N} \exp(jn\pi) \exp(j2\pi(\hat{f}_{d,I} - p/N_f)n) \right| \\ &= \left| \sum_{n=1}^{N} \exp(j2\pi((\hat{f}_{d,I} + \frac{1}{2}) - p/N_f)n) \right| \\ &= \left| \frac{\sin(N\pi(\hat{f}_{d,I} + 1/2 - p/N_f))}{\sin(\pi(\hat{f}_{d,I} + 1/2 - p/N_f))} \right|. \end{aligned} \tag{7.14}$$

Therefore, the above codes enable the automotive radar to shift the Doppler frequency of interference signal from $f_{d,I}$ to $f_{d,I} + f_r/2$, as shown in Figure 34(b). In particular, if f_r satisfies

$$4f_{d,\max} < f_r, \tag{7.15}$$

we can isolate the target reflections and the interference signal in the Doppler domain with any Doppler frequency $f_{D,I} \in [-f_{d,\max}, f_{d,\max}]$.

On the other hand, note that the maximum value of the first sidelobe of the function $|\sin(N\pi f)/\sin(\pi f)|$ equals

$$\mathrm{SLL}_1 = \frac{1}{\sin(\frac{3\pi}{2N})} \approx \frac{2N}{3\pi} (\text{for large } N). \tag{7.16}$$

As a result, although the Doppler shifting coding scheme is simple, it may suffer from large sidelobes and the interference signal cannot be extensively canceled.

7.3.2 Optimized Coding Scheme for SISO Radars

In this subsection, we seek to optimize $\mathbf{x}$ and $\mathbf{y}$ such that the corresponding $|r_{xy}^l(f)|$ has small values in a desired area. Given that the two radar systems usually have unsynchronized transmissions, the desired area should include all possible delays. Hence, we consider the following optimization problem *w.r.t.* the two codes $\mathbf{x}$ and $\mathbf{y}$:

$$\begin{aligned} &\min_{\mathbf{x},\mathbf{y}} \sum_{l=-(N-1)}^{N-1} \sum_{p=-P}^{P} |r_{lp}|^2 \\ &\text{s.t.} \qquad |x_n| = 1,\ |y_n| = 1,\ \forall\, n, \end{aligned} \tag{7.17}$$

where

$$r_{lp} = \sum_{n=1}^{N} x_n^* y_{(n+l) \bmod N} \exp(-j2\pi np/N_f) \tag{7.18}$$

is the discrete periodic CAF with $N < N_f$, $0 < P < N_f$, N_f is the overall number of discrete (Doppler) frequencies, and the value of P is closely related to the maximum Doppler frequency of interest.

After some algebraic manipulation, the criterion in Equation 7.17 can be reformulated as

$$\begin{aligned} &\min_{\mathbf{x},\mathbf{y}} \sum_{l=-(N-1)}^{N-1} \sum_{p=-P}^{P} |\mathbf{x}^H \mathrm{Diag}\left(\mathbf{f}_p\right) \mathbf{C}_l \mathbf{y}|^2 \\ &\text{s.t.} \qquad |x_n| = 1,\ |y_n| = 1,\ \forall\, n, \end{aligned} \tag{7.19}$$

where $\mathbf{C}_l = \mathbf{C}_{-l}^T = \begin{bmatrix} \mathbf{0} & \mathbf{I}_{N-l} \\ \mathbf{I}_l & \mathbf{0} \end{bmatrix}$ is a circular shift matrix and n^{th} element of $\mathbf{f}_p$ is $\exp(-j2\pi np/N_f)$.

Note that the optimization problem in Equation 7.19 is non-convex and appears to be difficult to solve [202,203]. Herein, we propose to tackle the problem in a cyclic manner. Specifically, in the s^{th} iteration of our cyclic optimization process, we first optimize $\mathbf{x}$ for fixed $\mathbf{y}^{(s-1)}$ and then optimize $\mathbf{y}$ for fixed $\mathbf{x}^{(s)}$. In the following, we present the solution to the two sub-problems involved in each iteration of the cyclic approach. For notational simplicity, we omit the superscripts of $\mathbf{y}^{(s-1)}$ and $\mathbf{x}^{(s)}$.

7.3.2.1 Optimization of x for fixed y

The associated optimization problem can be recast as

$$\begin{aligned} &\min_{\mathbf{x}} \mathbf{x}^H \mathbf{B}_y \mathbf{x}, \\ &\text{s.t.} \quad |x_n| = 1, \quad n = 1, 2, \cdots, N, \end{aligned} \tag{7.20}$$

where

$$\mathbf{B}_y = \sum_{l=-N+1}^{N-1} \sum_{p=-P}^{P} \mathrm{Diag}\left(\mathbf{f}_p\right) \mathbf{C}_l \mathbf{y}\mathbf{y}^H \mathbf{C}_l^H \mathrm{Diag}\left(\mathbf{f}_p\right)^H . \tag{7.21}$$

The problem in Equation 7.20 is called a (non-convex) unimodular quadratic program (UQP). Such problems can be tackled by employing the *power-method-like iterations* (PMLI) proposed in [76] and [51] (see also [204–206] for more applications of PMLI in radar code optimization). Specifically, let γ_y be a positive constant larger than the maximum eigenvalue of $\mathbf{B}_y$ to ensure $\mathbf{D}_y = \gamma_y \mathbf{I}_N - \mathbf{B}_y \succ \mathbf{0}$ (*i.e.*, $\mathbf{D}_y$ is positive definite). It is easy to verify that the problem in Equation 7.20 can be equivalently written as:

$$\begin{aligned} &\max_{\mathbf{x}} \ \mathbf{x}^H \mathbf{D}_y \mathbf{x}, \\ &\text{s.t. } |x_n| = 1, \ n = 1, 2, \cdots, N. \end{aligned} \tag{7.22}$$

In the t^{th} (inner) iteration, we update $\mathbf{x}$ by using the following PMLI:

$$\mathbf{x}^{(s,t)} = \exp(j \arg(\mathbf{D}_y \mathbf{x}^{(s,t-1)})). \tag{7.23}$$

7.3.2.2 Optimization of y for fixed x

The optimization of $\mathbf{y}$ for fixed $\mathbf{x}$ is formulated as follows:

$$\begin{aligned} &\min_{\mathbf{y}} \ \mathbf{y}^H \mathbf{B}_x \mathbf{y}, \\ &\text{s.t. } |y_n| = 1, n = 1, 2, \cdots, N, \end{aligned} \tag{7.24}$$

where

$$\mathbf{B}_x = \sum_{l=-N+1}^{N-1} \sum_{p=-P}^{P} \mathbf{C}_l^H \mathrm{Diag}\left(\mathbf{f}_p\right)^H \mathbf{x}\mathbf{x}^H \mathrm{Diag}\left(\mathbf{f}_p\right) \mathbf{C}_l. \tag{7.25}$$

Similar to the previous case, we can tackle the optimization problem in Equation 7.24 iteratively. Specifically, the solution in the t^{th} (inner) iteration is given by

$$\mathbf{y}^{(s,t)} = \exp(j \arg(\mathbf{D}_x \mathbf{y}^{(s,t-1)})), \tag{7.26}$$

where $\mathbf{D}_x = \gamma_x \mathbf{I}_N - \mathbf{B}_x$ and γ_x is a positive constant larger than the maximum eigenvalue of $\mathbf{B}_x$ to ensure $\mathbf{D}_x \succ \mathbf{0}$.

Finally, the steps of the proposed algorithm to minimize the discrete periodic CAF for two identical SISO systems are summarized in Algorithm 8.

Remark 5. (Optimality and the Convergence): The optimization problem in Equation 7.19 is NP-hard and multimodal, *i.e.*, the objective has multiple local optima [207]. Due to the non-convex nature of the objective function, one usually settles for an approximation algorithm that yields local optima. In the proposed approach, we tackle the non-convexity of the problem by resorting to a cyclic minimization algorithm. In each half of the cycle, we optimize for one set of variables keeping the other fixed, and these two subproblems are solved based on a local optimization method, namely PMLI for UQP, that yields good local optima [51]. From

Equation 7.19, it can be deduced that the objective value is lower bounded at 0. Furthermore, from Equation 7.20 and Equation 7.24, we know that for s-th iteration

$$\mathbf{x}^{(s+1)} = \arg\min_{\mathbf{x}\in\Omega_x} \ \mathbf{x}^H \mathbf{B}_y^{(s)} \mathbf{x}, \tag{7.27a}$$

$$\mathbf{y}^{(s+1)} = \arg\min_{\mathbf{y}\in\Omega_y} \ \mathbf{y}^H \mathbf{B}_x^{(s+1)} \mathbf{y} \tag{7.27b}$$

where $\Omega_z = \{\mathbf{z} \mid |z_n| = 1, \forall n\}$. Therefore, one can conclude that, in each iteration the objective value is monotonically decreasing, and that the algorithm converges. ■

Remark 6. (Computational Complexity): Note that, in the code optimization, one needs to calculate $\mathbf{B}_x$ and $\mathbf{B}_y$ at each iteration. Specifically, in the computation of $\mathbf{B}_y$, we need N complex multiplications to obtain $\text{Diag}\left(\mathbf{f}_p\right)\mathbf{C}_l\mathbf{y}$ (whose n^{th} element is $e^{-j2\pi np/N_f} y_{(n+l) \mod N}$). As a result, the overall computational complexity of computing $\mathbf{B}_y$ is of the order $\mathcal{O}\left(N_f(2N-1)(N^2+N)\right)$. Similarly, the overall computational complexity of computing $\mathbf{B}_x$ is of the order $\mathcal{O}\left(N_f(2N-1)(N^2+N)\right)$, which seems to be quite high. In Appendix C, we provide a computationally fast and inexpensive way to calculate $\mathbf{B}_x$ and $\mathbf{B}_y$. ■

In what follows, we extend our discussion to the more general case of MIMO automotive radar systems.

Algorithm 8 Automotive Radar Waveform Design Algorithm for Interference Mitigation (*SISO Case*)

Initialize: $\mathbf{x}^{(0)}$, $\mathbf{y}^{(0)}$, $s = 0$
Output: $\mathbf{x}^{\star}$, $\mathbf{y}^{\star}$

repeat
  $s \leftarrow s + 1$
  ▷ `Update of` $\mathbf{x}^{(s)}$`:`
  Calculate $\mathbf{B}_y^{(s)}$ with Equation 7.21
  $t = 0$, $\mathbf{x}^{(s,t)} = \mathbf{x}^{(s-1)}$
  repeat
    $\mathbf{x}^{(s,t)} = \exp(j \arg((\gamma_y^{(s)}\mathbf{I}_N - \mathbf{B}_y^{(s)})\mathbf{x}^{(s,t-1)}))$
    $t \leftarrow t + 1$
  until convergence
  $\mathbf{x}^{(s)} = \mathbf{x}^{(s,t)}$
  ▷ `Update of` $\mathbf{y}^{(s)}$`:`
  Calculate $\mathbf{B}_x^{(s)}$ with Equation 7.25
  $t = 0$, $\mathbf{y}^{(s,t)} = \mathbf{y}^{(s-1)}$
  repeat
    $\mathbf{y}^{(s,t)} = \exp(j \arg((\gamma_x^{(s)}\mathbf{I}_N - \mathbf{B}_x^{(s)})\mathbf{y}^{(s,t-1)}))$
    $t \leftarrow t + 1$
  until convergence
  $\mathbf{y}^{(s)} = \mathbf{y}^{(s,t)}$
until a pre-defined stop criterion is satisfied, *e.g.*, $|J^{(s)} - J^{(s-1)}| \leq \epsilon$, for some $\epsilon > 0$ where J denotes the objective function of the problem Equation 7.19
$\mathbf{x}^{\star} = \mathbf{x}^{(s)}, \mathbf{y}^{\star} = \mathbf{y}^{(s)}$

7.4 Extension to the MIMO Case

In a MIMO scenario, the mutual interference stems not only from the waveforms of a similar radar system nearby, but also from the various waveforms transmitted by the same radar system. In this case, our optimization problem for radar waveform design can be formulated as

$$\min_{\{\mathbf{x}_m\},\{\mathbf{y}_k\}} \sum_{m,k} \sum_{l=-(N-1)}^{N-1} \sum_{p=-P}^{P} \left\{ |\mathbf{x}_m^H \mathrm{Diag}\left(\mathbf{f}_p\right) \mathbf{C}_l \mathbf{y}_k|^2 + |\mathbf{x}_m^H \mathrm{Diag}\left(\mathbf{f}_p\right) \mathbf{C}_l \mathbf{x}_k|^2 + |\mathbf{y}_m^H \mathrm{Diag}\left(\mathbf{f}_p\right) \mathbf{C}_l \mathbf{y}_k|^2 \right\}$$

$$\text{s.t.} \quad \mathbf{x}_m \text{ and } \mathbf{y}_k \text{ are unimodular for all } m, k, \tag{7.28}$$

in which $\{\mathbf{x}_m\}_{m=1}^{M}$ and $\{\mathbf{y}_k\}_{k=1}^{K}$ are the codes used for modulation on different antennas of the two radar systems. Note that the first and third terms of Equation 7.28 account for the self-interference among the waveforms transmitted in the same radar systems, while the second term accounts for the mutual interference of different radar systems. Let

$$\mathbf{A}_{l,p} \triangleq \mathrm{Diag}\left(\mathbf{f}_p\right)\mathbf{C}_l, \tag{7.29a}$$

$$\mathbf{X} = [\mathbf{x}_1, \cdots, \mathbf{x}_M], \tag{7.29b}$$

$$\mathbf{Y} = [\mathbf{y}_1, \cdots, \mathbf{y}_K], \tag{7.29c}$$

and note that the objective in Equation 7.28 can be written in a compact form as

$$\mathcal{Q}_{mimo}(\mathbf{X}, \mathbf{Y}) = \sum_{l,p} \|\mathbf{X}^H \mathbf{A}_{l,p} \mathbf{Y}\|_F^2 + \|\mathbf{X}^H \mathbf{A}_{l,p} \mathbf{X}\|_F^2 + \|\mathbf{Y}^H \mathbf{A}_{l,p} \mathbf{Y}\|_F^2. \tag{7.30}$$

Tackling Equation 7.30 appears to be more difficult than the optimization problem formulated in the SISO case in Equation 7.17, as the new objective is *quartic* in both radar codes ($\mathbf{X}$ and $\mathbf{Y}$) and the fact that the number of CAF values to be suppressed is growing more quickly in terms of the problem dimension than the number of design variables. In the following, we formulate a quadratic alternative to Equation 7.28 that can be tackled more efficiently.

7.4.1 The Quartic to Quadratic Transformation

In order to recast the problem in a quadratic form, let

$$\mathbf{A}_{l,p}^{r} = \frac{1}{2}(\mathbf{A}_{l,p} + \mathbf{A}_{l,p}^{H}), \tag{7.31a}$$

$$\mathbf{A}_{l,p}^{i} = \frac{1}{2}(\mathbf{A}_{l,p} - \mathbf{A}_{l,p}^{H}) \tag{7.31b}$$

and note that

1. Both matrices $\mathbf{A}_{l,p}^{r}$ and $j\mathbf{A}_{l,p}^{i}$ are Hermitian [207].

2. For any generic vector $\mathbf{z}$,

$$\mathbf{z}^{H}\mathbf{A}_{l,p}\mathbf{z} = \mathbf{z}^{H}\mathbf{A}_{l,p}^{r}\mathbf{z} + \mathbf{z}^{H}\mathbf{A}_{l,p}^{i}\mathbf{z} \tag{7.32}$$

where

$$\mathbf{z}^{H}\mathbf{A}_{l,p}^{r}\mathbf{z} \in \mathbb{R}, \qquad j\mathbf{z}^{H}\mathbf{A}_{l,p}^{i}\mathbf{z} \in \mathbb{R}. \tag{7.33}$$

In particular it follows from the above that

$$|\mathbf{z}^{H}\mathbf{A}_{l,p}\mathbf{z}|^{2} = |\mathbf{z}^{H}\mathbf{A}_{l,p}^{r}\mathbf{z}|^{2} + |\mathbf{z}^{H}j\mathbf{A}_{l,p}^{i}\mathbf{z}|^{2}. \tag{7.34}$$

We particularly observe that the quartic behavior of Equation 7.28 and Equation 7.30 stems from self-interference terms: $\{|\mathbf{x}_m^H \mathbf{A}_{l,p} \mathbf{x}_m|^2\}, \{|\mathbf{y}_k^H \mathbf{A}_{l,p} \mathbf{y}_k|^2\}$ for all $m \in \{1, \cdots, M\}$ and $k \in \{1, \cdots, K\}$.

Based on Equation 7.31-Equation 7.34, one can write

$$\begin{aligned}
\sum_{l,p} |\mathbf{x}_m^H \mathbf{A}_{l,p} \mathbf{x}_m|^2 &= \sum_{l,p} |\mathbf{x}_m^H \mathbf{A}_{l,p}^r \mathbf{x}_m|^2 + |\mathbf{x}_m^H j\mathbf{A}_{l,p}^i \mathbf{x}_m|^2 \\
&= \sum_{l,p} |\mathbf{x}_m^H (\mathbf{A}_{l,p}^r + \zeta \mathbf{I}_N) \mathbf{x}_m - \zeta N|^2 + |\mathbf{x}_m^H (j\mathbf{A}_{l,p}^i + \zeta \mathbf{I}_N) \mathbf{x}_m - \zeta N|^2 \\
&= \sum_{l,p} |\mathbf{x}_m^H \tilde{\mathbf{A}}_{l,p}^r \mathbf{x}_m - \zeta N|^2 + |\mathbf{x}_m^H \tilde{\mathbf{A}}_{l,p}^i \mathbf{x}_m - \zeta N|^2, \qquad (7.35)
\end{aligned}$$

where

$$\tilde{\mathbf{A}}_{l,p}^r = \mathbf{A}_{l,p}^r + \zeta \mathbf{I}_N, \qquad (7.36a)$$

$$\tilde{\mathbf{A}}_{l,p}^i = j\mathbf{A}_{l,p}^i + \zeta \mathbf{I}_N, \qquad (7.36b)$$

and $\zeta \in \mathbb{R}$ is chosen such that

$$\zeta > -\min \left(\bigcup_{l,p} \left\{ \gamma_{\min} \left(\mathbf{A}_{l,p}^r \right), \gamma_{\min} \left(j\mathbf{A}_{l,p}^i \right) \right\} \right) \qquad (7.37)$$

to ensure the positive definiteness of $\{\tilde{\mathbf{A}}_{l,p}^r\}$ and $\{\tilde{\mathbf{A}}_{l,p}^i\}$, where $\gamma_{\min}(\cdot)$ denotes the minimum eigenvalue of its matrix argument. Observe that the quantity in Equation 7.35 is still quartic *w.r.t.* $\mathbf{x}_m$, which in fact is difficult to minimize. A quadratic alternative, however, can be

proposed in the following manner. Note that the quantity in Equation 7.35 will be made small when the quadratic quantities $\{\mathbf{x}_m^H \tilde{\mathbf{A}}_{l,p}^r \mathbf{x}_m\}$ and $\{\mathbf{x}_m^H \tilde{\mathbf{A}}_{l,p}^i \mathbf{x}_m\}$ are *close* to ζN. This is only possible when unit-norm vectors $\{\mathbf{u}_{l,p,m}^r\}$ and $\{\mathbf{u}_{l,p,m}^i\}$ exist such that $(\tilde{\mathbf{A}}_{l,p}^r)^{1/2}\mathbf{x}_m$ is *close* to $\sqrt{\zeta N}\mathbf{u}_{l,p,m}^r$, and likewise $(\tilde{\mathbf{A}}_{l,p}^i)^{1/2}\mathbf{x}_m$ is *close* to $\sqrt{\zeta N}\mathbf{u}_{l,p,m}^i$. As a result, minimization of Equation 7.35 can be approached by a reformulation, in the form of the following alternative quadratic optimization problem [46, 48, 85, 208]:

$$\begin{aligned} \min \ & \sum_{l,p} \left\{ \left\| (\tilde{\mathbf{A}}_{l,p}^r)^{1/2}\mathbf{x}_m - \sqrt{\zeta N}\mathbf{u}_{l,p,m}^r \right\|_2^2 + \left\| (\tilde{\mathbf{A}}_{l,p}^i)^{1/2}\mathbf{x}_m - \sqrt{\zeta N}\mathbf{u}_{l,p,m}^i \right\|_2^2 \right\} \\ \text{s.t.} \ & \mathbf{x}_m \text{ are unimodular for all } m, \\ & \|\mathbf{u}_{l,p,m}^r\|_2 = \|\mathbf{u}_{l,p,m}^i\|_2 = 1 \text{ for all } l, p, m. \end{aligned} \tag{7.38}$$

Interestingly, one can observe that Equation 7.38 is quadratic instead of quartic— a transformation that was made possible by judicious over-parametrization. In a similar manner, we argue that $\{|\mathbf{y}_k^H \mathbf{A}_{l,p}\mathbf{y}_k|^2\}$ can be made small by solving the alternative problem:

$$\begin{aligned} \min \ & \sum_{l,p} \left\{ \left\| (\tilde{\mathbf{A}}_{l,p}^r)^{1/2}\mathbf{y}_k - \sqrt{\zeta N}\mathbf{v}_{l,p,k}^r \right\|_2^2 + \left\| (\tilde{\mathbf{A}}_{l,p}^i)^{1/2}\mathbf{y}_k - \sqrt{\zeta N}\mathbf{v}_{l,p,k}^i \right\|_2^2 \right\} \\ \text{s.t.} \ & \mathbf{y}_k \text{ are unimodular for all } k, \\ & \|\mathbf{v}_{l,p,k}^r\|_2 = \|\mathbf{v}_{l,p,k}^i\|_2 = 1 \text{ for all } l, p, k. \end{aligned} \tag{7.39}$$

As a result, the objective in Equation 7.28 can be recast in its almost-equivalent quadratic form as described in Equation 7.40.

$$
\begin{aligned}
\min_{\substack{\{\mathbf{x}_m\},\{\mathbf{y}_k\},\\ \{\mathbf{u}^r_{l,p,m}\},\{\mathbf{u}^i_{l,p,m}\},\\ \{\mathbf{v}^r_{l,p,k}\},\{\mathbf{v}^i_{l,p,k}\}}} \quad & \sum_{l,p}\sum_{m\neq k}\{|\mathbf{x}_m^H\mathbf{A}_{l,p}\mathbf{x}_k|^2+|\mathbf{y}_m^H\mathbf{A}_{l,p}\mathbf{y}_k|^2\}+\sum_{l,p}\sum_{m,k}\{|\mathbf{x}_m^H\mathbf{A}_{l,p}\mathbf{y}_k|^2\} \\
& + \sum_{l,p}\left[\sum_m\left\{\left\|(\tilde{\mathbf{A}}^r_{l,p})^{1/2}\mathbf{x}_m-\sqrt{\zeta N}\mathbf{u}^r_{l,p,m}\right\|_2^2+\left\|(\tilde{\mathbf{A}}^i_{l,p})^{1/2}\mathbf{x}_m-\sqrt{\zeta N}\mathbf{u}^i_{l,p,m}\right\|_2^2\right\}\right. \\
& \left. + \sum_k\left\{\left\|(\tilde{\mathbf{A}}^r_{l,p})^{1/2}\mathbf{y}_k-\sqrt{\zeta N}\mathbf{v}^r_{l,p,k}\right\|_2^2+\left\|(\tilde{\mathbf{A}}^i_{l,p})^{1/2}\mathbf{y}_k-\sqrt{\zeta N}\mathbf{v}^i_{l,p,k}\right\|_2^2\right\}\right] \\
\text{s.t.} \quad & \mathbf{x}_m \text{ and } \mathbf{y}_k \text{ are unimodular for all } m,k, \\
& \|\mathbf{u}^r_{l,p,m}\|_2=\|\mathbf{u}^i_{l,p,m}\|_2=1 \text{ for all } l,p,m, \\
& \|\mathbf{v}^r_{l,p,k}\|_2 \ =\|\mathbf{v}^i_{l,p,k}\|_2 \ =1 \text{ for all } l,p,k. \qquad (7.40)
\end{aligned}
$$

Note that the optimization problem in Equation 7.40 is still non-convex, especially because of the unimodular constraints imposed on $\{\mathbf{x}_m\}$ and $\{\mathbf{y}_k\}$. In the following subsection, we provide an efficient way to tackle the above problem for all individual optimization variables.

7.4.2 The Optimization Procedure

In order to efficiently tackle the problem in Equation 7.40, we resort to a cyclic optimization framework. Namely, we iteratively optimize the criterion with respect to one of the variables while keeping the rest of them fixed. In s^{th} iteration, we separate each variable $\{\mathbf{x}_m\}$, $\{\mathbf{y}_k\}$, $\{\mathbf{u}^c_{l,p,m}\},\{\mathbf{v}^c_{l,p,k}\}$ for all $m\in\{1,\cdots,M\},k\in\{1,\cdots,K\},l\in\{-(N-1),\cdots,N-1\},p\in\{-P,\cdots,P\},c\in\{r,i\}$ from the objective function in Equation 7.40 and optimize them indi-

vidually while fixing all other variables to their values from $(s-1)^{th}$ iteration. In the following subsections, we describe such a process of variable separation and the corresponding solution techniques. We drop the superscript (s) for notational simplicity.

7.4.2.1 Optimization *w.r.t.* $\{\mathbf{x}_m\}_{m=1}^{M}$

We begin by reformulating the optimization problem in Equation 7.40 *w.r.t.* each of $\mathbf{x}_m$ for all m. Eliminating all the other variables that do not depend on $\mathbf{x}_m$, the objective function in Equation 7.40 becomes what is described in Equation 7.41,

$$\begin{aligned} Q_{\mathbf{x}_m} = \underbrace{\mathbf{x}_m^H \left(\sum_{m' \neq m} \sum_{l,p} \mathbf{A}_{l,p} \mathbf{x}_{m'} \mathbf{x}_{m'}^H \mathbf{A}_{l,p}^H \right) \mathbf{x}_m}_{M-1 \text{ terms}} + \underbrace{\mathbf{x}_m^H \left(\sum_{k} \sum_{l,p} \mathbf{A}_{l,p} \mathbf{y}_k \mathbf{y}_k^H \mathbf{A}_{l,p}^H \right) \mathbf{x}_m}_{K \text{ terms}} + \mathbf{x}_m^H \left(\sum_{l,p} \tilde{\mathbf{A}}_{l,p}^r + \tilde{\mathbf{A}}_{l,p}^i \right) \mathbf{x}_m \\ - 2\sqrt{\zeta N} \Re \left(\mathbf{x}_m^H \sum_{l,p} (\tilde{\mathbf{A}}_{l,p}^r)^{H/2} \mathbf{u}_{l,p,m}^r \right) - 2\sqrt{\zeta N} \Re \left(\mathbf{x}_m^H \sum_{l,p} (\tilde{\mathbf{A}}_{l,p}^i)^{H/2} \mathbf{u}_{l,p,m}^i \right) + \text{const.} \end{aligned} \tag{7.41}$$

or simply,

$$Q_{\mathbf{x}_m} = \mathbf{x}_m^H \mathbf{R}_{\mathbf{x}_m} \mathbf{x}_m + 2\Re\big(\mathbf{x}_m^H \mathbf{s}_{\mathbf{x}_m}\big) + \text{const.}, \tag{7.42}$$

where

$$\mathbf{R}_{\mathbf{x}_m} = \sum_{m' \neq m} \sum_{l,p} \mathbf{A}_{l,p} \mathbf{x}_{m'} \mathbf{x}_{m'}^H \mathbf{A}_{l,p}^H + \sum_{k} \sum_{l,p} \mathbf{A}_{l,p} \mathbf{y}_k \mathbf{y}_k^H \mathbf{A}_{l,p}^H + \sum_{l,p} \tilde{\mathbf{A}}_{l,p}^r + \tilde{\mathbf{A}}_{l,p}^i \tag{7.43}$$

and

$$\mathbf{s}_{\mathbf{x}_m} = -\sqrt{\zeta N}\sum_{l,p}\left((\tilde{\mathbf{A}}^r_{l,p})^{H/2}\mathbf{u}^r_{l,p,m} + (\tilde{\mathbf{A}}^i_{l,p})^{H/2}\mathbf{u}^i_{l,p,m}\right).$$

By dropping the constant term in Equation 7.42, the objective function can be reformulated as,

$$\begin{aligned} Q_{\mathbf{x}_m} &= \mathbf{x}_m^H\mathbf{R}_{\mathbf{x}_m}\mathbf{x}_m + 2\Re\big(\mathbf{x}_m^H\mathbf{s}_{\mathbf{x}_m}\big) \\ &= \begin{bmatrix}\mathbf{x}_m \\ 1\end{bmatrix}^H \begin{bmatrix}\mathbf{R}_{\mathbf{x}_m} & \mathbf{s}_{\mathbf{x}_m} \\ \mathbf{s}^H_{\mathbf{x}_m} & 0\end{bmatrix}\begin{bmatrix}\mathbf{x}_m \\ 1\end{bmatrix} \\ &= \bar{\mathbf{x}}_m^H\mathbf{B}_{\mathbf{x}_m}\bar{\mathbf{x}}_m \end{aligned} \tag{7.44}$$

where

$$\bar{\mathbf{x}}_m \triangleq [\mathbf{x}_m\ 1]^T, \tag{7.45a}$$

$$\mathbf{B}_{\mathbf{x}_m} \triangleq \begin{bmatrix}\mathbf{R}_{\mathbf{x}_m} & \mathbf{s}_{\mathbf{x}_m} \\ \mathbf{s}^H_{\mathbf{x}_m} & 0\end{bmatrix}. \tag{7.45b}$$

Hence, the minimization of Equation 7.40 *w.r.t.* $\mathbf{x}_m$ is equivalent to the following,

$$\begin{aligned} \min_{\bar{\mathbf{x}}_m} \quad & \bar{\mathbf{x}}_m^H \mathbf{B}_{\mathbf{x}_m} \bar{\mathbf{x}}_m \\ \text{s.t.} \quad & |x_n(m)| = 1, \quad n = 1, \cdots, N, \\ & \bar{\mathbf{x}}_m = \begin{bmatrix} \mathbf{x}_m \\ \\ 1 \end{bmatrix}. \end{aligned} \tag{7.46}$$

As a result of the unimodular constraint on $\mathbf{x}_m$, the term $\bar{\mathbf{x}}_m$ also has a constant ℓ_2-norm, and hence, a diagonal loading of $\mathbf{B}_{\mathbf{x}_m}$ will not change the solution to the above problem [207]. Therefore, Equation 7.46 can be rewritten in the following equivalent form:

$$\begin{aligned} \max_{\bar{\mathbf{x}}_m} \quad & \bar{\mathbf{x}}_m^H \mathbf{D}_{\mathbf{x}_m} \bar{\mathbf{x}}_m \\ \text{s.t.} \quad & |x_n(m)| = 1, \quad n = 1, \cdots, N, \\ & \bar{\mathbf{x}}_m = \begin{bmatrix} \mathbf{x}_m \\ \\ 1 \end{bmatrix}, \end{aligned} \tag{7.47}$$

where

$$\mathbf{D}_{\mathbf{x}_m} \triangleq \gamma_{\mathbf{x}_m} \mathbf{I}_{(N+1)} - \mathbf{B}_{\mathbf{x}_m}, \tag{7.48}$$

with $\gamma_{\mathbf{x}_m}$ being larger than the maximum eigenvalue of $\mathbf{B}_{\mathbf{x}_m}$. Note that the above problem similarly belongs to the family of UQPs [51], and can be efficiently tackled in an iterative manner using power-method-like iterations of the form [207]:

$$\mathbf{x}_m^{(s,t)} = \exp\left\{ j \arg\left(\begin{bmatrix} \mathbf{I}_{N\times N} \\ \\ \mathbf{0}_{1\times N} \end{bmatrix}^T \mathbf{D}_{\mathbf{x}_m} \bar{\mathbf{x}}_m^{(s,t-1)} \right) \right\}, \tag{7.49}$$

where t denotes the inner iteration number. Note that the proposed iterations can be initialized with the most recent design of $\mathbf{x}_m$ (used as $\mathbf{x}_m^{(s,0)}$).

7.4.2.2 Optimization *w.r.t.* $\{\mathbf{y}_k\}_{k=1}^K$

In order to solve Equation 7.40 for $\mathbf{y}_k$ for all k, we follow the same algebraic manipulation with slight modifications. In this case, the objective function, $Q_{\mathbf{y}_k}$, becomes

$$Q_{\mathbf{y}_k} = \mathbf{y}_k^H \mathbf{R}_{\mathbf{y}_k} \mathbf{y}_k + 2\Re\big(\mathbf{y}_k^H \mathbf{s}_{\mathbf{y}_k}\big) + \text{const.} \tag{7.50}$$

where

$$\mathbf{R}_{\mathbf{y}_k} = \sum_{k'\neq k} \sum_{l,p} \mathbf{A}_{l,p} \mathbf{y}_{k'} \mathbf{y}_{k'}^H \mathbf{A}_{l,p}^H + \sum_m \sum_{l,p} \mathbf{A}_{l,p}^H \mathbf{x}_m \mathbf{x}_m^H \mathbf{A}_{l,p} + \sum_{l,p} \tilde{\mathbf{A}}_{l,p}^r + \tilde{\mathbf{A}}_{l,p}^i \tag{7.51}$$

and

$$\mathbf{s}_{\mathbf{y}_k} = -\sqrt{\zeta N} \sum_{l,p} \left((\tilde{\mathbf{A}}_{l,p}^r)^{H/2} \mathbf{v}_{l,p,k}^r + (\tilde{\mathbf{A}}_{l,p}^i)^{H/2} \mathbf{v}_{l,p,k}^i \right). \tag{7.52}$$

As a result, we can formulate a UQP for each $\mathbf{y}_k$ in a similar manner. The corresponding solution can be approached iteratively using the power-method-like recursions of the form

$$\mathbf{y}_k^{(s,t)} = \exp\left\{ j \arg\left(\begin{bmatrix} \mathbf{I}_{N\times N} \\ \mathbf{0}_{1\times N} \end{bmatrix}^T \mathbf{D}_{\mathbf{y}_k} \bar{\mathbf{y}}_k^{(s,t-1)} \right) \right\}, \tag{7.53}$$

where

$$\mathbf{D}_{\mathbf{y}_k} \triangleq \gamma_{\mathbf{y}_k} \mathbf{I}_{(N+1)} - \mathbf{B}_{\mathbf{y}_k} \tag{7.54}$$

with $\gamma_{\mathbf{y}_k}$ being larger than the maximum eigenvalue of $\mathbf{B}_{\mathbf{y}_k}$, and

$$\bar{\mathbf{y}}_k \triangleq [\mathbf{y}_k \ 1]^T \tag{7.55a}$$

$$\mathbf{B}_{\mathbf{y}_k} \triangleq \begin{bmatrix} \mathbf{R}_{\mathbf{y}_k} & \mathbf{s}_{\mathbf{y}_k} \\ \mathbf{s}_{\mathbf{y}_k}^H & 0 \end{bmatrix}. \tag{7.55b}$$

7.4.2.3 Optimization *w.r.t.* $\{\mathbf{u}_{l,p,m}^c\}$ and $\{\mathbf{v}_{l,p,k}^c\}$

Solving Equation 7.40 *w.r.t.* $\{\mathbf{u}_{l,p,m}^c\}$ and $\{\mathbf{v}_{l,p,k}^c\}$ for $c \in \{r, i\}$ is immediate and resolves into closed-form solution as follows:

$$\widehat{\mathbf{u}}_{l,p,m}^r = \frac{(\tilde{\mathbf{A}}_{l,p}^r)^{1/2}\mathbf{x}_m}{\|(\tilde{\mathbf{A}}_{l,p}^r)^{1/2}\mathbf{x}_m\|_2}, \qquad \widehat{\mathbf{v}}_{l,p,k}^r = \frac{(\tilde{\mathbf{A}}_{l,p}^r)^{1/2}\mathbf{y}_k}{\|(\tilde{\mathbf{A}}_{l,p}^r)^{1/2}\mathbf{y}_k\|_2}, \tag{7.56a}$$

$$\widehat{\mathbf{u}}_{l,p,m}^i = \frac{(\tilde{\mathbf{A}}_{l,p}^i)^{1/2}\mathbf{x}_m}{\|(\tilde{\mathbf{A}}_{l,p}^i)^{1/2}\mathbf{x}_m\|_2}, \qquad \widehat{\mathbf{v}}_{l,p,k}^i = \frac{(\tilde{\mathbf{A}}_{l,p}^i)^{1/2}\mathbf{y}_k}{\|(\tilde{\mathbf{A}}_{l,p}^i)^{1/2}\mathbf{y}_k\|_2}, \tag{7.56b}$$

for all $m \in \{1, \cdots, M\}, k \in \{1, \cdots, K\}, l \in \{-(N-1), \cdots, N-1\}, p \in \{-P, \cdots, P\}$. Finally, the steps of the proposed algorithm for interference mitigation in the MIMO setting are summarized in Algorithm 9.

Remark 7. (Convergence): As mentioned earlier for Algorithm 8, the Algorithm 9 as well resorts to a cyclic optimization method to tackle the non-convexity of the problem Equation 7.40. For each iteration of Algorithm 9, one can observe that the objective value is monotonically decreasing and bounded from below, leading to the convergence of the algorithm. Note that the final output of the cyclic algorithms often depends on the initialization of all the optimization variables. Different initial points in the search space may lead to different final designs due to the non-convexity of the landscape. For this reason, it is desirable to run Algorithm 9 multiple times. A good candidate can be using the output of the current design as the initialization for the next design. ■

Remark 8. (Computational Complexity and Parallelization): Note that, in the step 3 of the Algorithm 9, the calculation of $\tilde{\mathbf{A}}$ requires $\mathcal{O}\left(N_f(2N-1)(N+N^3)\right)$ number of complex multiplications. The term N^3 comes from the eigenvalue decomposition of the $N \times N$ matrix $\mathbf{A}$. Furthermore, the overall computational complexity of calculating $\mathbf{D}_{\mathbf{x}_m}$ and $\mathbf{D}_{\mathbf{y}_k}$ is $\mathcal{O}\left((M+K)N_f(2N-1)[(M+K-1)N+N^3]\right)$. However, it is interesting to note that the computation of $\tilde{\mathbf{A}}$ is required only once in the entire optimization procedure and can be performed in parallel. Moreover, in the s^{th} iteration of the algorithm, solving for $\{\mathbf{u}_{l,p,m}^{c(s)}\}$, $\{\mathbf{v}_{l,p,k}^{c(s)}\}$ can also be done in parallel making the algorithm significantly more efficient from a computational viewpoint. ■

In the next section, several numerical examples are provided to showcase the performance and efficiency of the proposed waveform design schemes.

7.5 Generalization for the Multiple-MIMO Scenario

In a multiple-MIMO radar scenario, the mutual interference stems not only from the waveforms of a similar radar system nearby but also from the various waveforms transmitted by the same radar system. Following the formulation in Equation 7.28, firstly, the periodic CAF (PCAF) associated with the same radar system for all vehicles is given as,

$$\bar{Q}_i = \sum_{l,p} \sum_{v=1}^{V} \sum_{m=1}^{M_v} \sum_{m'=1}^{M_v} |\mathbf{x}_{v,m}^H \mathbf{A}_{l,p} \mathbf{x}_{v,m'}|^2 \tag{7.57}$$

where $\mathbf{A}_{l,p} \triangleq \text{Diag}\left(\mathbf{f}_p\right) \mathbf{C}_l$ for $l \in \{-N+1, \cdots, N-1\}$ and $p \in \{-P, \cdots, P\}$. Secondly, the PCAF for the codes emitted by all other vehicles is given as,

$$\bar{Q}_o = \sum_{l,p} \sum_{v \neq v'}^{V} \sum_{m=1}^{M_v} \sum_{m'=1}^{M_{v'}} |\mathbf{x}_{v,m}^H \mathbf{A}_{l,p} \mathbf{x}_{v',m'}|^2. \tag{7.58}$$

Combining Equation 7.57 and Equation 7.58, the total PCAF to be minimized can be obtained as,

$$\bar{Q} = \bar{Q}_i + \bar{Q}_o = \sum_{l,p} \sum_{v,v'}^{V} \sum_{m=1}^{M_v} \sum_{m'=1}^{M_{v'}} |\mathbf{x}_{v,m}^H \mathbf{A}_{l,p} \mathbf{x}_{v',m'}|^2. \tag{7.59}$$

Algorithm 9 Automotive Radar Waveform Design Algorithm for Interference Mitigation (*MIMO Case*)

Initialize: $\{\mathbf{x}_m^{(0)}\}$, $\{\mathbf{y}_k^{(0)}\}$, $\{\mathbf{u}_{l,p,m}^{r(0)}\}$, $\{\mathbf{u}_{l,p,m}^{i(0)}\}$, $\{\mathbf{v}_{l,p,k}^{r(0)}\}$, $\{\mathbf{v}_{l,p,k}^{i(0)}\}$, for $m \in \{1,\cdots,M\}, k \in \{1,\cdots,K\}, l \in \{-(N-1),\cdots,N-1\}, p \in \{-P,\cdots,P\}$, $s=0$

Output: $\{\mathbf{x}_m^\star\}_{m=1}^M, \{\mathbf{y}_k^\star\}_{k=1}^K$

repeat
  $s \leftarrow s+1$
  Calculate $\tilde{\mathbf{A}}_{l,p}^{r(s)}, \tilde{\mathbf{A}}_{l,p}^{i(s)}$ for all l,p following Equation 7.29, Equation 7.31, and Equation 7.36
  Calculate $\zeta^{(s)}$ using Equation 7.37
  ▷ `Update of` $\{\mathbf{x}_m^{(s)}\}_{m=1}^M$:
  for $m=1$ **to** M **do**
    Calculate $\mathbf{R}_{\mathbf{x}_m}^{(s)}, \mathbf{s}_{\mathbf{x}_m}^{(s)}$ using Equation 7.43 and Equation 7.44
    Calculate $\bar{\mathbf{x}}_m^{(s)}, \mathbf{B}_{\mathbf{x}_m}^{(s)}$ using Equation 7.45a and Equation 7.45b
    Calculate $\mathbf{D}_{\mathbf{x}_m}^{(s)}$ using Equation 7.48
    $t=0$, $\mathbf{x}_m^{(s,t)} = \mathbf{x}_m^{(s-1)}$
    repeat
      Calculate $\mathbf{x}_m^{(s,t)}$ using Equation 7.49
      $t \leftarrow t+1$
    until convergence
    $\mathbf{x}_m^{(s)} = \mathbf{x}_m^{(s,t)}$
  end for
  ▷ `Update of` $\{\mathbf{y}_k^{(s)}\}_{k=1}^K$:
  for $k=1$ **to** K **do**
    Calculate $\mathbf{R}_{\mathbf{y}_k}^{(s)}, \mathbf{s}_{\mathbf{y}_k}^{(s)}$ using Equation 7.51 and Equation 7.52
    Calculate $\bar{\mathbf{y}}_k^{(s)}, \mathbf{B}_{\mathbf{y}_k}^{(s)}$ using Equation 7.55a and Equation 7.55b
    Calculate $\mathbf{D}_{\mathbf{y}_k}^{(s)}$ using Equation 7.54
    $t=0$, $\mathbf{y}_k^{(s,t)} = \mathbf{y}_k^{(s-1)}$
    repeat
      Calculate $\mathbf{y}_k^{(s,t)}$ using Equation 7.53
      $t \leftarrow t+1$
    until convergence
    $\mathbf{y}_k^{(s)} = \mathbf{y}_k^{(s,t)}$
  end for
  ▷ `Update of` $\{\mathbf{u}_{l,p,m}^{c(s)}\}$ `and` $\{\mathbf{v}_{l,p,k}^{c(s)}\}$ `for all` $c \in \{r,i\}$:
  Calculate $\mathbf{u}_{l,p,m}^{r(s)}, \mathbf{u}_{l,p,m}^{i(s)}, \mathbf{v}_{l,p,k}^{r(s)}, \mathbf{v}_{l,p,k}^{i(s)}$ for each $m \in \{1,\cdots,M\}, k \in \{1,\cdots,K\}, l \in \{-(N-1),\cdots,N-1\}, p \in \{-P,\cdots,P\}$ using Equation 7.56
until a pre-defined stop criterion is satisfied, *e.g.*, $|\bar{J}^{(s)} - \bar{J}^{(s-1)}| \leq \epsilon$, for some $\epsilon > 0$ where $\bar{J}$ denotes the objective function of the problem Equation 7.40
$\{\mathbf{x}_m^\star\}_{m=1}^M = \{\mathbf{x}_m^{(s)}\}_{m=1}^M, \{\mathbf{y}_k^\star\}_{k=1}^K = \{\mathbf{y}_k^{(s)}\}_{k=1}^K$

By stacking the corresponding radar codes in matrix form and rewriting the above objective, we arrive at the criterion:

$$\mathcal{Q}_{multi-mimo}(\mathbf{X}_1, \cdots, \mathbf{X}_V) = \sum_{l} \sum_{p} \sum_{v,v'}^{V} \|\mathbf{X}_v^H \mathbf{A}_{l,p} \mathbf{X}_{v'}\|_F^2 \tag{7.60}$$

where $\{\mathbf{X}_v\}_{v=1}^{V}$ are radar code matrices, each containing the radar codes $\{\mathbf{x}_{v,m}\}_{m=1}^{M_v}$ in its columns. As we have seen earlier in Equation 7.30, the objective in Equation 7.60 is *quartic* in radar codes $\{\mathbf{X}_v\}_{v=1}^{V}$. Not only that, but tackling Equation 7.60 is difficult also since the number of PCAF values to be suppressed grows more quickly in terms of the problem dimension than the number of design variables.

In the following, we formulate a quadratic alternative to Equation 7.59 following the path shown in Section 7.4. One can partition Equation 7.59 in the following manner:

$$\begin{aligned}\bar{Q} = &\sum_{l,p} \sum_{v=1}^{V} \sum_{m=1}^{M_v} |\mathbf{x}_{v,m}^H \mathbf{A}_{l,p} \mathbf{x}_{v,m}|^2 + \sum_{l,p} \sum_{v=1}^{V} \sum_{m \neq m'}^{M_v} |\mathbf{x}_{v,m}^H \mathbf{A}_{l,p} \mathbf{x}_{v,m'}|^2 \\ &+ \sum_{l,p} \sum_{v \neq v'}^{V} \sum_{m=1}^{M_v} \sum_{m'=1}^{M_{v'}} |\mathbf{x}_{v,m}^H \mathbf{A}_{l,p} \mathbf{x}_{v',m'}|^2. \end{aligned} \tag{7.61}$$

Following a similar argument to tackle the quartic nature of the self-interference terms $\{\mathbf{x}_{v,m}^H \mathbf{A}_{l,p} \mathbf{x}_{v,m}\}$, for all $v \in \{1, \cdots, V\}$ and $m \in \{1, \cdots, M_v\}$, one can derive a quadratic version of Equation 7.61. The final optimization problem can thus be reformulated as,

$$\min \quad \sum_{l,p} \sum_{v=1}^{V} \sum_{m \neq m'}^{M_v} |\mathbf{x}_{v,m}^H \mathbf{A}_{l,p} \mathbf{x}_{v,m'}|^2 + \sum_{l,p} \sum_{v \neq v'}^{V} \sum_{m=1}^{M_v} \sum_{m'=1}^{M_{v'}} |\mathbf{x}_{v,m}^H \mathbf{A}_{l,p} \mathbf{x}_{v',m'}|^2 + \sum_{l,p} \sum_{c \in \{r,i\}} \sum_{v=1}^{V} \sum_{m=1}^{Mv} \left\| (\tilde{\mathbf{A}}_{l,p}^c)^{1/2} \mathbf{x}_{v,m} - \sqrt{\zeta N} \mathbf{u}_{v,m,l,p}^c \right\|_2^2 \tag{7.62a}$$

$$\text{s.t.} \quad \mathbf{x}_{v,m} \text{ are unimodular } \forall\ v \in \{1, \cdots, V\} \text{ and}, m \in \{1, \cdots, M_v\}, \tag{7.62b}$$

$$\|\mathbf{u}_{v,m,l,p}^c\|_2 = 1\ \forall\ c \in \{r, i\}; v \in \{1, \cdots, V\}; m \in \{1, \cdots, M_v\};$$

$$l \in \{-N+1, \cdots, N-1\} \text{ and } p \in \{-P, \cdots, P\}. \tag{7.62c}$$

Note that given the knowledge of the number of vehicles on the scene and the number of their corresponding MIMO antennas, Equation 7.62 can be solved in an online manner. However, to enhance situational preparedness and further decrease the communication overhead, the codes can also be pre-designed offline and stored in a database for future use. Upon arriving into such a situation, the vehicles just need to access their copy or download the codes from the said dataset before transmission. To efficiently solve Equation 7.62, we follow a similar iterative optimization framework as described in subsection 7.4.2.

7.5.1 Design of Optimized Waveforms

In s^{th} iteration, we separate each variable $\{\mathbf{x}_{v,m}\}$, $\{\mathbf{u}^r_{v,m,l,p}\}$, $\{\mathbf{u}^i_{v,m,l,p}\}$, and optimize Equation 7.62 individually *w.r.t.* that variable, while fixing all other variables to their current values. This will lead to a monotonically decreasing collective PCAF until convergence is achieved.

7.5.1.1 Optimization *w.r.t.* $\{\mathbf{x}_{v,m}\}_{v=1,m=1}^{V,\ M_v}$

We begin by reformulating the optimization problem in Equation 7.62 *w.r.t.* each of $\mathbf{x}_{v,m}$ for all v, m. The objective function in Equation 7.62 then becomes,

$$\begin{aligned}\bar{Q}_{v,m} = \mathbf{x}_{v,m}^H \left(\sum_{l,p} \sum_{m \neq m'}^{M_v} \mathbf{A}_{l,p} \mathbf{x}_{v,m'} \mathbf{x}_{v,m'}^H \mathbf{A}_{l,p}^H \right) \mathbf{x}_{v,m} + \mathbf{x}_{v,m}^H \left(\sum_{l,p} \sum_{v' \neq v}^{V} \sum_{m=1}^{M_v} \sum_{m'=1}^{M_{v'}} \mathbf{A}_{l,p} \mathbf{x}_{v',m'} \mathbf{x}_{v',m'}^H \mathbf{A}_{l,p}^H \right) \mathbf{x}_{v,m} \\ + \mathbf{x}_{v,m}^H \left(\sum_{l,p} \sum_{c \in \{r,i\}} \tilde{\mathbf{A}}_{l,p}^c \right) \mathbf{x}_{v,m} - 2\sqrt{\zeta N} \Re \left\{ \mathbf{x}_{v,m}^H \sum_{l,p} \sum_{c \in \{r,i\}} \sum_{m=1}^{M_v} (\tilde{\mathbf{A}}_{l,p}^c)^{H/2} \mathbf{u}_{v,m,l,p}^c \right\} + \text{const.}\end{aligned} \tag{7.63}$$

or simply,

$$\bar{Q}_{v,m} = \mathbf{x}_{v,m}^H \mathbf{R}_{v,m} \mathbf{x}_{v,m} + 2\Re\{\mathbf{x}_{v,m}^H \mathbf{s}_{v,m}\} + \text{const.} \tag{7.64}$$

where

$$\mathbf{R}_{v,m} = \sum_{l,p} \sum_{m \neq m'}^{M_v} \mathbf{A}_{l,p} \mathbf{x}_{v,m'} \mathbf{x}_{v,m'}^H \mathbf{A}_{l,p}^H + \sum_{l,p} \sum_{c \in \{r,i\}} \tilde{\mathbf{A}}_{l,p}^c + \sum_{l,p} \sum_{v' \neq v}^{V} \sum_{m=1}^{M_v} \sum_{m'=1}^{M_{v'}} \mathbf{A}_{l,p} \mathbf{x}_{v',m'} \mathbf{x}_{v',m'}^H \mathbf{A}_{l,p}^H \tag{7.65}$$

and

$$\mathbf{s}_{v,m} = -\sqrt{\zeta N}\sum_{l,p}\sum_{c\in\{r,i\}}\sum_{m=1}^{M_v}(\tilde{\mathbf{A}}_{l,p}^{c})^{H/2}\mathbf{u}_{v,m,l,p}^{c}. \tag{7.66}$$

As a result, one can formulate a UQP for each $\mathbf{x}_{v,m}$ in a similar fashion as described in subsection 7.4.2.1. The corresponding solution can be approached iteratively using PMLI of the form

$$\widehat{\mathbf{x}}_{v,m}^{(s,t)} = \exp\left\{ j\arg\left(\begin{bmatrix} \mathbf{I}_{N\times N} \\ \mathbf{0}_{1\times N} \end{bmatrix}^{T} \mathbf{D}_{v,m}\bar{\mathbf{x}}_{v,m}^{(s,t-1)} \right) \right\} \tag{7.67}$$

where $\mathbf{D}_{v,m} \triangleq \gamma_{v,m}\mathbf{I}_{(N+1)} - \mathbf{B}_{v,m}$, with $\gamma_{v,m}$ being larger than the maximum eigenvalue of $\mathbf{B}_{v,m}$ and

$$\bar{\mathbf{x}}_{v,m} \triangleq [\mathbf{x}_{v,m}\ 1]^{T}, \tag{7.68a}$$

$$\mathbf{B}_{v,m} \triangleq \begin{bmatrix} \mathbf{R}_{v,m} & \mathbf{s}_{v,m} \\ \mathbf{s}_{v,m}^{H} & 0 \end{bmatrix}. \tag{7.68b}$$

Note that the iterations can be initialized with the latest design of $\mathbf{x}_{v,m}$ (used as $\mathbf{x}_{v,m}^{(0)}$).

7.5.1.2 Optimization *w.r.t.* $\{\mathbf{u}^c_{v,m,l,p}\}$

Next, solving Equation 7.62 *w.r.t.* $\{\mathbf{u}^c_{v,m,l,p}\}$ for $c \in \{r, i\}$ is immediate and resolves into the closed-form solution:

$$\widehat{\mathbf{u}}^c_{v,m,l,p} = \frac{(\tilde{\mathbf{A}}^c_{l,p})^{1/2}\mathbf{x}_{v,m}}{\|(\tilde{\mathbf{A}}^c_{l,p})^{1/2}\mathbf{x}_{v,m}\|_2} \tag{7.69}$$

for all c, v, m, l, p. Notice that Equation 7.69 can be done in parallel making the design process more agile.

In the next section, we numerically examine the efficiency and applicability of all the above-mentioned proposed algorithms.

7.6 Numerical Simulations

In the following, we begin with demonstrating the effectiveness of the two coding schemes described in Section 7.3 for the SISO scenario using several examples. We then provide similar numerical analysis for the MIMO case detailed in Section 7.4 and further for the connected MIMO scenario detailed in Section 7.5.

7.6.1 The SISO Scenario

Consider two identical FMCW radar systems with the same carrier frequency of $f_c = 24$ GHz. The bandwidth of the chirp signal is $B = 150$ MHz. The sweep time is $T_c = 50$ μs. The number of periods within a CPI is $N = 256$.

Figure 35(a) and Figure 35(b) show the discrete periodic cross-ambiguity functions associated with the Doppler-shifting, and the optimized codes, respectively, where $P = 200$ and $N_f = 512$

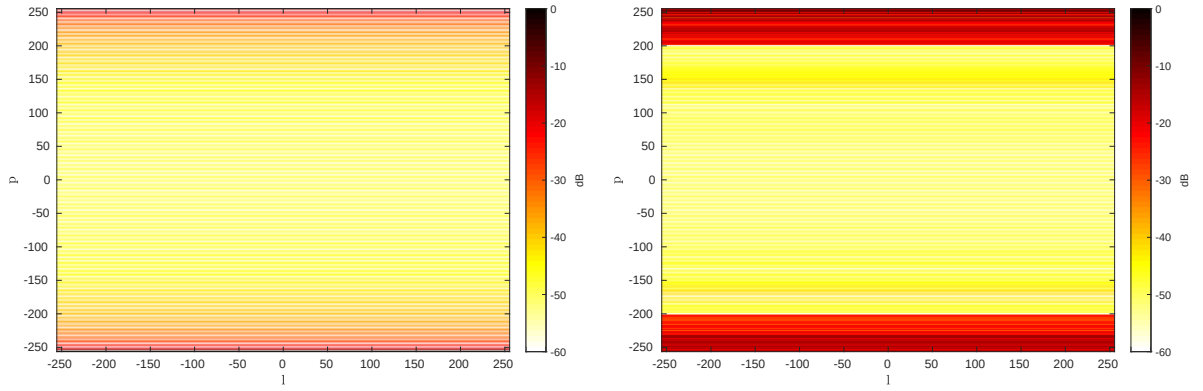

(a) (b)

Figure 35. Discrete periodic cross-ambiguity functions (SISO case): (a) Doppler-shift coding and (b) the optimized coding scheme for $N = 256$, $P = 200$ and $N_f = 512$.

(which implies that the maximum Doppler frequency of interest should be lower than 3906.25 Hz, corresponding to a maximum relative radial velocity of 87.9 km/h), and we initialize our algorithm with normally distributed randomly generated codes (for $\mathbf{x}$ and $\mathbf{y}$, respectively,) in the optimized coding scheme.

Figure 36 compares their discrete periodic cross-ambiguity functions at the zero-delay cut. One can observe that both coding schemes achieve very low sidelobes in the desired area. Moreover, although the optimized scheme achieves lower sidelobes in the desired area, the sidelobe increases in the regions outside the desired area. However, for the Doppler shift coding, the sidelobes are spread evenly throughout the entire region. Therefore, they can be used to effectively suppress the interference. Further note that the peak sidelobe (PSL) corresponding to the optimized codes is approximately 3.55 dB lower than that of the Doppler-shifting, within the

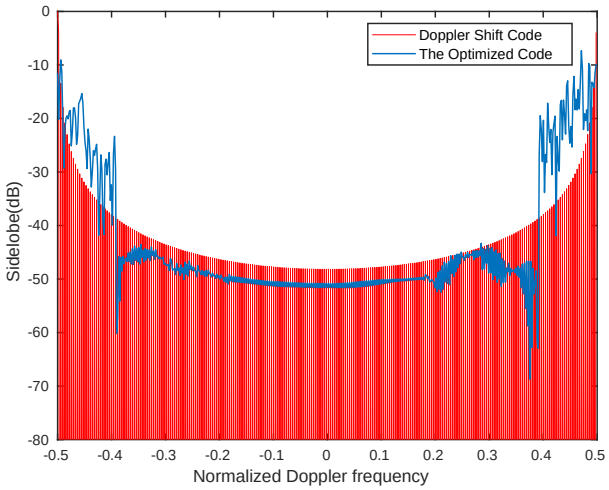

Figure 36. Comparison of the discrete periodic cross-ambiguity functions of the optimized code and that of the Doppler-shift code at the zero-delay cut for $N = 256$, $P = 200$ and $N_f = 512$. Although the optimized scheme achieves lower sidelobes in the desired area, the sidelobe increases in the regions outside the desired area.

desired range of Doppler frequency of interest. Interestingly, if we fix $\mathbf{y} = \mathbf{1}_N$ and only optimize $\mathbf{x}$, we obtain similar results, which corresponds to a more practical coding method, since no coordination between the two radar systems is needed.

Next, we apply these coding schemes to mitigate the mutual interference for two identical automotive radar systems operating in a typical scenario: The range of target and interference are at 50 m and 70 m, respectively. The speeds associated with them are 10.12 m/s and 23.45 m/s. The SNRs are 30 dB and 60 dB, respectively. The sampling frequency is $f_s = 4$ MHz. $M = 100$ samples are collected for each period. Figure 37 shows the range-Doppler image in this scenario without slow-time coding, using Doppler-shifting code, and the optimized coding scheme, respectively. We can observe that the power of the interference is much stronger than

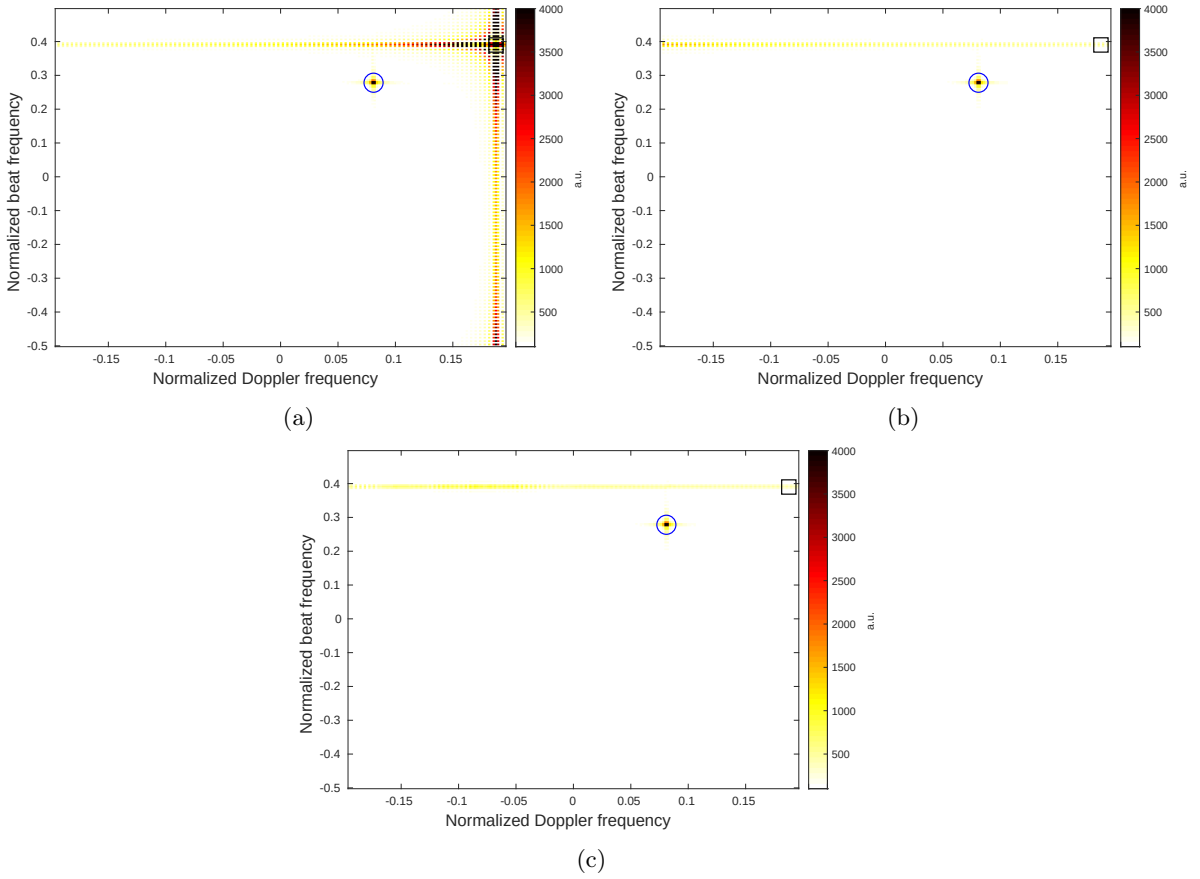

Figure 37. The range-Doppler image for the SISO case: (a) randomly generated code without slow-time coding, (b) Doppler-shift coding, and (c) the optimized coding scheme: ◯ represents the target and □ represents the interference.

that of the target such that a false alarm happens. When our slow-time coding schemes are applied, the interference power level is significantly reduced and the target can be easily detected without suffering from false alarm problems.

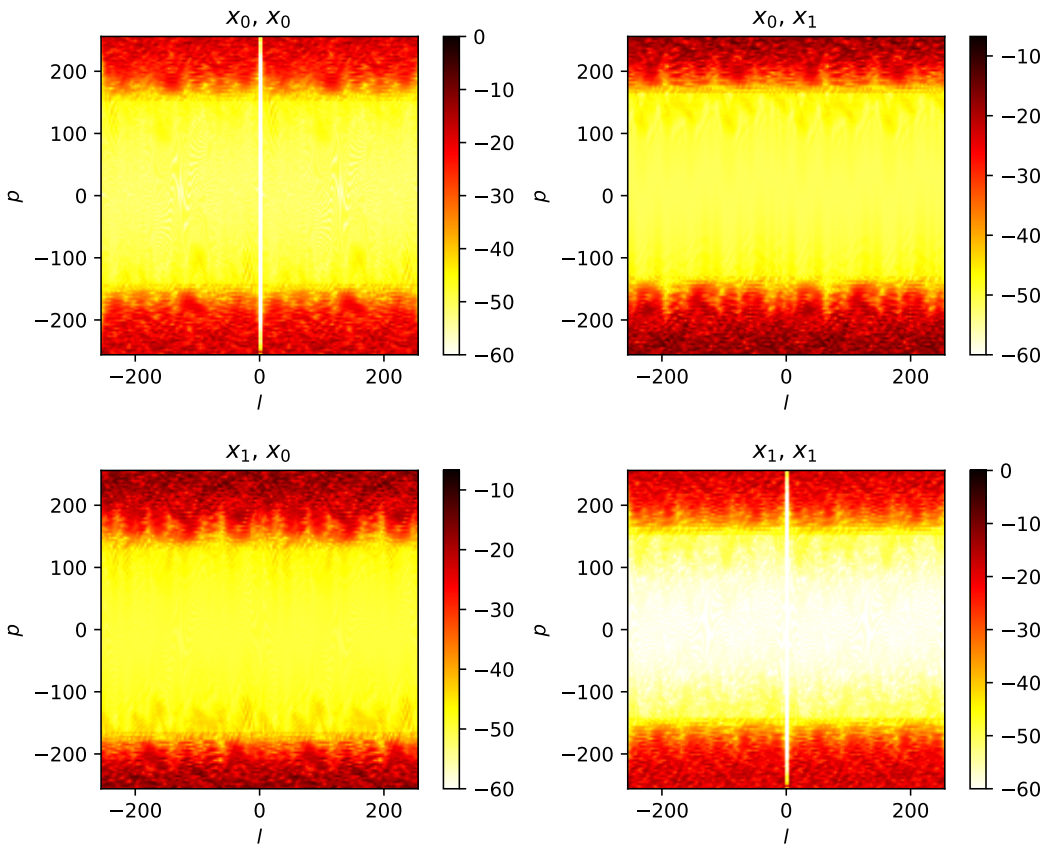

Figure 38. Discrete periodic (cross) ambiguity functions between different MIMO sequences from the set $\mathcal{X} = \{\mathbf{x}_m\}_{m=1}^{2}$ for $N = 256$, $P = 200$ and $N_f = 512$. Note that for identical sequences, the ambiguity function always assumes larger values near zero.

7.6.2 The MIMO Scenario

In order to examine the effectiveness of Algorithm 9 in the MIMO case, we use a similar set of FMCW parameters as in the SISO case. For the ease of display and sake of simplicity, we consider two similar MIMO FMCW radar systems that use set of codes $\mathcal{X} = \{\mathbf{x}_m\}_{m=1}^{2}$ and

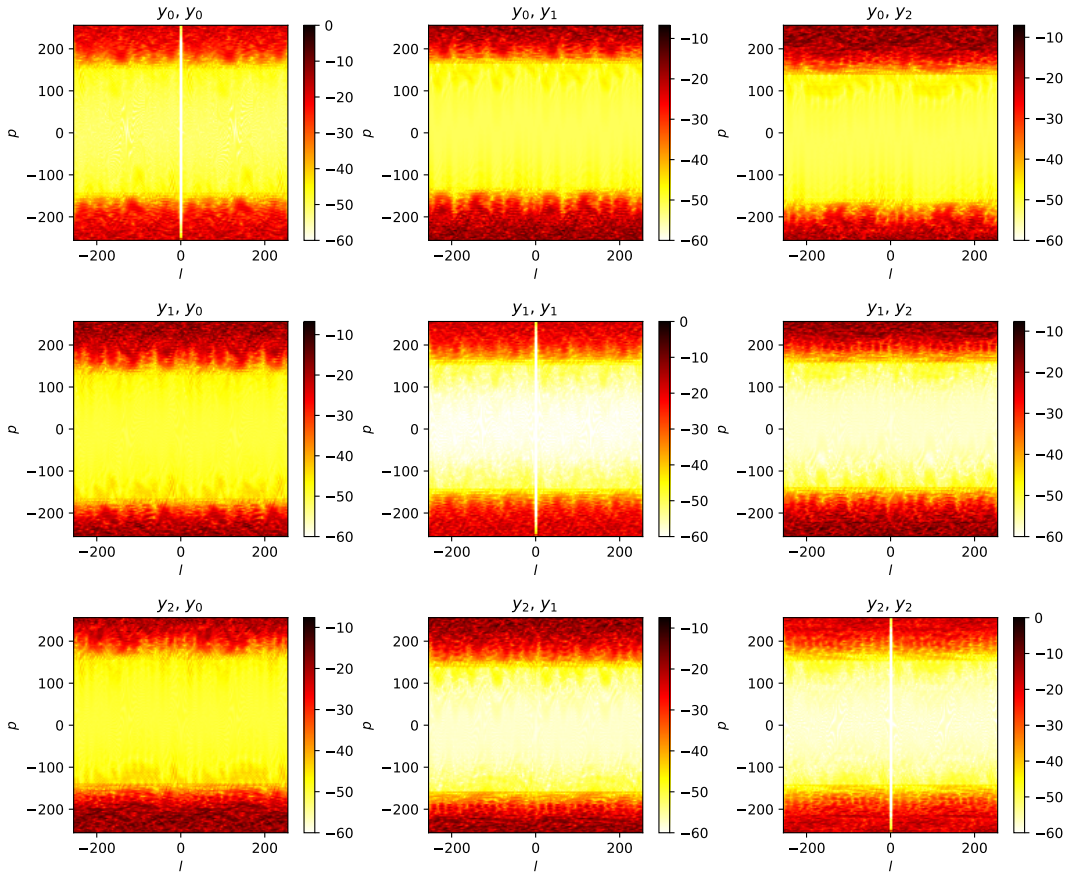

Figure 39. Discrete periodic (cross) ambiguity functions among different MIMO sequences from the set $\mathcal{Y} = \{\mathbf{y}_k\}_{k=1}^{3}$ for $N = 256$, $P = 200$ and $N_f = 512$.

$\mathcal{Y} = \{\mathbf{y}_k\}_{k=1}^{3}$ each of length $N = 256$, operating under the same carrier frequency of $f_c = 24$ GHz, the bandwidth of the chirp signal of $B = 150$ MHz, and the sweep time of $T_c = 50$ μs. As mentioned earlier, we first initialize the algorithm with normally distributed random numbers for all optimization variables: $\{\mathbf{x}_m\}$, $\{\mathbf{y}_k\}$ $\{\mathbf{u}_{l,p,m}^{c}\}$, $\{\mathbf{v}_{l,p,k}^{c}\}$, for $c \in \{r, i\}$. After running the algorithm once, we use the output codes $\{\mathbf{x}_m\}$, $\{\mathbf{y}_k\}$ as the initial codes for the next run but

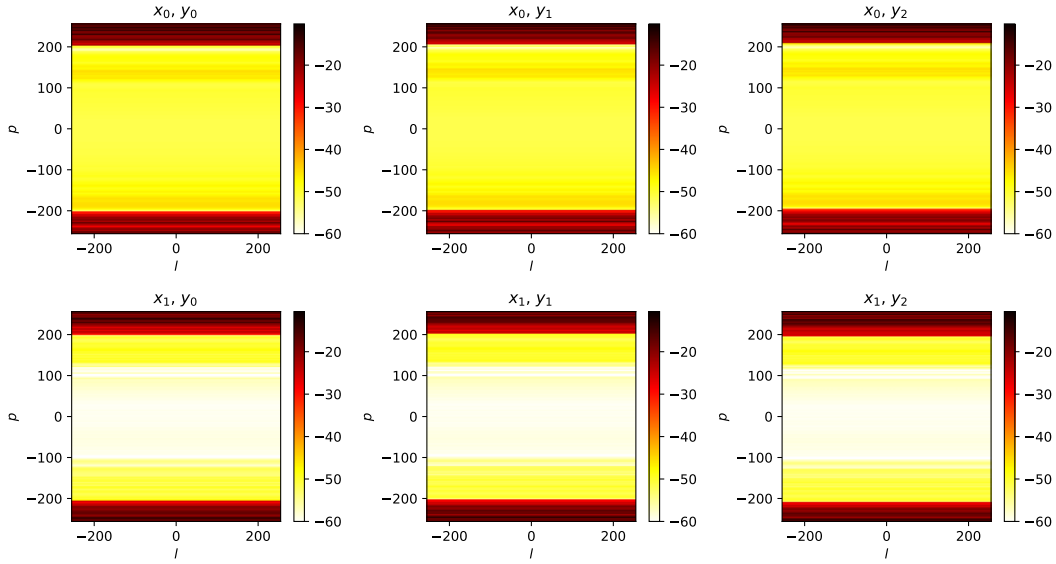

Figure 40. Discrete periodic cross-ambiguity functions between different MIMO sequences from the sets $\mathcal{X} = \{\mathbf{x}_m\}_{m=1}^{2}$ and $\mathcal{Y} = \{\mathbf{y}_k\}_{k=1}^{3}$ for $N = 256$, $P = 200$ and $N_f = 512$.

we still use random initialization for other variables, $\{\mathbf{u}_{l,p,m}^{c}\}$, $\{\mathbf{v}_{l,p,k}^{c}\}$, and repeat the process multiple times.

Figure 38-Figure 40 show the periodic (cross) ambiguity functions for the radar systems: $\{\mathcal{X}\}, \{\mathcal{Y}\}$, and $\{\mathcal{X}, \mathcal{Y}\}$ where $P = 200$ and $N_f = 512$. It is evident from each of these figures that for each set of sequences, the unambiguous regions are well separated (within the range of -40dB to -60dB), and hence, these sequences can be reliably used in MIMO FMCW radar systems that require mutual interference mitigation.

In the next example for the MIMO case, we apply the optimized coding scheme to mitigate the mutual interference in the presence of multiple targets. For this scenario, we use three targets

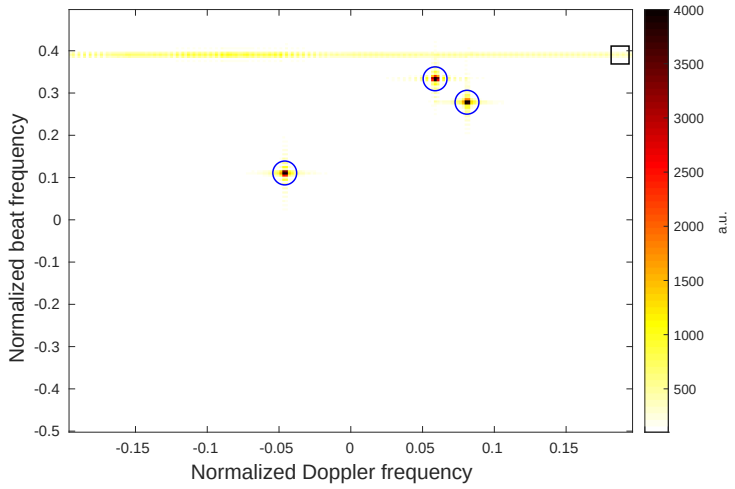

Figure 41. The range-Doppler image for the MIMO optimized coding scheme: ◯ represents the targets and □ represents the interference.

and one interfering radar system. The ranges of the targets and interference are at $50, 20, 60$ m, and 70 m, respectively. The speeds associated with them are $10.12, -5.75, 7.34$, m/s and 23.45 m/s. The SNRs are 30 dB and 60 dB for the targets and interference, respectively. The sampling frequency is similarly $f_s = 4$ MHz as assumed in the SISO case. Figure 41 shows the range-Doppler image for the optimized coding scheme. It is clear from the figure that the interference power level is significantly reduced and all three of the targets are easily detected without suffering from false alarm issues.

7.6.3 The Multiple-MIMO Scenario

For this case, we reuse the same experimental test scenario described in previous examples. In the first experiment, we consider $V = 5$ cars equipped with similar MIMO radar system, each capable of transmitting $M_v = 4$ unimodular codes for all $v \in \{1, \cdots, 5\}$. We apply the

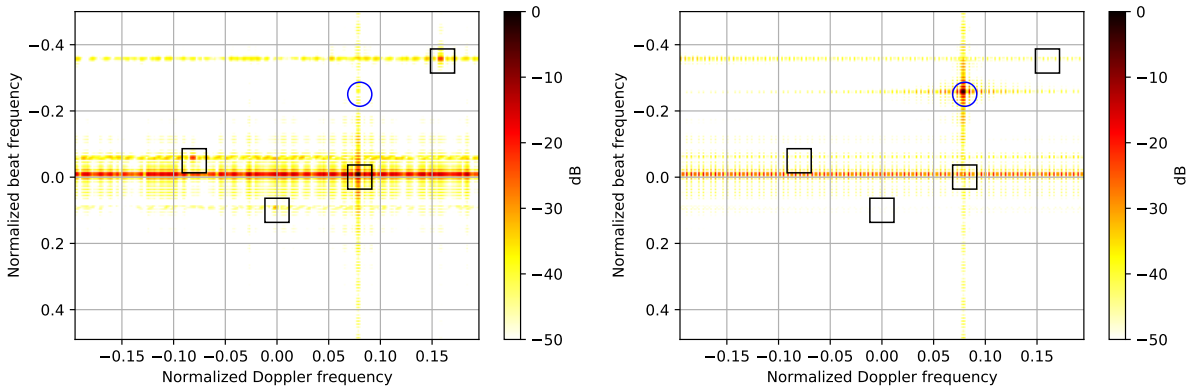

Figure 42. The range-Doppler image for the multiple-MIMO case: (a) with random coding (b) with the optimized coding scheme used in the first car. The blue circle is the target and black squares are the interferences.

optimized coding schemes to mitigate the mutual interference for these five identical automotive radar systems operating in a typical scenario: the first car is considered to be the actual target and the rest are interfering targets. The range of target and interferences are at 50 m and $\{70, 10, -20, 0\}$ m, respectively. The speeds associated with them are 10 m/s and $\{20, -10, 0, 10\}$ m/s, respectively. Furthermore, the corresponding signal-to-noise ratios (SNR) are 30 dB and $\{40, 40, 30, 60\}$ dB, respectively. One can observe that the powers of the interference are much stronger than that of the target, which will again lead to a false alarm. The sampling frequency is $f_s = 4$ MHz and $M = 100$ samples are collected for each period. Figure 42(a) shows the range-Doppler image of the scenario when random coding is used. For the sake of simplicity in Figure 42(b), we only show the range-Doppler image for the optimized code used in the first car.

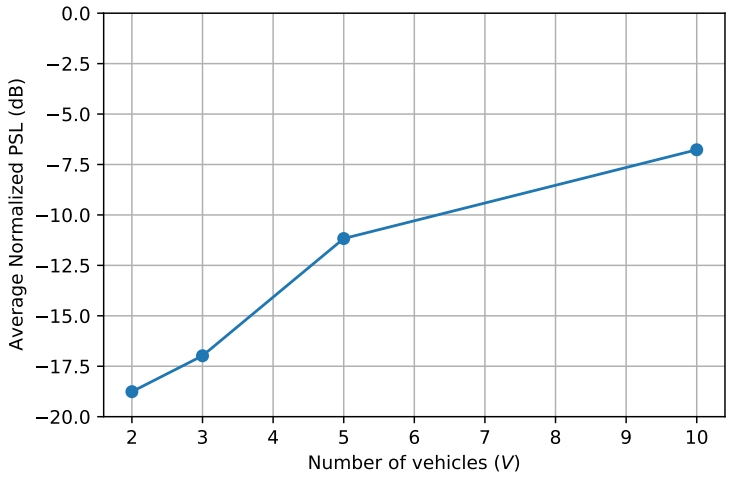

Figure 43. Results of Monte Carlo simulation ($n = 50$) showing average normalized peak sidelobe level height vs. number of vehicles (V).

It can be easily seen from Figure 42 that the interference power level is significantly reduced (> -20 dB) and the target can be easily detected without suffering from false alarm issues.

In the next experiment, we perform a Monte Carlo simulation of designing codes for $V = \{2, 3, 5, 10\}$ vehicles in order to show the average performance of the algorithm. In particular, we simulate $n = 50$ experiments for each of V having $M = 5$ MIMO antennas and report the average normalized peak sidelobe level (PSL) of the PCAF as depicted in Figure 43. It is evident that as the number of vehicles grows large, it becomes more difficult to find codes with good interference mitigation capabilities, while the performance is satisfactory for a moderate number of vehicles.

7.7 Concluding Remarks

In this chapter, we discussed the problem of mutual interference mitigation in identical or similar radar systems employed in automotive applications. We proposed two slow-time coding schemes for the SISO case. Specifically, the first coding scheme is designed through Doppler shifting and the second one is devised based on an efficient cyclic optimization approach. We further extended the problem formulation and proposed another efficient algorithm to generate the radar codes in the more general MIMO scenario. We then provided a general formulation for the multiple-MIMO case and derived a generalized solution that can be used in MIMO antennas mounted on multiple connected vehicles. We showed that these coding schemes can be used to reduce the interference power level significantly.

II-C

Receive Filter Design for One-Bit Cognitive Radar

CHAPTER 8

WAVEFORM DESIGN FOR ONE-BIT RADAR SYSTEMS UNDER UNCERTAIN INTERFERENCE STATISTICS

Overview: An important problem in cognitive radar is to enhance the estimation performance of the system by a joint design of its probing signal and receive filter using the *a priori* information on interference. In such cases, the knowledge of interference statistics (particularly the covariance) plays a vital role in the effective design of the radar waveforms. In most practical scenarios, however, the received signal and interference statistics are available subject to some uncertainty. An extreme manifestation of this practical observation occurs for radars employing one-bit receivers, where only a normalized version of the interference covariance matrix can be obtained. In this chapter, we formulate a waveform optimization problem and devise an algorithm to design the transmit waveform and the receive filter of one-bit radars given such uncertainties in acquired interference statistics.

8.1 Introduction and Prior Works

In cognitive active sensing applications, one of the objectives is to jointly optimize the transmit sequence, as well as the receive filter as a smart listener using *a priori* knowledge of *interference* and *clutter* in order to increase the estimation accuracy of the target parameters [74–76]. Clutter refers to the unwanted echoes that are usually correlated with the transmitted waveform, while the signal independent noise as well as (adverse) jamming signals are termed

---

as interference [75]. A natural way to minimize the effects of clutter and interference is to maximize the signal-to-clutter-plus-interference ratio (SCIR) of the receiver output. It is well known that a matched filter (MF) has the ability to maximize the signal-to-noise (SNR) in the presence of uncorrelated additive white noise. It, however, fails to perform well in the case of clutter or jamming suppression. As an alternative, one can use a *mismatched* filter (MMF) at the receiver by trading off SNR for SCIR [75]. In comparison to MF, an MMF allows more degrees of freedom by introducing a receive filter and is not subject to various power constraints of the transmit waveforms such as constant-modulus (a.k.a. unimodular sequences) or low peak-to-average ratio (PAR) constraint. Thus, a joint design of the transmit waveform and the MMF receive filter can offer a more efficient parameter estimation framework [210].

In [74], the authors presented a joint design scheme of the receive filter and transmit waveform by minimizing the MSE of the estimate of the target's scattering coefficient in the presence of interference and clutter subject to some practical constraints such as constant-modulus or low PAR constraint on the transmit signal. To this end, they presented three flavors of their algorithm: Cognitive REceiver and Waveform design (CREW); namely, CREW (gra), CREW (fre), and CREW (mat). Another variation of CREW; namely, CREW (cyclic) can be found in [76], where the authors formulated a cyclic approach to jointly design the transmit waveform and receive filter coefficients. Note that in all the aforementioned techniques, the receiver is assumed to have high precision analog-to-digital converters (ADC). Note that, in classical radar signal processing, the quantization noise is usually modeled under the assumption of additive noise that minimally affects the accuracy of algorithms that consider the infinite or

very high precision case, especially when the sampling interval is low [68] The assumption of high-precision data is, however, inappropriate when the measurements are extremely quantized to very low bit-rates. In the most extreme case, the sampling process is done by utilizing a simple sign comparator and the received signal is represented using only one bit per sample [68, 81]. One-bit quantizers, on one hand, are not only low SWaP-C devices but also much faster and simpler than the traditional digital quantizers, thus significantly reducing the complexity of hardware implementation. On the other hand, it is now well known that signals can be recovered with high accuracy from one-bit measurements, at a slightly increased computational cost [70]. This increased cost incurs from the fact that by using a one-bit receiver, the knowledge of interference statistics is available in only a *normalized* sense and such uncertainties prohibit one from using traditional algorithms. In the subsequent, we propose a specialized variation of CREW (cyclic) [76] to tackle the problem of jointly designing the probing signals and the receive filter coefficients in the presence of uncertainty in interference statistics.

The rest of this chapter goes as follows. In Section 8.2, we provide a description of the signal model and formulate the aforementioned problem. Section 8.3 presents the optimization scheme in order to jointly design the waveform and receive filter for the one-bit receiver. Numerical simulations are presented in Section 8.4. Ultimately, Section 8.5 summarizes the chapter.

8.2 Signal Model and Problem Formulation

Let $\boldsymbol{s} = [s_1\ s_2\ \cdots s_N]^T \in \mathbb{C}^N$ denote the transmitted waveform that is to be used to modulate the train of subpulses. We closely follow the discrete data model adopted in [74] in order to layout the problem formulation. Under the assumptions of negligible intrapulse Doppler shift,

and that the sampling is synchronized to the pulse rate, the received discrete-time baseband signal after pulse compression and alignment with the current range cell of interest, satisfies

$$\boldsymbol{y} = \boldsymbol{A}^H \boldsymbol{\alpha} + \boldsymbol{\epsilon}, \tag{8.1}$$

where

$$\boldsymbol{A}^H = \begin{bmatrix} s_1 & 0 & \cdots & 0 & s_N & s_{N-1} & \cdots & s_2 \\ s_2 & s_1 & & \vdots & 0 & s_N & & \vdots \\ \vdots & \vdots & \ddots & 0 & \vdots & \vdots & \ddots & s_N \\ s_N & s_{N-1} & \cdots & s_1 & 0 & 0 & \cdots & 0 \end{bmatrix}, \tag{8.2a}$$

$$\boldsymbol{\alpha} = [\alpha_0 \ \alpha_1 \ \cdots \ \alpha_{N-1} \ \alpha_{-N+1} \ \cdots \ \alpha_{-1}]^T \in \mathbb{C}^{2N-1}, \tag{8.2b}$$

where the parameter α_0 is the complex-valued scattering coefficient of the range cell of interest, while $\{\alpha_k\}_{k\neq 0}$ are that of the other adjacent range cells contributing to the clutter. Furthermore, $\boldsymbol{\epsilon}$ is the signal independent interference comprising of measurement noise as well as other disturbances such as jamming. In addition, we assume that $\boldsymbol{\Gamma} \triangleq \mathbb{E}\left\{\boldsymbol{\epsilon}\boldsymbol{\epsilon}^H\right\}$, and $\beta \triangleq \mathbb{E}\left\{|\alpha_k|^2\right\}$ for $k \neq 0$, and that $\boldsymbol{\epsilon}$ and $\{\alpha_k\}$ are zero-mean i.i.d. The motivation is to estimate the parameter α_0 provided other information is available *a priori*. Note that in a traditional radar system, β and $\boldsymbol{\Gamma}$ can be obtained via some prescanning procedure [75].

For a known β and $\mathbf{\Gamma}$, the estimation of the scattering coefficient of the current range cell, α_0, can be efficiently achieved by using an MMF, and is given as [76],

$$\hat{\alpha_0} = \frac{\boldsymbol{w}^H \boldsymbol{y}}{\boldsymbol{w}^H \boldsymbol{s}},$$

where $\boldsymbol{w} \in \mathbb{C}^N$ is the MMF coefficient vector. Therefore, the MSE of estimation of α_0 can be derived as

$$\text{MSE}(\hat{\alpha_0}) = \mathbb{E}\left\{\left|\frac{\boldsymbol{w}^H \boldsymbol{y}}{\boldsymbol{w}^H \boldsymbol{s}} - \alpha_0\right|^2\right\} = \frac{\boldsymbol{w}^H \boldsymbol{R} \boldsymbol{w}}{|\boldsymbol{w}^H \boldsymbol{s}|^2}, \tag{8.3}$$

where

$$\boldsymbol{R} = \beta \sum_{\substack{k=-N+1 \\ k\neq 0}}^{N-1} \boldsymbol{J}_k \boldsymbol{s}\boldsymbol{s}^H \boldsymbol{J}_k^H + \mathbf{\Gamma}, \tag{8.4}$$

and $\{\boldsymbol{J}_k\}$ denote the shift matrices satisfying,

$$\boldsymbol{J}_k = \begin{bmatrix} 0 & \dots & 0 & 1 & \dots & 0 \\ \vdots & & & & \ddots & \\ & & & & & 1 \\ \underbrace{0 \quad \dots \quad 0}_{k} & \dots & & & & \end{bmatrix}^H_{N\times N} = \boldsymbol{J}_{-k}^H, \qquad \forall\ k = 0, 1, \cdots, N-1. \tag{8.5}$$

It is interesting to note that the numerator of the MSE in Equation 8.3 is the total power of the interferences while the denominator is the total power of the received signal. As a result, minimization of the criterion in Equation 8.3 leads to maximization of the SCIR.

8.2.1 One-bit Receiver

In the case of receivers with one-bit ADC, the quantizer is nothing but a simple sign comparator and each measurement is represented using only one bit, *i.e.*, $+1$ or -1, and thus, the auto-correlation of the received signal is only obtainable in a *normalized* sense, as described in the subsequent [68].

Let $X(t)$ denote a scalar, real-valued, and wide sense stationary Gaussian random process that undergoes a one-bit sampler $Y(t) = \text{sign}\left(X(t)\right)$. The auto-correlation function of the process $Y(t)$, denoted by $R_Y(\tau)$, can be given as

$$R_Y(\tau) = \mathbb{E}\{Y(t+\tau)Y(t)\} = \frac{2}{\pi}\sin^{-1}\left(\bar{R}_X(\tau)\right), \tag{8.6}$$

where $\bar{R}_X(\tau) = R_X(\tau)/R_X(0)$ denotes the normalized auto-correlation of $X(t)$ [211]. On the contrary, according to the Bussgang theorem [212], the cross-correlation of $X(t)$ and $Y(t)$, denoted as $R_{YX}(\tau)$ is proportional to the auto-correlation of $X(t)$, *i.e.*, $R_{YX}(\tau) = \zeta R_X(\tau)$, where value of the scaling factor ζ relies on the power of $X(t)$.

The case of complex-valued vector processes can be elaborated in a similar manner [213]. Let $\boldsymbol{\upsilon}$ be the one-bit sampled data obtained from $\boldsymbol{y}$ using complex one-bit ADCs at the receiver, given by

$$\boldsymbol{\upsilon} = \frac{1}{\sqrt{2}}\text{csign}\left(\boldsymbol{y}\right) \triangleq \frac{1}{\sqrt{2}}\left[\text{sign}\left(\Re(\boldsymbol{y})\right) + j\text{sign}\left(\Im(\boldsymbol{y})\right)\right]. \tag{8.7}$$

Let $\boldsymbol{R_y}$ and $\boldsymbol{R_\upsilon}$ denote the auto-correlations of the processes $\boldsymbol{y}$ and $\boldsymbol{\upsilon}$, respectively. In [213], it has been shown that these two quantities are similarly related using the following *arcsine* equality:

$$\boldsymbol{R_\upsilon} = \frac{2}{\pi}\sin^{-1}\left(\bar{\boldsymbol{R}}_{\boldsymbol{y}}\right), \tag{8.8}$$

where the normalized auto-correlation matrix of $\boldsymbol{y}$ is given as

$$\bar{\boldsymbol{R}}_{\boldsymbol{y}} \triangleq \boldsymbol{W}^{-\frac{1}{2}}\boldsymbol{R_y}\boldsymbol{W}^{-\frac{1}{2}}, \tag{8.9}$$

and $\boldsymbol{W} = \boldsymbol{R_y} \odot \boldsymbol{I}$.

In the light of above, it can be verified that in the scenario of having complex one-bit sampled data, the matrix $\boldsymbol{R}$ in Equation 8.3 is obtainable only in a *normalized* sense, *i.e.*, one only has access to

$$\bar{\boldsymbol{R}} = \boldsymbol{D}^{-\frac{1}{2}}\boldsymbol{R}\boldsymbol{D}^{-\frac{1}{2}}, \tag{8.10}$$

where $\boldsymbol{D} = \boldsymbol{R} \odot \boldsymbol{I}$. Then, the problem of interest is to design the transmit waveform $\boldsymbol{s}$ and the receive filter $\boldsymbol{w}$ given the normalized interference statistics $\bar{\boldsymbol{R}}$. In the following, we denote $\boldsymbol{d} = \text{diag}\left(\boldsymbol{D}^{\frac{1}{2}}\right)$.

In such a case, a meaningful approach to the aforementioned design problem is to consider:

$$\min_{\boldsymbol{w},\boldsymbol{s}} \qquad \mathbb{E}\left\{\frac{\boldsymbol{w}^H \boldsymbol{D}^{\frac{1}{2}} \bar{\boldsymbol{R}} \boldsymbol{D}^{\frac{1}{2}} \boldsymbol{w}}{|\boldsymbol{w}^H \boldsymbol{s}|^2}\right\}, \tag{8.11}$$

under some practical signal power constraint. Note that the expectation is taken over $\boldsymbol{D}$. The above problem is clearly non-convex. In the following, we handle the non-convexity of the optimization objective in Equation 8.11 *w.r.t.* the probing sequence $\boldsymbol{s}$ and the receive filter $\boldsymbol{w}$ using an alternating approach and propose a specialized flavor of CREW (cyclic), named as CREW (one-bit).

8.3 Proposed Method: CREW (One-Bit)

8.3.1 Optimization *w.r.t.* $\boldsymbol{s}$

Following Equation 8.4, the numerator of Equation 8.3 can be rearranged, for a fixed $\boldsymbol{w}$, as

$$\begin{aligned} \boldsymbol{w}^H \boldsymbol{R} \boldsymbol{w} &= \boldsymbol{w}^H \left(\beta \sum_{\substack{k=-N+1 \\ k\neq 0}}^{N-1} \boldsymbol{J}_k \boldsymbol{s} \boldsymbol{s}^H \boldsymbol{J}_k^H + \boldsymbol{\Gamma} \right) \boldsymbol{w} \\ &= \boldsymbol{s}^H \left(\underbrace{\beta \sum_{\substack{k=-N+1 \\ k\neq 0}}^{N-1} \boldsymbol{J}_k \boldsymbol{w} \boldsymbol{w}^H \boldsymbol{J}_k^H}_{\boldsymbol{\chi}} \right) \boldsymbol{s} + \boldsymbol{w}^H \boldsymbol{\Gamma} \boldsymbol{w}. \end{aligned} \tag{8.12}$$

Thus, the criterion in Equation 8.3 can be reformulated as,

$$\frac{\mathrm{MSE}(\hat{\alpha_0})}{\beta} = \frac{\boldsymbol{s}^H \boldsymbol{\chi} \boldsymbol{s} + \mu}{\boldsymbol{s}^H \boldsymbol{W} \boldsymbol{s}}, \tag{8.13}$$

where $\mu = (\boldsymbol{w}^H \boldsymbol{\Gamma} \boldsymbol{w})/\beta$ and $\boldsymbol{W} = \boldsymbol{w}\boldsymbol{w}^H$. It is interesting to note that μ is unknown; however, independent of $\boldsymbol{s}$, and thus merely a constant scalar *w.r.t.* $\boldsymbol{s}$. To deal with the optimization problem of Equation 8.13, we follow the identical framework as [76] that exploits the idea of fractional programming [214].

Let $a(\boldsymbol{s}) = \boldsymbol{s}^H \boldsymbol{\chi} \boldsymbol{s} + \mu$, and $b(\boldsymbol{s}) = \boldsymbol{s}^H \boldsymbol{W} \boldsymbol{s} > 0$ (MSE needs to be finite). Further, denote $f(\boldsymbol{s}) = \dfrac{a(\boldsymbol{s})}{b(\boldsymbol{s})}$ and let $\boldsymbol{s}_*$ be the current value of $\boldsymbol{s}$. Additionally, let $g(\boldsymbol{s}) \triangleq a(\boldsymbol{s}) - f(\boldsymbol{s}_*) b(\boldsymbol{s})$, and $\boldsymbol{s}_\dagger \triangleq \arg\min_{\boldsymbol{s}} g(\boldsymbol{s})$. Following that one can easily verify that $g(\boldsymbol{s}_\dagger) \leq g(\boldsymbol{s}_*) = 0$. As a result, the following is satisfied: $g(\boldsymbol{s}_\dagger) = a(\boldsymbol{s}_\dagger) - f(\boldsymbol{s}_*) b(\boldsymbol{s}_\dagger) \leq 0$, and this further indicates that $f(\boldsymbol{s}_\dagger) \leq f(\boldsymbol{s}_*)$ as $b(\boldsymbol{s}_\dagger) > 0$. Thus $\boldsymbol{s}_\dagger$ decreases the function $f(\boldsymbol{s})$ monotonically. It is important to note that $\boldsymbol{s}_\dagger$ is not necessarily a minimizer of $g(\boldsymbol{s})$; instead, it is sufficient for $\boldsymbol{s}_\dagger$ so that $g(\boldsymbol{s}_\dagger) \leq g(\boldsymbol{s}_*)$ is satisfied.

Under the assumption that $\|\boldsymbol{s}\|_2^2 = N$, for a fixed $\boldsymbol{w}$, and any arbitrary $\boldsymbol{s}_*$ of the minimizer $\boldsymbol{s}$ of Equation 8.13, we have:

$$\begin{aligned} g(\boldsymbol{s}) &= \boldsymbol{s}^H (\boldsymbol{\chi} - f(\boldsymbol{s}_*) \boldsymbol{W}) \boldsymbol{s} + \mu \\ &= \boldsymbol{s}^H \boldsymbol{T} \boldsymbol{s} + \mu, \end{aligned} \tag{8.14}$$

where $\boldsymbol{T} \triangleq \boldsymbol{\chi} - f(\boldsymbol{s}_*)\boldsymbol{W}$. Then the problem in Equation 8.13 with respect to unimodular $\boldsymbol{s}$ can be recast as the following problem which is commonly known as unimodular quadratic program (UQP) [51]:

$$\begin{aligned} \max_{\boldsymbol{s}} \quad & \boldsymbol{s}^H \tilde{\boldsymbol{T}} \boldsymbol{s} \\ \text{s.t.} \quad & |s_k| = 1, \qquad 1 \leq k \leq N, \end{aligned} \tag{8.15}$$

where $\tilde{\boldsymbol{T}} \triangleq \lambda \boldsymbol{I} - \boldsymbol{T}$ is a positive definite matrix and λ is a real scalar greater than the maximum eigenvalue of $\boldsymbol{T}$. Note that Equation 8.15 is NP-hard in general, and a sub-optimal solution can be sought by semi-definite relaxation (SDR). To tackle this problem efficiently, we employ the *power method-like iterations* (PMLI) introduced in [51]; namely, the vector $\boldsymbol{s}$ is updated in each iteration n using the nearest-vector problem

$$\begin{aligned} \min_{\boldsymbol{s}^{(n+1)}} \quad & \left\| \boldsymbol{s}^{(n+1)} - \tilde{\boldsymbol{T}} \boldsymbol{s}^{(n)} \right\|_2 \\ \text{s.t.} \quad & \left| s_k^{(n+1)} \right| = 1, \qquad 1 \leq k \leq N. \end{aligned} \tag{8.16}$$

Interestingly, for nth iteration, the solution to Equation 8.16 is simply given analytically by $\boldsymbol{s}^{(n+1)} = e^{j \arg(\tilde{\boldsymbol{T}} \boldsymbol{s}^{(n)})}$ [76].

8.3.2 Optimization *w.r.t.* $\boldsymbol{w}$

For a fixed $\boldsymbol{s}$, the objective of Equation 8.11 can further be simplified as,

$$\begin{aligned}\mathbb{E}\left\{\frac{\boldsymbol{w}^H\boldsymbol{D}^{\frac{1}{2}}\bar{\boldsymbol{R}}\boldsymbol{D}^{\frac{1}{2}}\boldsymbol{w}}{|\boldsymbol{w}^H\boldsymbol{s}|^2}\right\} &= \frac{\mathbb{E}\left\{\mathrm{Tr}\left(\boldsymbol{w}\boldsymbol{w}^H\boldsymbol{D}^{\frac{1}{2}}\bar{\boldsymbol{R}}\boldsymbol{D}^{\frac{1}{2}}\right)\right\}}{|\boldsymbol{w}^H\boldsymbol{s}|^2} \\ &= \frac{\mathbb{E}\left\{\boldsymbol{d}^H\left(\boldsymbol{w}\boldsymbol{w}^H\odot\bar{\boldsymbol{R}}^H\right)\boldsymbol{d}\right\}}{|\boldsymbol{w}^H\boldsymbol{s}|^2} \\ &= \frac{\mathrm{Tr}\left(\left(\boldsymbol{w}\boldsymbol{w}^H\odot\bar{\boldsymbol{R}}^H\right)\mathbb{E}\left\{\boldsymbol{d}\boldsymbol{d}^H\right\}\right)}{|\boldsymbol{w}^H\boldsymbol{s}|^2}.\end{aligned} \tag{8.17}$$

It is clearly evident that the knowledge of $\boldsymbol{d}$ indirectly demands more information about β and $\boldsymbol{\Gamma}$. However, assuming the statistics of the noise is unchanging, one can estimate $\boldsymbol{\Gamma}$ in a normalized sense by just listening to the environment while not transmitting any waveform. As a result, from the one-bit receiver, the normalized interference covariance matrix $\bar{\boldsymbol{\Gamma}}$ can be obtained in a similar fashion as, $\bar{\boldsymbol{\Gamma}} \triangleq \boldsymbol{A}^{-\frac{1}{2}}\boldsymbol{\Gamma}\boldsymbol{A}^{-\frac{1}{2}}$, where $\boldsymbol{A} = \boldsymbol{\Gamma}\odot\boldsymbol{I}$. Thus the interference covariance matrix $\boldsymbol{R}$ in Equation 8.4 can be reformulated as,

$$\begin{aligned}\boldsymbol{R} &= \boldsymbol{D}^{\frac{1}{2}}\bar{\boldsymbol{R}}\boldsymbol{D}^{\frac{1}{2}} \\ &= \beta\boldsymbol{S} + \boldsymbol{A}^{\frac{1}{2}}\bar{\boldsymbol{\Gamma}}\boldsymbol{A}^{\frac{1}{2}},\end{aligned} \tag{8.18}$$

where $\boldsymbol{S} = \sum_{k\neq 0} \boldsymbol{J}_k \boldsymbol{s}\boldsymbol{s}^H \boldsymbol{J}_k^H$ is constant for a known $\boldsymbol{s}$. Hence, a judicious approach is to solve the following problem in order to optimize $\boldsymbol{d}, \boldsymbol{a}$, and β in a joint manner:

$$\begin{aligned} \{\hat{\boldsymbol{d}}, \hat{\boldsymbol{a}}, \hat{\beta}\} = \ & \arg\min_{\boldsymbol{d},\boldsymbol{a},\beta} \ \left\| \mathrm{Diag}\left(\boldsymbol{d}\right)^{\frac{1}{2}} \ \bar{\boldsymbol{R}} \ \mathrm{Diag}\left(\boldsymbol{d}\right)^{\frac{1}{2}} - \beta \boldsymbol{S} + \mathrm{Diag}\left(\boldsymbol{a}\right)^{\frac{1}{2}} \ \bar{\boldsymbol{\Gamma}} \ \mathrm{Diag}\left(\boldsymbol{a}\right)^{\frac{1}{2}} \right\|_F^2, \\ & \text{s.t.} \quad \boldsymbol{d} > \boldsymbol{0}, \boldsymbol{a} > \boldsymbol{0}, \beta > 0. \end{aligned} \tag{8.19}$$

The above minimization problem is non-convex, and hence in order to efficiently solve it, we resort to an alternating approach: by solving for each variable while keeping the other two variables constant. By doing so, *w.r.t.* each variable the problem becomes convex and can be solved using a number of available numerical solvers, such as the "fmincon" function in Matlab that implements BFGS. Note that by solving Equation 8.19, one can obtain β and $\boldsymbol{d}$ in an average sense which in other words justifies the usage of expectation in the formulation of Equation 8.17.

With this information in mind, let $\sum_{k=1}^{N} \nu_k \boldsymbol{u}_k \boldsymbol{u}_k^H$ represent the eigenvalue decomposition (EVD) of $\mathbb{E}\left\{\boldsymbol{d}\boldsymbol{d}^H\right\}$, where $\{\nu_k\}$ and $\{\boldsymbol{u}_k\}$ are the k-th eigenvalue and eigenvector, respectively. As a result, the numerator of Equation 8.17 can further be simplified as,

$$\begin{aligned} \mathrm{Tr}\left(\left(\boldsymbol{w}\boldsymbol{w}^H \odot \bar{\boldsymbol{R}}^H \right) \sum_{k=1}^{N} \nu_k \boldsymbol{u}_k \boldsymbol{u}_k^H \right) &= \sum_{k=1}^{N} \nu_k \boldsymbol{u}_k^H \left(\boldsymbol{w}\boldsymbol{w}^H \odot \bar{\boldsymbol{R}}^H \right) \boldsymbol{u}_k \\ &= \mathrm{Tr}\left(\left(\boldsymbol{w}\boldsymbol{w}^H \right) \sum_{k=1}^{N} \nu_k \ \mathrm{Diag}\left(\boldsymbol{u}_k\right) \ \bar{\boldsymbol{R}} \ \mathrm{Diag}\left(\boldsymbol{u}_k^H\right) \right) \\ &= \boldsymbol{w}^H \boldsymbol{Q} \boldsymbol{w}, \end{aligned} \tag{8.20}$$

where

$$\boldsymbol{Q} = \sum_{k=1}^{N} \nu_k \ \mathrm{Diag}\left(\boldsymbol{u}_k\right) \ \bar{\boldsymbol{R}} \ \mathrm{Diag}\left(\boldsymbol{u}_k^H\right). \tag{8.21}$$

It is interesting to notice that, $\boldsymbol{Q}$ can be viewed as $\mathbb{E}\{\boldsymbol{R}\}$. A relevant proof is discussed in Appendix B. Finally, the optimization problem translates to,

$$\min_{\boldsymbol{w},\boldsymbol{s}} \quad \frac{\boldsymbol{w}^H \boldsymbol{Q} \boldsymbol{w}}{|\boldsymbol{w}^H \boldsymbol{s}|^2}. \tag{8.22}$$

Hence, for a given $\boldsymbol{s}$, the optimization problem in Equation 8.22 *w.r.t.* $\boldsymbol{w}$ results in a closed-from solution: $\boldsymbol{w} = \boldsymbol{Q}^{-1}\boldsymbol{s}$, within a multiplicative constant. Finally, the algorithm CREW (one-bit) is summarized in Algorithm 10 in a concise manner.

8.4 Numerical Simulations

In this section, we evaluate the performance of CREW (one-bit) and compare it with three state-of-the-art methods; namely CAN-MMF, CREW (fre) [74] and CREW (cyclic) [76]. Note that no prior knowledge of interference is applied during waveform design using CAN-MMF. We herein, adopt the same simulation setups as in [76]. Especially, for the interference covariance matrix we consider the following:

$$\boldsymbol{\Gamma} = \sigma_J^2 \boldsymbol{\Gamma}_J + \sigma^2 \boldsymbol{I},$$

Algorithm 10 CREW (ONE-BIT)

Ensure: $\boldsymbol{s}^{(0)} \leftarrow$ unimodular (or low PAR) vector in $\mathbb{C}^N$, $\boldsymbol{w}^{(0)} \leftarrow$ random vector in $\mathbb{C}^N$, the outer loop index $t \leftarrow 1$.

1: **repeat**

2: **For fixed** $\boldsymbol{w}$,

i: Compute $\boldsymbol{\chi}, \boldsymbol{W}$ using Equation 8.12, and thus, in turn find $\tilde{\boldsymbol{T}}$.

ii: Solve the power method like iterations discussed in Equation 8.16, and calculate $\boldsymbol{s}^{(t)}$ in each iteration until convergence.

3: Measure $\bar{\boldsymbol{\Gamma}}$ at the output of the one-bit receiver and compute $\bar{\boldsymbol{R}}$ using $\boldsymbol{s}^{(t)}$.

4: **For fixed** $\boldsymbol{s}$,

i: Solve Equation 8.19 to obtain $\boldsymbol{d}$ and β in average sense.

ii: Compute the EVD of $\mathbb{E}\left\{\boldsymbol{d}\boldsymbol{d}^H\right\}$, and in turn find $\boldsymbol{Q}$.

iii: Update $\boldsymbol{w}^{(t)}$ as $\boldsymbol{Q}^{-1}\boldsymbol{s}^{(t)}$.

5: **until** convergence, *e.g.*, $\left|\mathrm{MSE}^{(t+1)} - \mathrm{MSE}^{(t)}\right| < \epsilon$ for some given $\epsilon > 0$.

where $\sigma_J^2 = 100$, and $\sigma^2 = 0.1$ are used for the jamming and noise powers, respectively. Furthermore, the elements of covariance matrix for jamming, $\boldsymbol{\Gamma}_J$ are given as $[\boldsymbol{\Gamma}_J]_{k,l} = \gamma_{k-l}$ where $[\gamma_0, \gamma_1, \cdots, \gamma_{N-1}, \gamma_{-(N-1)}, \cdots, \gamma_{-1}]^T$ represents an inverse FFT of the jamming power spectrum at frequencies $\dfrac{p-1}{2N-1}$, for $p = 1, \cdots, 2N-1$. For CREW(fre) and CREW(cyclic) we fix the average clutter power to $\beta = 1$. Finally, we use the sequences with good correlation properties such as the Golomb sequences for the purpose of initialization of transmit waveform $\boldsymbol{s}$.

In the presented simulations we consider two types of signal jamming: *spot* and *barrage* jamming. Spot jamming happens when concentrated power is transmitted directly toward one channel or frequency. In our example, we use spot jamming located at a normalized frequency $f_0 = 0.2$. On the other hand, barrage jamming is transmitted power spread over several channels

or frequencies simultaneously [76]. We consider a barrage jamming located in the normalized frequency bands $[f_1, f_2] = [0.2, 0.3]$.

Figure 44 (a)-(b) depict the MSE values for spot and barrage jamming, respectively, corresponding to CAN-MMF, CREW(fre), and CREW(cyclic), under the unimodularity constraint, for various sequence lengths. It is evident from the figures that when the sequence length N is small, the MSE is higher for CREW (one-bit) compared to other algorithms. However, as N increases, CREW (one-bit) shows similar performance as CREW (cyclic), and eventually, they coincide with one another for higher values of N. Consequently, it is implied that higher signal length introduces more degrees of freedom in designing transmit waveform and thus, compensates for the uncertainties in interference statistics.

8.5 Concluding Remarks

In this chapter, we investigated the problem of jointly designing the probing signals and the receive filter coefficients in the presence of uncertainty in interference statistics. An efficient method based on the state-of-the-art algorithm: CREW (cyclic), was proposed to tackle the said problem. We showed that the performance of the proposed method improves with increasing signal length as it introduces more degrees of freedom in designing transmit waveform and thus, compensates for the uncertainties in interference statistics. It is further important to notice that the knowledge of the one-bit measurements impacts the design of the receive filter and alternatively the design of the receive filter coefficients impacts the design of transmit waveform, which justifies the role of a cognitive radar.

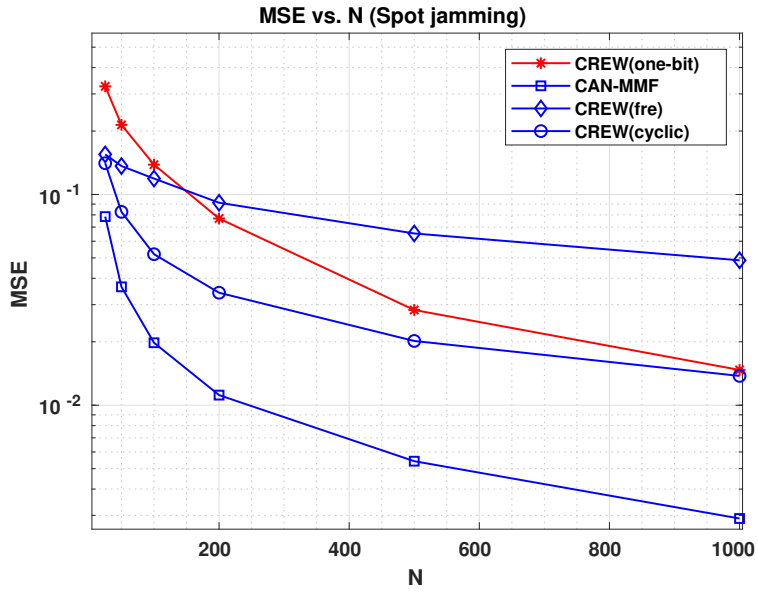

(a)

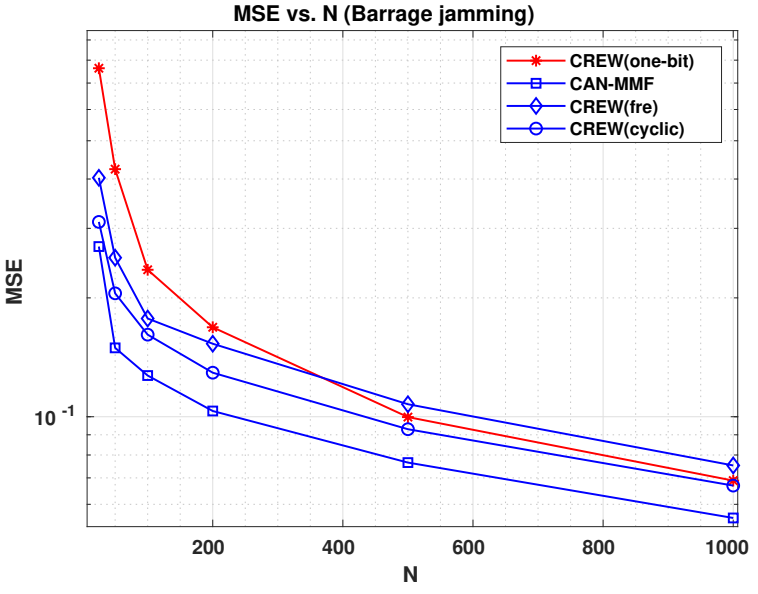

(b)

Figure 44. Comparison of mean square error values corresponding to different design algorithms for (a) spot jamming with normalized frequency $f_0 = 0.2$, and (b) barrage jamming in the normalized frequency interval $[f_1, f_2] = [0.2, 0.3]$ for the unimodularity constraint on the transmit sequence.

II-D

Deep Radar

CHAPTER 9

DEEP RADAR WAVEFORM DESIGN FOR EFFICIENT AUTOMOTIVE RADAR SENSING

Overview: The design of unimodular sequences has been studied widely in the last few decades, with most design algorithms requiring sophisticated *a priori* knowledge of environmental parameters which may be difficult to obtain in real-time scenarios. In this chapter, we propose a novel hybrid model-driven and data-driven architecture that adapts to the ever-changing environment and allows for adaptive unimodular waveform design. In particular, the approach lays the groundwork for developing extremely low-cost waveform design and processing frameworks for radar systems deployed in autonomous vehicles. The proposed model-based deep architecture imitates a well-known unimodular signal design algorithm in its structure, and can quickly infer statistical information from the environment using the observed data.

9.1 Introduction

In previous chapters, we have discussed various aspects of waveform designing where the underlying signal models have always followed different physics-based data descriptions. As we arrive at the last chapter of this thesis, we explore the idea of learning from observation along with following the traditional modeling of the system in the context of cognitive radars. As discussed in Chapter 8, it is evident that the quality of target parameter estimation depends

---

strongly on the transmit waveform design process [24, 25, 33, 51, 68, 69, 75, 76, 82, 90, 164, 206, 207, 209, 210, 215–233] and consequently there exist several approaches to tackle the task of waveform design in such radar systems which rely on known radar models. In such model-based approaches, one only considers a simplified mathematical model and often does not take into account the intricate interactions innate to the kind of complex information systems that are common in the real world. On the other hand, in a purely data-driven approach, including deep learning techniques, one does not need an explicit mathematical model of the problem and should be able to use the available data at hand for designing the waveforms. The major shortcoming of the data-driven approach stems from the fact that it is unclear how to incorporate the existing knowledge of the system model in the processing stage. Namely, purely data-driven approaches have a wider applicability at the cost of interpretability, and in some cases, reliability [234, 235]. In this chapter, we seek to bridge the gap between the model-based and data-driven approaches, and propose a novel methodology in order to design efficient waveforms for automotive radars by making use of the *deep unfolding framework* [80, 81, 235]. Note that the goal of waveform design for radar systems is to acquire the maximum amount of information from the desirable sources in the environment, where in fact, *the transmit signal can be viewed as a medium that collects information.* In light of this, we employ the deep unfolding framework that aims to take the well-established iterative approaches, and design a deep architecture for waveform design in radar systems under unimodular signal constraint, and boost the performance of the underlying inference optimization algorithm in terms of speed of convergence and effectiveness.

The remainder of the chapter is arranged as follows. First, Section 9.2 describes the data model considered and formulates the problem. Section 9.3 is then devoted to the description of the DRCoR architecture. We evaluate the performance of the proposed method in Section 9.4. Finally, Section 9.5 concludes the chapter.

9.2 Radar Model and Signal Design Formulation

Let us consider a radar system transmitting unimodular codes used to modulate a train of sub-pulses. We follow the similar data model as previously considered in Section 8.2. Let

$$\boldsymbol{s} = [s_1 \; s_2 \; \cdots \; s_N]^T \in \mathbb{C}^N, \tag{9.1}$$

denote the complex-valued probing sequence to be designed. Under the assumptions of negligible intrapulse Doppler shift, and that the sampling is synchronized to the pulse rate, the received discrete-time base-band signal $\boldsymbol{y}$, after pulse compression and alignment with the current range cell of interest, can be modeled as follows [75]:

$$\boldsymbol{y} = \boldsymbol{A}^H \boldsymbol{\alpha} + \boldsymbol{\epsilon} \tag{9.2}$$

where the definitions of the matrix $\boldsymbol{A}$, and the vectors $\boldsymbol{\alpha}$ and $\boldsymbol{\epsilon}$ are described in Equation 8.1, Equation 8.2, and the paragraph following. Given the measurement model in Equation 9.2, one of the main goals of a system designer is typically to design the probing signal $\boldsymbol{s}$ such that it allows for accurate recovery of the target scattering coefficient α_0.

Note that, in model-based radar waveform design, the statistics of the interference and noise is usually assumed to be known, *e.g.*, through stand-alone prescan procedures. Under such conditions, the waveform design boils down to constrained quadratic or fractional quadratic program as detailed in previous works [51, 75, 76, 164, 209]. An example for waveform design criteria comes from the waveform's merit for resolvability along with clutter rejection. Namely, using a matched filter (MF) in the pulse compression stage, one can look for codes that maximize the following criterion:

$$f(\boldsymbol{s}) \triangleq \frac{|\boldsymbol{s}^H \boldsymbol{y}|^2}{\sum_{k\neq 0} |\boldsymbol{s}^H \boldsymbol{J}_k \boldsymbol{y}|^2} = \frac{\boldsymbol{s}^H \boldsymbol{A} \boldsymbol{s}}{\boldsymbol{s}^H \boldsymbol{B} \boldsymbol{s}} \triangleq \frac{n(\boldsymbol{s})}{d(\boldsymbol{s})}, \tag{9.3}$$

where $\boldsymbol{A} = \boldsymbol{y}\boldsymbol{y}^H$, $\boldsymbol{B} = \sum_{k\neq 0} \boldsymbol{J}_k \boldsymbol{A} \boldsymbol{J}_k^H$, and $\{\boldsymbol{J}_k\}$ are shift matrices satisfying $[\boldsymbol{J}_k]_{p,q} = [\boldsymbol{J}_{-k}^H]_{p,q} \triangleq \delta_{q-p-k}$, with $\delta_{(\cdot)}$ being the Kronecker delta function. Note that the above function can be interpreted as an oracle to a signal-to-interference-noise (SINR) ratio as the numerator represents the signal power and the denominator represents the combined interference and noise power after applying the matched filter. We further note that, to lower the implementation cost, it is desirable to use unimodular codes, *i.e.*, $s_k = e^{j\phi_k},\ \phi_k \in [0, 2\pi),\ k \in \{1, \ldots, N\}$, that attain the smallest peak-to-average ratio possible for transmit signals. As a result, one can consider the following fractional program in its general form for radar waveform design:

$$\begin{aligned} \max_{\boldsymbol{s}} \quad & \frac{\boldsymbol{s}^H \boldsymbol{A} \boldsymbol{s}}{\boldsymbol{s}^H \boldsymbol{B} \boldsymbol{s}} \\ \text{s.t.} \quad & |s_k| = 1, \quad k \in \{1, \ldots, N\} \end{aligned} \tag{9.4}$$

Note that evaluating the objective function in Equation 9.4, *i.e.*, computing $f(\boldsymbol{s})$, only requires the knowledge of the transmit sequence $\boldsymbol{s}$ and the observed vector $\boldsymbol{y}$ at the receiver. Nevertheless, solving the above optimization program is still NP-hard and very hard to tackle in general. In order to approximate the solution, one can resort to power method-like iterations specifically designed to tackle unimodular quadratic programs (UQPs) [51]. In what follows, we reformulate the problem of Equation 9.4 as a UQP and present the corresponding power method-like iterations that lay the groundwork for our proposed hybrid model-aware and data-driven *adaptive* waveform design framework.

Observe that both the numerator $n(\boldsymbol{s})$ and the denominator $d(\boldsymbol{s})$ of the objective function $f(\boldsymbol{s})$ are quadratic in $\boldsymbol{s}$. Hence, in order to tackle the maximization of Equation 9.3 (or equivalently tackling Equation 9.4) we resort to fractional programming techniques [214, 236]. Since $f(\boldsymbol{s})$, the SINR, is finite, we must have that $d(\boldsymbol{s}) = \boldsymbol{s}^H \boldsymbol{B} \boldsymbol{s} > 0$. In addition, let $\boldsymbol{s}_\star$ denote the current value of the code sequence $\boldsymbol{s}$. Then, we define

$$e(\boldsymbol{s}) \triangleq n(\boldsymbol{s}) - f(\boldsymbol{s}_\star) d(\boldsymbol{s}), \tag{9.5}$$

$$\boldsymbol{s}_\dagger = \arg\max_{\boldsymbol{s}} \; e(\boldsymbol{s}). \tag{9.6}$$

Henceforth, it can be easily verified by the virtue of Equation 9.6 that $e(\boldsymbol{s}_\dagger) \geq e(\boldsymbol{s}_\star) = 0$. As a result, we have that $e(\boldsymbol{s}_\dagger) = n(\boldsymbol{s}_\dagger) - f(\boldsymbol{s}_\star) d(\boldsymbol{s}_\dagger) \geq 0$ implying that

$$f(\boldsymbol{s}_\dagger) \geq f(\boldsymbol{s}_\star), \tag{9.7}$$

as $d(\boldsymbol{s}_{\dagger}) > 0$. In other words, we can argue that with respect to $\boldsymbol{s}_{\star}$, the $\boldsymbol{s}_{\dagger}$ increases the objective function $f(\boldsymbol{s})$. It is noteworthy to mention that for the criteria in Equation 9.7 to hold, it is sufficient for $\boldsymbol{s}_{\dagger}$ to satisfy $e(\boldsymbol{s}_{\dagger}) \geq e(\boldsymbol{s}_{\star})$ and that $\boldsymbol{s}_{\dagger}$ shall not necessarily be the maximizer of $e(\boldsymbol{s})$.

For a given $\boldsymbol{s}_{\star}$ maximizer of Equation 9.4 we have that:

$$\begin{aligned} e(\boldsymbol{s}) &= \boldsymbol{s}^H \boldsymbol{A} \boldsymbol{s} - f(\boldsymbol{s}_{\star}) \left(\boldsymbol{s}^H \boldsymbol{B} \boldsymbol{s} \right) \\ &= \boldsymbol{s}^H \underbrace{\left(\boldsymbol{A} - f(\boldsymbol{s}_{\star}) \boldsymbol{B} \right)}_{\triangleq \tilde{\boldsymbol{\chi}}} \boldsymbol{s} \end{aligned}$$

Now, in order to ensure that $\tilde{\boldsymbol{\chi}}$ is positive definite, one can perform a diagonal loading procedure by defining $\boldsymbol{\chi} \triangleq \tilde{\boldsymbol{\chi}} + \lambda \boldsymbol{I}_N$, where $\lambda \geq \max\{0, -\lambda_{\min}(\tilde{\boldsymbol{\chi}})\}$. Next, the optimization problem of Equation 9.4 can be cast as the following UQP [51]:

$$\begin{aligned} \max_{\boldsymbol{s}} \quad & \boldsymbol{s}^H \boldsymbol{\chi} \boldsymbol{s} \\ \text{s.t.} \quad & |s_k| = 1, \quad k \in \{1, \ldots, N\}. \end{aligned} \tag{9.8}$$

As previously discussed in Chapter 7 and 8, in order to efficiently tackle Equation 9.8, one can employ a set of *power method-like iterations* (PMLI) suggested in [51, 76]. PMLI is capable of

monotonically improving the objective value in Equation 9.8 using the following nearest-vector problem:

$$\begin{aligned} &\min_{\boldsymbol{s}^{(n+1)}} \left\| \boldsymbol{s}^{(n+1)} - \boldsymbol{\chi}\boldsymbol{s}^{(n)} \right\|_2, \\ &\text{s.t.} \quad \left| s_k^{(n+1)} \right| = 1, \, \forall \, k. \end{aligned} \tag{9.9}$$

The solution to Equation 9.9 can be computed analytically and is given as follows [51, 76]:

$$\boldsymbol{s}^{(n+1)} = e^{j \arg(\boldsymbol{\chi}\boldsymbol{s}^{(n)})}. \tag{9.10}$$

where n denotes the internal iteration number, and $\boldsymbol{s}^{(0)}$ is the current value of $\boldsymbol{s}$. One can continue updating $\boldsymbol{s}$ until convergence in the objective of Equation 9.4, or for a fixed number of steps, say L. These iterations are already shown to provide a monotonic behavior of the quadratic objective (no matter what the signal constraints are), and subsume the well-known power method as a special case. Such a general approach to computationally efficient quadratic programming that can handle various signal constraints (many of which cause the problems to become NP-hard) opens new avenues in signal processing in low-cost scenarios.

Note that, in many practical scenarios, one might not have access to the *a priori* information about environmental parameters. In the following, we aim to devise a hybrid data-driven and model-based approach that allows us to jointly design adaptive transmit code sequences while learning these parameters given the fact that the environmental information is in fact embedded into the observed received signal $\boldsymbol{y}$. Namely, we propose a novel neural network structure for

waveform design, **D**eep **E**volutionary **Co**gnitive **R**adar (DECoR), by considering the above power method-like iterations as a baseline algorithm for the design of a model-based deep neural network. In particular, we consider an over-parametrization of the power method-like iterations and unfold them onto the layers of a deep neural network. Each layer of the resulting network is designed such that it imitates one iteration of the form Equation 9.10. Consequently, the resulting deep architecture is model-aware, uses the same non-linear operations as those in the power method, and hence, is interpretable (as opposed to general deep learning models). The structure yet allows us to utilize data-driven approaches to optimize the parameters of the network in an online learning manner—making the resulting network a great candidate for reliable adaptive waveform design in automotive radar applications.

9.3 The DECoR Architecture for Signal Design

Consider the dynamics of a general fully connected deep neural network. Let $\tilde{g}_{\phi_i}$ be defined as

$$\tilde{g}_{\phi_i}(\boldsymbol{z}) = a(\boldsymbol{u}), \tag{9.11}$$

where $\boldsymbol{u} = \boldsymbol{W}_i \boldsymbol{z}$ and $\phi_i = \{\boldsymbol{W}_i\}$ denotes the set of parameters of the function g_{ϕ_i}, and $a(\cdot)$ denotes a non-linear activation function. Then, given an input $\boldsymbol{x}_0$, the dynamics of a fully connected neural network with L layers can be expressed as follows:

$$\boldsymbol{x}_L = \mathcal{F}\left(\boldsymbol{x}_0; \boldsymbol{\Upsilon}\right) = \tilde{g}_{\phi_{L-1}} \circ \tilde{g}_{\phi_{L-2}} \circ \cdots \circ \tilde{g}_{\phi_0}(\boldsymbol{x}_0), \tag{9.12}$$

where, for a general DNN, $\boldsymbol{\Upsilon} = \{\phi_i\}_{i=0}^{L-1}$ denotes the set of weight matrices $\boldsymbol{W}_i$ for each layer. Now, consider the power method-like iterations of the form Equation 9.10. The connection between the two becomes clear by paying attention to the fact that a fully connected DNN with an activation function defined as $a(\boldsymbol{x}) = e^{j \arg(\boldsymbol{x})}$, and parameterized on a matrix $\boldsymbol{W}$ (that is tied along the layers), boils down to performing L iterations of the PMLI. Therefore, one can immediately see that a fully connected DNN with the specific choice of non-linear activation function given by the projection operator $\mathcal{S}(\boldsymbol{x}) \triangleq e^{j \arg(\boldsymbol{x})}$ is an optimal architecture for waveform design with respect to the power method-like iterations extensively used in waveform design in various applications [237, 238]. Hence, power method-like iterations are perfect candidates for unfolding into DNNs since they can be characterized by a linear step, followed by a possibly non-linear operation.

9.3.1 The Deep Evolutionary Cognitive Radar Architecture

The derivation begins by considering that in the vanilla PMLI algorithm, the matrix $\boldsymbol{\chi}$ is tied along all iterations. Hence, we enrich the PML iterations by introducing a weight matrix $\boldsymbol{\chi}_i$ *per iteration* i. Note that in the original PMLI algorithm, the matrix $\boldsymbol{\chi}$ changes from one outer iteration to another. Hence, such an over-parameterization of the iterations results in a deep architecture that is faithful to the original model-based signal design method. Such an over-parametrization yields the following computation model for our proposed deep architecture (DECoR). Let us define g_{ϕ_i} as

$$g_{\phi_i}(\boldsymbol{z}) = \mathcal{S}(\boldsymbol{u}), \tag{9.13}$$

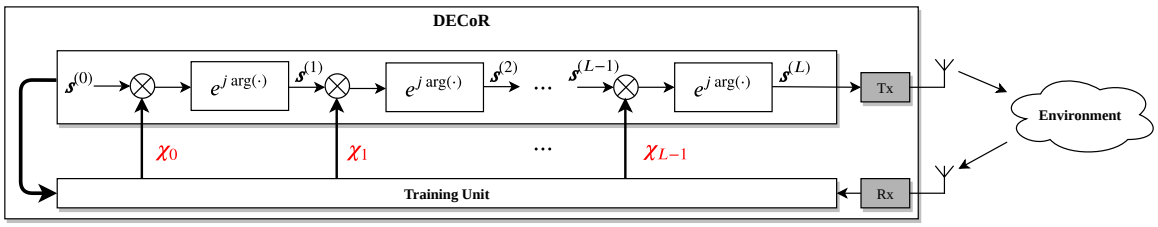

Figure 45. The proposed DECoR architecture for adaptive radar waveform design.

where $\boldsymbol{u} = \boldsymbol{\chi}_i \boldsymbol{z}$ and $\phi_i = \{\boldsymbol{\chi}_i\}$ denotes the set of parameters of the function g_{ϕ_i}, and recall that the non-linear activation function is defined as $\mathcal{S}(\boldsymbol{x}) = e^{j\arg(\boldsymbol{x})}$ applied element-wise on the vector argument. Then, the dynamics of the proposed DECoR architecture with L layers can be expressed as:

$$\boldsymbol{s}_L = \mathcal{G}\left(\boldsymbol{s}_0; \boldsymbol{\Omega}\right) = g_{\phi_{L-1}} \circ g_{\phi_{L-2}} \circ \cdots \circ g_{\phi_0}(\boldsymbol{s}_0), \tag{9.14}$$

where $\boldsymbol{s}_0$ denotes some initial unimodular vector, and $\boldsymbol{\Omega} = \{\boldsymbol{\chi}_0, \ldots, \boldsymbol{\chi}_{L-1}\}$ denotes the set of trainable parameters of the network. The block diagram of the proposed architecture is depicted in Figure 45.

Our goal is to optimize the set of parameters $\boldsymbol{\Omega}$ of the proposed DECoR architecture using an online learning strategy that allows for fast adaptation to different environments. Intuitively, given the nature of the PML iterations, learning the parameters $\boldsymbol{\Omega} = \{\boldsymbol{W}_l\}_{l=0}^{L-1}$ corresponds to learning the information corresponding to the signal-dependent interference and environmental noise profile.

9.3.2 The Proposed Online Learning Strategy

In an automotive radar application, the environment might undergo drastic changes along different coherent processing intervals, and the noise and interference statistics might vary as a result. Hence, it is natural to consider an online learning strategy for training the proposed DECoR architecture.

Let $\mathbf{\Omega}^{(t)}$ denote the set of parameters at time t. Then, the resulting code sequence given the set of parameters $\mathbf{\Omega}^{(t)}$ is simply given by the output of the last layer of the proposed DECoR architecture, *i.e.*, $s_L^{(t)} = \mathcal{G}\left(\boldsymbol{s}_0; \mathbf{\Omega}^{(t)}\right)$. We define the goal of our online training procedure as learning the set of parameters $\mathbf{\Omega}^{(t+1)}$ such that the resulted code sequence $\boldsymbol{s}^{(t+1)} = \mathcal{G}\left(\boldsymbol{s}_0; \mathbf{\Omega}^{(t+1)}\right)$ satisfies the following criterion:

$$f(\boldsymbol{s}^{(t+1)}) \geq f(\boldsymbol{s}^{(t)}). \tag{9.15}$$

Accordingly, we propose the following *random walk-based* training strategy for optimizing the parameters of the proposed DECoR architecture in an online manner as shown in Table V.

The proposed online learning strategy for the DECoR architecture is an amalgamation of natural evolutionary optimization techniques and policy optimization in reinforcement learning. In particular, the increase in the objective function $f(\boldsymbol{s})$ can be seen as a task for an agent that is interacting with an unknown environment over the action space of $\mathbf{\Omega}$ and the corresponding unimodular code $\boldsymbol{s}_L = \mathcal{G}(\boldsymbol{s}_0, \mathbf{\Omega})$. Note that the power method-like iterations and the model of the system impose a positive definite constraint on the weight matrices $\{\boldsymbol{\chi}_i\}_{i=0}^{L-1}$. In order to

TABLE V

THE PROPOSED TRAINING STRATEGY FOR DECOR ARCHITECTURE

Step 0: (Initialization): Choose an arbitrary unimodular transmit sequence $\boldsymbol{s}_0 \in \mathbb{C}^N$, and set the training counter to $t = 0$. Initialize the radius σ of the search region to some positive constant c, and choose $\delta \in (0, 1]$. Further initialize the set of weight matrices $\boldsymbol{\Omega}^{(0)} = \{\boldsymbol{\chi}_i^{(0)}\}_{i=0}^{L-1}$ such that $\boldsymbol{\chi}_i^{(0)} \succ 0$, for $i \in \{0, \ldots, L-1\}$.

Step 1: (Random walk- generation): For $l \in \{0, \ldots, L-1\}$, generate B random lower triangular matrices $\boldsymbol{L}_l^0, \ldots, \boldsymbol{L}_l^{B-1} \sim \mathcal{CN}(0, \sigma \boldsymbol{I})$, and form the set of Hermitian positive-definite search direction matrices $\boldsymbol{D}_l^i = \boldsymbol{L}_l^i \boldsymbol{L}_l^{iH}$, for each layer l and for $i \in \{0, \ldots, B-1\}$, where $\boldsymbol{D}_l^i \in \mathbb{C}^{N \times N}$.

Step 2: (Random walk- perturbation): For $i \in \{0, \ldots, B-1\}$, form the set of possible candidate updates for the current parameter space $\boldsymbol{\Omega}^{(t)}$ as $\boldsymbol{\Omega}_i^{(t)} = \{\boldsymbol{\chi}_0^{(t)} + \boldsymbol{D}_0^i, \ldots, \boldsymbol{\chi}_{L-1}^{(t)} + \boldsymbol{D}_{L-1}^i\}$. Compute the corresponding B unimodular codes $\boldsymbol{s}_{L,i}^{(t)} = \mathcal{G}(\boldsymbol{s}_0; \boldsymbol{\Omega}_i^{(t)})$ for $i \in \{0, \ldots, B\}$ and form the set of training transmission codes as $\boldsymbol{S}^{(t)} = \{\boldsymbol{s}_{L,0}^{(t)}, \ldots, \boldsymbol{s}_{L,B-1}^{(t)}\}$.

Step 3: (Collecting information): Transmit the unimodular codes in the set $\boldsymbol{S}^{(t)}$ and obtain the corresponding set of received signals $\boldsymbol{Y} = \{\boldsymbol{y}_0^{(t)}, \ldots, \boldsymbol{y}_{B-1}^{(t)}\}$. Compute the function $f(\boldsymbol{s})$ for each transmit/receive pair $(\boldsymbol{s}_{L,i}^{(t)}, \boldsymbol{y}_i^{(t)})$ and construct the set of objective values as $\mathcal{F} = \{f(\boldsymbol{s}_{L,i}^{(t)})\}_{i=0}^{B-1}$.

Step 4: (Optimizing the DECoR architecture): Choose the current optimal parameter space using

$$i_\star = \underset{i \in [B]}{\arg\max} \; f(\boldsymbol{s}_{L,i}^{(t)}).$$

Update the network parameters if $f(\boldsymbol{s}_{L,i_\star}^{(t)}) \geq f(\boldsymbol{s}_L^{(t-1)})$ and set the search radius as $\sigma \leftarrow c$. Otherwise, only update the search radius as $\sigma \leftarrow \delta\sigma$. Continue the online learning by going to Step 1.

impose such a constraint in incrementally learning the parameters $\boldsymbol{\Omega}$, we initialize each $\boldsymbol{\chi}_i^{(0)}$ with some positive-definite matrix. We then perform a random walk in the cone of positive definite matrices by forming positive definite search direction matrices $\boldsymbol{D}_l^i = \boldsymbol{L}_l^i \boldsymbol{L}_l^{iH}$. Such a training strategy results in a fast adaptation to the ever-changing environment. Hence, the radar agent can continually perform the training on the fly.

9.4 Numerical Simulations

We begin by evaluating the performance and effectiveness of the proposed online learning strategy for optimizing the parameters of the DECoR architecture. For this experiment, we fix the total number of layers of the proposed DECoR architecture as $L = 30$. Throughout the simulations, we assume an environment with dynamics described in Equation 9.2, and with more details in [75], with clutter power $\beta = 1$, and a noise covariance of $\mathbf{\Gamma} = \boldsymbol{I}$. These information were not made available to the DECoR architecture and we only use them for data generation purposes.

Figure 46(a) demonstrates the objective value $f(\boldsymbol{s}_L)$ in Equation 9.3 vs. training iterations, for a code length of $N = 10$. It can be clearly seen that the proposed learning strategy and the corresponding DECoR architecture results in a *monotonically* increasing objective value $f(\boldsymbol{s}_L)$. Furthermore, note that the proposed learning algorithm optimizes the parameters of the proposed DECoR architecture very quickly. Next, we evaluate the performance of the presented hybrid model-based and data-driven architecture in terms of recovering the target coefficient α_0. In particular, we compare the performance of our method (DECoR) in designing unimodular codes with two state-of-the-art model-based algorithms: (a) CREW(cyclic) [76], a cyclic optimization of the transmit sequence and the receive filter, (b) CREW(MF) [76], a version of CREW(cyclic) that uses a matched filter as the receive filter, and (c) CREW(fre) [20], a frequency domain algorithm to jointly design transmit sequence and the receive filter. Figure 46(b) illustrates the MSE of the estimated α_0 vs. code lengths $N \in \{10, 25, 50, 100, 200\}$. For each N, we perform the optimization of DECoR architecture by allowing the radar agent to

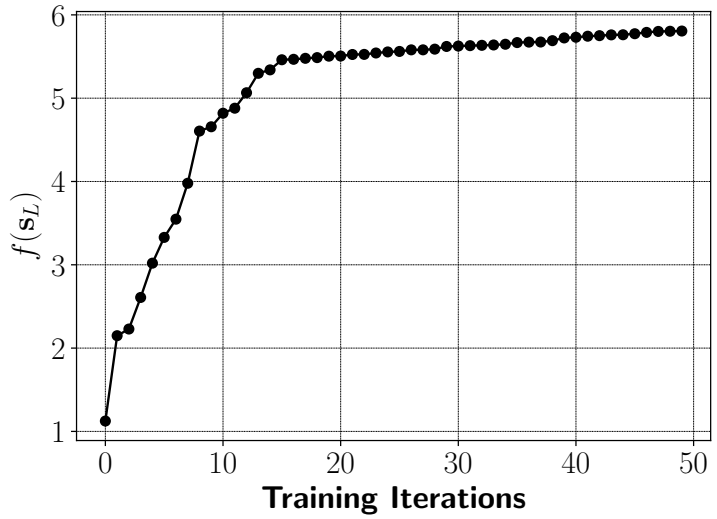

(a)

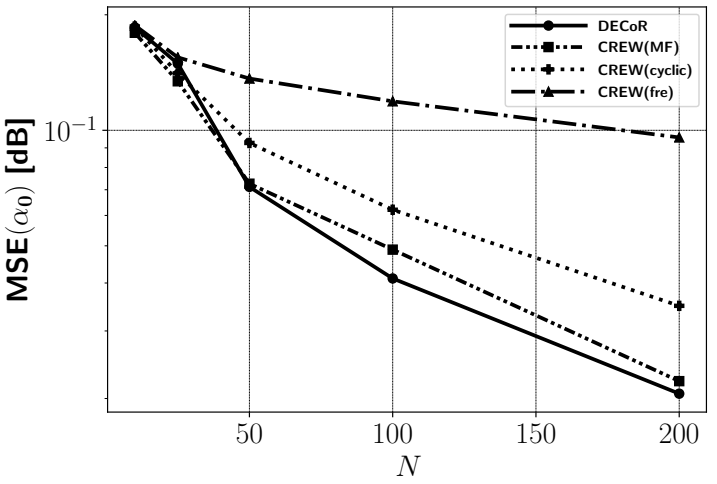

(b)

Figure 46. Illustration of (a) the objective value $f(\boldsymbol{s}_L)$ of the DECoR vs. training iterations for a code length of $N = 10$, and (b) MSE values obtained by the different design algorithms for code lengths $N \in \{10, 25, 50, 100, 200\}$.

interact with the environment for 50 training epochs. After the training is completed, we use the optimized architecture to generate the unimodular code sequence $\boldsymbol{s}_L$ and use an MF to estimate α_0. We let the aforementioned algorithms perform the code design until convergence, while the presented DECoR architecture has been only afforded $L = 30$ layers (equivalent of L iterations). It is evident that the proposed method significantly outperforms other state-of-the-art approaches.

9.5 Concluding Remarks

A learning-based signal designing method was proposed in this chapter. We employed a deep unfolding framework: DECoR, that aims to take the well-established iterative approaches, and design a deep architecture for waveform design in radar systems under unimodular signal constraint. Numerical simulations showed that the proposed method significantly outperforms other state-of-the-art approaches. It is interesting to note that although the DECoR framework does not have access to the statistics of the environmental parameters (as opposed to the other algorithms), it is able to learn them by exploiting the observed data from interaction with the environment.

CHAPTER 10

CONCLUSIONS

This thesis placed a large swath of the current state of waveform synthesis techniques for active sensing systems under one umbrella. The main objective of the thesis was structured into two parts. In the first part, we investigated various aspects of designing waveforms for the purpose of system identification. We provided, herein, the required and relevant background for the identification of SL and WL systems and consequently proposed multiple novel algorithms to design waveforms for such systems.

Chapter 2 and 3 of this thesis dealt with the SL systems. Firstly, a polynomial-time construction approach for designing binary waveforms with optimal PSL growth was proposed. The suggested approach utilized the potential of known sequence sets with good correlation properties in achieving an asymptotically optimal PSL growth both in a periodic and aperiodic sense using non-convex quadratic optimization methods. It was shown that the constructed sequences can outperform the widely used PN sequence in information embedding applications. Secondly, a novel efficient algorithm was proposed to design signals with both good auto-correlation and distribution properties that are required in specialized applications such as eye-tracking for Parkinson's Disease diagnosis and treatment. The proposed method was computationally efficient and can design very long sequences (of lengths up to $N \sim 10^6$ and even more) in relatively short time frames. These designed sequences showed significant enhancement in terms of out-of-phase auto-correlation as well as good distribution properties.

In Chapter 4 and 5, we then extended the notion of designing waveforms with good correlation properties toward WL systems. We proposed multiple algorithms that seek to design unimodular sequences or sequence sets that have good correlation as well as good complementary correlation properties. Interestingly this was made possible by considering a complete second-order characterization of the sequences or sequence sets. It was shown that the designed waveforms were not only capable of handling the WL systems but also were suitable for use in SL systems.

The second part of the thesis was devoted to the topic of signal designing for various advanced radar applications. For such specialized applications, we investigated the possibilities of smart waveform synthesis along with optimizing for secondary aspects of the radar systems. In Chapter 6, the problem of jointly designing the probing signal covariance matrix as well as the antenna positions to approximate a given beam-pattern was studied. A novel alternating optimization method was proposed to handle the non-convex nature of the design objective using a greedy local search algorithm. The proposed method was proved to be superior to the existing state-of-the-art methods in terms of accuracy and computational efficiency.

Consequently, in Chapter 7, we discussed the problem of mutual interference mitigation in identical or similar automotive radar systems. To this end, we investigated multiple coding schemes that can be applied not only in a simple SISO scenario but also can be extended to a more generalized MIMO case. We, herein, proposed an efficient optimization framework to convert a quartic objective to a quadratic one by careful over-parameterization. The designed

codes effectively redistributed the total energy of the collective ambiguity function to the desired region that resulted in reducing the interference power level significantly.

We furthermore, looked into another important waveform design problem for cognitive radar systems in Chapter 8. We investigated the problem of jointly designing the probing signals and the receive filter coefficients in the presence of uncertainty in interference statistics that arises with the usage of very low-bit quantization on the receiver side. An efficient method based on the state-of-the-art algorithm: CREW (cyclic) was proposed to tackle the said problem. We showed that the performance of the proposed method improves with increasing signal length as it introduces more degrees of freedom in designing transmit waveform and thus, compensates for the uncertainties in interference statistics. It was evident that the knowledge of low-resolution measurements impacts the design of the receive filter and alternatively, the design of the receive filter coefficients impacts the design of transmit waveform, which justifies the role of a cognitive radar.

Finally, Chapter 9 moved our attention from the model-based– to a learning-based signal designing problem. We particularly employed a deep unfolding framework: DECoR, that aims to take the well-established iterative approaches, and design a deep architecture for waveform design in radar systems under unimodular signal constraint. The proposed DECoR framework not only outperformed other state-of-the-art approaches but also was able to learn the statistical model of the environment by exploiting the observed data from interaction with the environment.

In each chapter, several numerical simulations were provided to evaluate the performance of the proposed algorithms. We, furthermore, laid out several recommendations for future research prospects for the waveform synthesis avenues we took.

APPENDICES

Appendix A

Time-complexity analysis of the Algorithm in Table IV

The computational complexity of the proposed method in Table IV for a problem size of (M, N) (*i.e.*, N antennas are to be selected from M locations) can be obtained through the following steps:

1. Evaluation of $\left(\boldsymbol{R}^{(t)}, \alpha^{(t)}\right)$ is a convex SDP problem and has a polynomial worst-case complexity [239].
2. Evaluation of $\boldsymbol{p}^{(t)}$ involves:
   (a) generation of $\boldsymbol{p}_{\mathrm{CS}}$, and calculation of $J(\boldsymbol{p})$ for each member of $\boldsymbol{p}_{\mathrm{CS}}$.
   (b) choosing the best $\boldsymbol{p}$.

A careful investigation of the optimization step for $\boldsymbol{p}$ reveals that it requires only $(M-N)$ inner-iterations (see Step 2 above). Note that the generation of $\boldsymbol{p}_{\mathrm{CS}}$ and choosing the best $\boldsymbol{p}$ (Step 2 above) linearly depend on the cardinality of the set $\boldsymbol{p}_{\mathrm{CS}}$, and thus, can be achieved in linear time-complexity. Namely, assuming $|\boldsymbol{p}_{\mathrm{CS}}| = l$, the problem of finding $\boldsymbol{p}^* \in \arg\min\ \boldsymbol{p}_{CS}$ has a complexity of $\mathcal{O}(l)$. For the k-th inner-iteration, let us denote the complexity of the calculations corresponding to the Step 2(a) above as a function of the cardinality of $\boldsymbol{p}_{\mathrm{CS}}$, *i.e.*, $\mathcal{C}(l)$, where $l = M - k$. Furthermore, the calculation of $J(\boldsymbol{p})$

Appendix A (Continued)

for each $\boldsymbol{p}$ has a constant cost c. Hence, the total cost of optimization with respect to the vector $\boldsymbol{p}$ at each outer-iteration admits the following upper-bound:

$$\begin{aligned}
\mathcal{C}_{\text{tot}} &= \sum_{k=1}^{M-N} c \cdot (M-k) + \mathcal{C}(M-k) \\
&\leq \sum_{k=1}^{M-N} cM + \mathcal{C}(M) \\
&= (M-N)(cM) + (M-N)\mathcal{C}(M) \\
&\leq cM^2 + M\mathcal{C}(M). \qquad \text{(A.1)}
\end{aligned}$$

Thus, the worst-case complexity is $\mathcal{O}\left(M^2\right)$ (note that $\mathcal{C}(M)$ corresponds to a complexity of $\mathcal{O}\left(M\right)$).

Appendix B

Proof that $\boldsymbol{Q} = \mathbb{E}\{\boldsymbol{R}\}$ in Equation 8.21

By using $\boldsymbol{D}^{\frac{1}{2}} = \text{Diag}(\boldsymbol{d})$, the following can be deduced:

$$\mathbb{E}\{\boldsymbol{R}\} = \mathbb{E}\left\{\boldsymbol{D}^{\frac{1}{2}}\bar{\boldsymbol{R}}\boldsymbol{D}^{\frac{1}{2}}\right\} = \mathbb{E}\left\{\boldsymbol{d}\boldsymbol{d}^H\right\} \odot \bar{\boldsymbol{R}}. \tag{B.1}$$

Assuming $\mathbb{E}\left\{\boldsymbol{d}\boldsymbol{d}^H\right\} = \boldsymbol{\eta}\boldsymbol{\eta}^H + \boldsymbol{\Sigma}$, Equation B.1 can reformulated as

$$\begin{aligned}
\mathbb{E}\{\boldsymbol{R}\} &= (\boldsymbol{\eta}\boldsymbol{\eta}^H + \boldsymbol{\Sigma}) \odot \bar{\boldsymbol{R}} \\
&= \sum_{k=1}^{N} \nu_k \boldsymbol{u}_k \boldsymbol{u}_k^H \odot \bar{\boldsymbol{R}} \\
&= \sum_{k=1}^{N} \nu_k \ \text{diag}(\boldsymbol{u}_k) \ \ \bar{\boldsymbol{R}} \ \text{diag}\left(\boldsymbol{u}_k^H\right),
\end{aligned} \tag{B.2}$$

and the proof is complete.

Appendix C

Efficient Computation of $\mathbf{B}_x$ and $\mathbf{B}_y$ as discussed in Remark 6

Note that $\mathbf{B}_y$ in Equation 7.21 can be rewritten as

$$\mathbf{B}_y = \sum_{p=-P}^{P} \mathrm{Diag}\left(\mathbf{f}_p\right) \left(\sum_{l=-N+1}^{N-1} \mathbf{C}_l \mathbf{y}\mathbf{y}^H \mathbf{C}_l^H \right) \mathrm{Diag}\left(\mathbf{f}_p\right)^H . \tag{C.1}$$

Define $\mathbf{R} = \sum_{l=-N+1}^{N-1} \mathbf{C}_l \mathbf{y}\mathbf{y}^H \mathbf{C}_l^H$. It is easy to verify $\mathbf{R}_y = 2\mathbf{R}_0 - \mathbf{y}\mathbf{y}^H$, considering that for $l < 0$, $\mathbf{C}_l \mathbf{y} = \mathbf{C}_{N-l}\mathbf{y}$, and $\mathbf{R}_0 = \sum_{l=0}^{N-1} \mathbf{C}_l \mathbf{y}\mathbf{y}^H \mathbf{C}_l^H$. Moreover, we can write $\mathbf{R}_0$ as

$$\mathbf{R}_0 = \mathbf{Y}\mathbf{Y}^H, \tag{C.2}$$

where

$$\mathbf{Y} = \begin{bmatrix} y_1 & y_2 & \cdots & y_{N-1} & y_N \\ y_2 & y_3 & \cdots & y_N & y_1 \\ \vdots & \vdots & \cdots & \vdots & \vdots \\ y_N & y_1 & \cdots & y_{N-2} & y_{N-1} \end{bmatrix} . \tag{C.3}$$

Appendix C (Continued)

As a result, $\mathbf{R}_0$ can be written as

$$\mathbf{R}_0 = \begin{bmatrix} c_{y,0} & c_{y,1} & \cdots & c_{y,N-2} & c_{y,N-1} \\ c_{y,1}^* & c_{y,0} & \cdots & c_{y,N-3} & c_{y,N-2} \\ \vdots & \vdots & \cdots & \vdots & \vdots \\ c_{y,N-1}^* & c_{y,N-2}^* & \cdots & c_{y,1}^* & c_{y,0} \end{bmatrix},$$

where $c_{y,l} = \sum_{n=1}^{N} y_n y_{(n+l) \bmod N}^*, l = 0, 1, \cdots, N-1$. It should be noted that $\mathbf{R}_0$ is a circulant matrix and its elements are determined by the values of the sequence $\{c_{y,l}\}_{l=0}^{N-1}$. Moreover, this sequence can be seen as the circular convolution between $\{y_n\}_{n=1}^{N}$ and $\{y_n\}_{n=1}^{N}$, and hence can be efficiently computed via FFT operations. Therefore, the computation of $\mathbf{R}_y$ requires $\mathcal{O}(N^2)$ flops (mainly due to the computation of $\mathbf{y}\mathbf{y}^H$).

It follows that $\mathbf{B}_y$ can be calculated efficiently using the following result:

$$\begin{aligned} \mathbf{B}_y &= \sum_{p=-P}^{P} \mathrm{Diag}(\mathbf{f}_p) \boldsymbol{R}_y \mathrm{Diag}(\mathbf{f}_p)^H \\ &= \sum_{p=-P}^{P} \mathbf{R}_y \odot (\mathbf{f}_p \mathbf{f}_p^H) \\ &= \mathbf{R}_y \odot (\mathbf{F}_P \mathbf{F}_P^H), \end{aligned} \tag{C.4}$$

where $\mathbf{F}_P = [\mathbf{f}_{-P}, \cdots, \mathbf{f}_P] \in \mathbb{C}^{N \times (2P+1)}$.

Appendix C (Continued)

Finally, we consider reducing the computational complexity of computing $\mathbf{B}_x$. To this end, we note that

$$\begin{aligned}\mathbf{B}_x &= \sum_{l=-N+1}^{N-1} \mathbf{C}_l^H \left(\sum_{p=-P}^{P} \mathrm{Diag}\left(\mathbf{f}_p\right)^H \mathbf{x}\mathbf{x}^H \mathrm{Diag}\left(\mathbf{f}_p\right) \right) \mathbf{C}_l \\ &= \sum_{l=-N+1}^{N-1} \mathbf{C}_l^H \left(\left(\mathbf{x}\mathbf{x}^H\right) \odot \left(\mathbf{F}_P^* \mathbf{F}_P^T\right) \right) \mathbf{C}_l. \end{aligned} \tag{C.5}$$

Let $\mathbf{R}_x = \left(\mathbf{x}\mathbf{x}^H\right) \odot \left(\mathbf{F}_P^* \mathbf{F}_P^T\right)$. We can observe that $\mathbf{C}_l^H \mathbf{R}_x \mathbf{C}_l$ can be computed very efficiently, since it only involves the permutation of the rows and columns of $\mathbf{R}_x$. Therefore, the computation of $\mathbf{B}_y$ only requires $\mathcal{O}\left(N^2\right)$ flops.

Appendix D

COPYRIGHT PERMISSIONS

In this appendix, we include the copyright permissions for the articles, whose contents were used for the production of this thesis. The permissions follow the same order as the appearance of the articles in the thesis.

Appendix D (Continued)

Appendix D (Continued)

Appendix D (Continued)

Appendix D (Continued)

Appendix D (Continued)

Appendix D (Continued)

Appendix D (Continued)

Appendix D (Continued)

Appendix D (Continued)

Appendix D (Continued)

CITED LITERATURE

1. NASA: Remote sensors. `https://earthdata.nasa.gov/learn/remote-sensors`, 2019. [Online; accessed: March 19, 2021].

2. Soltanalian, M.: Signal Design for Active Sensing and Communications. Doctoral dissertation, Uppsala University, Division of Systems and Control, Automatic control, Sweden, 2014.

3. Söderström, T. and Stoica, P.: System identification. New York, Prentice Hall, Inc., 1989.

4. Arriaga-Trejo, I. A. and Orozco-Lugo, A. G.: Unimodular sequences with low complementary autocorrelation properties. In Computer Science and Engineering—Theory and Applications, eds. M. A. Sanchez, L. Aguilar, M. Castañón-Puga, and A. Rodríguez-Díaz, pages 259–282. Cham, Springer International Publishing, 2018.

5. Picinbono, B. and Chevalier, P.: Widely linear estimation with complex data. IEEE Transactions on Signal Processing, 43(8):2030–2033, August 1995.

6. Stoica, P. and Moses, R.: Introduction to Spectral Analysis. Prentice Hall, 1997.

7. Soltanalian, M. and Stoica, P.: Design of perfect phase-quantized sequences with low peak-to-average-power ratio. In 2012 Proceedings of the 20th European Signal Processing Conference (EUSIPCO), pages 2576–2580. IEEE, August 2012.

8. Soltanalian, M., Stoica, P., Naghsh, M. M., and Maio, A. D.: Design of piecewise linear polyphase sequences with good correlation properties. In 2014 22nd European Signal Processing Conference (EUSIPCO), pages 1297–1301, September 2014.

9. Jensen, H. E. and Høholdt, T.: Binary sequences with good correlation properties. In Applied Algebra, Algebraic Algorithms and Error-Correcting Codes, eds. L. Huguet and A. Poli, pages 306–320, Berlin, Heidelberg, 1989. Springer Berlin Heidelberg.

10. Somaini, U.: Binary sequences with good autocorrelation and cross correlation properties. IEEE Transactions on Aerospace and Electronic Systems, AES-11(6):1226–1231, 1975.

11. Lin, R., Soltanalian, M., Tang, B., and Li, J.: Efficient design of binary sequences with low autocorrelation sidelobes. IEEE Transactions on Signal Processing, 67(24):6397–6410, 2019.

12. Golay, M.: A class of finite binary sequences with alternate auto-correlation values equal to zero (corresp.). IEEE Transactions on Information Theory, 18(3):449–450, September 2006.

13. Rudin, W.: Some theorems on fourier coefficients. Proceedings of the American Mathematical Society, 10(6):855–859, 1959.

14. Hoholdt, T. and Jensen, H. E.: Determination of the merit factor of legendre sequences. IEEE Transactions on Information Theory, 34(1):161–164, 1988.

15. Jedwab, J.: A survey of the merit factor problem for binary sequences. In Sequences and Their Applications - SETA 2004, eds. T. Helleseth, D. Sarwate, H.-Y. Song, and K. Yang, volume 3486 of Lecture Notes in Computer Science, pages 19–21. Springer Berlin / Heidelberg, 2005.

16. Høholdt, T.: The merit factor problem for binary sequences. In Applied Algebra, Algebraic Algorithms and Error-Correcting Codes, eds. M. P. C. Fossorier, H. Imai, S. Lin, and A. Poli, pages 51–59, Berlin, Heidelberg, 2006. Springer Berlin Heidelberg.

17. Adali, T., Schreier, P. J., and Scharf, L. L.: Complex-valued signal processing: The proper way to deal with impropriety. IEEE Transactions on Signal Processing, 59(11):5101–5125, November 2011.

18. Anttila, L., Valkama, M., and Renfors, M.: Circularity-based I/Q imbalance compensation in wideband direct-conversion receivers. IEEE Transactions on Vehicular Technology, 57(4):2099–2113, July 2008.

19. Rodriguez-Avila, R., Nunez-Vega, G., Parra-Michel, R., and Mendez-Vazquez, A.: Frequency-selective joint Tx/Rx I/Q imbalance estimation using Golay com-

plementary sequences. IEEE Transactions on Wireless Communications, 12(5):2171–2179, May 2013.

20. Stoica, P., He, H., and Li, J.: New algorithms for designing unimodular sequences with good correlation properties. IEEE Transactions on Signal Processing, 57(4):1415–1425, April 2009.

21. He, H.: Waveform Design for Active Sensing Systems — a Computational Approach. Doctoral dissertation, University of Florida, USA, 2011. AAI3497044.

22. Griffiths, H., Knott, P., and Koch, W.: Christian Hülsmeyer: Invention and demonstration of radar, 1904. IEEE Aerospace and Electronic Systems Magazine, 34(9):56–60, 2019.

23. Calderbank, R., Howard, S. D., and Moran, B.: Waveform diversity in radar signal processing. IEEE Signal Processing Magazine, 26(1):32–41, Jan 2009.

24. Gini, F., De Maio, A., and Patton, L.: Waveform Design and Diversity for Advanced Radar Systems, volume 22 of Electromagnetics and Radar Series. London: Institution of Engineering and Technology, 2012.

25. Kronauge, M. and Rohling, H.: New chirp sequence radar waveform. IEEE Transactions on Aerospace and Electronic Systems, 50(4):2870–2877, October 2014.

26. Patole, S. M., Torlak, M., Wang, D., and Ali, M.: Automotive radars: A review of signal processing techniques. IEEE Signal Processing Magazine, 34(2):22–35, March 2017.

27. Lien, J., Gillian, N., Karagozler, M. E., Amihood, P., Schwesig, C., Olson, E., Raja, H., and Poupyrev, I.: Soli: Ubiquitous gesture sensing with millimeter wave radar. ACM Trans. Graph., 35(4), July 2016.

28. Fishler, E., Haimovich, A., Blum, R., Chizhik, D., Cimini, L., and Valenzuela, R.: MIMO radar: an idea whose time has come. In Proceedings of the 2004 IEEE Radar Conference, pages 71–78, April 2004.

29. Robey, F. C., Coutts, S., Weikle, D., McHarg, J. C., and Cuomo, K.: MIMO radar theory and experimental results. In Conference Record of the Thirty-Eighth

Asilomar Conference on Signals, Systems and Computers, volume 1, pages 300–304, November 2004.

30. Fuhrmann, D. R. and San Antonio, G.: Transmit beamforming for MIMO radar systems using signal cross-correlation. IEEE Transactions on Aerospace and Electronic Systems, 44(1):171–186, January 2008.

31. Li, J. and Stoica, P.: MIMO radar with colocated antennas. IEEE Signal Processing Magazine, 24(5):106–114, September 2007.

32. Li, J., Stoica, P., Xu, L., and Roberts, W.: On parameter identifiability of MIMO radar. IEEE Signal Processing Letters, 14(12):968–971, December 2007.

33. Li, J. and Stoica, P.: MIMO Radar Signal Processing. Wiley - IEEE. Wiley, first edition, 2008.

34. Haimovich, A. M., Blum, R. S., and Cimini, L. J.: MIMO radar with widely separated antennas. IEEE Signal Processing Magazine, 25(1):116–129, 2008.

35. Forsythe, K. W. and Bliss, D. W.: Waveform correlation and optimization issues for MIMO radar. In Conference Record of the Thirty-Ninth Asilomar Conference on Signals, Systems and Computers, 2005., pages 1306–1310, October 2005.

36. MIMO radar. `https://en.wikipedia.org/wiki/MIMO_radar`, 2020. [Online; accessed: March 19, 2021].

37. Stoica, P., Li, J., and Xie, Y.: On probing signal design for MIMO radar. IEEE Transactions on Signal Processing, 55(8):4151–4161, August 2007.

38. Suleymanov, S.: Design and Implementation of an FMCW Radar Signal Processing Module for Automotive Applications. Master's thesis, University of Twente, August 2016.

39. Bliss, D. W. and Forsythe, K. W.: Multiple-input multiple-output (MIMO) radar and imaging: degrees of freedom and resolution. In The Thrity-Seventh Asilomar Conference on Signals, Systems Computers, 2003, volume 1, pages 54–59, November 2003.

40. Lehmann, N. H., Haimovich, A. M., Blum, R. S., and Cimini, L.: High resolution capabilities of MIMO radar. In 2006 Fortieth Asilomar Conference on Signals, Systems and Computers, pages 25–30, October 2006.

41. Fishler, E., Haimovich, A., Blum, R. S., Cimini, L. J., Chizhik, D., and Valenzuela, R. A.: Spatial diversity in radars–models and detection performance. IEEE Transactions on Signal Processing, 54(3):823–838, March 2006.

42. Godrich, H., Haimovich, A. M., and Blum, R. S.: Target localization accuracy gain in MIMO radar-based systems. IEEE Transactions on Information Theory, 56(6):2783–2803, June 2010.

43. He, Q., Blum, R. S., Godrich, H., and Haimovich, A. M.: Target velocity estimation and antenna placement for MIMO radar with widely separated antennas. IEEE Journal of Selected Topics in Signal Processing, 4(1):79–100, February 2010.

44. Bekkerman, I. and Tabrikian, J.: Target detection and localization using MIMO radars and sonars. IEEE Transactions on Signal Processing, 54(10):3873–3883, October 2006.

45. Stoica, P., Li, J., and Zhu, X.: Waveform synthesis for diversity-based transmit beampattern design. IEEE Transactions on Signal Processing, 56(6):2593–2598, June 2008.

46. Li, J., Stoica, P., and Zheng, X.: Signal synthesis and receiver design for MIMO radar imaging. IEEE Transactions on Signal Processing, 56(8):3959–3968, August 2008.

47. Li, H., Zhao, Y., Cheng, Z., and Feng, D.: Correlated LFM waveform set design for MIMO radar transmit beampattern. IEEE Geoscience and Remote Sensing Letters, 14(3):329–333, March 2017.

48. Soltanalian, M., Hu, H., and Stoica, P.: Single-stage transmit beamforming design for MIMO radar. Signal Processing, 102:132–138, 2014.

49. Ahmed, S., Thompson, J. S., Petillot, Y. R., and Mulgrew, B.: Finite alphabet constant-envelope waveform design for MIMO radar. IEEE Transactions on Signal Processing, 59(11):5326–5337, November 2011.

50. Cheng, Z., He, Z., Li, R., and Wang, Z.: Robust transmit beampattern matching synthesis for MIMO radar. Electronics Letters, 53(9):620–622, 2017.

51. Soltanalian, M. and Stoica, P.: Designing unimodular codes via quadratic optimization. IEEE Transactions on Signal Processing, 62(5):1221–1234, March 2014.

52. Cheng, Z., He, Z., Zhang, S., and Li, J.: Constant modulus waveform design for MIMO radar transmit beampattern. IEEE Transactions on Signal Processing, 65(18):4912–4923, September 2017.

53. Zhang, X., He, Z., Rayman-Bacchus, L., and Yan, J.: MIMO radar transmit beampattern matching design. IEEE Transactions on Signal Processing, 63(8):2049–2056, April 2015.

54. Cheng, Z., Lu, Y., He, Z., , Li, J., and Luo, X.: Joint optimization of covariance matrix and antenna position for MIMO radar transmit beampattern matching design. In 2018 IEEE Radar Conference (RadarConf18), pages 1073–1077, April 2018.

55. Cheng, Z., He, Z., Fang, M., Wang, Z., and Zhang, J.: Alternating direction method of multipliers for MIMO radar waveform design. In 2017 IEEE Radar Conference (RadarConf), pages 0367–0371, May 2017.

56. Zhang, Z., Zhao, Y., and Huang, J.: Array optimization for MIMO radar by genetic algorithms. In 2009 2nd International Congress on Image and Signal Processing, pages 1–4, 2009.

57. Saxena, P. and Kothari, A.: Optimal pattern synthesis of linear antenna array using grey wolf optimization algorithm. International Journal of Antennas and Propagation, 2016:1205970, Apr 2016.

58. Understanding FMCW automotive radar: And how to obtain precise measurements for mission-critical radar devices. Technical report, Keysight Technologies, 07 2020.

59. Automotive radar basics. `https://www.everythingrf.com/community/automotive-radar-basics`, 2020. [Online; accessed: March 19, 2021].

60. Tang, B., Huang, W., and Li, J.: Slow-time coding for mutual interference mitigation. In 2018 IEEE International Conference on Acoustics, Speech and Signal Processing (ICASSP), pages 6508–6512, 2018.

61. Wang, P., Boufounos, P., Mansour, H., and Orlik, P. V.: Slow-time MIMO-FMCW automotive radar detection with imperfect waveform separation. In IEEE International Conference on Acoustics, Speech and Signal Processing (ICASSP), pages 8634–8638, 2020.

62. Lin, J.-J., Li, Y.-P., Hsu, W.-C., and Lee, T.-S.: Design of an fmcw radar baseband signal processing system for automotive application. SpringerPlus, 5(1):42, Jan 2016.

63. Barrick, D. and (U.S.), E. R. L.: FM/CW Radar Signals and Digital Processing. Number v. 55 in FM/CW Radar Signals and Digital Processing. Environmental Research Laboratories, 1973.

64. Stove, A. G.: Linear FMCW radar techniques. IEE Proceedings F: Radar and Signal Processing, 139(5):343–350, October 1992.

65. Engels, F., Heidenreich, P., Zoubir, A. M., Jondral, F. K., and Wintermantel, M.: Advances in automotive radar: A framework on computationally efficient high-resolution frequency estimation. IEEE Signal Processing Magazine, 34(2):36–46, 2017.

66. Bilik, I., Longman, O., Villeval, S., and Tabrikian, J.: The rise of radar for autonomous vehicles: Signal processing solutions and future research directions. IEEE Signal Processing Magazine, 36(5):20–31, 2019.

67. Ren, J. and Li, J.: One-bit digital radar. In 2017 51st Asilomar Conference on Signals, Systems, and Computers, pages 1142–1146, October 2017.

68. Ameri, A., Bose, A., Li, J., and Soltanalian, M.: One-bit radar processing with time-varying sampling thresholds. IEEE Transactions on Signal Processing, 67(20):5297–5308, October 2019.

69. Khobahi, S. and Soltanalian, M.: Signal recovery from 1-bit quantized noisy samples via adaptive thresholding. In 2018 52nd Asilomar Conference on Signals, Systems, and Computers, pages 1757–1761, October 2018.

70. Laska, J. N., Wen, Z., Yin, W., and Baraniuk, R. G.: Trust, but verify: Fast and accurate signal recovery from 1-bit compressive measurements. IEEE Transactions on Signal Processing, 59(11):5289–5301, November 2011.

71. Dabeer, O. and Karnik, A.: Signal parameter estimation using 1-bit dithered quantization. IEEE Transactions on Information Theory, 52(12):5389–5405, 2006.

72. Cvetkovic, Z. and Daubechies, I.: Single-bit oversampled A/D conversion with exponential accuracy in the bit-rate. In Proceedings of Data Compression Conference, pages 343–352. IEEE, 2000.

73. Jacques, L., Laska, J. N., Boufounos, P. T., and Baraniuk, R. G.: Robust 1-bit compressive sensing via binary stable embeddings of sparse vectors. IEEE Transactions on Information Theory, 59(4):2082–2102, April 2013.

74. Stoica, P., He, H., and Li, J.: Optimization of the receive filter and transmit sequence for active sensing. IEEE Transactions on Signal Processing, 60(4):1730–1740, April 2012.

75. Stoica, P., Li, J., and Xue, M.: Transmit codes and receive filters for radar. IEEE Signal Processing Magazine, 25(6):94–109, November 2008.

76. Soltanalian, M., Tang, B., Li, J., and Stoica, P.: Joint design of the receive filter and transmit sequence for active sensing. IEEE Signal Processing Letters, 20(5):423–426, May 2013.

77. Chien, J. and Lee, C.: Deep unfolding for topic models. IEEE Transactions on Pattern Analysis and Machine Intelligence, 40(2):318–331, February 2018.

78. Wisdom, S., Powers, T., Pitton, J., and Atlas, L.: Building recurrent networks by unfolding iterative thresholding for sequential sparse recovery. In 2017 IEEE International Conference on Acoustics, Speech and Signal Processing (ICASSP), pages 4346–4350, March 2017.

79. Wisdom, S., Hershey, J., Le Roux, J., and Watanabe, S.: Deep unfolding for multichannel source separation. In 2016 IEEE International Conference on Acoustics, Speech and Signal Processing (ICASSP), pages 121–125, March 2016.

80. Hershey, J. R., Roux, J. L., and Weninger, F.: Deep unfolding: Model-based inspiration of novel deep architectures. ArXiv, abs/1409.2574, 2014.

81. Khobahi, S., Naimipour, N., Soltanalian, M., and Eldar, Y. C.: Deep signal recovery with one-bit quantization. In ICASSP 2019 - 2019 IEEE International Conference on Acoustics, Speech and Signal Processing (ICASSP), pages 2987–2991, May 2019.

82. Bose, A. and Soltanalian, M.: Constructing binary sequences with good correlation properties: An efficient analytical-computational interplay. IEEE Transactions on Signal Processing, 66(11):2998–3007, June 2018.

83. Bose, A. and Soltanalian, M.: Efficient construction of polyphase sequences with optimal peak sidelobe level growth. In 2017 IEEE Global Conference on Signal and Information Processing (GlobalSIP), pages 81–85, November 2017.

84. Sarwate, D. V.: Meeting the Welch bound with equality. In Sequences and their Applications (SETA), pages 79–102. New York: Springer, 1999.

85. He, H., Stoica, P., and Li, J.: Designing unimodular sequence sets with good correlations - including an application to MIMO radar. IEEE Transactions on Signal Processing, 57(11):4391–4405, November 2009.

86. Mertens, S.: Exhaustive search for low-autocorrelation binary sequences. Journal of Physics A: Mathematical and General, 29(18):L473, 1996.

87. Dittes, F.-M.: Optimization on rugged landscapes: A new general purpose Monte Carlo approach. Physical Review Letters, 76:4651–4655, June 1996.

88. Bernasconi, J.: Low autocorrelation binary sequences: Statistical mechanics and configuration space analysis. Journal de Physique Archives, 48(4):559–567, 1987.

89. Golay, M. J. E. and Harris, D. B.: A new search for skewsymmetric binary sequences with optimal merit factors. IEEE Transactions on Information Theory, 36(5):1163–1166, September 1990.

90. Soltanalian, M. and Stoica, P.: Computational design of sequences with good correlation properties. IEEE Transactions on Signal Processing, 60(5):2180–2193, May 2012.

91. Jedwab, J. and Yoshida, K.: The peak sidelobe level of families of binary sequences. IEEE Transactions on Information Theory, 52(5):2247–2254, May 2006.

92. Golomb, S. W. and Gong, G.: Signal Design for Good Correlation: for Wireless Communication, Cryptography, and Radar. Cambridge, Cambridge University Press, 2005.

93. He, H., Li, J., and Stoica, P.: Waveform Design for Active Sensing Systems: A Computational Approach. Cambridge University Press, 2012.

94. Ling, J., He, H., Li, J., Roberts, W., and Stoica, P.: Covert underwater acoustic communications. Journal of the Acoustical Society of America, 128(5):2898–2909, November 2010.

95. Stoica, P., He, H., and Li, J.: On designing sequences with impulse-like periodic correlation. IEEE Signal Processing Letters, 16(8):703–706, August 2009.

96. Kocabas, S. and Atalar, A.: Binary sequences with low aperiodic autocorrelation for synchronization purposes. IEEE Communications Letters, 7(1):36–38, January 2003.

97. Tseng, S. M. and Bell, M.: Asynchronous multicarrier DS-CDMA using mutually orthogonal complementary sets of sequences. IEEE Transactions on Communications, 48(1):53–59, January 2000.

98. Spasojevic, P. and Georghiades, C.: Complementary sequences for ISI channel estimation. IEEE Transactions on Information Theory, 47(3):1145–1152, March 2001.

99. Zhang, Z., Zeng, F., and Xuan, G.: Design of complementary sequence sets based on orthogonal matrixes. In International Conference on Communications, Circuits and Systems (ICCCAS), pages 383–387, July 2010.

100. Golay, M. J. E.: Multi-slit spectrometry. Journal of the Optical Society of America, 39(6):437, 1949.

101. Golay, M. J. E.: Complementary series. IRE Transactions on Information Theory, 7(2):82–87, April 1961.

102. Davis, J. and Jedwab, J.: Peak-to-mean power control in OFDM, Golay complementary sequences, and Reed-Muller codes. IEEE Transactions on Information Theory, 45(7):2397–2417, November 1999.

103. Turyn, R.: Ambiguity functions of complementary sequences (corresp.). IEEE Transactions on Information Theory, 9(1):46–47, January 1963.

104. Tanada, Y.: Synthesis of a set of real-valued shift-orthogonal finite-length PN sequences. In IEEE 4th International Symposium on Spread Spectrum Techniques and Applications Proceedings, volume 1, pages 58–62, September 1996.

105. Soltanalian, M. and Stoica, P.: On prime root-of-unity sequences with perfect periodic correlation. IEEE Transactions on Signal Processing, 62(20):5458–5470, August 2014.

106. Parker, M.: Even length binary sequence families with low negaperiodic autocorrelation. In Applied Algebra, Algebraic Algorithms and Error-Correcting Codes, eds. S. Boztas and I. Shparlinski, volume 2227 of Lecture Notes in Computer Science, pages 200–209. Springer Berlin / Heidelberg, 2001.

107. Bomer, L. and Antweiler, M.: Binary and biphase sequences and arrays with low periodic autocorrelation sidelobes. In International Conference on Acoustics, Speech, and Signal Processing (ICASSP), volume 3, pages 1663–1666, April 1990.

108. Moon, J. W. and Moser, L.: On the correlation function of random binary sequences. SIAM Journal on Applied Mathematics, 16(2):340–343, 1968.

109. Wang, S.: Efficient heuristic method of search for binary sequences with good aperiodic autocorrelations. Electronics Letters, 44(12):731–732, 2008.

110. Song, J., Babu, P., and Palomar, D. P.: Optimization methods for designing sequences with low autocorrelation sidelobes. IEEE Transactions on Signal Processing, 63(15):3998–4009, August 2015.

111. Park, K. H., Song, H. Y., Kim, D. S., and Golomb, S. W.: Optimal families of perfect polyphase sequences from the array structure of Fermat-Quotient sequences. IEEE Transactions on Information Theory, 62(2):1076–1086, February 2016.

112. Bose, A. and Soltanalian, M.: Non-convex shredded signal reconstruction via sparsity enhancement. In 2017 IEEE International Conference on Acoustics, Speech and Signal Processing (ICASSP), pages 4691–4695, March 2017.

113. Bose, A., Mohammadi, N., and Soltanalian, M.: Designing signals with good correlation and distribution properties. In 2018 IEEE International Conference on Acoustics, Speech and Signal Processing (ICASSP), pages 4349–4353, April 2018.

114. Maiti, S., Bose, A., Agarwal, C., Sarkar, S. K., and Islam, N.: An improved method of pre-filter based image watermarking in DWT domain. International Journal of Computer Science and Technology, 4(1):133–140, 2013.

115. Agarwal, C., Bose, A., Maiti, S., Islam, N., and Sarkar, S. K.: Enhanced data hiding method using DWT based on saliency model. In International Conference on Signal Processing, Computing and Control (ISPCC), 2013, pages 1–6. IEEE, 2013.

116. Maity, S. P. and Kundu, M. K.: A blind CDMA image watermarking scheme in wavelet domain. In International Conference on Image Processing (ICIP), volume 4, pages 2633–2636. IEEE, 2004.

117. Cox, I. J., Kilian, J., Leighton, F. T., and Shamoon, T.: Secure spread spectrum watermarking for multimedia. IEEE Transactions on Image Processing, 6:1673–1687, 1997.

118. Fang, Y., Huang, J., and Shi, Y. Q.: Image watermarking algorithm applying CDMA. In International Symposium on Circuits and Systems (ISCAS), volume 2, pages 948–951. IEEE, 2003.

119. Soltanalian, M., Naghsh, M. M., and Stoica, P.: On meeting the peak correlation bounds. IEEE Transactions on Signal Processing, 62(5):1210–1220, 2014.

120. Schmidt, K.-U.: Sequences with small correlation. Designs, Codes and Cryptography, 78(1):237–267, January 2016.

121. Leung, K. H. and Schmidt, B.: The field descent method. Designs, Codes and Cryptography, 36(2):171–188, August 2005.

122. Levanon, N. and Mozeson, E.: Radar Signals. Wiley - IEEE. New York, Wiley, 2004.

123. Cohen, M. N., Fox, M. R., and Baden, J. M.: Minimum peak sidelobe pulse compression codes. In IEEE 1990 International Radar Conference, pages 633–638. IEEE, 1990.

124. Coxson, G. E., Hirschel, A., and Cohen, M. N.: New results on minimum-PSL binary codes. In IEEE Radar Conference, pages 153–156. IEEE, 2001.

125. Coxson, G. and Russo, J.: Efficient exhaustive search for optimal-peak-sidelobe binary codes. IEEE Transactions on Aerospace and Electronic Systems, 41:302–308, 2005.

126. Turyn, R. J.: Sequences with small correlation. In Error Correcting Codes, ed. H. B. Mann, pages 195–228. New York, Wiley, 1968.

127. Lindner, J.: Binary sequences up to length 40 with best possible autocorrelation function. Electronics Letters, 11:507–507, 1975.

128. Elders-Boll, H., Schotten, H., and Busboom, A.: A comparative study of optimization methods for the synthesis of binary sequences with good correlation properties. In IEEE Symposium on Communication and Vehicular Technology in the Benelux, pages 24–31. IEEE, 1997.

129. Ein-Dor, L., Kanter, I., and Kinzel, W.: Low autocorrelated multiphase sequences. Physical Review E, 65:020102, January 2002.

130. Mercer, I. D.: Autocorrelations of random binary sequences. Combinatorics, Probability and Computing, 15(05):663–671, 2006.

131. Dmitriev, D. and Jedwab, J.: Bounds on the growth rate of the peak sidelobe level of binary sequences. Advances in Mathematics of Communications, page 475, 2007.

132. Welch, L.: Lower bounds on the maximum cross correlation of signals. IEEE Transactions on Information Theory, 20(3):397–399, 1974.

133. He, H., Stoica, P., and Li, J.: On aperiodic-correlation bounds. IEEE Signal Processing Letters, 17(3):253–256, March 2010.

134. Liang, J., So, H. C., Li, J., and Farina, A.: Unimodular sequence design based on alternating direction method of multipliers. IEEE Transactions on Signal Processing, 64(20):5367–5381, 2016.

135. Li, Y. and Vorobyov, S. A.: Fast algorithms for designing unimodular waveform(s) with good correlation properties. IEEE Transactions on Signal Processing, 66(5):1197–1212, March 2018.

136. Sayed, A. H.: Adaptive Filters. John Wiley & Sons, Inc., 2008.

137. Karystinos, G. and Liavas, A.: Efficient computation of the binary vector that maximizes a rank-deficient quadratic form. IEEE Transactions on Information Theory, 56(7):3581–3593, July 2010.

138. Kyrillidis, A. T. and Karystinos, G. N.: Rank-deficient quadratic-form maximization over M-phase alphabet: Polynomial-complexity solvability and algorithmic developments. In IEEE International Conference on Acoustics, Speech and Signal Processing (ICASSP), pages 3856–3859, Prague, Czech Republic, May 2011. IEEE.

139. Gold, R.: Optimal binary sequences for spread spectrum multiplexing. IEEE Transactions on Information Theory, 13(4):619–621, October 1967.

140. Kasami, T.: Weight distribution formula for some class of cyclic codes. Technical report, Coordinated Science Laboratory, University of Illinois, April 1966.

141. Rushanan, J.: Weil sequences: A family of binary sequences with good correlation properties. In IEEE International Symposium on Information Theory, pages 1648–1652, Seattle, Washington, USA, July 2006.

142. Pott, A.: Finite Geometry and Character Theory. Lecture Notes in Mathematics. Springer-Verlag Berlin Heidelberg, 1995.

143. Beth, T., Jungnickel, D., and Lenz, H.: Design Theory. Design Theory. Cambridge University Press, 1999.

144. Hughes, E. J.: Radar waveform optimisation as a many-objective application benchmark. In Proceedings of Evolutionary Multi-Criterion Optimization: 4th International Conference, Matsushima, Japan, eds. S. Obayashi, K. Deb, C. Poloni, T. Hiroyasu, and T. Murata, pages 700–714. Berlin, Heidelberg, Springer Berlin Heidelberg, March 2007.

145. Haykin, S.: Cognitive radar: a way of the future. IEEE Signal Processing Magazine, 23(1):30–40, January 2006.

146. Jansson, D.: Mathematical modeling of the human smooth pursuit system. Doctoral dissertation, Uppsala University, Division of Systems and Control, Automatic control, 2014.

147. Itti, L.: New eye-tracking techniques may revolutionize mental health screening. Neuron, 88(3):442–444, 2015.

148. Marino, S., Sessa, E., Di Lorenzo, G., Lanzafame, P., Scullica, G., Bramanti, A., La Rosa, F., Iannizzotto, G., Bramanti, P., and Di Bella, P.: Quantitative analysis of pursuit ocular movements in Parkinson's Disease by using a video-based eye tracking system. European Neurology, 58(4):193–197, November 2007.

149. Nakamura, T., Kanayama, R., Sano, R., Ohki, M., Kimura, Y., Aoyagi, M., and Koike, Y.: Quantitative analysis of ocular movements in Parkinson's Disease. Acta Oto-Laryngologica, 111(sup481):559–562, 1991.

150. White, O. B., Saint-Cyr, J. A., Tomlinson, R. D., and Sharpe, J. A.: Ocular motor deficits in Parkinson's Disease: Ii. control of the saccadic and smooth pursuit systems. Brain, 106(3):571, 1983.

151. L. Kuipers, H. N.: Uniform distribution of Sequences, (Pure and Applied Mathematics). John Wiley and Sons Inc., 1974.

152. Schoißengeier, J. and Tričković, S. B.: On the divergence of a certain series. Journal of Mathematical Analysis and Applications, 324(1):238–247, 2006.

153. Arriaga-Trejo, I. A., Bose, A., Orozco-Lugo, A. G., and Soltanalian, M.: Design of unimodular sequence sets with good correlation and complementary correlation properties. In 2018 IEEE Global Conference on Signal and Information Processing (GlobalSIP), pages 121–125, November 2018.

154. Arriaga-Trejo, I. A., Orozco-Lugo, A. G., and Flores-Troncoso, J.: Design of unimodular sequences with good autocorrelation and good complementary autocorrelation properties. IEEE Signal Processing Letters, 24(8):1153–1157, August 2017.

155. Picinbono, B. and Bondon, P.: Second-order statistics of complex signals. IEEE Transactions on Signal Processing, 45(2):411–420, February 1997.

156. Wang, Y. C., Dong, L., Xue, X., and Yi, K. .: On the design of constant modulus sequences with low correlation sidelobes levels. IEEE Communications Letters, 16(4):462–465, April 2012.

157. Song, J., Babu, P., and Palomar, D. P.: Sequence set design with good correlation properties via majorization-minimization. IEEE Transactions on Signal Processing, 64(11):2866–2879, June 2016.

158. Tang, L., Zhu, Y., and Fu, Q.: Designing waveform sets with good correlation and stopband properties for MIMO radar via the gradient-based method. Sensors, 17(5), 2017.

159. Tang, L., Zhu, Y., and Fu, Q.: Designing PAR-constrained periodic/aperiodic sequence via the gradient-based method. Signal Processing, 147:11–22, 2018.

160. Arriaga-Trejo, I. A.: Construction of complementary sets of sequences with low aperiodic correlation and complementary correlation. In 2016 IEEE Global Conference on Signal and Information Processing (GlobalSIP), pages 85–89, December 2016.

161. Bose, A., Arriaga-Trejo, I. A., Orozco-Lugo, A. G., and Soltanalian, M.: Generalized cyclic algorithms for designing unimodular sequence sets with good (complementary) correlation properties. In 2018 IEEE 10th Sensor Array

and Multichannel Signal Processing Workshop (SAM), pages 287–291, July 2018.

162. Byrd, R., Lu, P., Nocedal, J., and Zhu, C.: A limited memory algorithm for bound constrained optimization. SIAM Journal on Scientific Computing, 16(5):1190–1208, 1995.

163. Bose, A., Khobahi, S., and Soltanalian, M.: Efficient waveform covariance matrix design and antenna selection for MIMO radar. Signal Processing, 183:107985, 2021.

164. Bose, A., Khobahi, S., and Soltanalian, M.: Joint optimization of waveform covariance matrix and antenna selection for MIMO radar. In 2019 53rd Asilomar Conference on Signals, Systems, and Computers, pages 1534–1538, 2019.

165. Khobahi, S., Bose, A., and Soltanalian, M.: Deep radar waveform design for efficient automotive radar sensing. In 2020 IEEE 11th Sensor Array and Multichannel Signal Processing Workshop (SAM), pages 1–5, 2020.

166. Cui, G., Li, H., and Rangaswamy, M.: MIMO radar waveform design with constant modulus and similarity constraints. IEEE Transactions on Signal Processing, 62(2):343–353, January 2014.

167. Cheng, Z., He, Z., Liao, B., and Fang, M.: MIMO radar waveform design with PAPR and similarity constraints. IEEE Transactions on Signal Processing, 66(4):968–981, February 2018.

168. Lipor, J., Ahmed, S., and Alouini, M.: Fourier-based transmit beampattern design using MIMO radar. IEEE Transactions on Signal Processing, 62(9):2226–2235, May 2014.

169. Bouchoucha, T., Ahmed, S., Al-Naffouri, T. Y., and Alouini, M.: Closed-form solution to directly design face waveforms for beampatterns using planar array. In 2015 IEEE International Conference on Acoustics, Speech and Signal Processing (ICASSP), pages 2359–2363, April 2015.

170. Bouchoucha, T., Ahmed, S., Al-Naffouri, T. Y., and Alouini, M.: DFT-based closed-form covariance matrix and direct waveforms design for MIMO radar

to achieve desired beampatterns. IEEE Transactions on Signal Processing, 65(8):2104–2113, April 2017.

171. Ahmed, S., Thompson, J. S., Petillot, Y. R., and Mulgrew, B.: Unconstrained synthesis of covariance matrix for MIMO radar transmit beampattern. IEEE Transactions on Signal Processing, 59(8):3837–3849, August 2011.

172. Boyd, S., Parikh, N., Chu, E., Peleato, B., and Eckstein, J.: Distributed optimization and statistical learning via the alternating direction method of multipliers. Foundations and Trends in Machine Learning, 3(1):1–122, January 2011.

173. Nocedal, J. and Wright, S.: Numerical optimization. Springer Science & Business Media, 2006.

174. Da Ronco, C. C. and Benini, E.: A Simplex-Crossover-Based Multi-Objective Evolutionary Algorithm, pages 583–598. Dordrecht, Springer Netherlands, 2014.

175. Grant, M. and Boyd, S.: CVX: Matlab software for disciplined convex programming, version 2.1. `http://cvxr.com/cvx`, March 2014.

176. Bose, A., Tang, B., Huang, W., Soltanalian, M., and Li, J.: Waveform design for mutual interference mitigation in automotive radar. 2021.

177. Bose, A., Tang, B., Soltanalian, M., and Li, J. L.: Mutual interference mitigation for multiple connected automotive radar systems. 2021.

178. Patole, S. M., Torlak, M., Wang, D., and Ali, M.: Automotive radars: A review of signal processing techniques. IEEE Signal Processing Magazine, 34(2):22–35, 2017.

179. Schneider, M.: Automotive radar: Status and trends. In In Proceedings of the German Microwave Conference GeMIC 2005, pages 144–147, 2005.

180. Rohling, H.: Milestones in radar and the success story of automotive radar systems. In 11-th International Radar Symposium, pages 1–6, 2010.

181. Dickmann, J., Klappstein, J., Hahn, M., Appenrodt, N., Bloecher, H., Werber, K., and Sailer, A.: Automotive radar the key technology for autonomous driving: From detection and ranging to environmental understanding. In IEEE Radar Conference (RadarConf), pages 1–6, 2016.

182. Lien, J., Gillian, N., Karagozler, M. E., Amihood, P., Schwesig, C., Olson, E., Raja, H., and Poupyrev, I.: Soli: Ubiquitous gesture sensing with millimeter wave radar. ACM Trans. Graph., 35(4), July 2016.

183. Wang, S., Song, J., Lien, J., Poupyrev, I., and Hilliges, O.: Interacting with soli: Exploring fine-grained dynamic gesture recognition in the radio-frequency spectrum. In Proceedings of the 29th Annual Symposium on User Interface Software and Technology, UIST '16, page 851–860, New York, NY, USA, 2016. Association for Computing Machinery.

184. Saponara, S., Greco, M. S., and Gini, F.: Radar-on-chip/in-package in autonomous driving vehicles and intelligent transport systems: opportunities and challenges. IEEE Signal Processing Magazine, 36(5):71–84, 2019.

185. Greco, M. S., Li, J., Long, T., and Zoubir, A.: Advances in radar systems for modern civilian and commercial applications: Part 1 [from the guest editors]. IEEE Signal Processing Magazine, 36(4):13–15, 2019.

186. Greco, M. S., Li, J., Long, T., and Zoubir, A.: Advances in radar systems for modern civilian and commercial applications: Part 2 [from the guest editors]. IEEE Signal Processing Magazine, 36(5):16–18, 2019.

187. Dokhanchi, S. H., Mysore, B. S., Mishra, K. V., and Ottersten, B.: A mmwave automotive joint radar-communications system. IEEE Transactions on Aerospace and Electronic Systems, 55(3):1241–1260, 2019.

188. Dokhanchi, S. H., Bhavani Shankar, M. R., Mishra, K. V., and Ottersten, B.: Multi-constraint spectral co-design for colocated MIMO radar and MIMO communications. In Proceedings of the IEEE International Conference on Acoustics, Speech and Signal Processing (ICASSP), pages 4567–4571, 2020.

189. Sedighi, S., Shankar, B., Mishra, K. V., and Ottersten, B.: Optimum design for sparse FDA-MIMO automotive radar. In 2019 53rd Asilomar Conference on Signals, Systems, and Computers, pages 913–918, 2019.

190. Alaee-Kerahroodi, M., Shankar, B., Naghsh, M. M., and Ottersten, B.: CDM-MIMO in next-generation mmWave automotive radar sensors. In Proceedings of URSI AP-RASC, 2019.

191. Uysal, F.: Synchronous and asynchronous radar interference mitigation. IEEE Access, 7:5846–5852, 2019.

192. Brooker, G. M.: Mutual interference of millimeter-wave radar systems. IEEE Transactions on Electromagnetic Compatibility, 49(1):170–181, 2007.

193. Rao, S. and Mani, A. V.: Interference characterization in fmcw radars. In 2020 IEEE Radar Conference (RadarConf20), pages 1–6, 2020.

194. Wang, P., Millar, D., Parsons, K., and Orlik, P. V.: Nonlinearity correction for range estimation in FMCW millimeter-wave automotive radar. In IEEE MTT-S International Wireless Symposium (IWS), pages 1–3, 2018.

195. Goppelt, M., Blöcher, H. L., and Menzel, W.: Automotive radar - investigation of mutual interference mechanisms. Advances in Radio Science, 8:55–60, September 2010.

196. Goppelt, M., Blöcher, H. L., and Menzel, W.: Analytical investigation of mutual interference between automotive FMCW radar sensors. In 2011 German Microwave Conference, pages 1–4, 2011.

197. Bourdoux, A., Parashar, K., and Bauduin, M.: Phenomenology of mutual interference of FMCW and PMCW automotive radars. In 2017 IEEE Radar Conference (RadarConf), pages 1709–1714, 2017.

198. Yang, X. and Ji, M.: Connected Vehicle System Design for Signalized Arterials. University of Utah, 2019. [Online; accessed: March 19, 2021].

199. Aubry, A., De Maio, A., Jiang, B., and Zhang, S.: Ambiguity function shaping for cognitive radar via complex quartic optimization. IEEE Transactions on Signal Processing, 61(22):5603–5619, 2013.

200. Chen, C.-Y. and Vaidyanathan, P.: MIMO radar ambiguity properties and optimization using frequency-hopping waveforms. IEEE Transactions on Signal Processing, 56(12):5926–5936, 2008.

201. He, H., Stoica, P., and Li, J.: On synthesizing cross ambiguity functions. In IEEE International Conference on Acoustics, Speech and Signal Processing (ICASSP), pages 3536–3539. IEEE, 2011.

202. Razaviyayn, M., Hong, M., and Luo, Z.-Q.: A unified convergence analysis of block successive minimization methods for nonsmooth optimization. SIAM Journal on Optimization, 23(2):1126–1153, 2013.

203. Aubry, A., De Maio, A., Zappone, A., Razaviyayn, M., and Luo, Z.: A new sequential optimization procedure and its applications to resource allocation for wireless systems. IEEE Transactions on Signal Processing, 66(24):6518–6533, 2018.

204. Tang, B., Naghsh, M. M., and Tang, J.: Relative entropy-based waveform design for MIMO radar detection in the presence of clutter and interference. IEEE Transactions on Signal Processing, 63(14):3783–3796, 2015.

205. Tang, B. and Tang, J.: Joint design of transmit waveforms and receive filters for MIMO radar space-time adaptive processing. IEEE Transactions on Signal Processing, 64(18):4707–4722, 2016.

206. Naghsh, M. M., Modarres-Hashemi, M., ShahbazPanahi, S., Soltanalian, M., and Stoica, P.: Unified optimization framework for multi-static radar code design using information-theoretic criteria. IEEE Transactions on Signal Processing, 61(21):5401–5416, 2013.

207. Hu, H., Soltanalian, M., Stoica, P., and Zhu, X.: Locating the few: Sparsity-aware waveform design for active radar. IEEE Transactions on Signal Processing, 65(3):651–662, February 2017.

208. Tropp, J., Dhillon, I., Heath, R., and Strohmer, T.: Designing structured tight frames via an alternating projection method. IEEE Transactions on Information Theory, 51(1):188–209, January 2005.

209. Bose, A., Ameri, A., and Soltanalian, M.: Waveform design for one-bit radar systems under uncertain interference statistics. arXiv preprint arXiv:1912.00556, December 2019.

210. Spafford, L. J.: Optimum radar signal processing in clutter. IEEE Transactions on Information Theory, 14(5):734–743, September 1968.

211. Van Vleck, J. H. and Middleton, D.: The spectrum of clipped noise. Proceedings of the IEEE, 54(1):2–19, 1966.

212. Bussgang, J. J.: Crosscorrelation functions of amplitude-distorted Gaussian signals. Technical Report 216, March 1952.

213. Liu, C.-L. and Vaidyanathan, P. P.: One-bit sparse array DOA estimation. In 2017 IEEE International Conference on Acoustics, Speech and Signal Processing (ICASSP),, pages 3126–3130. IEEE, 2017.

214. Dinkelbach, W.: On nonlinear fractional programming. Management Science, 13(7):492–498, 1967.

215. Rohling, H. and Kronauge, M.: Continuous waveforms for automotive radar systems, pages 173–205. Radar, Sonar & Navigation. Institution of Engineering and Technology, 2012.

216. Rohling, H. and Meinecke, M.: Waveform design principles for automotive radar systems. In 2001 CIE International Conference on Radar Proceedings, pages 1–4, October 2001.

217. Rohling, H. and Moller, C.: Radar waveform for automotive radar systems and applications. In 2008 IEEE Radar Conference, pages 1–4, May 2008.

218. Naghsh, M. M., Soltanalian, M., and Modarres-Hashemi, M.: Radar code design for detection of moving targets. IEEE Transactions on Aerospace and Electronic Systems, 50(4):2762–2778, 2014.

219. Skolnik, M.: Radar Handbook, Third Edition. Electronics electrical engineering. McGraw-Hill Education, 2008.

220. Aubry, A., Maio, A. D., Piezzo, M., Farina, A., and Wicks, M.: Cognitive design of the receive filter and transmitted phase code in reverberating environment. IET Journal on Radar, Sonar, and Navigation, 6(9):822–833, December 2012.

221. Aubry, A., Maio, A. D., Farina, A., and Wicks, M.: Knowledge-aided (potentially cognitive) transmit signal and receive filter design in signal-dependent clutter. IEEE Transactions on Aerospace and Electronic Systems, 49(1):93–117, January 2013.

222. Naghsh, M. M., Soltanalian, M., Stoica, P., Modarres-Hashemi, M., De Maio, A., and Aubry, A.: A Doppler robust design of transmit sequence and receive filter in the presence of signal-dependent interference. IEEE Transactions on Signal Processing, 62(4):772–785, February 2014.

223. Li, J., Xu, L., Stoica, P., Forsythe, K., and Bliss, D.: Range compression and waveform optimization for MIMO radar: A Cramer-Rao bound based study. IEEE Transactions on Signal Processing, 56(1):218–232, 2008.

224. Xu, L. and Li, J.: Iterative generalized-likelihhod ratio test for MIMO radar. IEEE Transactions on Signal Processing, 55:2375–2385, 2007.

225. Bell, M. R.: Information theory and radar waveform design. IEEE Transactions on Information Theory, 39(5):1578–1597, 1993.

226. Friedlander, B.: Waveform design for MIMO radars. IEEE Transactions on Aerospace and Electronic Systems, 43:1227–1238, July 2007.

227. De Maio, A., Huang, Y., Piezzo, M., Zhang, S., and Farina, A.: Design of optimized radar codes with a peak to average power ratio constraint. IEEE Transactions on Signal Processing, 59:2683–2697, June 2011.

228. Blum, R. S. and Yang, Y.: MIMO radar waveform design based on mutual information and minimum mean-square error estimation. IEEE Transactions on Aerospace and Electronic Systems, 43:330–343, January 2007.

229. Xu, L., Li, J., and Stoica, P.: Target detection and parameter estimation for MIMO radar systems. IEEE Transactions on Aerospace and Electronic Systems, 44(3):927–939, 2008.

230. Delong, D. F. and Hofstteter, E. M.: On the design of optimum radar waveforms for clutter rejection. IEEE Transactions on Information Theory, 13(3):454–463, July 1967.

231. Tang, B., Tang, J., and Peng, Y.: MIMO radar waveform design in colored noise based on information theory. IEEE Transactions on Signal Processing, 58:4684–4697, September 2010.

232. Song, X., Willett, P., Zhou, S., and Luh, P.: The MIMO radar and jammer games. Signal Processing, IEEE Transactions on, 60(2):687–699, February 2012.

233. Kay, S. M.: Waveform design for multistatic radar detection. IEEE Transactions on Aerospace and Electronic Systems, 45:1153–1165, July 2009.

234. Mason, E., Yonel, B., and Yazici, B.: Deep learning for radar. In 2017 IEEE Radar Conference (RadarConf), pages 1703–1708, May 2017.

235. Khobahi, S. and Soltanalian, M.: Model-aware deep architectures for one-bit compressive variational autoencoding. arXiv preprint arXiv:1911.12410, 2019.

236. Tofallis, C.: Fractional programming: Theory, methods and applications. Journal of the Operational Research Society, 49(8):895–895, 1998.

237. Soltanalian, M., Gharanjik, A., Shankar, M. R. B., and Oftersten, B.: Grab-n-pull: An optimization framework for fairness-achieving networks. In 2016 IEEE International Conference on Acoustics, Speech and Signal Processing (ICASSP), pages 3301–3305, March 2016.

238. Khobahi, S., Soltanalian, M., Jiang, F., and Swindlehurst, A. L.: Optimized transmission for parameter estimation in wireless sensor networks. IEEE Transactions on Signal and Information Processing over Networks, 2019.

239. Vandenberghe, L. and Boyd, S.: Semidefinite programming. SIAM Review, 38(1):49–95, 1996.

VITA

ARINDAM BOSE

EDUCATION

Ph.D., University of Illinois at Chicago, Chicago, IL, USA, 2021
M.S., University of Illinois at Chicago, Chicago, IL, USA, 2020
B.Tech., West Bengal University of Technology, Kolkata, India, 2012

EXPERIENCE

Senior Research Engineer in KMB Telematics, Arlington, VA, USA
Nov. 2020 – Present
Research Assistant in UIC WaveOPT Laboratory, Electrical and Computer Engineering Department, Chicago, IL, USA
Jul. 2016 – Nov. 2020
Teaching Assistant in Electrical and Computer Engineering Department, Chicago, IL, USA
Aug. 2015 – Nov. 2020
Summer Intern in KMB Telematics, Arlington, VA, USA
May. 2019 – Aug. 2019
Summer Intern in Mitsubishi Electric Research Laboratories, Cambridge, MA, USA
May. 2018 – Aug. 2018
Programmer Analyst in Cognizant Technology Solutions, Kolkata, WB, India
Aug. 2014 – Apr. 2016

PUBLICATIONS

Journal Publications

A. Bose, B. Tang, M. Soltanalian, and J. Li, "Mutual Interference Mitigation for Multiple Connected Automotive Radar Systems," submitted in IEEE Transactions on Vehicular Technology, 2021.

A. Bose, B. Tang, W. Huang, M. Soltanalian, and J. Li, "Waveform Design for Mutual Interference Mitigation in Automotive Radar," submitted in IEEE Transactions on Signal Processing, 2021.

A. Bose, S. Khobahi and M. Soltanalian, "Efficient Waveform Covariance Matrix Design and Antenna Selection for MIMO Radar," Signal Processing, vol. 183, no. 107985, June, 2021.

A. Ameri, A. Bose, J. Li and M. Soltanalian, "One-Bit Radar Processing With Time-Varying Sampling Thresholds," in IEEE Transactions on Signal Processing, vol. 67, no. 20, pp. 5297-5308, Oct, 2019.

A. Bose and M. Soltanalian, "Constructing Binary Sequences With Good Correlation Properties: An Efficient Analytical-Computational Interplay," in IEEE Transactions on Signal Processing, vol. 66, no. 11, pp. 2998-3007, June, 2018.

Conference Publications

A. Bose, A. Ghauri, and M. Soltanalian, "Limits of Transmit Beamforming for Massive MIMO Radar," 2020 IEEE Asilomar Conference on Signals, Systems, and Computers, Pacific Grove, CA, USA, 2020.

S. Khobahi, A. Bose, and M. Soltanalian, "Deep One-Bit Compressive Autoencoder," 2020 IEEE Statistical Signal Processing Workshop (SSP), Rio de Janeiro, Brazil, 2020. submitted.

C. Agarwal, S. Khobahi, A. Bose, M. Soltanalian, and D. Schonfeld, "Deep-URL: A Model-Aware Approach to Blind Deconvolution Based on Deep Unfolded Richardson-Lucy Network," 2020 IEEE International Conference on Image Processing (ICIP), Abu Dhabi, UAE, 2020. submitted.

S. Khobahi, A. Bose, and M. Soltanalian, "Deep Radar Waveform Design for Efficient Automotive Radar Sensing," 2020 IEEE Sensor Array and Multichannel Signal Processing Workshop (SAM), Hangzhou, China, 2020. submitted.

A. Bose, S. Khobahi, and M. Soltanalian, "Joint Optimization of Waveform Covariance Matrix and Antenna Selection for MIMO Radar," 2019 IEEE Asilomar Conference on Signals, Systems, and Computers, Pacific Grove, CA, USA, 2019.

A. Bose, A. Ameri, and M. Soltanalian, "Waveform Design for One-Bit Radar Systems Under Uncertain Interference Statistics," 2019 IEEE Asilomar Conference on Signals, Systems, and Computers, Pacific Grove, CA, USA, 2019.

P. Wang *et al.*, "Learning-Based Shadow Mitigation for Terahertz Multi-Layer Imaging," 2019 44th International Conference on Infrared, Millimeter, and Terahertz Waves (IRMMW-THz), Paris, France, 2019, pp. 1–2.

A. Bose *et al.*, "THz Multi-Layer Imaging via Nonlinear Inverse Scattering," 2019 44th International Conference on Infrared, Millimeter, and Terahertz Waves (IRMMW-THz), Paris, France, 2019, pp. 1–2.

A. Ameri, A. Bose and M. Soltanalian, "Comprehensive Personalized Ranking Using One-Bit Comparison Data," 2019 IEEE Data Science Workshop (DSW), Minneapolis, MN, USA, 2019, pp. 338–342.

I. A. Arriaga-Trejo, A. Bose, A. G. Orozco-Lugo and M. Soltanalian, "Design of Unimodular Sequence Sets with Good Correlation and Complementary Correlation Properties," 2018 IEEE Global Conference on Signal and Information Processing (GlobalSIP), Anaheim, CA, USA, 2018, pp. 121–125.

A. Bose, I. A. Arriaga-Trejo, A. G. Orozco-Lugo and M. Soltanalian, "Generalized Cyclic Algorithms for Designing Unimodular Sequence Sets with Good (Complementary) Correlation Properties," 2018 IEEE 10th Sensor Array and Multichannel Signal Processing Workshop (SAM), Sheffield, UK, 2018, pp. 287–291.

A. Bose, A. Ameri, M. Klug and M. Soltanalian, "Low-Rank Matrix Recovery from One-Bit Comparison Information," 2018 IEEE International Conference on Acoustics, Speech and Signal Processing (ICASSP), Calgary, AB, Canada, 2018, pp. 4734–4738.

A. Bose, N. Mohammadi and M. Soltanalian, "Designing Signals with Good Correlation and Distribution Properties," 2018 IEEE International Conference on Acoustics, Speech and Signal Processing (ICASSP), Calgary, AB, Canada, 2018, pp. 4349–4353.

A. Bose and M. Soltanalian, "Efficient construction of polyphase sequences with optimal peak sidelobe level growth," 2017 IEEE Global Conference on Signal and Information Processing (GlobalSIP), Montreal, QC, Canada, 2017, pp. 81–85.

A. Bose and M. Soltanalian, "Non-convex shredded signal reconstruction via sparsity enhancement," 2017 IEEE International Conference on Acoustics, Speech and Signal Processing (ICASSP), New Orleans, LA, USA, 2017, pp. 4691–4695.

C. Agarwal, A. Bose, S. Maiti, N. Islam and S. K. Sarkar, "Enhanced data hiding method using DWT based on Saliency model," 2013 IEEE International Conference on Signal Processing, Computing and Control (ISPCC), Solan, 2013, pp. 1–6.

PRESENTATIONS

Invited Articles on Conferences

2020 IEEE Asilomar Conference on Signals, Systems and Computers

Nov. 2020

2020 IEEE Sensor Array and Multichannel Signal Processing Workshop, Hangzhou, China

Jun. 2019

2019 IEEE Asilomar Conference on Signals, Systems, and Computers, Pacific Grove, CA, USA

Nov. 2019

Conference Presentations

2019 IEEE Asilomar Conference on Signals, Systems, and Computers, Pacific Grove, CA, USA

Nov. 2019

2019 IEEE Data Science Workshop (DSW), Minneapolis, MN, USA

Jun. 2019

2017 IEEE Global Conference on Signal and Information Processing (GlobalSIP), Montreal, QC, Canada
Nov. 2017

Poster Presentations

2018 IEEE International Conference on Acoustics, Speech and Signal Processing (ICASSP), Calgary, AB, Canada
Apr. 2018

2017 IEEE International Conference on Acoustics, Speech and Signal Processing (ICASSP), New Orleans, LA, USA
Mar. 2017

AWARDS

Signal Processing Society Chicago Chapter Appreciation, IEEE
Dec. 2019

Associate of the Month, Cognizant Technology Solutions
May 2014

Winner, The Telegraph Knowhow Innovation Hub, INFOCOM 10-11, jointly organized by The Telegraph, Knowhow and the National Council of Science Museums
Jan. 2011

Educational Scholarship from the Central Government of India
2008 – 2012

MEMBERSHIPS

IEEE Signal Processing Society
Siam Student Member

SERVICES

Journal Article Referee at
- IEEE Transaction of Signal Processing (2018 – Present)
- IEEE Signal Processing Letters (2018 – Present)
- Elsevier Signal Processing (2018 – Present)
- IET Signal Processing (2020 – Present)
- IEEE Transactions on Aerospace and Electronic Systems (2020 – Present)

Conference Paper Referee at
- IEEE VTC 2018
- EUSIPCO 2019

IEEE SAM 2020

IEEE YP Chair Chicago Chapter, IEEE Signal Processing Society

Apr. 2019 – Present

Vice President, UIC ECE Journal Club

Aug. 2016 – Aug. 2017

Chief Robotics Coordinator, Future Institute of Engineering and Management

Apr. 2011 – May 2012